UNIVERSITY OF ALBERTA

Numerical Modeling of Hydraulic Fracturing

by

Ali Pak ©

A thesis submitted to the Faculty of Graduate Studies and Research in partial fulfillment of the requirements for the degree of Doctor of Philosophy

in

Geotechnical Engineering

Department of Civil and Environmental Engineering

Edmonton, Alberta

Spring 1997

National Library of Canada
Acquisitions and Bibliographic Services
395 Wellington Street
Ottawa ON K1A 0N4
Canada

Bibliothèque nationale du Canada
Acquisitions et services bibliographiques
395, rue Wellington
Ottawa ON K1A 0N4
Canada

Your file Votre référence

Our file Notre référence

The author has granted a non-exclusive licence allowing the National Library of Canada to reproduce, loan, distribute or sell copies of his/her thesis by any means and in any form or format, making this thesis available to interested persons.

L'auteur a accordé une licence non exclusive permettant à la Bibliothèque nationale du Canada de reproduire, prêter, distribuer ou vendre des copies de sa thèse de quelque manière et sous quelque forme que ce soit pour mettre des exemplaires de cette thèse à la disposition des personnes intéressées.

The author retains ownership of the copyright in his/her thesis. Neither the thesis nor substantial extracts from it may be printed or otherwise reproduced with the author's permission.

L'auteur conserve la propriété du droit d'auteur qui protège sa thèse. Ni la thèse ni des extraits substantiels de celle-ci ne doivent être imprimés ou autrement reproduits sans son autorisation.

0-612-21618-7

Canada

UNIVERSITY OF ALBERTA

Library Release Form

Name of the Author: **Ali Pak**

Title of Thesis: **Numerical Modeling of Hydraulic Fracturing**

Degree: **Doctor of Philosophy**

Year this Degree Granted: **1997**

Permission is hereby granted to the University of Alberta Library to reproduce single copies of this thesis and lend or sell such copies for private, scholarly, or scientific research purposes only.

The author reserves all other publication and other rights in association with the copyright in the thesis, and expect as hereinbefore provided, neither the thesis nor any substantial portion thereof may be printed or otherwise reproduced in any material form whatever without the author's prior written permission.

Ali Pak

#68 Nasrin, Laleh St.,
Jomhori Ave., 11398,
Tehran, Iran

Date: Jan. 15, 1997

UNIVERSITY OF ALBERTA

FACULTY OF GRADUATE STUDIES AND RESEARCH

The undersigned certify that they have read, and recommend to the Faculty of Graduate Studies and Research for acceptance, a thesis entitled *Numerical Modelling of Hydraulic Fracturing* by *Ali Pak* in partial fulfillment of the requirements for the degree of Doctor in Philosophy in Geotechnical Engineering.

Prof. D.H. Chan (Supervisor)

Prof. N.R. Morgenstern (Chairman)

Prof. J.D. Scott

Prof. P.M. Steffler

Prof. D. Li

Prof. H.H. Vaziri (External examiner)

Date: Dec. 4, 1996

ABSTRACT

Hydraulic fracturing is a widely used method for enhancing oil extraction in the petroleum industry. Application of this method has been extended from rocks to porous media such as oilsand. In spite of the technological advances in the techniques of in-situ hydraulic fracturing, the industry lacks a realistic and reliable numerical model in order to design a cost-effective and efficient hydraulic fracturing treatment. This is due to the complex interactions among the different mechanisms that are involved in hydraulic fracturing, namely ground deformation, fluid flow, heat transfer and fracturing process.

In modeling the hydraulic fracturing process in a multiphase medium in a non-isothermal condition, three governing partial differential equations of equilibrium, continuity of fluid flow, and heat transfer are solved simultaneously in a fully implicit (coupled) manner using the finite element method. In order to model discrete fractures the node splitting technique and 6-node isoparametric rectangular fracture elements are used. The fracture element is capable of transmitting fluid and heat as well as modeling the leak-off of fluid from the fracture into the surrounding material.

The thermal hydro-mechanical fracture finite element model developed in this research has been verified by comparing the numerical results with existing analytical and numerical solutions for thermal consolidation problems. The model was also validated by simulating large scale hydraulic fracture laboratory experiments.

The numerical results from modeling large scale hydraulic fracture tests agree well with the experimental observations which indicate that fracture propagation in the uncemented granular materials (such as oilsand) can be different from fracture in rocks and other cemented materials. In granular materials, a fracture zone is more likely to occur rather than a distinct planar fracture. The numerical model emphasizes the importance of the pore fluid pressures in the initiation and propagation of fractures in the soils. Elastic and elastoplastic analysis show that in uncemented porous materials, tensile fracture and shear failure occur simultaneously due to the effect of high pore pressure.

The developed model can be used in other engineering applications such as well communication problem, geotechnical aspects of temperature variation in soils, study of hydraulic fracturing in embankment dams, and increasing soil permeability through hydraulic fracturing for remediation of contaminated sites.

Acknowledgment

I am thankful to God, the creator of the universe, for his innumerable blessings.

I would like to express my deep appreciation to my supervisor, Dr. Dave Chan for his expert guidance, encouragements, and extraordinary patience throughout this research. I also thank all of the professors and staff of the geotechnical group of the university of Alberta to whom I am indebted for my knowledge in geotechnical engineering.

The valuable advice and information provided by Dr. S. Tortike are gratefully acknowledged.

I sincerely thank my parents for their love, devotion, and continued encouragement to gain further education. I express my gratitude to my wife and my children for staying with me and putting up with me during my study in Canada. Without their help I could hardly have made it this far.

I gratefully acknowledge the financial support of the ministry of culture and higher education of Iran. This study was partly funded by NSERC of Canada which is also thankfully acknowledged.

I dedicate this thesis to my parents, my wife, and my children.

Table of Contents

Chapter 1 Introduction 1
1.1 General 1
1.2 Petroleum reservoir simulation 3
1.3 Hydraulic fracture modeling 3
1.4 Problems in modeling hydraulic fracturing for the oilsand industry 5
1.5 Other applications of hydraulic fracturing 8
1.6 Scope of this research 10

Chapter 2 Geotechnical Aspects of Heavy Oil Recovery 13
2.1 Recovery techniques 13
2.2 Recovery methods for oilsand deposits 14
2.2.1 Thermal recovery for oilsand deposits 15
2.3 Oilsand's geomechanical behaviour 19
2.3.1 Oilsand characteristics 19
2.3.2 Athabasca and Cold Lake oilsands 20
2.3.3 Effects of temperature on oilsand 21
2.3.4 Modeling of stress-strain behaviour for oilsand 23

Chapter 3 Literature Survey on Numerical Modeling of hydraulic fracturing 33
3.1 Isothermal fluid flow in a deformable reservoir 33
3.2 Thermal fluid flow in a deformable reservoir 36
3.3 Inclusion of (hydro)fracture mechanics 38
3.4 Discussion 40

Chapter 4 Mathematical and finite element formulation 41
4.1 General 41
4.2 Equilibrium equation 43
4.3 Fluid flow continuity equation 47
4.4 Heat transfer equation 55
4.5 Coupling process 61

Chapter 5 Modeling of hydraulic fracture 65
5.1 Introduction 65
5.2 Natural fractures vs. induced fractures 66
5.3 Effects of natural fractures on hydraulic fracturing process 67
5.4 Fracture mechanics for geomaterials 68
5.4.1 Different modes of fracture 68
a) Tensile mode 68
b) Shear modes 69
c) Mixed modes 70
5.4.2 LEFM and EPFM 70
5.4.3 Criteria for fracture initiation and propagation 71
5.5 Numerical modeling of fracture 79
5.5.1 Smeared approach 80
5.5.2 Dual porosity model 81
5.5.3 Discrete approach 81
5.6 Modeling discrete fractures using the finite element method 82
5.6.1 Elements for predefined fractures (interface elements) 82
a) Thin layer solid elements 82
b) Zero thickness joint elements 83
5.6.2 Elements for advancing fractures 83
5.6.2.1 Crack at the element boundaries 83
a) Nodal grafting method 83
b) Node splitting technique 84
c) Distinct element method 84
5.6.2.2 Crack inside elements 84
5.6.2.3 Dynamic remeshing and adaptive mesh 85
5.7 Modeling moving front of fluid and heat in the fractures 86
5.7.1 Fluid flow inside the fractures 86
5.7.2 Heat transfer inside fractures 87
5.7.3 Leak-off problem 87
5.8 Hydraulic fracture modeling in this study 88

Chapter 6 Implementation and verification of the model 99
6.1 Introduction 99
6.2 Program verification 101
6.3 Patch tests 102
6.3.1 Coupling of deformation and fluid flow 102
6.3.2 Coupling of deformation and heat transfer 102
6.3.3 Coupling of fluid flow and heat transfer 103
6.4 Plane strain thermo-elastic consolidation 103
6.5 Axisymmetric thermo-elastic consolidation 104
6.6 Thermal hydro-mechanical fracture propagation 106
6.7 Discussion 107

Chapter 7 Modeling hydraulic fracture experiments on large scale triaxial chambers 131
7.1 Introduction 131
7.2 Earlier experimental studies 131
7.3 Description of large scale hydraulic fracture experiments 135
7.3.1 Material used 136
7.3.2 Procedures 136
7.3.3 Review of the hydraulic fracture experiments 137
7.4 Numerical modeling of the chamber tests 140
7.4.1 Fracture propagation in elastic medium 141
7.4.2 Effect of changes in soil permeability on the fracture 144
7.4.3 Effect of different fracture initiation criteria 145
7.4.3 Elastoplastic fracture propagation 146
7.5 Discussion 148

Chapter 8 Summary and Conclusions 187
8.1 Summary 187
8.2 The developed computer program and its applications 189
8.3 Conclusions 190
8.3.1 Modeling of large scale hydraulic fracture experiments 190
8.3.2 Pattern of hydraulic fracture in different geomaterials 191
8.4 Further research 194

References 196

Appendix A Details of the finite element formulation 213
A.1 Rectangular isoparametric element 213
A.2 Triangular element 217
A.3 Boundary conditions 220
A.3.1 Traction boundary conditions 221
A.3.2 Flow and Heat boundary conditions 224

List of Tables:

Chapter 6.

Table (6-1) Input data for patch tests 110
Table (6-2) Input data for thermoelastic consolidation and fracture problems 111
Table (6-3) Time increment for thermo-consolidation problems 112
Table (6-4) Fracturing sequence in time 112

Chapter 7.

Table (7-1) Summary of hydraulic fracturing test program (Phase 1,2 and 3) 152
Table (7-2) Input data for modeling of fracture in chamber test 153

List of Figures:

Chapter 1.
Figure (1-1) Typical hydraulic fracturing treatment in petroleum industry 12
Figure (1-2) Smeared approach vs. discrete approach for modeling of fracture 12

Chapter 2.
Figure (2-1) Different methods for extraction of oilsands 26
Figure (2-2) Steam Assisted Gravity Drainage method (SAGD) 27
Figure (2-3) HAS Drive method 27
Figure (2-4) Oilsand structure 28
Figure (2-5) Grain fabric for oilsand compare to dense sand 28
Figure (2-6) Typical results of direct shear box test on oilsand 29
Figure (2-7) Comparison of behaviour of Athabasca and Cold Lake oilsands 30
Figure (2-8) Effect of temperature on the soil hydraulic conductivity 31
Figure (2-9) Effect of temperature on the viscosity of in-situ fluid 31
Figure (2-10) Behaviour of oilsand under different confining stresses 32

Chapter 4.
Figure (4-1) Boundary conditions of a typical domain 64

Chapter 5.
Figure (5-1) Schematic representation of linearly propagating fracture according to Perkins and Kern (1961) 92
Figure (5-2) Schematic representation of linearly propagating fracture according to Geertsma and deKlerk (1969) 92
Figure (5-3) Stresses and displacements around a crack tip of mode I 93
Figure (5-4) Stresses and displacements around a crack tip of mode II 93
Figure (5-5) Stresses and displacements around a crack tip of mode III 94
Figure (5-6) Crack tip plastic zone and applicability of different analyses schemes 94
Figure (5-7) Griffith criterion of specific surface energy 95
Figure (5-8) Irwin criterion of stress intensity factor 95
Figure (5-9) Crack tip plastic zone (Irwin method) 96
Figure (5-10) Crack tip plastic zone (Dugdale method) 96
Figure (5-11) Comparing dimensions of plastic zone in plane stress and plane strain 97
Figure (5-12) Closed contours for J-integral 97
Figure (5-13) Crack tip coordinates for mixed mode fracture criteria 98
Figure (5-14) 6-node rectangular fracture element 98

Chapter 6.

Figure (6-1) Finite element mesh and boundary conditions for coupling of deformation and fluid flow analysis 113
Figure (6-2) Variation of vertical displacements with time 114
Figure (6-3) Variation of pore pressure with time 114
Figure (6-4) Finite element mesh and boundary conditions for coupling of deformation and heat transfer analysis 115
Figure (6-5) Variation of displacements with time 116
Figure (6-6) Variation of temperature with time 116
Figure (6-7) Finite element mesh and boundary conditions for coupling of fluid flow and heat transfer 117
Figure (6-8) Variation of temperature with time 118
Figure (6-9) Variation of pore pressure (induced by temperature) with time 118
Figure (6-10) Variation of horizontal displacement with time 119
Figure (6-11) Finite element mesh and boundary conditions for plane strain thermoelastic consolidation 120
Figure (6-12) Variation of settlement with time 121
Figure (6-13) Variation of pore pressure with time 121
Figure (6-14) Variation of temperature with time 122
Figure (6-15) Finite element mesh and boundary conditions for axisymmetric thermoelastic consolidation 123
Figure (6-16) Comparison between analytical and numerical solutions for horizontal displacement 124
Figure (6-17) Comparison between analytical and numerical solutions for pore pressure 124
Figure (6-18) Comparison between analytical and numerical solutions for temperature 125
Figure (6-19) Finite element mesh and boundary conditions for one dimensional fracture propagation 126
Figure (6-20) Variation of pore pressure at some nodes in the soil and at the fracture 127
Figure (6-21) Variation of pore pressure in the soil due to the effect of fracturing 127
Figure (6-22) Variation of pore pressure along the fracture 128
Figure (6-23) Variation of temperature in the soil and at the fracture 129
Figure (6-24) Variation of soil temperature due to hot fluid injection 129
Figure (6-25) Variation of temperature along the fracture due to hot fluid injection 130

Chapter 7.

Figure (7-1) Schematic view of large scale triaxial chamber 154
Figure (7-2) Typical drained triaxial test on McMurray oilsand 155
Figure (7-3) Typical drained triaxial test on Lane Mountain sand 156
Figure (7-4) 'p-q' diagram for Lane Mountain sand 157
Figure (7-5) Plan view of instrumentation around the injection zone 158

Figure (7-6) Response of piezometers, test #4 of phase I 159
Figure (7-7) Fracture Pattern, test #4 of phase I 160
Figure (7-8) Response of piezometers, test #5 of phase II 161
Figure (7-9) Fracture Pattern, test #5 of phase II 162
Figure (7-10) Response of piezometers, test #1 of phase III 163
Figure (7-11a) Fracture pattern, test #1 of phase III 164
Figure (7-11b) Typical photographs of fracture pattern, test #1 of phase III 165
Figure (7-12) Sample dimensions and position of internal instrumentation for test 4, phase 2 166
Figure (7-13) Finite element mesh and boundary conditions for modeling hydraulic fracture test #4 of phase II 167
Figure (7-14) Comparison between calculated and measured pore pressure at the injection zone 168
Figure (7-15) Comparison between calculated and measured pore pressure at piezometer 100 mm above the injection zone 169
Figure (7-16) Comparison between calculated and measured pore pressure at piezometer 100 mm below the injection zone 169
Figure (7-17) Pattern of fracture propagation from numerical model 170
Figure (7-18) Fracture pattern from laboratory experiment 171
Figure (7-19) Pore pressure variation at the injection zone with different permeabilities for fracture elements 172
Figure (7-20) Pattern of fracture propagation from numerical modeling (K_{frac}=1000K_{mtx}) 173
Figure (7-21) Pattern of fracture propagation from numerical modeling (K_{frac}=1000K_{mtx}) 174
Figure (7-22) Pore pressure variation with different permeabilities for fracture elements at piezometer 100mm above the injection zone 175
Figure (7-23) Pore pressure variation with different permeabilities for fracture elements at piezometer 100mm below the injection zone 175
Figure (7-24) Fracture pattern with prescribed pore pressure (simulating lab recorded pore pressures) 176
Figure (7-25) Pore pressure variation with change in permeability of soil matrix 177
Figure (7-26) Fracture pattern with change in permeability of soil matrix 178
Figure (7-27) Pattern of fracture at 30 seconds with different fracture criteria 179
Figure (7-28) Pore pressure variation at the injection zone with different fracture criteria 180
Figure (7-29) Pore pressure variation at the injection zone with associated Mohr-Coulomb model 181
Figure (7-30) Fracture pattern with associated Mohr-Coulomb model 182
Figure (7-31) Principal stress ratio indicating the yield zone at second 1 after starting the injection 183
Figure (7-32) Principal stress ratio indicating the yield zone at second 4 after starting the injection 184
Figure (7-33) Principal stress ratio indicating the yield zone at second 8 after starting the injection 185

Figure (7-34) Patterns of hydraulic fracture in different geomaterials 186

Appendix A

Figure (A-1) 8-node rectangular element for displacements 228
Figure (A-2) 4-node rectangular element for pore pressure and temperature 228
Figure (A-3) 6-node triangular element 229
Figure (A-4) Local and global coordinates for 8-node rectangular element 229
Figure (A-5) Traction on the element boundary in two directions 230
Figure (A-6) Local and global coordinates for 6-node triangular element 230
Figure (A-7) 6-node rectangular fracture element 231

Nomenclature:

a	crack length
B	derivative of shape function *[N]*
C	cohesion
c'	damping coefficient
C_b	compressibility of bulk soil matrix
C_s	compressibility of solid particles
C_p	heat capacity of fluid at constant pressure
C_v	heat capacity of fluid at constant volume
D_{ijkl}	general matrix for elastoplastic soil/rock behaviour
d	plastic zone length(Dugdale)
d_p	plastic zone diameter(Irwin)
E	internal energy per unit mass, modules of elasticity
E_f	internal energy per unit mass of fluid
E_s	internal energy per unit mass of soil/rock
F	body force, external load, work done by external load
f	fluid flux
g	acceleration of gravity
G	fluid sink or source, shear modules, crack extension force
H	total head(m.)
h_f	enthalpy of fluid
i	hydraulic slope, index notation accepting 1,2 or 3
j	index notation accepting 1,2 or 3
J	Jacobian, mechanical equivalent of heat, value resulted from J-integral expression
k	absolute permeability (m^2), index notation accepting 1,2 or 3
K	hydraulic conductivity (m/sec.)
K_I	stress intensity factor for mode I
K_{II}	stress intensity factor for mode II
K_{III}	stress intensity factor for mode III
K_o	in-situ stress ratio
L	length
L_e	volumetric thermal energy flux
m	Kronecker vector
m'	mass coefficient
M_σ	volume heat capacity of soil/ rock
N	shape function matrix for displacements
n	unit vector normal to the surface
N_P	shape function vector for pore pressure
N_T	shape function vector for temperature
P	pore fluid pressure
Q	heat sink or source
R	radius

r	radius in the polar coordinates
S	degree of saturation
S_σ	surface boundary on which stresses are applied ($\bar{t}_s$)
S_L	surface boundary on which thermal flux is specified
S_P	surface boundary on which a prescribed pore pressure is applied
S_T	surface boundary on which a prescribed temperature is applied
S_u	surface boundary on which a prescribed displacement is applied
S_v	surface boundary on which a flux is specified
T	temperature
t	time
T_s	applied traction
U	strain energy, elastic strain energy
U_o	strain energy of uncracked element subjected to external load
U_p	potential energy
u	displacement in the x direction
v	displacement in the y direction, apparent velocity of fluid
V	soil/rock matrix velocity
V_b	volume of bulk soil matrix
V_s	volume of soil grains
V_v	volume of voids
w	displacement in the z direction
x	horizontal coordinate/axis
y	horizontal coordinate/axis
z	vertical coordinate/axis
Z	velocity equivalent
α	Biot's coefficient
ϕ	porosity of the soil mass, angle of internal friction, shape functions
θ	central angle in the polar coordinates, factor for time discretization (finite difference)
λ	coefficient of conductivity for soil/rock
δ	crack opening (aperture)
∇	del operator
ρ	density of fluid
Δ	increment of a variable
Γ	surface of the domain, perimeter of the plate
γ	unit weight of fluid (=ρg)
γ_s	specific surface energy
γ_{xy}	shear strain
δ	variation of a variable, Kronecker delta
μ	viscosity of fluid
Ω	volume of the domain
σ	stress
σ_y	uniaxial yield stress
σ'	effective stress

τ	shear stress
α_f	Isobar thermal expansion coefficient of fluid
α_s	coefficient of thermal expansion for soil/rock matrix
β_T	Isothermal pressure densification coefficient of fluid
ε	total strain
ε_v	volumetric strain
ε_d	deviatoric strain
ε_x	strain in the x direction
ε_y	strain in the y direction
ε_z	strain in the z direction
ν	Poisson's ratio
ω	weighting factor in W.R.M., strain energy density
ξ	local coordinate axis
η	local coordinate axis
ζ_1	triangular coordinate
ζ_2	triangular coordinate
ζ_3	triangular coordinate

Subscripts:

,	derivative with respect to the coordinate axis
c	critical value
h	horizontal value
o	initial value
P	related to pore pressure
T	related to temperature
t	value at time 't'
v	vertical value

Superscripts:

*	nodal value
_	prescribed value
.	first derivative with respect to time
..	second derivative with respect to time
T	transpose of the matrix

Symbols:

< >	row vector
{}	column vector
[]	matrix

Chapter 1

Introduction

1.1 General

Hydraulic fracturing is a technique consisting of pumping a fluid into an oil-rich layer in the ground at high enough rates and pressures to create and extend a fracture hydraulically. The fluid that is used for injection is usually water blended with sand and/or some special chemicals. Hydraulic fracturing has made a significant contribution to enhancing oil and gas production rates. The technique was first introduced to the industry in 1947 and is now a standard operating practice. By 1981, more than 800,000 hydrofracturing treatments had been performed and recorded. As of 1988, this has grown to exceed 1 million. Today about 35 to 40 percent of all currently drilled wells are hydraulically fractured (Veatch Jr. et al., 1989).

Since its inception, hydraulic fracturing has developed from a simple, low-volume, low rate reservoir stimulation technique to a highly engineered and complex procedure that is used for many purposes. Figure (1-1) depicts a typical hydraulic fracturing process in the petroleum industry. The procedure is as follows: first, a neat fluid such as water (called 'pad') is pumped into the well at the desired depth (pay zone) to initiate the fracture and to establish its propagation. This is followed by pumping a slurry of fluid mixed with a propping agent such as sand (which is often called a 'proppant'). This slurry continues to extend the fracture and concurrently carries the proppant deeply into the fracture. After pumping, the injected fluid chemically breaks down to a lower viscosity and flows back out of the well, leaving a highly conductive propped fracture for oil and/or gas to flow easily from the extremities of the formation

into the well. It is generally assumed that the induced fracture has two wings extending in opposite directions from the well and is oriented more or less in a vertical plane. Other fracture configurations such as horizontal fractures are also reported to occur, but they constitute a relatively low percentage of the situations documented. Experiences indicate that at depths below 600 meters (2000 ft), fractures are usually oriented vertically. At shallow depths, horizontal fractures have been reported (Veatch Jr. et al., 1989). The fracture pattern, however, may not be the same for different types of soils and rocks.

Over the years, the technology associated with fracturing has improved significantly. A number of fracturing fluids (injectant) have been developed for different types of reservoirs ranging from shallow, low-temperature formations to those located in deep, hot areas. Many different types of proppants have been developed, ranging from silica-sand (standard) to high-strength materials, such as sintered bauxite. The latter is used in the deep formations where fracture closure stresses exceed the sand capabilities. New analytical and diagnostic methods and design models have emerged, and the service industry has continually developed new equipment to meet emerging challenges (Veatch Jr. et al., 1989).

Although technology in hydraulic fracturing is advancing significantly, its design still involves a good deal of judgment and practical experience. After 50 years of fracturing practice and research, the ability to determine the fracture shape, dimensions (length, width, height), azimuths, and fracture conductivities is still not fully developed. In addition, the ability to measure in-situ rock properties and stress fields which have a significant affect on fracture propagation is not perfected. Consequently, the optimization of hydraulic fracturing treatments is often subject to limitations (Veatch Jr. et al., 1989). A numerical model capable of analyzing different aspects of reservoir engineering as well as fracture mechanics can be a valuable tool to overcome many uncertainties in the design of hydraulic fracturing and help the industry to optimize the process. As a result, reservoir engineering and fracture mechanics are two important subjects that should be used for developing the numerical model.

1.2 Petroleum Reservoir Simulation

Simulation of petroleum reservoirs requires a clear understanding of flow in porous media. Since oil, water, and gas can flow simultaneously in a heavy oil reservoir, it is necessary to understand the mechanism of multiphase unsaturated flow. The effect of high temperature, which causes interactions between oil, water, and gas, further complicates the problem. In general, the pressures of these three phases can be different and the pressure difference between any two phases is attributed to 'capillary pressure'. Large changes in pressures either cause gas to dissolve into the fluid or the fluid to volatile into the gas phase. This results in a new mass balance in the system which causes the degree of saturation of each phase to change.

For decades petroleum engineers have been developing numerical simulators for modeling oil reservoirs and hydraulic fracturing. These simulators solve the fluid mass balance equation and/or heat transfer equation in the reservoir. Most of these simulators are based on the finite difference method and are developed for some special boundary conditions. The degree of sophistication of these simulators varies considerably. In some cases, the ability to make a reasonably accurate prediction of the response of a reservoir is poor. This is due, in part, to the lack of geomechanics in some reservoir models (Tortike, 1991). A detailed deformation analysis of the reservoir is required to improve the results of the conventional reservoir simulators.

Modeling of a thermal multiphase flow in a deformable oil reservoir requires coupling of at least three basic conservation laws for fluid flow, heat flow and applied loads. Where uncemented heavy oil deposits such as oilsands are of interest, the peculiar characteristics of oilsand should also be considered in the model. Oilsand exhibits significantly different behaviour from that of typical cemented sandstone and limestone (which are usually characterized by linear and nonlinear elastic behaviour, respectively). Oilsand's behaviour is elastoplastic and temperature dependent which will be discussed later.

1.3 Hydraulic Fracture Modeling

So far fracture modeling has been carried out in three different ways: the discrete approach, the smeared approach, and the dual porosity approach.

Discrete fracture approach is used where few fractures exist. In contrast, when the fracturing is so intense that the whole medium can be represented by a uniformly damaged material with modified material characteristics (for example modified equivalent stiffness and/or permeability), the smeared approach would be a more reasonable choice. It should be noted that in the smeared approach no fracture is introduced inside the medium and fractures are modeled by modifying the material characteristics in the fractured zone. Therefore the basic assumptions of continuum mechanics hold true for the smeared approach but not for the discrete approach. This point is illustrated in Figure (1-2). The dual porosity approach is basically used for 'naturally fractured' oil reservoirs. These types of reservoirs, in theory, are modeled as blocks stacked over each other with low porosity and low permeability. Between the blocks, fractures with very high porosity and permeability exist. Fluid flow in the reservoir consists of two parts: flow through the fractures with high permeability, and flow through the blocks with low permeability. All of these approaches will be discussed, in more detail, in chapter 5.

Fracture mechanics theories, which were originally developed for metals, have been used successfully for geological materials in recent years. Linear elastic fracture mechanics *(L.E.F.M)* or elastoplastic fracture mechanics *(E.P.F.M)* have been used for analyzing fractures in soils and rocks. They are used to establish criteria for crack initiation, crack propagation, and crack arrest (which will be discussed later). Modeling of fracture requires a knowledge of geological conditions in the ground. Local stress fields and variations of stresses between adjacent formations are often thought to be the main factors which control fracture orientation and fracture growth.

Regional stresses in the ground can have an impact on the azimuthal trend of the hydraulically created fractures. It is usually believed that the fracture propagates perpendicular to the direction of the minimum principal stress; i.e., tensile fracture is the prime mechanism in hydraulic fracturing. Recently, the possibility of shear failure

before tensile failure has been of interest especially where the injection rate is high and the amount of fluid leak-off into the formation is significant.

The importance of performing a deformation analysis, once again, emerges here because fracturing criteria are based on the stresses and deformations in the ground. Therefore, in order to obtain a realistic model for design purposes, the geomechanical behaviour of the ground has to be accounted for in reservoir simulation and hydraulic fracture analysis.

1.4 Problems in Modeling Hydraulic Fracturing for the Oilsand Industry

By application of the hydraulic fracturing technique to uncemented materials such as oilsands some new problems have emerged. These problems originate from complex interactions among soil/rock, fluid flow, and heat transfer when the fracturing occurs on one hand, and peculiar characteristics of the oilsand on the other hand. Conventional design methods, which have been developed for hydraulic fracturing in cemented rocks, are not capable of providing insight into the problem. Fracture orientation and pattern are quite different from what conventional methods usually predict (Settari, 1989).

a) Considerations regarding oilsands

Oilsands have a behaviour that is distinctly nonlinear even under in-situ stress conditions. Undisturbed oilsands have strength characteristics similar to that of a soft sandstone. This relatively high strength is attributed to the frictional contact among densely packed interlocking sand grains. This kind of fabric which has been identified by Dusseault and Morgenstern (1978) is called 'locked sand'. However, injecting hot fluid at a high rate into the oilsand can cause disturbance and disruption of material fabric by forcing individual sand grains to slide relative to each other in order to accommodate the induced mechanical and thermal strains. These structural changes are also nonlinear and inelastic. Failure of the material after plastic straining and dilation associated with shear deformation are some of the most important aspects of oilsand behaviour. Shear dilation will most likely create zones of higher permeability and higher compressibility and will alter the stress field in the ground (Tortike, 1991). Such

an alteration affects initiation and propagation of fractures. Oilsand deformation behaviour can be predicted by employing a suitable elastoplastic constitutive model. This model should be able to take into account the effects of temperature on the material behaviour. Unfortunately, there is no such model presently available that can be used with confidence; thus, the effect of changes in temperature on the yield surface is currently ignored. Some researchers have tried to incorporate the effect of temperature on the oilsand behaviour in an indirect way. For example, Campanella and Mitchell (1968) suggested the application of a 'coefficient of structural volume change' in the analysis of oilsand. They explained the phenomenon of reorientation of sand grains by considering the reduction of bitumen viscosity and associated weakening of bonds between the sand grains caused by an increase in the temperature.

Hydraulic conductivity (effective permeability in petroleum literature) of undisturbed oilsand is low because of the high viscosity of the bitumen. This causes the soil to respond in an undrained manner to external loading. During unloading process, if the confining stress decreases below the gas-liquid saturation pressure, the dissolved gas may come out of the solution which drastically increases the compressibility of the medium. Temperature increase can also result in evolution of dissolved gasses provided that it raises the gas-liquid saturation pressure above the level of confining stresses (Vaziri, 1986).

Drastic changes of bitumen viscosity causes severe problems in numerical modeling. Observations have shown that viscosity of bitumen increases with pressure linearly (or close to linear form) and decreases with temperature exponentially. Although there is no theoretical method to relate these parameters, the number of empirical relationships is enormous. These issues should be addressed in the modeling of hydraulic fracturing in oilsands.

b) Considerations involved in hydraulic fracturing

Application of hydraulic fracturing to oilsands poses a problem because the geometry of fractures and their effectiveness in the extraction process are not known. Fracture locations and orientations are functions of lithology, material properties, pore fluid pressure, local stress concentration and regional stress fields. The analysis of the

injection pressure and/or production history is not usually sufficient to identify the fracture orientation. This is one of the concerns of the industry as oil production is higher for multiple vertical fractures compared to a single vertical fracture. On the other hand, horizontal fractures give higher productivity and lower heat loss compared to the vertical fractures under the same conditions (Settari and Raisbeck, 1981). Studies on heat transfer patterns indicate that fractures which are vertical when initiated, gradually become horizontal when they reach shallower depths. Mattews et al. (1969) suggested in a patent that heating of vertical fractures will eventually produce horizontal fractures. The in-situ heating of oilsand produces changes in the stress field that eventually may change the fracture orientation. This has significant implications for field applications of hydraulic fracturing.

Even in the isothermal case, some field observations of hydraulic fracturing in oilsands contradict conventional methods and classical fracture mechanics. For example, fracture dimensions are relatively small, fracture width are large, and injectivity is larger than that which would correspond to in-situ mobility ratios. This indicate that the injecting fluid is leaking off the fracture surfaces. Settari et al. (1989) in a study using a classical fracture model and linear elasticity formulation, showed that mechanical properties such as E (modulus of elasticity), ν (Poisson's ratio), K_{IC} (fracture toughness) and choice of fracture geometry model do not influence the fracture length or fracture leak-off area, however, they influence the fracture width. Fracture dimensions are controlled by leak-off related parameters such as permeability, pressure (P_{frac}-P_{init}), fluid mobilities and overall compressibility. They concluded that the total volume of the fluid in the fracture constitutes a very small fraction of the volume injected. This indicates that the problem is leak-off dominated, therefore, accurate representation of fluid flow at conditions of low effective stress at fracture face must be studied in detail.

When fluid is injected into a porous and permeable reservoir, such as oilsand deposits, the in-situ stresses are overcome by pressures higher than the minimum total stress, thus a primary fracture develops. At this stage two phenomena may occur either individually or simultaneously. The first is that the minimum effective stress may

become negative (tensile), and because the tensile strength of soil is negligible, a 'tensile fracture' occurs in the formation. The second is that existing shear stresses may prevail the already reduced shearing resistance of the formation and this cause 'shear fracture'. At the fracture face the minimum effective stress is close to zero (due to high local pore pressure) and a region of shear failure develops around the main fracture. In this region permeability and porosity are enhanced by dilatant shear. Changes in porosity, in turn, alter water saturation, mobility of fluids, and pressure distribution. The leak-off zone will extend past the shear zone and within it the compressibility and permeability of the soil structure will increase strongly as the effective stress decreases due to rising pressure. As a result, a large volume of injected fluid is lost through the interconnected pores between mineral grains. This leak-off phenomenon depends on the rate of injection, the permeability of the reservoir, and relative viscosities of the injected fluid and the resident pore fluid.

Ideally, a numerical model which can be used as a design tool for the optimization of hydraulic fracturing in the oilsand industry should be able to address all of the issues discussed above. Such a model, however, is expected to be very complicated and therefore not easy to use. The main goal of this study is the development of a numerical model capable of capturing the key issues in the problem using simplified assumptions where applicable.

1.5 Other Applications of Hydraulic Fracturing

Today, hydraulic fracturing is used for many purposes in petroleum engineering. It is also used in other disciplines such as geotechnical and environmental engineering.

In petroleum engineering hydrofracturing can be used to enhance oil recovery by overcoming drilling and completion damages near the wellbore; it can also be used to make deep penetrating, high-conductivity fractures in low permeability reservoirs. The fracturing of injection wells to increase injectivity is common. Fracturing has also been used to improve injectivity and sweep efficiency in secondary and tertiary recovery processes such as waterflood, fireflood and steamflood operations. Some of these

methods will be discussed in chapter 2. Hydraulic fracturing is currently the most widely used tool for stimulating oil and gas wells (Veatch Jr. et al., 1989).

Geothermal energy extraction is another area where hydraulic fracturing is used in practice. Hydraulic fracturing of hot dry rock is an efficient way to extract geothermal energy from circulating fluid.

Environmental engineering is an area in which hydraulic fracturing has proved to be useful. Remediation of contaminated sites by hydrofracturing has been very effective (Frank and Barkley, 1995). For sites contaminated with non-aqueous phase liquids (*NAPL*) above or below the water table, or for the sites contaminated with the vapours in the soil above the water table, hydraulically fractured wells can greatly enhance the performance of soil vapour extraction, pump and treat, and in-situ bioremediation techniques.

Another environmental issue in which fracturing is a concern is in radioactive waste disposal sites in deep clay or rock layers or in ocean floors. The decay of radioactive material produces heat which causes a rise in temperature and expansion of both pore fluid and soil skeleton. This can cause high pore pressure, which may, in turn, induce fracture or liquefaction in the soil.

Another application in which hydraulic fracturing is used extensively is in rock engineering for determining in-situ stress fields. In this case water is pumped into a section of the borehole isolated by packers. As the water pressure is increased, initial compressive stresses on the walls of the borehole are reduced and at some points become tensile. When this tensile stress exceeds the tensile strength of the rock, a crack is formed. Various methods exist to interpret the data obtained from a hydrofracturing test in order to get the best estimation of the in-situ stresses in the rock.

Finally, dam engineering is an area where hydraulic fracturing is a major concern. It is well known that hydraulic fracturing can be one of the causes of cracks in earth dams. Excessive leakage and, in some cases, failure of earth dams have been attributed to hydraulic fracturing (Jaworski, Duncan, and Seed, 1981). Improvement of dam foundations by grouting should be conducted according to the criteria for hydraulic

fracturing; since grouting, in principle, should not cause any harm to the natural ground underlying the dam.

1.6 Scope of This Research

Development of a computer program to simulate the fracturing phenomenon in oil-rich materials induced by injection of steam or fluid at high pressure and temperature is the prime focus of this research. Due to presence of oil, water, and gas in the pores, mobility of these phases affect each other. Pressure and temperature of these phases can be different, therefore, a multiphase flow model is preferred. Since the geomechanical behaviour is of prime interest to this study, mixture of oil, water, and gas is considered as a fluid with a single pore pressure and a single temperature. It should be noted that due to the presence of gas in the porous medium, the soil is most likely unsaturated. However, since the gas is in the form of occluded bubbles inside the oil, it can be assumed that the soil is fully saturated by an equivalent fluid (Sparks, 1963; Vaziri, 1986). Summing of the degrees of saturation of oil, water, and gas is, therefore, equal to one.

The equilibrium equation for deformations, the continuity equation for fluid flow and the heat transfer equation will be solved simultaneously in order to capture the basic physics of the problem. The finite element method will be used for solving the coupled system of partial differential equations.

Soil behaviour will be considered elastoplastic and dilation characteristic of oilsand as well as the leak-off phenomenon will be investigated in detail.

Since injecting fluid in a hydrofracturing treatment basically induces a few fractures inside the layer which primarily has not been fractured, the 'discrete fracture' approach will be used to determine the induced fracture pattern.

Darcy's law is assumed to be valid in the medium although for high rates of flow and turbulent conditions, different nonlinear relationships have been proposed.

The developed model for simulating hydraulic fracturing in a deformable multiphase heated porous medium can be used in the following applications:

1) Design of optimum (economical) hydraulic fracturing treatments for heavy oil reservoirs;

2) Interpretation of well tests (well-communication) with thermal effects;

3) Determination of land subsidence due to geothermal energy production (thermo-elastic and thermo-elastoplastic consolidation);

4) Study of the effects of radioactive waste disposal in clay layers or rock formations;

5) Study of the geotechnical aspects of temperature variation in soils due to underground power cables or pipelines;

6) Study of the cracks induced by hydraulic fracturing in embankment dams;

7) Design of grouting process in dam foundations in order to avoid undesirable fracturing of the ground.

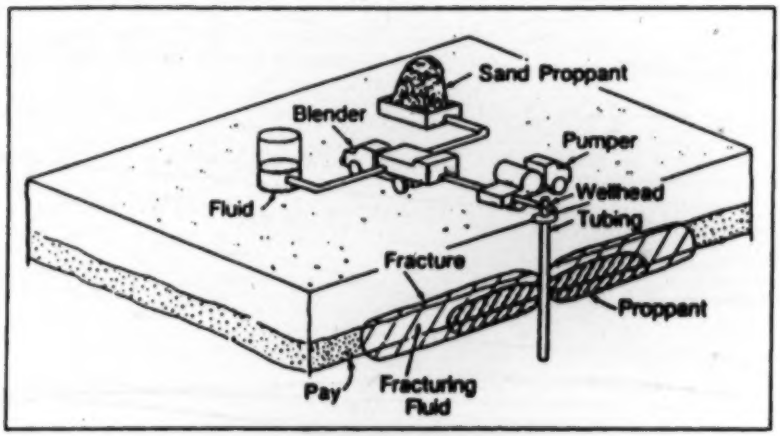

Figure (1-1) Typical hydraulic fracturing
treatment in petroleum industry
(after Veatch Jr et al. 1989)

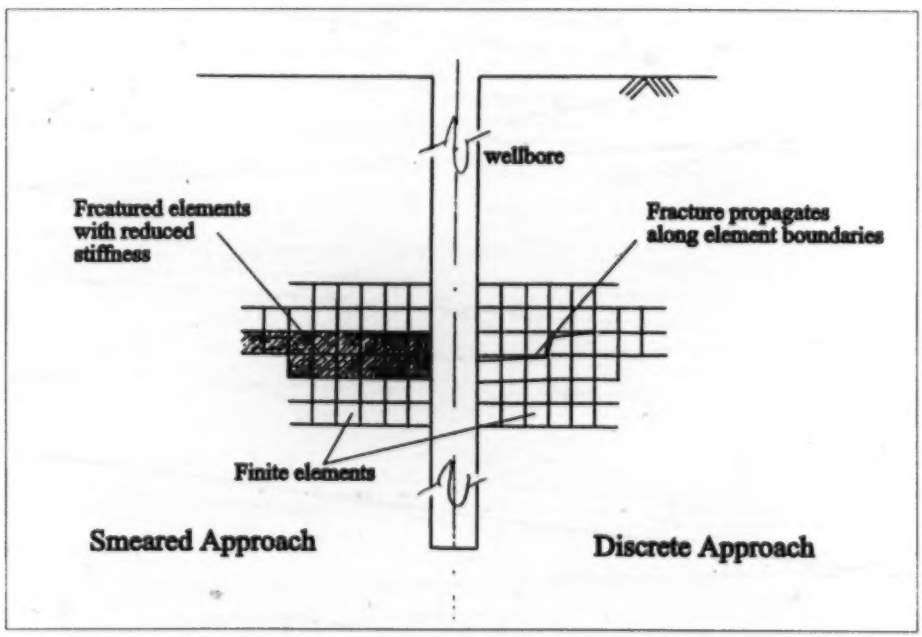

Figure (1-2) Smeared approach vs. Discrete approach
in modeling fracture using finite element method

Chapter 2

Geotechnical Aspects of Heavy Oil Recovery

2.1 Recovery Techniques

An oil reservoir is a porous medium in which the pores contain some hydrocarbon components usually designated by the generic term 'oil'.

The porous medium is often heterogeneous, which means that the rock properties may vary from one place to another. The most heterogeneous oil fields are the so-called fractured oil fields which consist of a collection of blocks of porous material separated by a network of fractures.

The nature of the fluids that reside in the porous medium is an important characteristic of oil reservoirs. Some of the oil reservoirs are single phase and some multiphase. In a single phase oil reservoir, pores are filled with one type of fluid which can be either oil or gas, while in a multiphase reservoir water, oil, gas and other hydrocarbon constituents are present. Some of these components may change their properties under some circumstances (for example at high pressures gas may dissolve in the oil etc.) and thus change the characteristics of the fluids.

Usually, oil reservoirs are pressurized and gas or oil can be produced by natural decompression (Chavent, 1986). The amount of oil or gas extracted in this way, however, is a small percentage of the resources in the ground. This first stage of production is called 'primary recovery'.

A common practice for the extraction of the remaining oil is to drill two sets of wells namely, injection wells and production wells, and then inject an inexpensive fluid (usually water) into the porous medium so as to force the oil towards the production wells (waterflooding). This stage of production is called 'secondary recovery'. If the

pressure in the field, during this period, is maintained above the bubble pressure of the oil, the flow in the reservoir will be a two-phase immisible flow (water and oil being the two phases) and no mass exchange will takes place between them. But if the pressure drops below the bubble pressure at some points, the oil may split into a liquid phase and a gaseous phase at the thermodynamical equilibrium. This is called 'black oil reservoir' with one water phase which does not exchange mass with the other phases and two hydrocarbon phases (oil and gas) which exchange mass when the pressure and temperature change (Chavent, 1986).

Although the secondary recovery can be very effective, it is unable to recover more than 50% of the total oil in the field. The reason lies in the fact that the injected water cannot fill all the pores and wash out all of the resident fluids. This is, in part, because of the capillary forces which keep 20 to 30 percent of the oil in the pores. The remaining oil is called 'residual oil saturation'. In some cases, since the oil is heavy and viscous, the injected water cannot push the oil, instead it finds some paths in the ground and reaches the production well. In these circumstances, what comes out of the production well is mainly water rather than oil.

In order to achieve better than the above mentioned levels of recovery, the petroleum industry has developed a set of different techniques known under the name of 'enhanced recovery techniques', or tertiary methods. One of the main goals of these techniques is to achieve miscibility of fluids and thus eliminate the residual oil saturation. This miscibility is sought using temperature increase or introduction of water components, such as certain polymers, which yield miscibility of oil and water when they are in the right proportions. Similarly, miscibility of the gas and liquid phases in a 'black oil reservoir' flow may be restored by adding a medium weight hydrocarbon component in adequate proportion (Chavent, 1986).

2.2 Recovery Methods for Oilsand Deposits

Oilsand is an important world energy resource by virtue of its known reserves. Estimated in-place volume of heavy hydrocarbons in oilsand deposits throughout the world approaches 3000 billion barrels. This is almost equivalent to the total discovered

light and medium gravity reserves in-place in the world (Agar et al., 1983). More than 90% of known heavy hydrocarbon reserves occur in oilsand deposits located in Alberta and eastern Venezuela (Demaison, 1977). Approximately 4% of Alberta oilsand reserves are buried at depths less than 50 meters and are thus economically recoverable by surface mining techniques (Alberta energy and natural resources, 1979). The remaining 96% is exploitable by in-situ extraction procedures, which generally require some form of heating because the extremely high viscosity of the crude bitumen in oilsand makes conventional recovery by pumping impractical (Mossop, 1978). In-situ extraction methods generally involve heating the oilsand with pressurized steam (e.g. cyclic steam stimulation or steam drive), or by in-situ combustion. These processes require drilling of injection and production wells from the ground surface. General methods for oilsand recovery at different depths are depicted in Figure (2-1).

In practice, however, other techniques have been used for extracting bitumen from oilsand which do not involve any form of heating. These processes generally require excavation of a small diameter hole (e.g. 0.25 m) extending to the base of the oil bearing stratum. Some form of casing is installed into the hole in order to keep it open. This casing must contain perforations within the zone of oil comprising material. Providing the screen prevents the collapse of soil into the well while the perforations allow the fluid to flow into the well which can be subsequently recovered. One of the drawbacks of this method is that the screen can become clogged with washed out fines which can deteriorate the production rate.

2.2.1 Thermal recovery for oilsand deposits

To recover oil from oilsand, the proposed technique must overcome the following major inherent constraints (Settari and Raisbeck, 1979):

- low permeability in oil-saturated sands;
- low oil mobility;
- low reservoir temperature and pressure.

All thermal recovery processes tend to reduce the reservoir flow resistance by reducing the viscosity of the crude oil. Generally thermal recovery can be divided into two classes or categories, namely 'stimulation' and 'flooding'.

Stimulation is commonly used for small reservoirs with poor continuity. The major drawback of the stimulation process is that the ultimate recovery may be low relative to the total oil in place in the reservoir. This is due to the fact that in stimulation only the reservoir near the production well is heated and the natural driving forces present in the reservoir (such as gravity, solution gas, and natural water drive) are the only agents responsible for mobility of the oil. For relatively small reservoirs, however, this method may be more economical.

Flooding, particularly cold water flooding is said to be the oldest recovery method; which has been replaced by hot water in the thermal recovery process. Flooding is usually used for relatively large reservoirs and for communication between injection and production wells. In flooding, fluid is injected continuously into a number of injection wells to displace oil and obtain production from other wells.

Some of the common thermal recovery techniques are described below:

a) Hot fluid injection

This method is basically used for flooding purposes but it can also be combined with other methods in order to improve the rate of recovery. Although the injected fluids are generally heated at the surface, wellbore heaters have been used on some occasions. All processes in which hot fluid is injected through the well suffer from heat losses to the formation overlying the reservoir. Such heat losses can be a significant portion of the injected heat when the wells are deep or poorly insulated and the injection rates are low. Under such conditions the temperature of an injected noncondensable fluid entering the formation may be markedly lower than that at the wellhead. When the injected fluid is condensable, as in the case of steam, the heat losses cause some of the vapours to be condensed, but the temperature remains approximately constant as long as there is vapour present (Pratts, 1982).

Hot fluid injection can be subdivided into three methods: hot-water drives, steam drives, and hot gas drives (i.e. natural gas, carbon dioxide, etc.).

b) In-situ combustion:

This technique proceeds in the following way: oxygen is injected into a reservoir, the crude oil in the reservoir is ignited, and part of that crude is burned in the formation to generate heat. Air injection is by far the most common way to introduce oxygen to a reservoir. This technique has proved to be useful in low permeability reservoirs.

Although combustion is mostly used for stimulation purposes it can also be used in combination with water injection in order to enhance recovery (Pratts, 1982).

c) Wellbore heating:

The wellbore is normally heated either by using a gas-fired downhole burner; by a downhole electric heater hanging on an electric power cable, or by circulating fluids heated at the surface. Generally production and heating are performed concurrently but in some instances they are alternated. This stimulation process has been replaced by the techniques described below (Pratts, 1982).

d) Cyclic steam stimulation:

The common practice for cyclic steam stimulation is to inject steam into a formation for a few weeks, wait a few days to let the heat soak in and allow the steam to condense, and then put the well on production. This process is called cyclic steam stimulation method. Other fluids can be used (e.g. hot water) but none have been found to be as effective as steam.

Cyclic steam stimulation is a popular method because the production response is obtained earlier and the amount of recovered oil per amount of the injected steam is often higher than in thermal drives (flooding). Moreover, relatively small steam boilers can be used which can be moved from well to well. This method is desirable for stimulation but the ultimate recovery may be low relative to the total oil in place in the reservoir (because the oil is supposed to flow with natural driving forces like gravity). The rate of recovery can be enhanced by cyclic steam injection followed by a steam drive (Pratts, 1982).

e) Steam-Assisted Gravity Drainage (*SAGD*):

This is one of the new methods in which horizontal wells are employed rather than vertical wells. Generally, this method proceeds by placing parallel horizontal wells low in the cold oilsand layer. Steam is then injected at the upper well. This creates a steam chamber which grows as the steam condenses on the chamber walls and ceiling and releases heat. This causes heated bitumen to drain by gravity towards the lower production well (Figure 2-2).

f) Heated Annulus Steam Drive (*HAS* Drive):

Another new method which uses horizontal wells is called *HAS* Drive. In this method steam is circulated in a closed horizontal pipe placed in the pay zone. This heats a zone around the pipe and mobilizes the bitumen which provides a path for steam flooding (Figure 2-3).

g) Hydraulic fracturing

Hydraulic fracturing can be used independently or in combination with some of the methods that have been discussed so far. The concept of generating fractures in soil or rock by injecting fluids at high pressures and rates, referred to as 'hydraulic fracturing', has been recognized by the petroleum industry since 1947. In its simplest form, hydraulic fracturing consists of sealing off a section of a wellbore and injecting a (hot or cold) fluid at sufficiently high pressure and rate, to overcome the in-situ strength of the formation until a fracture is created at the wellbore. This fracture is then extended by further injection of the fracturing fluid. The prime objective of such a process is to enhance the effective reservoir permeability and/or create paths for introducing steam or air for heating the viscous hydrocarbons.

Although oilsand can become soft and expand considerably when brought to the surface, studies suggest that it exhibits high strength characteristics under in-situ confining pressures (Dusseault, 1977; Harris and Sobkowicz, 1978). In-situ heating reduces the strength of oilsand, but fractures are expected because the time necessary to initiate and propagate fractures is small relative to the time necessary to heat the formation.

As mentioned earlier, fracturing induced by injection of hot water or steam in the oilsand results in complex interactions between fluid flow, heat flow and uncemented soil matrix in the reservoir.

2.3 Oilsand's Geomechanical Behaviour

2.3.1 Oilsand characteristics

Oilsand may be considered as a 4- phase system comprised of a dense inter-locked skeleton of predominantly quartz sand grains whose void spaces are occupied by bitumen, water and gases. Bitumen occupies a large portion of the pore space being separated from the solid grains by a thin film of water. Gases which are mostly methane and carbon dioxide can exist in the form of discrete bubbles (free gas) or dissolved in both the bitumen and water. Figure (2-4) illustrates the oilsand structure (Dusseault, 1977).

In-situ oilsand is a very dense, uncemented fine grained sand; exhibiting high shear strength and dilatency and low compressibility characteristics compared to normal dense sand of similar mineralogy. Permeability for samples with no bitumen are on the order of 10^{-4} cm/sec; the presence of a highly viscous bitumen, however, reduces the permeability of oil-rich samples to 10^{-8} cm/sec (Agar, 1984). This low permeability causes the soil to respond in an undrained manner to external loading. Another unusual characteristics of oilsand is its response during load removal. An unloading process that causes the level of confining stresses to decrease below the gas/liquid saturation pressure will result in gas exsolution. This is why obtaining undisturbed samples from oilsand requires special measures. An increase in temperature can also result in evolution of dissolved gasses provided that it raises the liquid/gas saturation pressure above the level of confining stresses. Due to the low permeability of oilsand to gasses, the evolution of gasses are likely to occur under undrained conditions which will consequently induce a change in the volume of the soil matrix (Vaziri, 1986).
The production and expansion of the gas has a two-fold effect on the response of oilsand under undrained conditions: first, it results in higher pore pressures that reduce the effective stresses; and second, it causes the pore fluid to become more compressible and

thus reduces the change in pore pressure resulting from changes of total stresses. In the case of gassy soils such as oilsand, the large volume of free or dissolved gas in the pore fluids indicates that the compressibility of pore fluid is much larger than the compressibility of soil skeleton; consequently, any total stress change is almost entirely taken up by the soil skeleton and the pore pressure change is very small. For problems involving unloading of oilsand, the relatively stiffer soil matrix will undergo most of the stress change and will respond with a corresponding reduction in effective stresses until tension develops. Since the soil cannot sustain tension, it will develop a substantial increase in compressibility which results in stress changes being transferred to the stiffer fluid phase. The physical consequences of such a process are a significant increase in volume and a marked reduction in shear strength.

When the decrease in total stress occurs slowly over a period of time, the oilsand may respond in a drained manner. In this case, the pore pressure change and resulting pore volume change will not disturb the soil fabric and the oilsand will maintain its dense condition and high shear strength (Vaziri, 1986).

Geomechanical behaviour of Alberta's oilsand has been the object of significant studies since mid 1970s. These studies have noted that there are some essential differences between the geomechanical behaviour of Athabasca and Cold Lake oilsands. Differences in geomechanical behaviour can be attributed to differences in soil fabrics. Some of these differences are explained below.

2.3.2 Athabasca and Cold lake oilsands

Dusseault (1977) studied the Athabasca and Cold lake oilsand's geomechanical behaviour. He showed that the Athabasca oilsand has an extremely stiff structure (large modulus of elasticity) in its undisturbed state, and a large degree of dilation when loaded to yield and subsequent failure. Agar (1984) examined the stress-strain behaviour for different stress paths and at elevated pressures and temperatures. Kosar (1989) continued this work and noted some essential differences in the geomechanical behaviour of Athabasca and Cold lake oilsands.

In the case of the Athabasca oilsand the investigators noted very high initial elastic modulus of the confined and undisturbed material. This was attributed to its extreme compactness providing extensive grain to grain contact so that the stiffness of the sand skeleton is close to that of the grains (Dusseault and Morgenstern, 1978). This grain orientation is compared to ideal and rounded sand grains in Figure (2-5). The angularity of the Athabasca sand grains also illustrates why significant dilation can be expected as the sand is sheared. The results of a typical direct shear box test are presented in Figure (2-6). The Mohr-Coulomb failure envelope is curved. This curvature indicates a bi-modal failure mechanism in which shearing of asperities occurs under high stresses. Investigations by Dusseault and Morgenstern (1978) indicate that the more quartzose and coarse grained is the material, the greater is the shear strength.

Friction angle varies considerably as the effective confining stress is increased. The residual (post-failure) friction angle for Athabasca oilsand is considerably less than its initial value. The extrapolation of the peak strength curve to the zero normal stress axis gives an apparent cohesion to the material. This apparent cohesion is dispelled by data points taken at low values of normal stress.

In contrast, the Cold lake oilsand is less stiff and undergoes little loss of strength after the initial yielding. The dilatant behaviour of the Athabasca and Cold lake oilsands is also different. Cold lake oilsand does not exhibit dilatant behaviour like the Athabasca oilsand; instead, it displays contractile behaviour during a triaxial confining compression test. As a result, the change in pore pressure during undrained testing of Cold lake oilsand remains fairly constant as the degree of axial strain is increased. In the case of Athabasca oilsand, the increase in volume is apparent due to the sharp decrease in pore pressure. Figure (2-7) illustrates the differences in geomechanical behaviour of the two oilsands. The differences in behaviour can be explained in terms of the differences in mineralogy. The Cold lake deposit has a greater proportion of weaker minerals than the highly siliceous Athabasca sand. These weaker minerals are prone to crushing at high stress levels (Kosar, 1989).

2.3.3 Effects of temperature on oilsand

a) Fabric

The oily nature of the oilsand (existence of bitumen between the sand grains) makes it sensitive to change in temperature and causes a reorientation of sand grains when such changes occurs. This reorientation happens because an increase in temperature causes a decrease in the frictional resistance and the shearing strength of individual interparticle contacts. Consequently, there is a partial collapse of the soil structure and a decrease in void ratio until a sufficient number of additional bonds is formed to enable the soil to carry the same effective stress at the higher temperature. This phenomenon was originally recognized by Campanella and Mitchell (1968). They further quantified its magnitude in terms of change in temperature and introduced a parameter known as the 'coefficient of structural volume change', (α_{ST}), of soil due to change in temperature. Later Scott and Kosar (1982, 1985) stated that α_{ST} is not a constant soil property but varies with temperature. This coefficient, in fact, compensates for temperature independency of currently used costitutive models for soils.

b) Volume change

Oilsand subjected to increase in temperature will experience an increase in volume, and the amount of volume change is dependent on the amount of pore fluid drainage which is permitted. Assuming that oilsand under in-situ conditions is fully saturated, the application of a rapid increase in temperature will result in the development of a significant positive pore pressure due to greater volumetric expansion of the pore fluid relative to the mineral solids. Provided that the boundary conditions are such that a hydraulic gradient is set up, the fluid will then drain from the soil at a rate governed by its permeability. Based on physical reasoning, thermal expansion in drained condition can be considered as a lower bound for thermal expansion while the upper bound occurs under undrained condition. This point was examined by Scott and Kosar (1982). They showed that there exists a considerable difference in volumetric expansion between drained and undrained cases in a typical oilsand sample. The change in volume is comprised of the expansion of solid particles and soil skeleton together with the pore fluid. The latter plays the predominant role under undrained

condition, being responsible for over 90% of the overall volume change even before any gas exsolution. If gases evolve from solution, additional volume changes will occur irrespective of the drainage conditions.

The experimental studies by Agar et al. (1987) showed that the magnitude of dilation was greater for heated samples than that for unheated samples.

c) Shear strength

At ambient temperatures of the in-situ oilsand, no measurable cohesion was observed (Dusseault and Morgenstern, 1978). However, at high stresses the altered Mohr failure envelope gives the impression that positive cohesion exists. This cohesion is only an apparent one because, as noted, failure at lower stresses clearly indicates that there is no cohesive strength. Agar (1984) noted the development of low levels of cohesion in heated samples of Athabasca oilsand. Conversely, the increase of susceptibility to failure of individual grains due to an increase in temperature was marked for Cold lake oilsand.

Agar et al. (1987) in their extensive research on the effects of temperature on oilsand behaviour showed that, under drained condition, heating up to 200 degrees has a relatively small effect on the measured shear strength of oilsand compared to the effects of fabric disturbance and heating in undrained condition. Generation of pore pressure during undrained heating with the concomitant loss of available shearing resistance was considered to be of much greater practical significance than the more subtle effects of drained heating noted above.

d) Hydraulic conductivity

Another property of oilsand which is significantly affected by the induction of heat is its hydraulic conductivity. As mentioned before, the bitumen in oilsand is immobile at in-situ temperature; its viscosity, however, is significantly decreaseded at elevated temperatures. This decrease results in an increase in soil hydraulic conductivity. Figures (2-8) and (2-9) demonstrate the effect of temperature on the hydraulic conductivity of oilsand and viscosity of bitumen, respectively.

2.3.4 Modeling of stress-strain behaviour for oilsand

Several aspects of the stress-strain behaviour of oilsand require significant departure from linear elastic theory :

1) Strain is not a linear function of stress;

2) Oilsand is stress-path dependent (i.e. the magnitude of strain at a given stress level depends on the stress-path followed during the history of loading and unloading);

3) Shear stresses not only cause shear strains but also volumetric strains (dilation and contraction);

4) There is a structural reorientation of sand gains when subjected to heating;

5) Time dependency which is primarily related to the change of pore pressure with time, due to consolidation and gas exsolution;

6) Soil is essentially anisotropic.

Dusseault and Morgenstern (1978) showed that the Athabasca oilsand has an elastoplastic behaviour with strain softening after peak. It has been observed (Kosar, 1989) that under low confining pressures, oilsand behaves as a typically brittle material i.e., it reaches a well defined peak deviatoric stress at relatively small strain (ε_1=1%), and then exhibits a strain softening trend and sharp drop in shear resistance with increasing strain (Figure 2-10). Such a brittle behaviour seems to disappear at higher lateral confining pressures σ_3. With further increase in σ_3 the material response is strain hardening but the effective yield strength in this case is lower.

Ideally, modeling of oilsand behaviour should include the following features:

-Irrecoverable strains

-Deformation history of the material

-Strain softening with dilation (at low confining pressure and temperature)

-Work hardening (at high confining pressure and temperature)

-Effect of raising the temperature on the behaviour

Obviously an advanced elastoplastic model is required to handle all of these features. Presently, there is no established soil model that can take care of the effects of temperature on yield surface. Until such model is developed, the phenomenon of the reorientation of sand grains can be incorporated into the analysis by using the

coefficient proposed by Campanella and Mitchell (1968). To date, most of the work on this issue has been based on various kinds of elasticity theory such as hypo-elasticity or hyperelasticity, (e.g. Agar et al.,1987; Vaziri, 1988; Settari et al., 1989). Nevertheless, there has been some attempts for employing an elastoplastic model (Wan et al., 1989; Tortike, 1991).

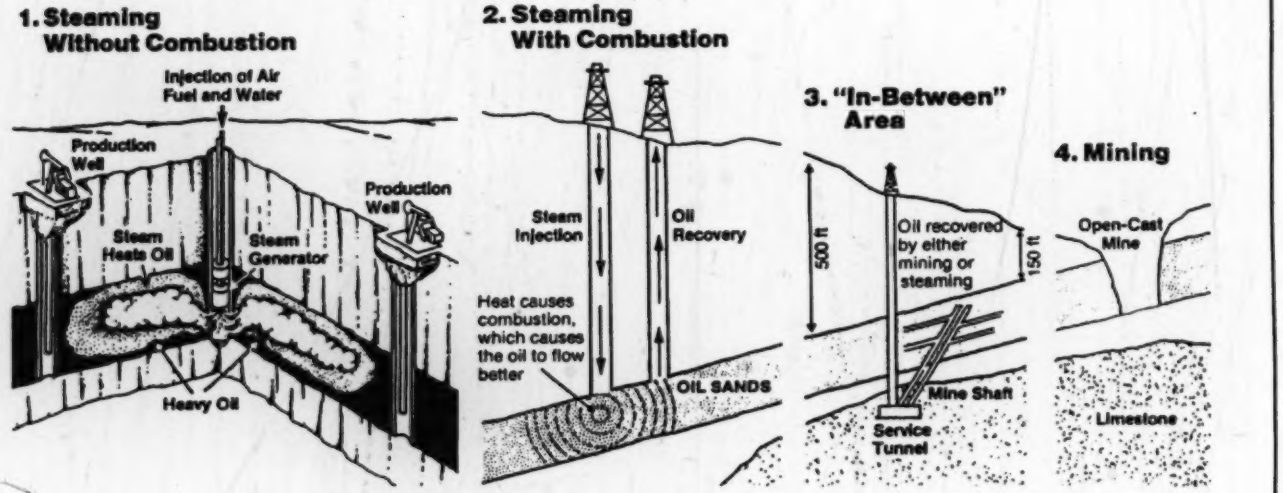

Figure 2-1 Different methods for extraction of oilsands
(after Morgenstern 1981)

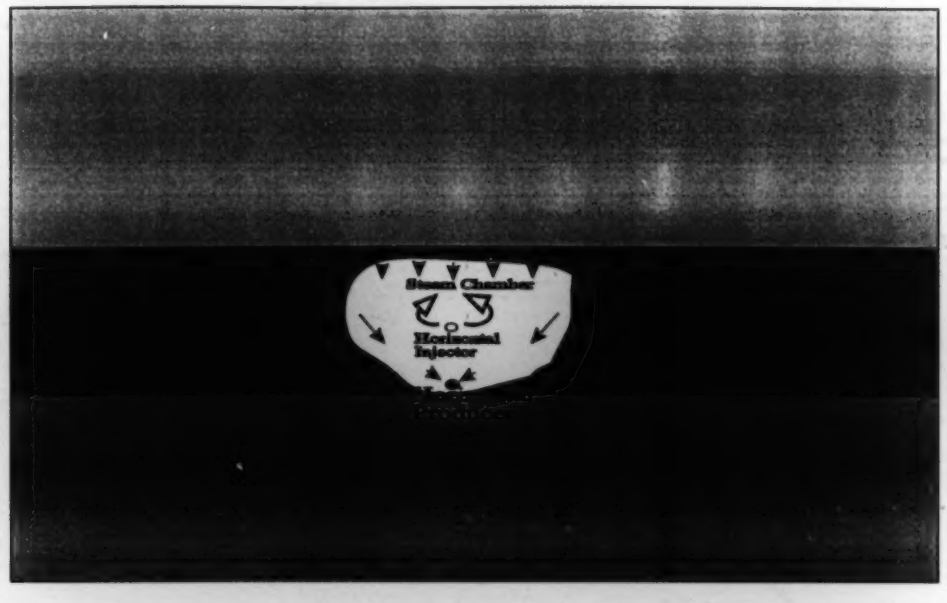

Figure (2-2) Steam Assisted Gravity Drainage Method (SAGD)

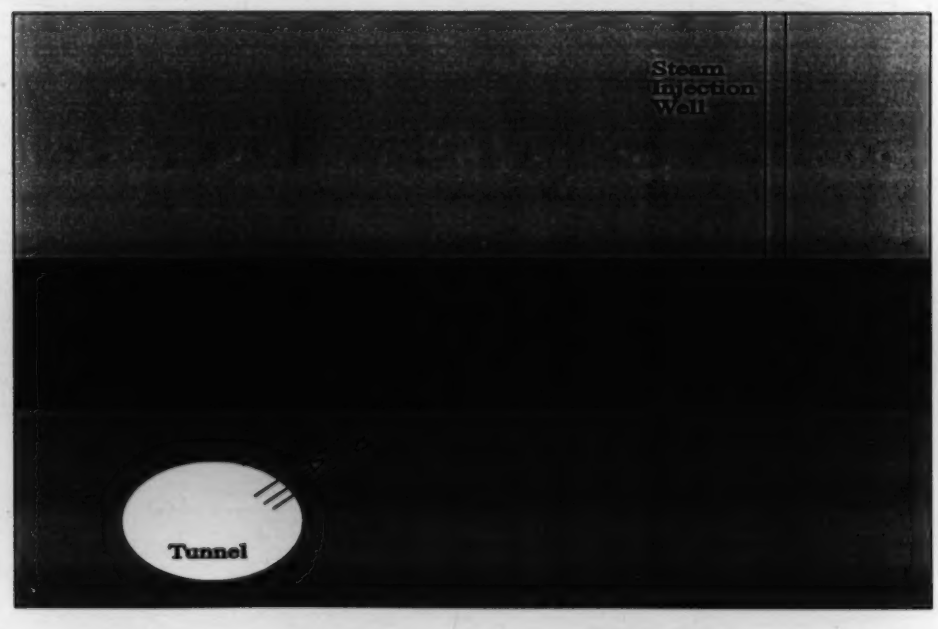

Figure (2-3) HAS Drive Method

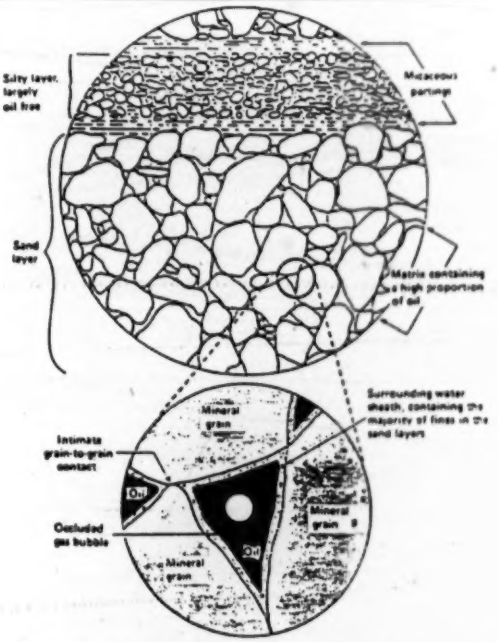
Silty layer, largely oil free
Micaceous partings
Sand layer
Matrix containing a high proportion of oil
Surrounding water sheath, containing the majority of fines in the sand layers
Intimate grain-to-grain contact
Occluded gas bubble
Mineral grain
Oil

Figure(2-4) Oil sand structure (from Dusseault 1977)

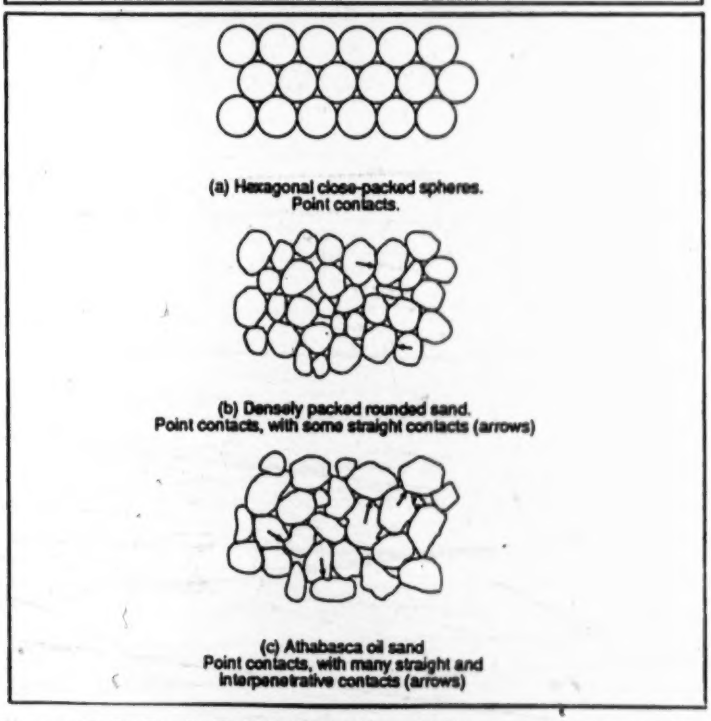
(a) Hexagonal close-packed spheres.
Point contacts.
(b) Densely packed rounded sand.
Point contacts, with some straight contacts (arrows)
(c) Athabasca oil sand
Point contacts, with many straight and interpenetrative contacts (arrows)

Figure (2-5) Grain Fabric for Oilsand Compared to Dense Sand

(adapted from Dusseault and Morgenstern, 1978)

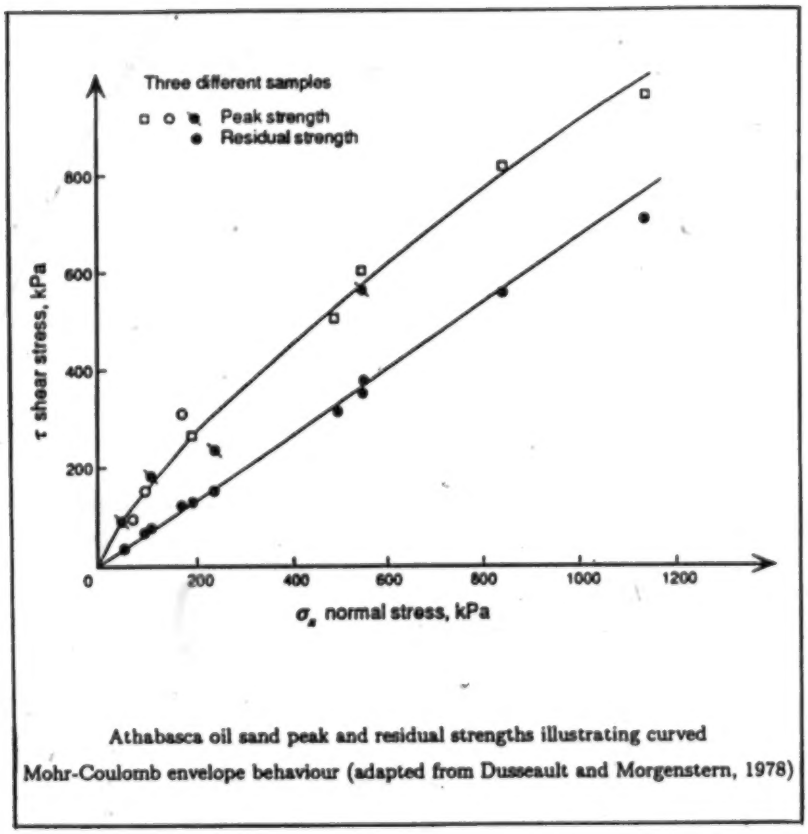

Athabasca oil sand peak and residual strengths illustrating curved Mohr-Coulomb envelope behaviour (adapted from Dusseault and Morgenstern, 1978)

Figure (2-6) Typical Results of Direct Shear Box Test on Oilsand

Figure(2-7a) Comparison of behaviour of Athabasca and Cold Lake oil sands under drained compression tests with 4 Mpa confining stress
(Athabasca: from Agar 1984, Cold Lake: from Kosar 1989)

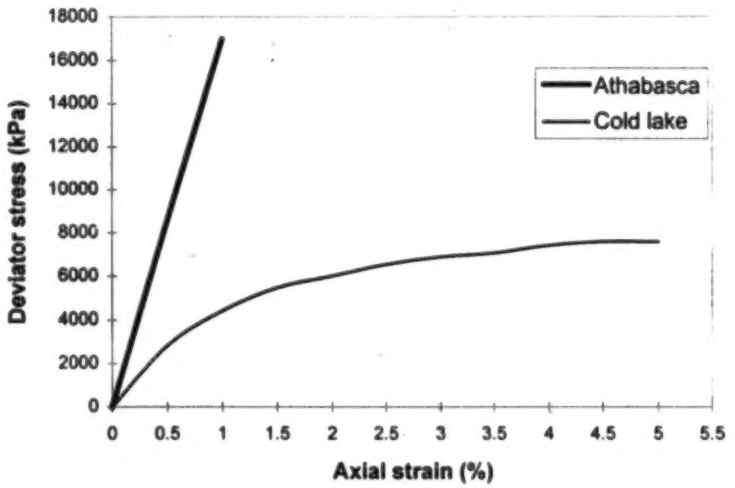

Figure (2-7b) Comparison of behaviour of Athabasca and Cold Lake oil sands under drained compression tests with 4 Mpa confining stress
(Athabasca: from Agar 1984, Cold Lake: from Kosar 1989)

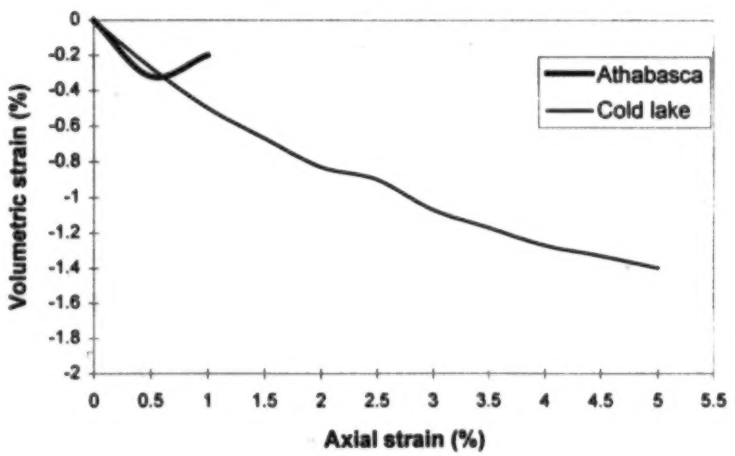

Figure (2-8) Effect of temperature on the soil hydraulic conductivity
(From Scott and Kosar, 1984)

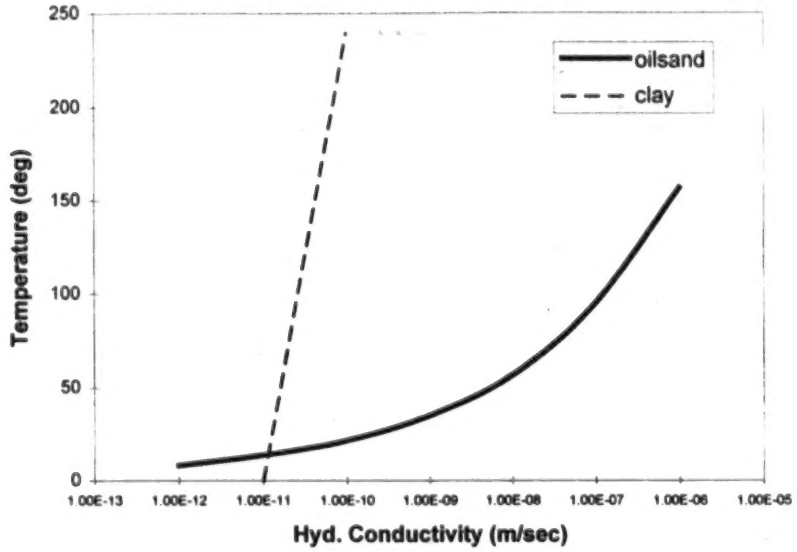

Figure (2-9) Effect of temperature on the viscosity of in-situ fluid
(From Scott and Kosar, 1984)

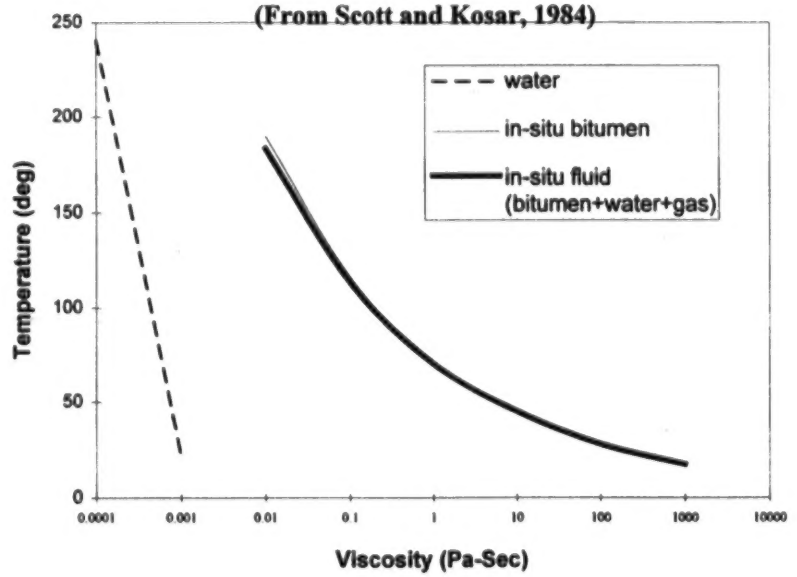

Figure(2-10) Behaviour of oilsand under different confining stresses
(adapted from Kosar 1989)

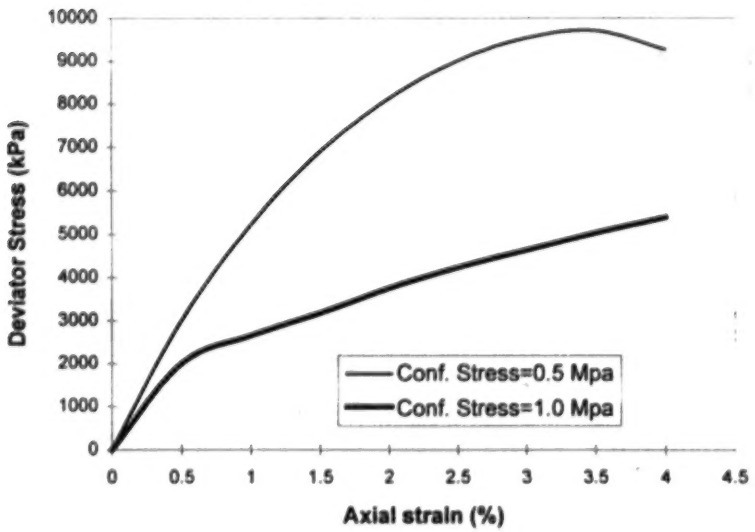

Chapter 3

Literature Survey on Numerical Modeling of Hydraulic Fracturing

Extensive literature exists on the subject of fluid flow in porous media. The fluid in porous media can be water, oil or a mixture of water, oil and dissolved gases. Although the effect of geomechanics on reservoir behaviour has not been considered until recently, there are some papers on coupling fluid flow and soil/rock deformation in the reservoir. In general, research in this area can be divided into two categories: isothermal flow and thermal flow. On the other hand, the number of papers on hydraulic fracture modeling in an oil reservoir is enormous. Most of them, however, do not deal with the coupled problem of thermal fluid flow, reservoir deformation and hydraulic fracturing.

The aim of this chapter is to provide a brief historical overview of the subject of fluid flow in the reservoir in isothermal and non isothermal conditions considering the geomechanical response of the soil/rock (deforming reservoir). A discussion of endeavors to incorporate hydraulic fracture modeling will follow.

3.1 Isothermal Fluid Flow in a Deformable Reservoir

Classical reservoir engineering pays little attention to the influence of geomechanical behaviour of soil. However, the relatively poor results and predictions of the old reservoir simulators revealed that an important piece of physics is missing, particu-

larly in the case of uncemented (unconsolidated in petroleum literature) oilsands, where soil behaviour is significantly different from that of rocks.

After Geertsma's paper on the subject in 1957, the petroleum industry realized the importance of inclusion of rock mechanics in reservoir engineering. In some cases the behaviour of rock and soil containing hydrocarbon can dominate and control the recovery process. Corapcioglu and Karahanoglu (1980) have reviewed and discussed the earlier works before paying attention to the deformation characteristics of the reservoir.

From a geotechnical point of view the fluid flow-deformation analysis in porous medium is basically a consolidation problem which was initially solved by Terzaghi (1925). Terzaghi developed a one-dimensional closed form solution for the consolidation problem of soils. In this pioneering work Terzaghi made some simplifying assumptions in order to find a partial differential equation which was solved for the pore pressures at different times. Biot (1941) extended the consolidation theory to a three dimensional model using a conventional elastic approach. Boit's generalized solution to his original formulation was reported in Biot (1956a) and the extension to anisotropic media in Biot (1955).

Sandhu (1968) developed the first finite element formulation for the two dimensional consolidation problem. In this work soil was considered as an elastic porous medium. Christian (1968) presented a finite element solution for stress analysis in a soil layer in undrained condition. Later he and Boehmer (1970) extended these ideas and developed the finite element formulation for consolidation analysis. The finite element method was applied to a variational principle equivalent to the equilibrium equation, but finite difference method was applied to the relation between volume change of soil and hydraulic gradient.

Small, Booker and Davis (1976) used the principle of virtual work to formulate the finite element consolidation equations of a saturated soil with an elastoplastic stress-strain behaviour. This work was extended by Carter et al. (1977; 1979) to include finite deformations.

Lewis et al. (1976) assumed a hyperbolic stress-strain model for the soil and used a nonlinear law for soil permeability in their formulation for modeling of consoli-

dation. A method of analysis which takes the compressibility of the pore fluid into account was proposed by Ghaboussi and Wilson (1973). Their analysis was extended by Ghaboussi and Karshenas (1978) to consider nonlinear material behaviour and subsequently nonlinear compressibility of the fluid (Ghaboussi and Kim, 1982).

Chang and Duncan (1983) developed a finite element model for partly saturated elastoplastic clays. They assumed that the behaviour of compacted clays in the core of earth dams can be simulated using a modified cam-clay model.

In petroleum reservoir engineering literature, application of soil stress-fluid flow analysis has been mainly for 'compaction-subsidence' problem in various situations. Some investigators have solved the problem using an uncoupled model that solves the fluid flow equation to produce the pressure profiles. These profiles are then used to evaluate the amount of subsidence of the formation.

Finol and Farouq Ali (1975), presented a two-phase, two dimensional flow model using finite difference method which included the prediction of subsidence. The problem was formulated using two discretized equations for oil and water flow, and one analytical equation of poroelasticity. The variation of permeability and porosity were considered in the analyses of the effect of compaction on ultimate recovery.

Settari and Raisbeck (1979) investigated the result of combining a planar fracture model and a single phase compressible fluid flow model assuming elastic behaviour. Settari (1980) and Settari and Raisbeck (1981) further developed their previous work to include two phase thermal fluid flow.

Settari (1988) and Settari et al. (1989) studied the effects of soil deformations on the reservoir in a partially coupled manner for isothermal and thermal fluid flow. They described a new model to quantify the leak-off rates from fracture surfaces into oil-sands. These works will be discussed in greater detail further on.

Fung (1992) described a control-volume finite element (*CVFE*) approach for coupled isothermal two-phase fluid flow and soil behaviour. The material was assumed to follow a hyperbolic stress-strain law modified for dilative behaviour using Rowe's stress dilatancy theory. The model was verified by analyzing the one dimensional consolidation problem and comparing it to the analytical solution by Biot. A two dimen-

sional fracture loading example was given and changes in stress and fluid flow in time were shown. The approach appears to yield accurate solutions, but is limited to non-plastic material behaviour and isothermal flow.

3.2 Thermal Fluid Flow in a Deformable Reservoir

Changes in temperature affect pore pressures and interparticle forces and induces changes in volume. Temperature can also alter some of the engineering properties of soils such as permeability and compressibility. Some of these effects have been discussed by Campanella and Mitchell (1968). In their paper they proposed a method to predict the volume change of saturated soils subjected to variation of pore pressure and temperature in an undrained condition.

Sobkowicz (1982) and Sobkowicz and Morgenstern (1984) have undertaken a comprehensive investigation of the gas exsolution phenomenon, both theoretically and experimentally.

In petroleum engineering, Lipman et al. (1976) studied the effect of geothermal production on the deformation of geothermal systems. The numerical model for the mass and energy equations were combined with the Terzaghi's consolidation equation.

Brownell et al. (1977) discussed the interaction of a porous solid matrix and fluid flow in geothermal systems, including momentum and energy transfer and the dependence of porosity and permeability upon fluid and solid stresses.

Ertekin (1978) presented a two dimensional, two phase fluid flow, a three dimensional heat flow, and a two dimensional displacement model for a hot water flooded oil reservoir. He used the finite difference method to solve the fluid flow and energy equations and then applied the results to a finite element model to determine the displacements.

Effect of temperature on the consolidation process has been investigated since the early 1980's. In the finite element model developed by Lewis and Karahanoglu (1981) an elastoplastic constitutive relationship was used. This model was applied by Lewis et al. (1986) to the solution of the one dimensional consolidation problem.

Aboustit et al. (1985) studied the consolidation phenomenon due to the heat produced from buried radio-active waste. Environmental effects of geothermal energy production with an emphasis on surface subsidence was studied by Borsetto et al. (1983).

In connection with the analysis of nuclear waste disposal in clay, Borsetto et al. (1984) discussed the constitutive relationship for clay under the combined action of heating, elastoplastic deformation, and ground water flow. The dependence of the coefficient of permeability on the temperature was also considered. The resulting governing equations can be solved to obtain displacements, pressure, temperature and porosity. Since the solution required considerable numerical efforts, Borsetto et al. (1984) proposed simplifications such as uncoupling the heat flow equation and reducing the number of independent unknowns.

The only theoretical solution dealing with coupled heat and consolidation process is given by Booker and Savvidou (1985) who provided an approximate analytical solution for the problem of consolidation around a cylindrical heat source in an elastic fully saturated material. The temperature field was uncoupled from the determination of displacements and pressure, by neglecting the mechanical contribution to energy balance and the convective terms.

Lewis et al. (1986) developed a coupled finite element model for consolidation of nonisothermal reservoir with elastoplastic behaviour. In analysis of the deformation of elastoplastic porous media due to fluid and heat flow, a displacement-pressure-temperature formulation resulted in an unsymmetric coefficient matrix, even in the case of associated plasticity. A partitioned solution procedure was applied to restore the symmetry of the coefficient matrix. Lewis et al. (1989) extended the previous work to include two-phase fluid flow. Lewis and Sukirman (1993) further extended the two-phase fluid flow formulation to three-phase fluid flow; this recent work, however, did not include the effect of temperature.

Vaziri (1988) coupled thermal single-phase flow with a nonlinear elastic (hyperbolic) model. He formulated a two dimensional finite element scheme by combining the stress equilibrium equation with fluid continuity equation. He was able to model the effect of a second phase, gas, by including compressibility in the definition of

the bulk modulus. In his formulation temperature was not treated as an independent state variable, but the effect of temperature on the deformations and pore pressure was taken into account by employing an equivalent system of loads on the domain.

Tortike (1991) developed a numerical model for simulation of three dimensional, thermal multiphase fluid flow in an elastoplastic deforming reservoir. It was the first implementation of soil plasticity in a multiphase thermal reservoir simulation. In this work a combination of finite element modeling of soil behaviour and finite difference modeling of multiphase thermal fluid flow was used which was claimed to be more successful than a fully finite element approach.

Vaziri (1995), extended his previous work (1988) to a coupled multiphase fluid flow and heat transfer, within a deforming porous medium. In this work temperatures, displacements and pore pressures were considered as independent state variables. Also in this paper an elastoplastic constitutive model for soil (cam-clay) was used.

3.3 Inclusion of (Hydro)Fracture Mechanics

Analysis of fracture is one of the essential requirements to achieve a reasonable evaluation of injection/production rates and prediction of the behaviour of the hydraulically induced reservoirs. General status of this technology and the current petroleum engineering procedures were summarized in a monograph by Gidley et al. (1987).

First generation models of hydraulic fracturing were pioneered by Zheltov and Khristianovich (1955), Perkins and Kern (1961), and Geertsma and deKlerk (1969). They provided closed form solutions for predicting fracture length and width based on a prescribed geometry for a planar fracture.

Settari and Raisbeck (1979; 1981) developed two of the early models for simulating hydraulic fracture during cyclic steam stimulation in oilsands. In 1979 they developed a two dimensional finite difference model for single-phase compressible fluid flow in a linear elastic porous material with an elliptic mode *I* (tensile) fracture. This model was extended to two phase thermal flow (Settari and Raisbeck, 1981) to describe the process of first cycle steam injection for three different fracture geometries. Although the two-phase model gave a more realistic representation of the process they

concluded that the analysis of the injection pressure and/or production history is generally not sufficient to identify whether the fracture is vertical or horizontal.

Atukorala (1983) developed a finite element model for simulating either horizontal or vertical hydraulic fracturing in oilsands. In this work, for the sake of simplicity, the fluid flow analysis was separated from stress analysis. These two equations were solved iteratively by imposing a compatibility condition on the volume of the fluid inside the fracture. The fracture shape was assumed to be elliptic with blunt tips in order to avoid singularity of stresses at the crack tip. A linear elastic fracture mechanics criterion was used for analyzing tensile fracture in a nonlinear elastic domain. No thermal effect was considered in this study.

Settari et al. (1989) investigated the effects of soil deformations and fracture on the reservoir in a partially coupled manner. Effect of leak-off on the fracture dimensions was emphasized. Oilsand failure was considered to be a shear failure with Mohr-Coulomb criterion. Dilation was not modeled in this work but it was assumed that a constant change in volumetric strain occurs after peak shear stress (failure). They developed a computer program called '*CONS*' based on the above partially coupled stress-flow analysis. Settari (1989) extended this work by incorporating temperature effects (thermal flow) in the formulation.

Advani et al. (1990) developed a finite element program for modeling three dimensional hydraulic fractures in multi-layered reservoirs. They extended the earlier work of pseudo three dimensional (*P3D*) model presented by Advani and Lee (1982) and other investigators in the early 80's. In this work, propagation of a tensile planar hydraulic fracture in layered reservoirs (with elastic behaviour) was investigated. Formation energy release rate was used as a criterion for crack extension. Injected fluid was an incompressible non-Newtonian fluid in isothermal condition. No temperature effect was considered.

Settari et al. (1992) developed a technique to represent a dynamic fracture in thermal reservoir simulators. They stated that simplification of the fracturing process by using stationary or pressure dependent change of transmissibilities causes inaccuracy in simulating fracture propagation and fluid flow in the fracture. The approach in this

paper was partial coupling of a planar fracture model with any conventional thermal reservoir simulator, provided that the host is a finite difference model. The key features of this model were the dynamic enhancement of transmissibilities in the fracture plane, and a concept of pseudoized relative permeabilities for multiphase flow. Leak-off was incorporated in the model by assuming a one-dimensional flow system from the fracture walls into the reservoir. Dynamic (growing) fracture predicted by this model was then imposed on a conventional thermal simulator. Elasticity theory was used for predicting soil behaviour as well as fracture extension. One of the limitations of this work is that the region simulated by the model should be an element of symmetry with the fractured well at the origin. This model cannot deal with fractures inside the grid or simultaneous fractures in several wells.

3.4 Discussion

In most of the researches carried out in reservoir modeling the finite difference method has been used. A few researchers have considered the effect of ground deformation in their reservoir models, however, in most of these studies the stress and deformation analysis have been incorporated in an uncoupled manner. Usually, the finite difference method is used for fluid flow and heat transfer while the finite element method is used for soil/rock deformations. Coupled thermal hydro-mechanical models using the finite element method are rare (Lewis et al., 1986; Vaziri and Britto, 1992). Even in these models the effect of fracturing in the ground is not considered. The current study aims at developing such a fully coupled thermal hydro-mechanical finite element model which can simulate the hydraulic fracturing by employing fracture mechanics applicable to geologic media.

Chapter 4

Mathematical and Finite Element Formulations

4.1 General

The objective of this chapter is to provide the mathematical formulation of a numerical model to analyze the interaction between ground deformation, fluid flow, and heat transfer in a saturated heated reservoir. The mathematical formulation will be discussed in detail in this chapter; fracture modeling will be described in chapter 5.

In this study, mixture of water and oil (with occluded gas bubbles) is considered as one fluid which flows through the porous medium. As long as the gas remains in occluded form, the soil can be regarded as fully saturated and the effective stress principle-whereby the pore pressure is represented by the pressure of the 'equivalent compressible fluid'-applies (Sparks,1963; Vaziri, 1986). This equivalent fluid has the same compressibility as the mixture of water, oil and gas. In this case the four phase unsaturated soil is phenomenologically treated as a material saturated with a homogenized compressible fluid phase.

The governing equations of equilibrium, fluid flow and heat transfer in the reservoir have been employed, in an incremental form, to be implemented in a finite element program. Primary unknowns are ΔU (change of the displacements Δu and Δv in x and y directions respectively), ΔP (change in pore fluid pressure), and ΔT (change in temperature) for each point in the reservoir. Three governing equations are solved si-

multaneously in a fully coupled manner. The objective is to incorporate all of the essential physics of the problem into the model while making appropriate simplifying assumptions. Partial differential equations (*P.D.E*) of the governing laws have no closed form solutions; therefore, the practical approach to solve the problem is using numerical methods such as finite element. In the finite element method, domain is divided into a number of elements (spatial discretization) in order to convert the *P.D.E*'s into a system of ordinary differential equations (*O.D.E*) in time, for each point inside the domain. Then, discretization in time, by using a differential approximation, transforms the system of *O.D.E'* s to a system of algebraic equations.

Before proceeding with the formulation, it should be noted that generally there are two methods for formulating the governing partial differential equation for a field problem: the Lagrangian method and the Eulerian method. In the former, which is also called material description, every particle is identified by its coordinates at a given instant of time. In the latter, coordinates of a particle are assumed to be independent of time. Instead, the instantaneous velocity field at any point fixed in the space and the variation of velocity with time are of interest. Eulerian method is usually used for fluid mechanics and Lagrangian method for solid mechanics due to the nature of these two kinds of problems (Fung, 1965).

For deformation analysis the choice between small (infinitesimal) strain analysis and large (finite) strain analysis is important and can greatly affect the formulation. Carter et al. (1977) showed that for soils with stiffness to strength ratio greater than 100, the finite deformation predictions are very close to those predicted by the infinitesimal theory at loads up to failure. For softer soils, however, the small strain theory would under-estimate the actual displacement. Lee and Sill (1981) argued that in the case of softer soils, one must also consider the effect of self weight in the analysis particularly when its magnitude is comparable to the externally applied loads. This study, based on the field observations, postulated that the dimensions of the induced hydraulic fractures in the reservoir compared to the huge dimensions of the reservoir itself are small; hence, small strain theory is assumed throughout the formulation. Applying the small strain

theory implies that changes in displacements (ΔU) as well as changes in pore fluid pressures (ΔP), and temperatures (ΔT), are small during any increment of time. One can, therefore, neglect the second order terms such as $(\Delta U)^2$ etc. that emerge in the formulation.

In this chapter superscript '.' means derivative with respect to time, '*' stands for nodal values and '-' means prescribed values.

4.2 Equilibrium Equation

General equilibrium equation can be expressed in the following indicial form (Bathe, 1982):

$$\sigma_{ij,j} + F_i = m'\dot{V}_i + c'V_i \tag{4-1}$$

where σ_{ij} stress tensor at any point

F_i external load

V_i soil matrix velocity

m' mass coefficient

c' damping coefficient

i,j indices taking 1, 2 and 3 representing coordinate axes

Soil/rock matrix velocity, V, is the variation of displacements, U, in time i.e. $\{V\}=\{\dot{U}\}$. The equilibrium equation in incremental form is:

$$\Delta\sigma_{ij,j} + \Delta F_i - m'\Delta\ddot{U}_i - c'\Delta\dot{U}_i = 0 \tag{4-2}$$

To be consistent with the fluid flow and heat transfer equations, weighted residual method *(W.R.M)* is employed to obtain the weak form of the equilibrium equation.

$$\int_V (\Delta\sigma_{ij,j} + \Delta F_i - m'\Delta\ddot{U}_i - c'\Delta\dot{U}_i)\omega dV = 0 \tag{4-3}$$

or

$$\int_V \Delta\sigma_{ij,j}\omega d\Omega = \int_V (-\Delta F_i + m'\Delta\ddot{U}_i + c'\Delta\dot{U}_i)\omega dV \tag{4-4}$$

integration by parts of equation (4-4) leads to the following equation:

$$\int_S \Delta\sigma_{ij} n_j \omega ds - \int_V \Delta\sigma_{ij} \omega_{,j} dV = \int_V (-\Delta F_i + m' \Delta\ddot{U}_i + c' \Delta\dot{U}_i) \omega dV \qquad (4\text{-}5)$$

The following boundary conditions are considered :

-stress boundary condition (natural *B.C.*) on $S\sigma$: $\Delta\sigma_{ij} n_j = \Delta\bar{t}_{s_i}$ (4-6)

-geometric boundary condition (essential *B.C.*) on *Su*: $U_i = \overline{U}_i$ (4-7)

Principle of effective stress can be written as:

$$\Delta\sigma_{ij} = \Delta\sigma'_{ij} - \alpha\Delta P \delta_{ij} \qquad (4\text{-}8)$$

where $\alpha = 1 - (C_s/C_b)$ Biot's coefficient

σ'_{ij} effective stress tensor (tension positive)

δ_{ij} kronecker delta

C_s compressibility of solid particles

C_b compressibility of bulk soil matrix

ΔP change in pore fluid pressure (compression positive)

Note that for consistency with the other two equations, *P* is considered to be positive when compressive.

Substituting (4-6) and (4-8) in (4-5):

$$\begin{aligned} &-\int_v \Delta\sigma'_{ij} \omega_{,j} dV + \int_v \alpha\Delta P \delta_{ij} \omega_{,j} dV = \\ &-\int_{S\sigma} \Delta\bar{t}_{si} \omega dS + \int_v (-\Delta F_i + m' \Delta\ddot{U}_i + c' \Delta\dot{U}_i) \omega dV \end{aligned} \qquad (4\text{-}9)$$

Behaviour for the soil/rock is considered to be elastoplastic. The constitutive law would be used in the general form as $d\sigma = D.d\varepsilon$ where *D* is the elastoplastic stiffness matrix:

$$\Delta\sigma'_{ij} = D_{ijkl} (\Delta\varepsilon_{kl} - \frac{1}{3}\alpha_s \delta_{kl} \Delta T + \frac{1}{3} c_s \delta_{kl} \Delta P) \qquad (4\text{-}10)$$

where D_{ijkl} stiffness matrix

ε_{kl} strain tensor (total strain)

α_s coefficient of thermal expansion for soil (porous matrix)

ΔT change in temperature

ΔP change in pore fluid pressure

Effects of creep, swelling and so on have been disregarded in equation (4-10). By substituting (4-10) into (4-9):

$$-\int_v D_{ijkl}\Delta\varepsilon_{kl}\omega_{,j}dV+\int_v D_{ijkl}\frac{1}{3}\alpha_s\delta_{kl}\Delta T\omega_{,j}dV+\int_v\alpha\Delta P\delta_{ij}\omega_{,j}dV-\int_v D_{ijkl}\frac{1}{3}c_s\delta_{kl}\Delta P\omega_{,j}dV=$$
$$-\int_{s\sigma}\Delta\bar{t}_{si}\omega dS+\int_v(-\Delta F_i+m'\Delta\ddot{U}_i+c'\Delta\dot{U}_i)\omega dV \qquad (4\text{-}11)$$

For obtaining the finite element form of (4-11) discretization in space and time has to be carried out.

Discretization in space :

$$\Delta U=[N]\{\Delta U^*\} \qquad \Delta P=<N_P>\{\Delta P^*\}$$
$$\Delta\varepsilon=[B]\{\Delta U^*\} \qquad \Delta T=<N_T>\{\Delta T^*\} \qquad (4\text{-}12)$$

And by employing Galerkin method :

$$\omega=[N] \quad , \quad \omega_{,j}=[B] \qquad (4\text{-}13)$$

'N' indicates the shape function matrix and 'B' is the derivative of shape functions with respect to the spatial coordinates x, y, and z. In order to make it possible to use different interpolation schemes for calculating displacements, pore fluid pressures, and temperatures, different N and B will be used for pore fluid pressures and temperatures. These will be designated by subscripts 'P' and 'T' respectively.

After discretization in space by using (4-12) and (4-13) one can obtain:

$$-\int_V[B]^T[D][B]\{\Delta U^*\}dV+\int_V[B]^T[D]\frac{1}{3}\alpha_s\{m\}<N_T>\{\Delta T^*\}dV+$$
$$+\int_V[B]^T\alpha\{m\}<N_P>\{\Delta P^*\}dV-\int_V[B]^T[D]\frac{1}{3}c_S\{m\}<N_P>\{\Delta P^*\}dV= \qquad (4\text{-}14)$$
$$-\int_{S_\sigma}[N]^T\{\Delta\bar{t}_s\}dS+\int_V[N]^T(-\{\Delta F\}+m'\{\Delta\ddot{U}\}+c'\{\Delta\dot{U}\})dV$$

where 'm' represents δ_{ij} in vector form i.e. <1 1 0 1>^{T} in two dimensions and <1 1 1 0 0 0>^{T} in three dimensions.

This is an ordinary differential equation (*O.D.E*) in time. For obtaining the algebraic equation the following finite difference approximations are used in order to discretize the equation (4-14) in time.

$$\Delta\dot{U} = \Delta(\frac{U_t - U_{t-\Delta t}}{\Delta t}) \qquad \Delta\ddot{U} = \Delta(\frac{U_t - 2U_{t-\Delta t} + U_{t-2\Delta t}}{\Delta t^2}) \tag{4-15}$$

Since we are looking for increment of displacement ΔU, between time 't' and '$t+\Delta t$', the backward difference will be used to avoid getting ΔU at time '$t+\Delta t$'.

Now the right hand side of (4-14) would be:

$$-\int_{S_\sigma}[N]^T\{\Delta\bar{t}_s\}dS_\sigma - \int_V[N]^T\{\Delta F\}dV + \int_V[N]^T m'\Delta(\frac{U_t - 2U_{t-\Delta t} + U_{t-2\Delta t}}{\Delta t^2})dV + \int_V[N]^T c'\Delta(\frac{U_t - U_{t-\Delta t}}{\Delta t})dV = R.HS \tag{4-16}$$

By defining these integrals, the matrix form of equation (4-14) would be obtained:

$$\int_V[B]^T[D][B]dV = [K] \tag{4-17}$$

$$\int_V[B]^T[D]<m>\{N_T\}dV = [K_T] \tag{4-18}$$

$$\alpha\int_V[B]^T\{m\}<N_p>dV + \frac{1}{3}c_S\int_V[B]^T[D]\{m\}<N_p>dV = [K_p] \tag{4-19}$$

$$\int_{S_\sigma}[N]^T\{\Delta\bar{t}_S\}dS = \{T_s\} \tag{4-20}$$

$$\int_V[N]^T\{\Delta F\}dV = \{F\} \tag{4-21}$$

$$\int_V[N]^T[N]dV = [N_N] \tag{4-22}$$

So the final matrix form of the equilibrium equation after multiplying both sides by Δt^2 would be:

$$-[K]\{\Delta U^*\}\Delta t^2 + \frac{1}{3}\alpha_S[K_T]\{\Delta T^*\}\Delta t^2 + [K_p]\{\Delta P^*\}\Delta t^2 = -\{T_S\}\Delta t^2 - \{F\}\Delta t^2 + m'[N_N]\{\Delta U^*{}_t\} - 2m'[N_N]\{\Delta U^*{}_{t-\Delta t}\} + m'[N_N]\{\Delta U^*{}_{t-2\Delta t}\} + c'[N_N]\{\Delta U^*{}_t\}\Delta t - c'[N_N]\{\Delta U^*{}_{t-\Delta t}\}\Delta t \tag{4-23}$$

Noting that $\Delta U^{*} \equiv (\Delta U^{*})_{t}$, ,equation (4-23) can be rewritten as :

$$([K]\Delta t^{2} + m'[N_{N}] + c'[N_{N}]\Delta t)\{\Delta U^{*}\} - ([K_{P}]\Delta t^{2})\{\Delta P^{*}\} - (\frac{1}{3}\alpha_{S}[K_{T}]\Delta t^{2})\{\Delta T^{*}\} = \{T_{S}\}\Delta t^{2} + \{F\}\Delta t^{2} + (2m'[N_{N}] + c'[N_{N}]\Delta t)\{\Delta U^{*}_{t-\Delta t}\} - m'[N_{N}]\{\Delta U^{*}_{t-2\Delta t}\} \quad (4\text{-}24)$$

Since the compressibility of solid grains C_s compared to the compressibility of the soil matrix C_b is negligible, the assumption $C_s=0$ (or Biot's factor α=1.0) has been considered in the program.

In equation (4-24), [K] is the well known stiffness matrix for displacements. $m'[N_N]$ represents the effect of mass inertia and $C'[N_N]$ shows the effect of damping. [K_P] and [K_T] are coupling terms representing force induced by pore pressure and forces created by thermal stresses respectively. On the right hand side $\{T_s\}$ is the surface traction vector and $\{F\}$ is the body force vector.

4.3 Fluid Flow Continuity Equation

The continuity equation is the governing equation for a single phase (equivalent fluid) flow which can be expressed in terms of either mass flux or volumetric flux. Since density of the fluid changes due to high compressibility of fluid (with occluded gas bubbles), a mass continuity equation in the reservoir is being used in this formulation (Thomas, 1977):

$$\nabla\cdot(\rho v) - G = -\frac{\partial}{\partial t}(\phi\rho) \quad (4\text{-}25)$$

where

ρ	density of fluid
v	velocity vector of flowing fluid
G	fluid mass flux from sink (output) or source (input)
ϕ	porosity of soil mass
t	time

Assuming that sink or source term may be considered later as a boundary condition, equation (4-25) may be written in the following indicial form:

$$(\rho v)_{,i} = -(\dot{\phi}\rho) \quad (4\text{-}26)$$

Applying weighted residual method for obtaining the weak form of equation(4-26) yields:

$$\int_V \{(\rho v)_{,i} + \dot{\phi}\rho + \dot{\rho}\phi\}\omega dV = 0 \tag{4-27}$$

Integration by parts:

$$\int_V (\dot{\phi}\rho + \dot{\rho}\phi)\omega dV - \int_V (\rho v)_{,i}\omega_{,i} dV = -\int_S (\rho \bar{v})_{,i} n_i \omega dS \tag{4-28}$$

Again two kinds of boundary conditions are being considered:

-velocity boundary conditions $v_i = \bar{v}_i$ on S_v (4-29)

-pore fluid pressure boundary conditions $P = \bar{P}$ on S_p (4-30)

Before dealing with details of integration, it should be noted that ϕ, ρ, and v_i have to specified in terms of the primary unknowns ΔU^*, ΔP^* and ΔT^*.

Porosity ϕ at any time 't' can be defined as (Tortike, 1991):

$$\phi_t = \frac{V_V}{V_b} = \frac{V_b - V_r}{V_b} \tag{4-31}$$

where V_v volume of voids

V_r volume of solid grains

V_b volume of bulk soil matrix

Thus:

$$\phi_{t+\Delta t} = \frac{(V_b + \Delta V_b) - (V_r + \Delta V_r)}{V_b + \Delta V_b} = \frac{(V_b + \varepsilon_V V_b) - (V_r + \Delta V_r)}{V_b + \varepsilon_V V_b} = \frac{1}{1+\varepsilon_V}\left[\frac{(1+\varepsilon_V)V_b - (V_r + \Delta V_r)}{V_b}\right]$$
$$= \frac{1}{1+\varepsilon_V}\left[\frac{V_b - V_r}{V_b} + \varepsilon_V - \frac{\Delta V_r}{V_b}\right] = \frac{1}{1+\varepsilon_V}\left[\phi_t + \varepsilon_V - \frac{\Delta V_r}{V_b}\right] = \frac{1}{1+\varepsilon_V}\left[\phi_t + \varepsilon_V - \frac{\Delta V_r}{V_r}\frac{V_r}{V_b}\right] \tag{4-32}$$

Change in volume of solid grains can be attributed to thermal expansion of grains if we disregard the volume change of solid grains due to the changes of pore pressure and effective stresses (i.e. assuming compressibility of solid grains *Cs* to be negligible):

$$\Delta V_r = V_r \alpha_S (T_{t+\Delta t} - T_t) \tag{4-33}$$

If compressibility of solid grains is significant, the effects of pore fluid pressure and effective stresses on the volume change of solid grains should also be taken into account. In this case equation (4-33) should be modified accordingly as:

$$\Delta V_r = V_r \alpha_S (T_{t+\Delta t} - T_t) - V_r C_S (P_{t+\Delta t} - P_t) - V_r C_S [\frac{1}{3}(\sigma'_{t+\Delta t} - \sigma'_t)_{hyd.}] \quad (4\text{-}34)$$

In (4-33) and (4-34):

P pore fluid pressure

T temperature

α_S coefficient of thermal expansion for soil

Note that α_S is the tangent or incremental coefficient of thermal expansion which is different from classical definition where instead of V_t, V_o(initial volume) is taken into account. Substituting (4-33) into (4-32) leads to:

$$\phi_{t+\Delta t} = \frac{1}{1+\varepsilon_V}[\phi_t + \varepsilon_V - \frac{V_r \alpha_S (T_{t+\Delta t} - T_t)}{V_r}\frac{V_r}{V_b}] = \frac{1}{1+\varepsilon_V}[\phi_t + \varepsilon_V - \alpha_S \Delta T(1-\phi_t)] \quad (4\text{-}35)$$

Now $d\phi/dt$ can be determined as:

$$\frac{\partial \phi}{\partial t} \approx \frac{\phi_{t+\Delta t} - \phi_t}{\Delta t} = \left\{\frac{[\phi_t + \varepsilon_v - \alpha_s \Delta T(1-\phi_t)] - \phi_t - \phi_t \varepsilon_v}{1+\varepsilon_v}\right\}\frac{1}{\Delta t} = \frac{(1-\phi_t)}{1+\varepsilon_v}\frac{-\alpha_s \Delta T + \varepsilon_v}{\Delta t}$$

(4-36)

Changes in fluid density can be described by using the following terms:

Isobar thermal expansion coefficient of fluid:

$$\alpha_P = -\frac{1}{\rho}(\frac{\partial \rho}{\partial T})_P = \frac{1}{V_0}(\frac{\partial V_0}{\partial T})_P \quad (4\text{-}37)$$

Isothermal pressure densification coefficient of fluid (compressibility):

$$\beta_T = \frac{1}{\rho}(\frac{\partial \rho}{\partial P})_T \quad (4\text{-}38)$$

If the effects of pressure and temperature both are to be considered, then

$$\rho_1 = \rho_0 e^{[-\alpha_P (T - T_0)]} \quad (4\text{-}39a)$$

and

$$\rho_2 = \rho_1 e^{[\beta_T (P - P_0)]} \quad (4\text{-}39b)$$

By employing Taylor expansion and neglecting terms with power greater than two:

$$\rho_1 = \rho_0[1 - \alpha_P(T - T_0) + \frac{\alpha_P{}^2(T - T_0)^2}{2} - \ldots + \ldots] \approx \rho_0[1 - \alpha_P(T - T_0)] \qquad (4\text{-}40)$$

and $$\rho_2 = \rho_1[1 + \beta_T(P - P_0)] \qquad (4\text{-}41)$$

or $$\rho_2 = \rho_0\{[1 + \beta_T(P - P_0)][1 - \alpha_P(T - T_0)]\} \qquad (4\text{-}42)$$

If α_P and β_T are defined as tangential coefficients, the relation (4-42) may be written, for each increment, as : $$\rho = \rho_t\{[1 + \beta_T \Delta P][1 - \alpha_P \Delta T]\} \qquad (4\text{-}43)$$

Having 'ρ' at any time based on (4-43), $\Delta\rho$ can be determined .

$$\Delta\rho = \rho_t(\beta_T \Delta P - \alpha_P \Delta T) \qquad (4\text{-}44)$$

similarly $d\rho/dt$ can be approximated as follows:

$$\frac{\partial \rho}{\partial t} \approx \frac{\Delta\rho}{\Delta t} = \frac{\rho_t}{\Delta t}(\beta_T \Delta P - \alpha_P \Delta T) \qquad (4\text{-}45)$$

Fluid velocity v_i can be determined based on Darcy's law for flow in porous media as:

$$v = -Ki \qquad (4\text{-}46)$$

in general index form:

$$v_i = -K_{ij}\frac{\partial H}{\partial x_j} \quad . \qquad (4\text{-}47)$$

where K hydraulic conductivity (m/sec)

i hydraulic slope

H total head

Although incorporating the effect of soil velocity in v (in order to use absolute velocity of the fluid) seems to make the formulation more precise, it should be noted that since 'material coordinate' is used for writing the equilibrium equation and 'spatial coordinate' is used for writing the continuity equation, the soil velocity in the two equations does not represent the same quantity because of different coordinate systems. There is a relationship between these two velocities (Malvern, 1968) which contains the gradient of displacements. However, in the hydraulic fracturing process the gradient of displacements, compared to the very high gradient of the injected fluid, is negligible.

Hence the effect of soil velocity in the flow equation has been ignored in the coupling process.

Since temperature has a drastic effect on the viscosity of oil and consequently on the hydraulic conductivity, K, it was found useful to replace K with $k\gamma/\mu$ in which k is the absolute permeability (m^2), γ is the unit weight of fluid, and μ is the viscosity of the fluid. Therefore (4-46) can be written as:

$$v_i = -\frac{k_{ij}\gamma}{\mu}(z + \frac{P}{\gamma})_{,j} \tag{4-48}$$

The fluid density $\gamma\ (= \rho g)$ is not a direct function of x, y and z (see for example equation 4-43), thus (4-48) can be expanded out as below. Note that dependency of pressure 'P' and temperature 'T' inside equation (4-43) on x, y, and z are second order effects.

$$v_i = -\frac{k_{ij}\gamma}{\mu}\frac{\partial z}{\partial x_j} - \frac{k_{ij}\gamma}{\mu}\frac{\partial(\frac{P}{\gamma})}{\partial x_j} = -\frac{k_{i3}\gamma}{\mu} - \frac{k_{ij}\gamma}{\mu}(\frac{\frac{\partial P}{\partial x_j}\gamma - \frac{\partial \gamma}{\partial x_j}P}{\gamma^2}) \tag{4-49}$$

$$v_i = -\frac{k_{i3}\rho g}{\mu} - \frac{k_{ij}}{\mu}\frac{\partial P}{\partial x_j} + \frac{k_{ij}P(\frac{\partial \rho}{\partial x_j})}{\mu\rho} \tag{4-50}$$

To summarize, the following relations can be used for ϕ, ρ, $d\phi/d$, $d\rho/dt$, and v_i:

$$\phi = (1-\theta)\phi_t + \theta\phi_{t+\Delta t} = \phi_t + \theta\Delta\phi = \phi_t + \theta[\frac{1-\phi_t}{1+\varepsilon_v}(\varepsilon_v - \alpha_s\Delta T)] \tag{4-51}$$

$$\rho = (1-\theta)\rho_t + \theta\rho_{t+\Delta t} = \rho_t + \theta\Delta\rho = \rho_t + \theta\rho_t(\beta_T\Delta P - \alpha_p\Delta T) \tag{4-52}$$

$$\frac{\partial\phi}{\partial t} = \frac{1-\phi_t}{1+\varepsilon_v}(\frac{-\alpha_s\Delta T + \varepsilon_v}{\Delta t}) \tag{4-53}$$

$$\frac{\partial\rho}{\partial t} = \frac{\rho_t}{\Delta t}(\beta_T\Delta P - \alpha_p\Delta T) \tag{4-54}$$

θ may vary from zero (fully explicit scheme) to 1.0 (fully implicit scheme).

$$v_i = -\frac{k_{i3}\rho g}{\mu} - \frac{k_{ij}}{\mu}\frac{\partial P}{\partial x_j} + \frac{k_{ij}P(\frac{\partial \rho}{\partial x_j})}{\mu\rho} \tag{4-55}$$

Relations (4-51) to (4-55) should be substituted into (4-28) which was the weak form of the continuity equation .

By applying the Galerkin scheme: $\omega =< N_P >$ and $\omega_j = [B_P]$ (4-56)

, the integral equation would be:

$$\int_S \{N_P{}^T\}\rho(\bar{v}_i n_i)dS - \int_V [B_P{}^T]\rho v_i dV + \int_V \{N_P{}^T\}\frac{\partial(\phi\rho)}{\partial}dV = 0 \qquad (4\text{-}57)$$

Substitution for ϕ, ρ, $d\phi/dt$, $d\rho/dt$ in (4-57) leads to equation (4-58).

$$\int_S \{N_P^T\}\rho_t(\bar{v}_i n_i)dS + \int_S \{N_P^T\}\theta\rho_t\beta_T\Delta P(\bar{v}_i n_i)dS - \int_S \{N_P^T\}\theta\rho_t\alpha_P\Delta T(\bar{v}_i n_i)dS -$$
$$\int_V [B_P^T]\rho_t v_i dV - \int_V [B_P^T]\theta\rho_t\beta_T\Delta P v_i dV + \int_V [B_P^T]\theta\rho_t\alpha_P v_i\Delta T dV +$$
$$\int_V \{N_P^T\}\frac{1-\phi_t}{1+\varepsilon_V}(\frac{-\alpha_S\Delta T}{\Delta t})\rho_t dV + \int_V \{N_P^T\}\frac{1-\phi_t}{1+\varepsilon_V}\frac{\varepsilon_V}{\Delta t}\rho_t dV + \int_V \{N_P^T\}\frac{\rho_t}{\Delta t}\beta_t\Delta P\phi_t dV -$$
$$\int_V \{N_P^T\}\frac{\rho_t}{\Delta t}\alpha_P\Delta T\phi_t dV = 0$$

(4-58)

Discretization in space:

$$\begin{aligned}
&\Delta U_i = [N]\{\Delta U^*\} && \Delta P =< N_P >\{\Delta P^*\} && \Delta T =< N_T >\{\Delta T^*\}\\
&\Delta\varepsilon_{ij} = [B]\{\Delta U^*\} && \Delta P_{,j} = [B_P]\{\Delta P^*\} && \Delta T_{,j} = [B_T]\{\Delta T^*\}\\
&\Delta\varepsilon_V = [C]\{\Delta U^*\}
\end{aligned} \qquad (4\text{-}59)$$

By discretization in space the relationship for velocity can be expanded as:

$$v_i = -\frac{k_{i3}\rho_t g}{\mu_t} + \frac{k_{ij}[B_P]\{P_t^*\}}{\mu_t} - \frac{k_{ij}\theta[B_P]\{\Delta P^*\}}{\mu_t} + \frac{k_{ij} < N_P >\{P_t^*\}}{\mu_t\rho_t}\frac{\partial\rho_t}{\partial x_j} + \frac{k_{ij}\theta < N_P >\{\Delta P^*\}}{\mu_t\rho_t}\frac{\partial\rho_t}{\partial x_j}$$

(4-60)

For simplicity, three terms without the primary unknown (ΔP^*) are lumped together and are called Z_i which represents the velocity at time 't'. Other terms having ΔP^* constitute Δv_i which are multiplied by $\theta(0 \le \theta \le 1)$ for implicit or explicit scheme. Hence:

$$v_i = -Z_i - \theta(\frac{k_{ij}[B_P]}{\mu_t} - \frac{k_{ij} < N_P >}{\mu_t\rho_t}\frac{\partial\rho_t}{\partial x_j})\{\Delta P^*\} \qquad (4\text{-}61)$$

where $Z_i = \frac{k_{i3}\rho_i g}{\mu_i} + \frac{k_{ij}[B_p]\{P_i^*\}}{\mu_i} - \frac{k_{ij} < N_p > \{P_i^*\}}{\rho_i \mu_i} \frac{\partial \rho_i}{\partial x_j}$

k_{ij}, μ and ρ in (4-61) are considered to be at time 't' which are the last updated values. For greater precision changes in fluid density and viscosity can be considered as well (change in absolute permeability relative to $\Delta\mu$ and $\Delta\rho$ is zero). In this case the following relation should can used for velocity:

$$v_i = -\frac{k_{i3}(\rho_i + \theta\Delta\rho)g}{\mu_i + \Delta\mu} - \frac{k_{ij}[B_p](\{P_i^*\}+\theta\{\Delta P^*\})}{\mu_i + \Delta\mu} + [\frac{k_{ij} < N_p > (\{P_T^*\}+\theta\{\Delta P^*\})}{\mu_i\rho_i + \theta\Delta\mu\rho_i + \theta\Delta\rho\mu_i}] \frac{\partial \rho_i}{\partial x_j}$$

By substituting v_i from (4-61) into (4-58), multiplying both sides of equation (4-58) by Δt and factorization with respect to the primary unknowns ΔU^*, ΔP^*, and ΔT^*, the following equation will be obtained:

$$\begin{aligned}
&\Big(\int_V \{N_P^T\}\rho_i \frac{1-\phi_i}{1+\varepsilon_V} < C > dV \Big)\{\Delta U^*\} + \\
&\Big(\Delta t \int_S \{N_P^T\}\theta\rho_i\beta_T\bar{v}_i n_i < N_P > dS + \Delta t \int_V [B_P^T]\rho_i \frac{k_{ij}\theta[B_P]}{\mu_i} dV + \\
&\Delta t \int_V [B_P^T]\theta\rho_i\beta_i Z_i < N_P > dV + \int_V \{N_P^T\}\rho_i\beta_i\phi_i < N_P > dV \Big)\{\Delta P^*\} - \\
&\Big(\Delta t \int_S \{[N_P^T]\theta\rho_i\alpha_P\bar{v}_i n_i < N_T > dS + \Delta t \int_V [B_P^T]\theta\rho_i\alpha_P Z_i < N_T > dV + \\
&\int_V \{N_P^T\}\frac{1-\phi_i}{1+\varepsilon_V}\alpha_S\rho_i < N_T > dV + \int_V \{N_P^T\}\rho_i\alpha_P\phi_i < N_T > dV \Big)\{\Delta T^*\} = \\
&-\Delta t \int_S \{N_P^T\}\rho_i(\bar{v}_i n_i)dS - \Delta t \int_V [B_P^T]\rho_i Z_i dV
\end{aligned}$$

(4-62)

Now by defining the following integrals the matrix form of the continuity equation would be obtained.

$$\int_V \{N_P^T\}\rho_i \frac{1-\phi_i}{1+\varepsilon_V} < C > dV = [NC\rho] \qquad (4\text{-}63)$$

$$\int_S \{N_P^T\}\rho_i\bar{v}_i n_i < N_P > \overline{dS} = [NWv] \qquad (4\text{-}64)$$

$$\int_V [B_p]^T \frac{k_{ij}\rho_l}{\mu_l}[B_p]dV = [BK1] \tag{4-65}$$

$$\int_V [B_p]^T \rho_l Z_l < N_p > dV = [BK2] \tag{4-66}$$

$$\int_V \{N_p^T\}\rho_l \phi_l < N_p > dV = [NW] \tag{4-67}$$

$$\int_S \{N_p^T\}\rho_l \bar{v}_l n_l < N_T > dS = [NYv] \tag{4-68}$$

$$\int_V [B_p]^T \rho_l Z_l < N_T > dV = [BK3] \tag{4-69}$$

$$\int_V \{N_p^T\}\frac{1-\phi_s}{1+\varepsilon_v}\rho_s < N_T > dV = [N\rho] \tag{4-70}$$

$$\int_V \{N_p^T\}\rho_l \phi_l < N_T > dV = [NY] \tag{4-71}$$

$$\int_S \{N_p^T\}\rho_l \bar{v}_l n_l dS = \{Nv\} \tag{4-72}$$

$$\int_V [B_p]^T \rho_l \bar{Z}_l dV = \{BZ\} \tag{4-73}$$

At this point sink (or source) term 'G' can be taken into account:

$$\int_V \{N_p^T\}GdV = \{G\} \tag{4-74}$$

'G' is the fluid mass output from sink when it is negative or input from source when it is positive.

Hence, the final finite element form of the continuity equation would be:

$$([NC\rho])\{\Delta U^*\} + (\ \Delta t\theta\beta_T[NWv]+\Delta t\theta[BK1]+\Delta t\theta\beta_T[BK2]+\beta_T[NW]\ )\{\Delta P^*\} +$$
$$(-\Delta t\theta\alpha_p[NYv]-\Delta t\theta\alpha_p[BK3]-\alpha_s[N\rho]-\alpha_p[NY]\ )\{\Delta T^*\} = -\Delta t\{Nv\}-\Delta t\{BZ\}+\Delta t\{G\} \tag{4-75}$$

In equation (4-75), the matrix $[NC\rho]$ represents fluid flow caused by the ground deformation. The terms $[NWv]$ and $[NYv]$ are fluid flow due to the specified velocity on the boundaries. The matrix $[BK1]$ is the main fluid flow term due to the apparent velocity of the fluid. The terms $[BK2]$ and $[BK3]$ represent fluid flow resulting from the change of density inside the element. The terms $[NW]$ and $[NY]$ show the fluid flow in-

duced by the change of porosity. In the right hand side, the vector $\{Nv\}$ is the flow due to specified flux on the boundaries while vector $\{BZ\}$ indicates the effect of changes in velocity.

For the fluid flux boundary condition, positive and negative values are used for outward and inward flow respectively.

4.4 Heat Transfer Equation

Governing partial differential equation for heat transfer in a reservoir is (Pratts, 1982):

$$\nabla.(L_e) - Q = -\frac{\partial(\rho E)}{\partial t} \tag{4-76}$$

where

L_e	volumetric thermal energy flux
E	internal energy per unit mass
ρ	fluid density
Q	energy flux from source (input) or sink (output)
t	time

Since 'Q' could be introduced later by means of boundary conditions, equation (4-76) can be written in the following compact form:

$$L_{ei,i} + \frac{\partial(\rho E)}{\partial t} = 0 \tag{4-77}$$

The term (ρE) can be interpreted as the internal energy per unit bulk volume.

Employing the weighted residual method in order to obtain the weak form of equation (4-77) yields:

$$\int_V [L_{ei,i} + \frac{\partial(\rho E)}{\partial t}]\omega dV = 0 \tag{4-78}$$

Integration by parts:

$$\int_S (L_{ei} n_i)\omega dS - \int_V L_{ei}\omega_{,i} dV + \int_V (\dot{\rho E})\omega dV = 0 \tag{4-79}$$

The first integral represents a boundary condition such as $L_{ei} = \bar{L}_{ei}$ on S_L.

Two terms (ρE) and L_e should be replaced by some functions of pore fluid pressure (ΔP) and temperature (ΔT) which are our primary unknowns.

$$(\rho E) = (1-\phi)M_\sigma(T-T_0) + \phi S\rho E_f$$
$$L_{ei} = -\lambda\frac{\partial T}{\partial x_i} + f_i\rho(h_f + \frac{gz}{J}) \qquad (4\text{-}80)$$

where ϕ porosity of soil matrix

$M\sigma$ volume heat capacity of soil/rock

S degree of saturation

λ coefficient of conductivity

f_i volumetric flux of flowing fluid

g acceleration of gravity

z elevation

J mechanical equivalent of heat

$E_f = C_v(T-To)$ internal energy per unit mass of fluid (4-81)

$h_f = C_p(T-To)$ enthalpy (4-82)

C_v heat capacity of fluid at constant volume

C_p heat capacity of fluid at constant pressure

For a single phase fully saturated medium (S=1.00), equation (4-80) becomes:

$$(\rho E) = (1-\phi)M_\sigma(T-T_0) + \phi\rho C_V(T-T_0) \qquad (4\text{-}83)$$

Note that f_i is equal to the velocity v_i by dimensional analysis, so equation(4-61) can be used for substituting f_i.

By substituting L_{ei} and ρE from (4-80) into equation(4-79):

$$\int_S(\bar{L}_{ei}n_i)\omega dS + \int_V\lambda\frac{\partial T}{\partial x_i}\omega_{,i}dV - \int_V v_i\rho C_P(T-T_0)\omega_{,i}dV - \int_V v_i\rho\frac{gz}{J}\omega_{,i}dV +$$
$$\int_V\frac{\partial}{\partial t}[(1-\phi)M_\sigma(T-T_0)]\omega dV + \int_V\frac{\partial}{\partial t}[\phi\rho C_V(T-T_0)]\omega dV = 0 \qquad (4\text{-}84)$$

Employing Galerkin's method: $\omega = < N_T >$ and $\omega_{,i} = [B_T]$ (4-85)

Substituting (4-85) into (4-84) yields:

$$\int_S \{N_T^T\}(\bar{L}_{el} n_i)dS + \int_V [B_T]^T \lambda \frac{\partial T}{\partial x_i} dV - \int_V [B_T]^T v_i \rho C_p (T - T_0) dV - \int_V [B_T]^T v_i \rho \frac{gz}{J} dV -$$
$$\int_V \{N_T^T\} \frac{\partial \phi}{\partial t} M_\sigma (T - T_0) dV + \int_V \{N_T^T\} \frac{\partial T}{\partial t} (1 - \phi) M_\sigma dV + \int_V \{N_T^T\} \frac{\partial (\phi \rho)}{\partial t} C_V (T - T_0) dV +$$
$$\int_V \{N_T^T\} (\phi \rho) C_V \frac{\partial T}{\partial t} dV = 0$$

(4-86)

Replacing ρ, ϕ, $d\rho/dt$ and $d\phi/dt$ with relations (4-51) to (4-54) will lead to the equation (4-87) as follows:

$$\int_S \{N_T^T\}(\bar{L}_{el} n_i)dS + \int_V [B_T]^T \lambda \frac{\partial (T_t + \theta \Delta T)}{\partial x_i} dV - \int_V [B_T]^T v_i \rho_t C_P (T_t + \theta \Delta T - T_0) dV -$$
$$\int_V [B_T]^T v_i \theta \rho_t \beta_T \Delta P C_P (T_t - T_0) dV + \int_V [B_T]^T v_i \theta \rho_t \alpha_P \Delta T C_P (T_t - T_0) dV - \int_V [B_T]^T v_i \rho_t \frac{gz}{J} dV -$$
$$\int_V [B_T]^T v_i \theta \rho_t \beta_T \Delta P \frac{gz}{J} dV + \int_V [B_T]^T v_i \theta \rho_t \alpha_P \Delta T \frac{gz}{J} dV + \int_V \{N_T^T\} \frac{1 - \phi_t}{1 + \varepsilon_V} \frac{\alpha_S \Delta T}{\Delta t} M_\sigma (T_t - T_0) dV -$$
$$\int_V \{N_T^T\} \frac{1 - \phi_t}{1 + \varepsilon_V} \frac{\varepsilon_V}{\Delta t} M_\sigma (T_t - T_0) dV + \int_V \{N_T^T\} \frac{\partial T}{\partial t} (1 - \phi_t) M_\sigma dV - \int_V \{N_T^T\} \frac{\partial T}{\partial t} \theta \frac{1 - \phi_t}{1 + \varepsilon_V} \varepsilon_V M_\sigma dV +$$
$$\int_V \{N_T^T\} \frac{\partial T}{\partial t} \theta \frac{1 - \phi_t}{1 + \varepsilon_V} \alpha_S M_\sigma \Delta T dV - \int_V \{N_T^T\} \frac{1 - \phi_t}{1 + \varepsilon_V} \frac{\alpha_S \Delta T}{\Delta t} \rho_t C_V (T_t - T_0) dV +$$
$$\int_V \{N_T^T\} \frac{1 - \phi_t}{1 + \varepsilon_V} \frac{\varepsilon_V}{\Delta t} \rho_t C_V (T_t - T_0) dV + \int_V \{N_T^T\} \frac{\rho_t}{\Delta t} \beta_T \Delta P \phi_t C_V (T_t - T_0) dV$$
$$- \int_V \{N_T^T\} \frac{\rho_t}{\Delta t} \alpha_P \Delta T \phi_t C_V (T_t - T_0) dV + \int_V \{N_T^T\} \rho_t \phi_t C_V \frac{\partial T}{\partial t} dV = 0$$

(4-87)

Discretization in space:

$$\begin{array}{lll} \Delta U_i = [N]\{\Delta U^*\} & \Delta P = < N_P > \{\Delta P^*\} & \Delta T = < N_T > \{\Delta T^*\} \\ \Delta \varepsilon_{ij} = [B]\{\Delta U^*\} & \Delta P_{,j} = [B_P]\{\Delta P^*\} & \Delta T_{,j} = [B_T]\{\Delta T^*\} \\ \Delta \varepsilon_V = [C]\{\Delta U^*\} & & \end{array} \qquad (4\text{-}88)$$

Substituting v_i from (4-61) into (4-87), multiplying both sides by Δt and neglecting the incremental terms to the power two or more, leads to the equation (4-89).

$$\Delta t\int_S\{N_T^T\}(\bar{L}_{ei}n_i)dS+\Delta t\int_V[B_T]^T\lambda[B_T]\{T_i^*\}dV+\Delta t\theta\int_V[B_T]^T\lambda[B_T]\{\Delta T^*\}dV+$$

$$\Delta t\int_V[B_T]^T Z_i\rho_i C_P(T_i-T_0)dV+\Delta t\theta\int_V[B_T]^T Z_i\rho_i C_P<N_T>\{\Delta T^*\}dV+$$

$$\Delta t\theta\int_V[B_T]^T Z_i\rho_i\beta_T<N_P>\{\Delta P^*\}C_P(T_i-T_0)dV-\Delta t\theta\int_V[B_T]^T Z_i\rho_i\alpha_P<N_T>\{\Delta T^*\}C_P(T_i-T_0)dV+$$

$$\Delta t\theta\int_V[B_T]^T\frac{k_{ij}}{\mu_i}[B_P]\{\Delta P^*\}\rho_i C_P(T_i-T_0)dV+\Delta t\int_V[B_T]^T Z_i\rho_i\frac{gz}{J}dV+$$

$$\Delta t\theta\int_V[B_T]^T Z_i\rho_i\beta_T<N_P>\{\Delta P^*\}\frac{gz}{J}dV-\Delta t\int_V[B_T]^T Z_i\theta\rho_i\alpha_P<N_T>\{\Delta T^*\}\frac{gz}{J}dV+$$

$$\Delta t\theta\int_V[B_T]^T\frac{k_{ij}}{\mu_T}[B_P]\{\Delta P^*\}\rho_i\frac{gz}{J}dV+\int_V\{N_T^T\}\frac{1-\phi_i}{1+\varepsilon_V}\alpha_S<N_T>\{\Delta T^*\}M_\sigma(T_i-T_0)dV-$$

$$\int_V\{N_T^T\}\frac{1-\phi_i}{1+\varepsilon_V}<C>\{\Delta U^*\}M_\sigma(T_i-T_0)dV+\int_V\{N_T^T\}<N_T>\{\Delta T^*\}(1-\phi_i)M_\sigma dV-$$

$$\int_V\{N_T^T\}\frac{1-\phi_i}{1+\varepsilon_V}\alpha_S<N_T>\{\Delta T^*\}\rho_i C_V(T_i-T_0)dV+\int_V\{N_T^T\}\frac{1-\phi_i}{1+\varepsilon_V}<C>\{\Delta U^*\}\rho_i C_V(T_i-T_0)dV+$$

$$\int_V\{N_T^T\}\rho_i\beta_T<N_P>\{\Delta P^*\}\phi_i C_V(T_i-T_0)dV-\int_V\{N_T^T\}\rho_i\alpha_P<N_T>\{\Delta T^*\}\phi_i C_V(T_i-T_0)dV+$$

$$\int_V\{N_T^T\}\rho_i\phi_i C_V<N_T>\{\Delta T^*\}dV=0 \qquad (4\text{-}89)$$

Factorization with respect to the ΔU^*, ΔP^* and ΔT^* yields equation (4-90):

$$
\begin{aligned}
&\Big(-\int_V \{N_T^T\}\frac{1-\phi_t}{1+\varepsilon_V} < C > M_\sigma (T_T - T_0)dV + \int_V \{N_T^T\}\frac{1-\phi_t}{1+\varepsilon_V} < C > \rho_t C_V (T_t - T_0)dV \Big)\{\Delta U^*\} + \\
&\Big(\Delta t\theta \int_V [B_T]^T Z_t \rho_t \beta_t C_P (T_t - T_0) < N_P > dV + \Delta t\theta \int_V [B_T]^T \frac{k_{ij}}{\mu_t}[B_P]\rho_t C_P (T_t - T_0)dV + \\
&\Delta t\theta \int_V [B_T]^T Z_t \rho_t \beta_T \frac{gz}{J} < N_P > dV + \Delta t\theta \int [B_T]^T \frac{k_{ij}}{\mu_t}[B_P]\rho_t \frac{gz}{J}dV + \\
&\int_V \{N_T^T\}\rho_t \beta_T \phi_t C_V (T_t - T_0) < N_P > dV \Big)\{\Delta P^*\} + \Big(\Delta t\theta \int_V [B_T]^T \lambda [B_T]dV + \\
&\Delta t\theta \int_V [B_T]^T Z_t \rho_t C_P < N_T > dV - \Delta t\theta \int_V [B_T]^T Z_t \rho_t \alpha_P C_P (T_t - T_0) < N_T > dV - \\
&\Delta t\theta \int_V [B_T]^T Z_t \rho_t \alpha_P \frac{gz}{J} < N_T > dV + \int_V \{N_T^T\}\frac{1-\phi_t}{1+\varepsilon_V}\alpha_S M_\sigma (T_t - T_0) < N_T > dV + \\
&\int_V \{N_T^T\} M_\sigma (1-\phi_t) < N_T > dV - \int_V \{N_T^T\}\frac{1-\phi_t}{1+\varepsilon_V}\alpha_S \rho_t C_V (T_t - T_0) < N_T > dV - \\
&\int_V \{N_T^T\}\rho_t \alpha_P \phi_t C_V (T_t - T_0) < N_T > dV + \int_V \{N_T^T\} C_V \rho_t \phi_t < N_T > dV \Big)\{\Delta T^*\} \\
&= -\Delta t \int_S \{N_T^T\}(\bar{L}_{et} n_t)dS - \Delta t \int_V [B_T]^T \lambda [B_T]\{T_t^*\}dV - \Delta t \int_V [B_T]^T Z_t \rho_t C_P (T_t - T_0)dV \\
&- \Delta t \int_V [B_T]^T Z_t \rho_t \frac{gz}{J}dV
\end{aligned}
\tag{4-90}
$$

Now in order to obtain the finite element form of the equation, the integrals shown in (4-90) have to be defined as matrices:

$$\int_V \{N_T^T\}\frac{1-\phi_t}{1+\varepsilon_V} < C > (T_t - T_0)dV = [NCT] \tag{4-91}$$

$$\int_V \{N_T^T\}\frac{1-\phi_t}{1+\varepsilon_V} < C > \rho_t (T_t - T_0)dV = [NC\rho T] \tag{4-92}$$

$$\int_V [B_T]^T Z_t \rho_t (T_t - T_0) < N_P > dV = [BNT] \tag{4-93}$$

$$\int_V [B_T]^T \frac{k_{ij}}{\mu_t}[B_P]\rho_t (T_t - T_0)dV = [ANW3] \tag{4-94}$$

$$\int_V [B_T]^T Z_t \rho_t \frac{gz}{J} < N_P > dV = [BNZ] \tag{4-95}$$

$$\int_V [B_T]^T \frac{k_{ij}}{\mu_t}[B_P]\rho_t \frac{gz}{J}dV \tag{4-96}$$

$$\int_V \{N_T^T\}\rho_l\phi_l(T_l - T_0) < N_p > dV = [HT1] \tag{4-97}$$

$$\int_V [B_T]^T [B_T] dV = [BB] \tag{4-98}$$

$$\int_V [B_T]^T Z_l \rho_l < N_T > dV = [HT2] \tag{4-99}$$

$$\int_V [B_T]^T Z_l \rho_l (T_l - T_0) < N_T > dV = [HT3] \tag{4-100}$$

$$\int_V [B_T]^T Z_l \rho_l \frac{gz}{J} < N_T > dV = [HT4] \tag{4-101}$$

$$\int_V \{N_T^T\}\frac{1-\phi_l}{1+\varepsilon_v}(T_l - T_0) < N_T > dV = [NT] \tag{4-102}$$

$$\int_V \{N_T^T\}(1-\phi_l) < N_T > dV = [\phi] \tag{4-103}$$

$$\int_V \{N_T^T\}\frac{1-\phi_l}{1+\varepsilon_v}\rho_l(T_l - T_0) < N_T > dV = [N\rho T] \tag{4-104}$$

$$\int_V \{N_T^T\}\rho_l\phi_l(T_l - T_0) < N_T > dV = [HT5] \tag{4-105}$$

$$\int_V \{N_T^T\}\rho_l\phi_l < N_T > dV = [N\phi] \tag{4-106}$$

$$\int_S \{N_T^T\}(\bar{L}_{el} n_l) dS = \{NL\} \tag{4-107}$$

$$\int_V [B_T]^T [B_T]\{T_l^*\} dV = \{BT\} \tag{4-108}$$

$$\int_V [B_T]^T Z_l \rho_l (T_l - T_0) dV = \{RHS1\} \tag{4-109}$$

$$\int_V [B_T]^T Z_l \rho_l \frac{gz}{J} dV = \{RHS3\} \tag{4-110}$$

At this point the source (or sink) term 'Q' can be taken into account:

$$\int_V \{N_T^T\} Q dV = \{Q\} \tag{4-111}$$

where 'Q' is the energy input from sources per unit volume. For energy output from sinks, negative values can be used and vice versa.

Therefore the final finite element form of the heat transfer equation would be written as:

$$\begin{aligned}
&\left(-M_\sigma[NCT] + C_v[NC\rho T] \right)\{\Delta U^*\} + \\
&\left(\Delta t\theta C_P\beta_T[BNT] + \Delta t\theta C_P[ANW3] + \Delta t\theta\beta_T[BNZ] + \Delta t\theta[ANW1] + C_v\beta_T[HT1] \right)\{\Delta P^*\} \\
&+\left(\Delta t\theta\lambda[BB] + \Delta t\theta C_P[HT2] - \Delta t\theta C_P\alpha_P[HT3] - \Delta t\theta\alpha_P[HT4] + \alpha_S M_\sigma[NT] + \right. \\
&\left. M_\sigma[\phi] - C_v\alpha_S[N\rho T] - C_v\alpha_P[HT5] + C_v[N\phi] \right)\{\Delta T^*\} = \\
&-\Delta t\{NL\} - \Delta t\lambda\{BT\} - \Delta tC_P\{RHS1\} - \Delta t\{RHS3\} + \Delta t\{Q\}
\end{aligned} \tag{4-112}$$

Integrals (4-91) and (4-92) are to be used as coefficients of $\{\Delta U^*\}$ in equation(4-112). Despite the mathematical evolution of these terms, they have little physical significance as they represent the contribution of displacements in the heat transfer in the reservoir which is obviously immaterial. Therefore, these terms are neglected in the code (i.e. the heat flow due to the effect of deformation of the reservoir is ignored). In (4-112) [*BB*] represents heat flux due to conduction. The terms [φ] and [$N\varphi$] represent the effect of heat capacitance of the solid phase and the fluid phase respectively. The terms [*NT*] and [$N\rho T$] show the effect of thermal expansion of solid phase and fluid phase, respectively, on the heat capacity of the medium. The matrix [*HT2*] represents the heat flux due to the heat capacitance of flowing fluid (convection). The terms [*BNT*] and [*HT3*] arise from the change of fluid density due to ΔP and ΔT respectively. Effect of the density change on internal energy due to ΔP and ΔT is shown in [*HT1*] and [*HT5*]. The terms [*BNZ*] and [*HT4*] emerge from the effect of change in fluid density on the gravitational thermal energy. The [*ANW1*] and [*ANW3*] matrices represent the effect of change of fluid velocity on the gravitational heat flux and fluid enthalpy respectively. On the right hand side of the equation, {*NL*} represents the thermal energy flux on the boundaries. Finally {*BT*}, {*RHS1*} and {*RHS3*} altogether stand for energy flux at the previous time step .

4.5 Coupling Process

The final finite element form of the equilibrium, fluid flow, and heat transfer equations, i.e. (4-24), (4-75), and (4-112) respectively, can be coupled to make a system of simultaneous equations. In all three equations the unknowns are ΔU^*, ΔP^*, and ΔT^* which represent the incremental values of displacements, pore fluid pressures, and temperatures at nodal points of the mesh during a time increment of 'Δt'. The obtained incremental values will affect the previous amounts of displacements, pore pressures, and temperatures at any node inside the medium (which were at time 't') and the new values will be determined for the time '$t+\Delta t$'. By marching through time all of the state variables at any point and at any time would be determined.

The general incremental finite element formulation can be summarized as follows:

$$\begin{bmatrix} K11 & K12 & K13 \\ K21 & K22 & K23 \\ K31 & K32 & K33 \end{bmatrix} \begin{Bmatrix} \Delta U^* \\ \Delta P^* \\ \Delta T^* \end{Bmatrix} = \begin{Bmatrix} F1 \\ F2 \\ F3 \end{Bmatrix} \tag{4-113}$$

where:

$$K11 = [K]\Delta t^2 + m'[N_N] + C'[N_N]\Delta t \tag{4-114}$$

$$K12 = [K_P]\Delta t^2 \tag{4-115}$$

$$K13 = -\frac{1}{3}\alpha_S[K_T]\Delta t^2 \tag{4-116}$$

$$K21 = [NC\rho] \tag{4-117}$$

$$K22 = \Delta t\theta\beta_T[NWv] + \Delta t\theta[BK1] + \Delta t\beta_T\theta[BK2] + \beta_T[NW] \tag{4-118}$$

$$K23 = -\Delta t\theta\alpha_P[NYv] - \Delta t\theta\alpha_P[BK3] - \alpha_P[NY] - \alpha_S[N\rho] \tag{4-119}$$

$$K31 = [0] \tag{4-120}$$

$$K32 = \Delta t\theta C_P[ANW3] + \Delta t\theta C_P\beta^T[BNT] + \Delta t\theta[ANW1] + \Delta t\theta\beta_T[BNZ] + C_V\beta_T[HT1] \tag{4-121}$$

$$K33 = \Delta t\theta\lambda[BB] + \Delta t\theta C_P[HT2] - \Delta t\theta C_P\alpha_P[HT3] - \Delta t\theta\alpha_P[HT4] + \alpha_S M_\sigma[NT] - \alpha_S C_V[N\rho T] - C_V\alpha_P[HT5] + M_\sigma[\phi] + C_V[N\phi] \tag{4-122}$$

$$F1 = \{T\}\Delta t^2 + \{F\}\Delta t^2 + (2m'[N_N] + C'[N_N]\Delta t)\Delta U^*_{t-\Delta t} - m'[N_N]\Delta U^*_{t-2\Delta t} \quad (4\text{-}123)$$

$$F2 = -\{Nv\}\Delta t - \{BZ\}\Delta t + \Delta t\{G\} \quad (4\text{-}124)$$

$$F3 = -\{NL\}\Delta t - \lambda\{BT\}\Delta t - C_p\{RHS1\}\Delta t - \{RHS3\}\Delta t + \Delta t\{Q\} \quad (4\text{-}125)$$

An important aspect of the coupling process is finding an appropriate value for the time increment, Δt, suitable for all three equations. Due to high speed of stress waves in soil/rock, the time increment in the equilibrium equation should be small enough to capture the behaviour of the soil/rock accurately. This 'Δt' is not necessarily the best 'time scale' for the fluid flow and/or heat transfer equation but in order to satisfy all three conservation laws simultaneously, we should use the smallest time increment.

On the other hand, it should be noted that the equilibrium equation is multiplied by 'Δt^2' but the fluid flow and heat transfer equations are multiplied by 'Δt'. This implies that if the time increment is less than unity the equilibrium equation has less influence in the coupling process compared to the other equations. Conversely, if the time increment is greater than unity, the equilibrium equation will have more influence in the system of equations. Usually, due to stability consideration, 'Δt' should not be large. Therefore, this problem may become a concern when a time increment of two or three orders of magnitude less than one is used. Hence, a very small time increments may not be suitable for a coupled analysis. Furthermore, in time-dependent problems in which time marching is required, a very small 'Δt' can increase the amount of the computational time considerably. Based on the above discussion the largest possible time increment should be used in the analysis. Obviously, this time increment depends on the nature of the problem and should be chosen by stability and accuracy analysis.

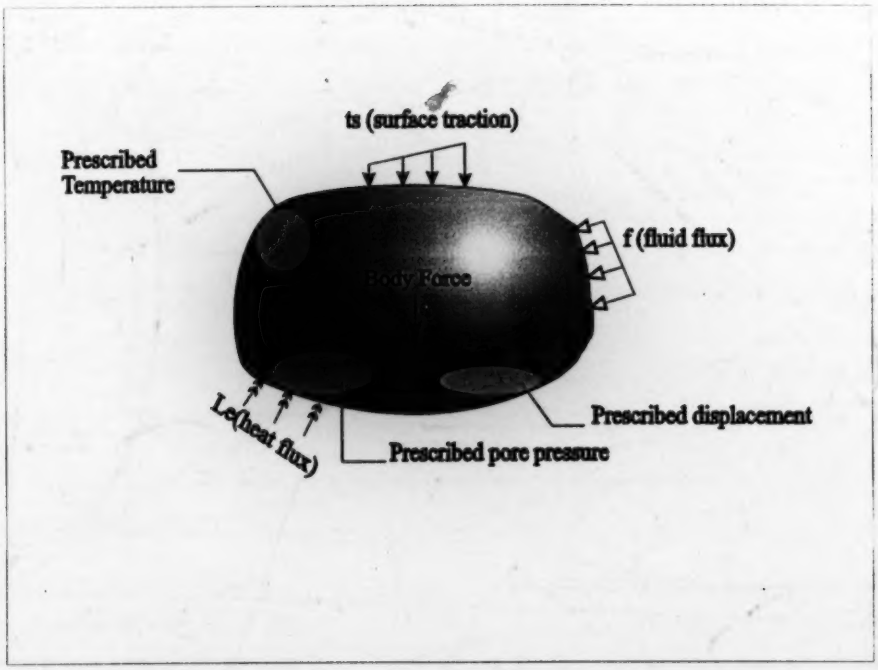

Figure (4-1) Boundary Conditions of a Typical Domain

Chapter 5

Modeling of Hydraulic Fracture

5.1 Introduction

Since 1947 when the hydraulic fracturing technique was introduced to the petroleum industry, its application has grown rapidly. In the early 1960's, the industry felt the necessity of having a design tool for this fast growing technique. In response to this need a number of two dimensional closed form solutions were developed for designing hydraulic fracturing treatments. Two models which have been more popular are Geertsma and deKlerk, *GdK*, (1969) and Perkins and Kern (1961). The latter was modified later by Nordgren (1972) to account for fluid leak-off, hence it is often called *PKN* model. In the *PKN* model, a fracture has a fixed height (h_f) independent of the fracture length, and the fracture cross section is assumed to be elliptic (Figure 5-1). In the *GdK* model, while a fixed height for the fracture is assumed that is independent of the fracture length, the fracture shape is considered to be approximately parabolic with a rectangular cross section (Figure 5-2). These models presented equations for calculating the fracture length, the maximum fracture opening (aperture) and the injection pressure for a constant injection rate.

These kinds of simple closed form solutions have been used by the industry with some success, however, as the technology has progressed from simple low volume/rate treatments to high volume/rate and sophisticated massive hydraulic fracturing projects, the industry has demanded more rigorous design methods in order to minimize the cost. During the last 25 years, several two and three dimensional computer models have been

developed (some of these models are reviewed in Chapter 3). The common equations used in these models are the fluid flow equation and the poroelasticity equations. Thermal effects are also considered in some of these models. The *GdK* or *PKN* models have mostly been used for fracture simulation. Linear elastic fracture mechanics (*LEFM*) criteria have been used to some extent.

In this chapter different aspects of the hydraulic fracture modeling will be discussed and the method chosen for this study will be described.

5.2 Natural Fractures vs. Induced Fractures

Geological discontinuities are common features on the earth's crust. Glaciation, tectonic effects, and weathering have caused different kinds of discontinuities in the ground throughout the earth's history. Generally, natural discontinuities can be divided into joints, faults, bedding planes, stress contrasts and/or a combination of these features. Technically, the term 'joint' is restricted to those fractures exhibiting evidence of dominantly opening displacements. This means that the displacements are perpendicular to the fracture surface (Pollard and Aydin, 1988). Faults refer to large scale rupture surfaces which have experienced shearing displacements. Normally faults are much larger than joints. Joints are usually unfilled and have high permeabilities, whereas faults are normally filled and therefore have low permeabilities. Bedding planes are weak interfaces between layers due to sedimentation process under water (Tannant, 1990).

'Fracture' is a generic name to describe near planar failure surfaces and is appropriate for structural features displaying any combination of opening and shearing displacements. Fracture zones, measuring 10 to 100 meters in length typically consist of several closely spaced and often interconnected joints and faults.

Man-made or induced fractures, on the other hand, are hydraulic or pneumatic fractures induced by overcoming tensile or shear strength of the ground at desirable depths. Although it is believed that hydraulic fracturing causes one or two distinct vertical or inclined fracture planes, in fact, the actual shape of the induced fracture is very complicated. Laboratory tests of hydraulic fracturing have indicated that,

especially in uncemented soils, one distinct fracture surface rarely occurs (Golder Ass., 1994; Komak panah, 1990). However, in the case of rocks and cohesive soils one distinct fracture plane has been observed (Rummel, 1987; Komak panah, 1990; Guo, 1993). Warpinski and Teufel (1987) studied a field experiment of hydraulic fracturing and showed that frequently there is nothing that can be called fracture plane; instead, the hydraulic fracture could be better described as a zone of multiple fractures sometimes 5 to 10 meters wide. Due to the nature of the hydraulic fracturing technique, there is always a moving front of fluid inside the fracture. This moving front is sometimes combined with heat, if hot fluid or steam is used. Stress field at the fracture tip is controlled by the fluid/heat front. These stresses may push the fracture further ahead or keep the fracture in place.

5.3 Effects of Natural Fractures on Hydraulic Fracturing Process

Geologic discontinuities, such as joints, faults, and bedding planes can significantly affect the geometry of hydraulic fractures. For example, such discontinuities may arrest the growth of the fracture, increase fluid leak-off, and/or enhance the creation of multiple fractures.

According to Warpinski and Teufel (1987), geologic discontinuities can influence the overall geometry of fractures and effectiveness of the hydraulic fracturing technique by:

1) arresting vertical propagation;

2) arresting lateral propagation at a fault or sand lens boundary;

3) reducing total length by increasing the amount of fluid leak-off;

4) reducing total length by facilitating the formation of multiple parallel fracture systems;

5) hindering proppant transport because of the nonplanarity of the fracture or fracture system, and

6) inducing additional fracture height growth due to higher fluid pressures because of many of the above features (items 2, 4 and 5, for instance).

5.4 Fracture Mechanics of Geomaterials

The analysis of crack problems through 'fracture mechanics' has its roots in attempts to understand the failure of glass, the stability of metal engineering structures in service, and more recently, the fracture properties of engineering ceramics. Fracture mechanics has grown in popularity because of the success of its relatively simple fracture criteria in describing the failure of these materials. Recent years have seen a dramatic increase in attention paid to both experimental fracture mechanics of rocks and the application of fracture mechanics to solve fracture problems in geophysics, earthquake engineering, hydraulic fracturing, hot dry rock energy extraction, and other rock mechanics and geological problems (Atkinson, 1987).

5.4.1 Different modes of fracture

Starting with the concept of an ideally flat and perfectly sharp crack of zero thickness, we should note that there are three basic modes of crack tip displacement. These modes are mode *I*: tensile (or opening), mode *II*: in-plane shear (or sliding), and mode *III*: anti-plane shear (or tearing). In problems concerning crack loading, the superposition of these three basic modes is sufficient to describe the most general cases of crack tip deformation and stress field (Smith, 1991).

a) Tensile mode: Tensile mode or opening mode is the most important mode in engineering practice, and therefore the majority of the fracture mechanics literature is devoted to analysis of this kind of fracture. Stresses and displacements around a crack tip of mode *I*, illustrated in Figure (5-3), can be determined using the following relations (Smith, 1991):

$$\sigma_x = \frac{K_I}{\sqrt{2\pi r}} \cos\frac{\theta}{2}\left(1 - \sin\frac{\theta}{2}\sin\frac{3\theta}{2}\right) \qquad (5\text{-}1)$$

$$\sigma_y = \frac{K_I}{\sqrt{2\pi r}} \cos\frac{\theta}{2}\left(1 + \sin\frac{\theta}{2}\sin\frac{3\theta}{2}\right) \qquad (5\text{-}2)$$

$$\tau_{xy} = \frac{K_I}{\sqrt{2\pi r}} \sin\frac{\theta}{2}\cos\frac{\theta}{2}\cos\frac{3\theta}{2} \qquad (5\text{-}3)$$

$$u = \frac{K_I}{4G}\sqrt{\frac{r}{2\pi}}\left((2\kappa - 1)\cos\frac{\theta}{2} - \cos\frac{3\theta}{2}\right) \tag{5-4}$$

$$v = \frac{K_I}{4G}\sqrt{\frac{r}{2\pi}}\left((2\kappa - 1)\sin\frac{\theta}{2} - \sin\frac{3\theta}{2}\right) \tag{5-5}$$

where $K_I = lim_{r\to 0}\sqrt{2\pi r}\,\sigma_y$ (5-6)

$\kappa = 3 - 4\nu$ (for plane strain)

$\kappa = (3-\nu)/(1+\nu)$ (for plane stress)

ν Poisson's ratio

G shear modulus

r, θ polar coordinates with respect to the crack tip

b) Shear modes : As mentioned above, there are generally two shear modes: sliding (mode *II*) and tearing (mode *III*). Although shear modes are less important for fractures in metals, they can be of prime interest for geological materials especially in the case of soils where the pore fluid pressure plays an important role in the soil behaviour. For mode *II*, illustrated in Figure (5-4), stresses and displacements around the crack tip can be determined by using these relations (Smith, 1991):

$$\sigma_x = -\frac{K_{II}}{\sqrt{2\pi r}}\sin\frac{\theta}{2}\left(2 + \cos\frac{\theta}{2}\cos\frac{3\theta}{2}\right) \tag{5-7}$$

$$\sigma_y = \frac{K_{II}}{\sqrt{2\pi r}}\sin\frac{\theta}{2}\left(\cos\frac{\theta}{2}\cos\frac{3\theta}{2}\right) \tag{5-8}$$

$$\tau_{xy} = \frac{K_{II}}{\sqrt{2\pi r}}\cos\frac{\theta}{2}\left(1 - \sin\frac{\theta}{2}\sin\frac{3\theta}{2}\right) \tag{5-9}$$

$$u = \frac{K_{II}}{4G}\sqrt{\frac{r}{2\pi}}\left((2\kappa + 3)\sin\frac{\theta}{2} + \sin\frac{3\theta}{2}\right) \tag{5-10}$$

$$v = -\frac{K_{II}}{4G}\sqrt{\frac{r}{2\pi}}\left((2\kappa - 3)\cos\frac{\theta}{2} + \cos\frac{3\theta}{2}\right) \tag{5-11}$$

where $K_{II} = lim_{r\to 0}\sqrt{2\pi r}\,\tau_{xy}$ (5-12)

For mode *III* crack, all of the stresses and displacements in the *x-y* plane are zero (Figure 5-5). Other stresses and displacements in the *z* direction are as follow (Smith, 1991):

$$\tau_{xz} = -\frac{K_{III}}{\sqrt{2\pi r}} \sin\frac{\theta}{2} \tag{5-13}$$

$$\tau_{yz} = \frac{K_{III}}{\sqrt{2\pi r}} \cos\frac{\theta}{2} \tag{5-14}$$

$$w = 2\frac{K_{III}}{G}\sqrt{\frac{r}{2\pi}} \sin\frac{\theta}{2} \tag{5-15}$$

where $$K_{III} = \lim_{r\to 0} \sqrt{2\pi r}\,\tau_{xy} \tag{5-16}$$

c) Mixed mode: In some situations in engineering practice, the medium is subjected to shear, torsion, bending as well as tensile loading. This leads to mixed mode cracking. When two or three modes are present simultaneously, the corresponding stresses and displacements for each mode may be added together based on the principle of superposition. But this is valid only if the behaviour of the material is linear elastic. Usually, extremely high stresses at the crack tip do not take place. This is because some irrecoverable (plastic) deformations occur at the crack tip which result in stress release at this region. It should be noted that application of the superposition is justified only when this plastic region is small. This point will be discussed in the next section.

5.4.2 Linear Elastic Fracture Mechanics and Elastic-Plastic Fracture Mechanics

Linear elastic fracture mechanics (*LEFM*) was originally developed to describe crack growth under elastic conditions for materials like metals, glasses, ceramics, rocks and ice. But there are many important classes of materials that are too ductile to permit description of their behaviour by *LEFM*. The crack tip plastic zone is too large to be ignored. Figure (5-6) illustrates different plastic zone sizes at the crack tip. In fracture mechanics literature, the zone in front of the crack tip that shows inelastic behaviour is called 'process zone'. The process zone can be a zone of plastic deformation in the case

of metals or a zone of microcracking in the case of geomaterials. If the dimensions of the process zone relative to the characteristic length of the domain (for example the least distance between the crack and the free edge of the domain) is small, the inelastic behaviour of the process zone can be overlooked and linear elastic theory can be used everywhere inside the domain. For cases where the process zone is large, other methods should be established which may be called elastoplastic fracture mechanics (*EPFM*).

A key concept of fracture mechanics is that extension of a fracture will occur once a critical value has been reached or exceeded. For example, *LEFM* essentially deals with stresses and energy around the crack tip. Based on elastic analysis, stresses at the crack tip approach infinity, therefore some measure of stresses at the crack tip such as the stress intensity factor (*Kc*) is needed and its values can be compared with some critical value for fracture initiation. Upon exceeding the critical value, the crack will propagate instantly provided that the crack is isolated and its surfaces are traction free. *EPFM* has other methods that attempt to describe the elastoplastic deformation field, in order to find a criterion for local failure. Of the concepts developed for this purpose, two have found a fairly general acceptance: the *J*-integral and the Crack Opening Displacement (*C.O.D*) which will be discussed later.

5.4.3 Crack extension laws

There are two types of crack extension laws in fracture mechanics (Atkinson, 1987):

(a) Equilibrium laws which specify that cracks may extend in a stable or unstable manner, at some critical value of a fracture mechanics parameter.

(b) Kinetic laws which specify that at certain subcritical values of fracture mechanics parameters a crack can extend at a velocity which is a function of the magnitude of the crack driving force.

In general, the equilibrium approach to crack extension (such as K_C, G_C or J_c parameters) is not a sufficiently general view of crack growth during long term loading. Experiments on a wide range of materials have shown that significant rates of crack growth can occur at values of K or G often far below the critical values of these

parameters. This is known as subcritical crack growth. Subcritical crack growth takes place in longer terms due to the chemical interaction between crack tip material and environmental factors such as water enhanced stress corrosion (Atkinson, 1987). In this study, in dealing with hydraulic fractures, only the first category will be considered.

5.4.3.1 Tensile strength criterion

This is the simplest approach to the mode *I* crack initiation problem. Based on tensile strength criterion, a crack occurs whenever the tensile stress at a point exceeds the tensile strength (sometimes called cohesive strength) of the material (Ingraffea, 1987).

$$\sigma_t \geq \sigma_t' \text{ (tensile strength)} \qquad (5\text{-}17)$$

It should be noted that material 'strength' is the maximum stress that a material can tolerate before yielding or breaking. Material 'toughness', on the other hand, represents the strain energy before breaking which is the area under the stress-strain curve.

5.4.3.2 Griffith criterion

Griffith (1921; 1924) used the concept of specific surface energy of material per unit area (γ_s) associated with the rupturing of molecular bonds (Figure 5-7).

$$\sigma \geq \sqrt{\frac{2E\gamma_s}{\pi a}} \qquad \text{for plane stress} \qquad (5\text{-}18)$$

$$\sigma \geq \sqrt{\frac{2E\gamma_s}{\pi a(1-\nu^2)}} \qquad \text{for plane strain} \qquad (5\text{-}19)$$

where γ_s specific surface energy of material per unit area

E modulus of elasticity

ν Poisson's ratio

a half of the existing crack length

Griffith assumed that there are always some flaws in solids and his criterion is for crack initiation (or more precisely crack extension) at the tip of the most favorably oriented crack or flaw. When applied stresses on the plate exceed the value on the right hand side of (5-18) or (5-19), crack extension takes place.

5.4.3.3 Irwin criterion

Two different criteria can be mentioned here. The first is based on stress intensity factor K_I; the second is based on strain energy release rate G. If an infinite plate has a crack with length $2a$ and the plate is under an applied stress σ (Figure 5-8), the 'stress intensity factor' at the crack tip can be calculated from:

$$K_I = \sigma\sqrt{a\pi} \qquad (5\text{-}20)$$

For any material, there is a critical value for stress intensity factor, K_{Ic}, that lets the fracture re-initiate and propagate further (Irwin, 1957; 1958). This critical value which is considered to be a material constant is called 'fracture toughness' (in fact, this is not a suitable nomination since K_I does not represent energy).

Irwin (1957) defined elastic strain energy per unit crack length increment as:

$$G = \partial U / \partial a \qquad (5\text{-}21)$$

This is also called 'strain energy release rate'. Note that this rate is with respect to the crack length and not with respect to the time. As with K, there is a critical value for G under which the crack starts to propagate. This value is a constant for a specific material and is called 'crack extension force'(G_C). When K_I (or G) exceeds K_{Ic} (or G_C) crack extension occurs.

There is a relationship between K and G:

$$K_I = \sqrt{EG} \qquad \text{for plane stress condition} \qquad (5\text{-}22)$$

$$K_I = \sqrt{\frac{EG}{(1-\nu^2)}} \qquad \text{for plane strain condition} \qquad (5\text{-}23)$$

These relations indicate that both K_{Ic} and G_c can be used for crack extension criterion in this category.

It is noteworthy that in this method an existing crack in the medium is posited. Therefore, in principle, this method cannot be used to quantify crack initiation. In practice, then, an initial crack length such as grain dimension or surface roughness is assumed.

5.4.3.4 Irwin's and Dugdale's methods for estimation of process zone dimension

As mentioned before if the size of the process zone is not large, *LEFM* can adequately describe the criteria for crack extension. When the size of the process zone becomes larger (but not larger than one tenth of the crack length, for instance) some modifications should be applied to the elastic analysis. Irwin (1960) and Dugdale (1960) proposed two different methods to estimate the size of the process zone. By using either of these methods some compensation can be made for the changes produced in the stress field by the plastic deformation.

Irwin (1960) postulated a circular process zone in front of the crack tip, illustrated in Figure (5-9), with the diameter of:

$$d = \frac{1}{\pi}\left(\frac{K_I}{\sigma_Y}\right)^2 \qquad (5\text{-}24)$$

where d process zone diameter

K_I stress intensity factor in mode I

σ_Y uniaxial yield stress

Irwin assumed that the crack tip extends to the center of the process circle so that the effective crack length will change to *(a+1/2 d)*. Based on this method the opening at the crack tip would be:

$$\delta_{tip} = \frac{4}{\pi}\frac{K_I^2}{E\sigma_Y} \qquad (5\text{-}25)$$

Dugdale (1960) assumed that the plastic deformation occurs in a strip ahead of the crack tip, as shown in Figure (5-10). The crack is supposed to extend all the way through the process zone and is therefore subjected to a negative (closing) pressure of σ_Y throughout this zone.

$$d = \frac{\pi}{8}\left(\frac{K_I}{\sigma_Y}\right)^2 \qquad (5\text{-}26)$$

As seen, the process zone in this theory is a little greater than Irwin's. Based on Dugdale's method the opening at the crack tip would be:

$$\delta_{tip} = \frac{K_I^2}{E\sigma_Y} \qquad (5\text{-}27)$$

Inherent in Irwin's and Dugdale's process zone size estimation is the assumption of yielding under uniaxial yield stress $\sigma\gamma$. This may not be an accurate yield criterion for metals, since yielding in metals is always associated with shear stress (not hydrostatic stress). If we transform σ_x, σ_y and τ_{xy} at the crack tip into principal stresses σ_1, σ_2, and σ_3 and then substitute these stresses into the Tresca and Von Mises criteria, two relationships for d in plane stress and plane strain conditions will be obtained. By plotting d from these relationships, yielding configurations depicted in Figure (5-11) will be obtained. Plane stress condition is normally assumed if d is of the same order of magnitude as the plate thickness (generally speaking very thin plates) and plane strain condition is assumed if d is about 10% or less of the plate thickness (very thick plates). It should be noted that, in practice, the plane strain zone size is usually observed to be larger than that shown in Figure (5-11) while the plane stress zone size tends to be smaller (Smith, 1991).

As mentioned earlier, Irwin's and Dugdale's methods are basically linear elastic approaches with corrections for small plastic zones around the crack tip. There are many applications where more extensive plastic deformation may occur at the crack tip; therefore there is a need for models that can handle more extensive plasticity. Two models for fracture in the presence of moderate plasticity are considered below. It is still assumed that plasticity is not very extensive to give general yielding, i.e., plastic collapse (Figure 5-6).

5.4.3.5 *J*-integral

Rice (1969) introduced the concept of *J*-integral. '*J*' is basically the potential energy release rate. For the plate as shown in Figure (5-12), one can write:

$$\frac{dU_p}{da} = -\int_\Gamma \omega dy + \int_\Gamma T_s \frac{du}{dx} ds \Rightarrow J = \int_\Gamma \omega dy - \int_\Gamma T_s \frac{du}{dx} ds \qquad (5\text{-}28)$$

where:

U_P potential energy

ω strain energy density

T_S applied surface traction on length S

u displacement on length S

Γ perimeter of the plate

a crack length

Using Green's theorem it can be shown that for a closed contour the value of J is zero. For elastic behaviour:

$$J = \frac{d}{da}(F - U_a) = \frac{dF}{da} - \frac{dU_a}{da} \qquad (5\text{-}29)$$

where: dF/da energy provided by external work F per unit crack extension

dU_a/da increase of elastic energy owing to the external work dF/da

This is the amount of energy that remains available for crack extension. For an elastic medium, 'J' is equal to 'G' (elastic energy release rate) by definition.

$$U_p = (U_O + U_a) - F \qquad (5\text{-}30)$$

where: U_p potential energy

U_0 strain energy of uncracked element subjected to external load

F work done by external load

By definition:

$$\frac{dU_p}{da} = \frac{d}{da}(U_a - F) = \frac{-d}{da}(F - U_a) = -J \qquad (5\text{-}31)$$

This indicates a reduction in potential energy due to an increase of the crack length (da), i.e., an equivalent amount of crack driving energy is released. If the amount of the released energy i.e. J, exceeds some critical value, J_c (a material characteristic), crack extension occurs.

$$J \geq J_C \qquad \text{at onset of crack extension} \qquad (5\text{-}32)$$

J-integral concept is particularly useful when the plastic region at the crack tip is large. Since the integral is path independent, instead of finding J at the crack tip, one can determine J at a similar path outside the plastic region.

5.4.3.6 Crack opening displacement *(C.O.D)*

Contrary to the former criteria, *C.O.D* is a displacement controlled fracture criterion. It can be stated based on plastic zone size according to Irwin (1960) or

according to Dugdale (1960). For plane stress condition the *C.O.D* for these models are:

$$\delta_{tip} = C.O.D = \frac{4}{\pi}\frac{K_I^2}{E\sigma_Y} \qquad \text{(Irwin's model)} \qquad (5\text{-}33)$$

$$\delta_{tip} = C.O.D = \frac{K_I^2}{E\sigma_Y} \qquad \text{(Dugdale's model)} \qquad (5\text{-}34)$$

If the crack tip plasticity is not accounted for, the displacement and crack opening at the crack tip (δ_{tip}) are equal to zero. The *C.O.D* approach was introduced by Wells (1962). He argued that the stress at the crack tip always reaches a critical value (in the case of pure elasticity the stress approaches infinity); if this is so then it is the plastic strain in the crack tip region that controls the fracture. A measure of the amount of crack tip plastic strain is the displacements of the crack flanks, especially at or very close to the tip. Hence, it might be expected that at the onset of fracture this crack opening displacement (*C.O.D*) has a characteristic critical value for a particular material and could therefore be used as a fracture criterion. Burdekin and Stone (1966) provided an improved basis for the *C.O.D* concept. They used Dugdale model to find an expression for *C.O.D* (Ewalds and Wanhill, 1984).

Experiments on different materials indicate that the crack tip displacement at the onset of crack extension, δ_{cr}, has some certain value in plane stress condition. When the experiments are carried out in plane strain condition, material is able to have a greater *C.O.D* before crack extension. That is why, using δ_{cr} in plane stress condition is always on the safe side.

5.4.3.7 Mixed mode fracture initiation criteria

All of the criteria cited above are for mode *I* (tensile) fracture only. For pure shear fracture (only mode *II* or mode *III*) Irwin's method has been extended and criteria such as G_{IIc} for mode *II* and G_{IIIc} for mode *III* have been obtained (Gdoutos, 1990). However, mixed mode fractures occur commonly in practice. For single-mode fracture the alignment of fracture propagation is always considered to be in the same direction of the original crack. In mixed mode fracture there is an additional complexity in determining the 'direction of crack propagation'. Surprisingly, still there is no

universally accepted theory in this category. Two methods that have gained more credibility among others are briefly described here. Both of these methods are applicable when the process zone size in front of the crack tip is reasonably small.

a) The stress criterion: This method was presented by Erdogan and Sih (1963). Consider a crack in a mixed mode stress field, shown on Figure (5-13), governed by the values of the opening mode K_I and sliding mode K_{II} stress intensity factors. Stress field in the vicinity of the crack tip is:

$$\sigma_r = \frac{K_I}{\sqrt{2\pi r}}\left(\frac{5}{4}\cos\frac{\theta}{2} - \frac{1}{4}\cos\frac{3\theta}{2}\right) + \frac{K_{II}}{\sqrt{2\pi r}}\left(-\frac{5}{4}\sin\frac{\theta}{2} + \frac{3}{4}\sin\frac{3\theta}{2}\right) \tag{5-35}$$

$$\sigma_\theta = \frac{K_I}{\sqrt{2\pi r}}\left(\frac{3}{4}\cos\frac{\theta}{2} + \frac{1}{4}\cos\frac{3\theta}{2}\right) + \frac{K_{II}}{\sqrt{2\pi r}}\left(-\frac{3}{4}\sin\frac{\theta}{2} - \frac{3}{4}\sin\frac{3\theta}{2}\right) \tag{5-36}$$

$$\tau_{r\theta} = \frac{K_I}{\sqrt{2\pi r}}\left(\frac{1}{4}\sin\frac{\theta}{2} + \frac{1}{4}\sin\frac{3\theta}{2}\right) + \frac{K_{II}}{\sqrt{2\pi r}}\left(\frac{1}{4}\cos\frac{\theta}{2} + \frac{3}{4}\cos\frac{3\theta}{2}\right) \tag{5-37}$$

The assumptions made in this criterion for crack extension in brittle materials may be stated as:

(i) The crack extension starts from its tip along the radial direction $\theta = \theta_c$ on which σ_θ becomes maximum.

(ii) Fracture starts when the maximum value of σ_θ reaches a critical stress, σ_C, equal to the fracture stress in uniaxial tension.

These hypotheses can be expressed mathematically by the relationships:

$$\frac{\partial \sigma_\theta}{\partial \theta} = 0, \frac{\partial^2 \sigma_\theta}{\partial \theta^2} < 0 \qquad \sigma_\theta(\theta_c) = \sigma_c \tag{5-38}$$

For determination of the direction of crack propagation the following equation should be solved for θ (Ingraffea, 1987):

$$K_I \sin\theta + K_{II}(3\cos\theta - 1) = 0 \tag{5-39}$$

b) The strain energy release rate criterion: This method was proposed by Sih (1973; 1974). Sih has shown that the strain energy density variation at a distance 'r' from a crack tip (Figure 5-13) is:

$$\frac{dU}{dV} = \frac{1}{r}\left(\frac{a_{11}K_I^2 + 2a_{12}K_I K_{II} + a_{22}K_{II}^2}{\pi}\right) \tag{5-40}$$

calling the bracket S, one can summarize (5-40) as:

$$\frac{dU}{dV} = \frac{S}{r} \tag{5-41}$$

where $$a_{11} = \frac{1}{16G}[(1+\cos\theta)(\chi - \cos\theta)] \tag{5-42}$$

$$a_{12} = \frac{\sin\theta}{16G}[2\cos\theta - (\chi - 1)] \tag{5-43}$$

$$a_{22} = \frac{1}{16G}[(\chi+1)(1-\cos\theta) + (1+\cos\theta)(3\cos\theta - 1)] \tag{5-44}$$

$$\chi = [3 - \frac{\nu}{1+\nu}] \quad \text{for plane stress} \tag{5-45}$$

G shear modulus

ν Poisson's ratio

This theory considers the following assumptions:

(i) Crack extension occurs in the direction along which dU/dV possesses a minimum value. i.e. θ_0 such that $\frac{\partial S}{\partial \theta} = 0, \frac{\partial^2 S}{\partial \theta^2} \geq 0$; (5-46)

(ii) Crack extension occurs when $S(\theta)$ reaches a critical, material value, S_c;

(iii) $S(\theta)$ is evaluated along a contour $r=r_0$, where r_0 is a material constant.

Combining (ii) and (iii) shows that $(\frac{dU}{dV})_c = \frac{S_c}{r_0}$ (5-47)

For cases where the process zone size at the crack tip is large, some attempts have been made to generalize the J-integral theory to the mixed mode cracking but experimental results have not confirmed the theory. Hence, for large process zone no satisfactory criterion is currently available for mixed mode cracking (Gdoutos, 1990).

5.5 Numerical Modeling of Fracture

Fracturing phenomenon and its importance on the material behaviour have been of interest to metallurgical, mechanical, and civil engineers for a long time. Of

particular importance for civil engineers is the changing behaviour of material before and after fracture which, in turn, plays an important role in modeling civil engineering structures and in determining the stresses, strains, and deformation of the structure under various loading conditions.

In general, for geomaterials such as soils, rocks and concrete there are three approaches for modeling both natural and induced fractures as described below.

5.5.1 The smeared approach

This approach takes the properties of the fracture and smears them over an area of soil/rock matrix without introducing any real fracture. This method eliminates the need for using discrete joint elements in the model and is most appropriate for situations in which well defined and uniformly spaced fractures predominate. In fact this approach is a statistical method where the geometry of the fracture system is represented by proper statistical distribution in a continuum (Tannant, 1990).

The smeared approach was first applied to concrete mainly by adjusting the material stiffness in the finite element analysis. This method, first proposed by Rashid (1968) and refined by many others, has provided good results in some practical applications (Bazant, 1986; deBorst, 1984; and others). Nevertheless, there are problems with the method. This method exhibits spurious mesh sensitivity and convergence to an incorrect failure mode with zero energy dissipation (deBorst, 1984; Darwin, 1985; Bazant and Oh, 1983). As a related deficiency, the numerical results obtained with geometrically similar meshes exhibit no size effect, while test results for brittle failures of concrete structures as well as fracture specimens show a pronounced size effect (Bazant, 1984; 1986). To improve the results Bazant and Oh (1983; 1984) proposed a 'crack band model' in which no finite element is allowed to become smaller than a certain characteristic length. This characteristic length is a material property which is related to the size of nonhomogeneity in the material. Later, Bazant and Lin (1989) presented a 'nonlocal smeared cracking model' to eliminate some of the problems associated with the crack band model.

5.5.2 The dual porosity model

The dual porosity model is a model essentially designed for naturally fractured reservoirs. Compared to other models, dual porosity model stands somewhere between the smeared approach and the discrete approach. In this model, it is assumed that the soil/rock medium has some porosity which plays a significant role in the deformation and hydraulic characteristics of the reservoir. On the other hand, there is a system of fractures with a different porosity which controls the fluid dynamics and deformation behaviour of the reservoir to some extent. In other words, the dual porosity approach assumes that the fractured porous media can be represented by two overlapping continua referred to as the fractures and the matrix. The 'fracture continuum' consists of an interconnected network of fractures and/or solution vugs which make the primary conduits for fluid flow. The 'matrix continuum' consists of the intergranular pore spaces of the rock which comprises the majority of the storage in the reservoir (Fung, 1990).

The concept of dual porosity dates back to the early sixties (Barenblatt, 1960; Warren and Rout, 1963). Since that time it has been used extensively in petroleum reservoir engineering. Early dual porosity models include Kazemi et al. (1976) and Saidi (1975) models. Saidi (1975) modeled a fractured reservoir by dividing it into sectors wherein the fracture was assumed to have infinite transmissibility. Kazemi et al. (1976) discretized the fracture continuum into grid blocks and simulated fluid flow by a set of fracture mass balance equations. Much of the more recent literature on dual porosity models has been devoted to improve modeling the gravity effects in the transfer calculation (Fung, 1990).

Although extensive work is being done on dual porosity models in petroleum engineering, it has seldom be used in the reservoir simulation by civil engineers or hydrogeologists. This is basically because in this approach the mechanical behaviour of the discontinuities such as dilation and slip are not considered; any effect resulting from accompanying changes in the deformation or flow would therefore be lost.

5.5.3 Discrete fracture approach

This approach is the most realistic and at the same time the most rigorous one to the fracture problem. The basic idea in this approach is that after the occurrence of fracture, the continuous medium no longer exists and each individual fracture and its particular characteristics (i.e. opening, length, permeability, and surrounding stress) are of interest. Discrete fracture approach is best suited to cases where a limited number of dominant fractures exist.

Over the past 15 years most of the research on discrete fracture modeling has been conducted using finite element method. Various methods for modeling discrete fractures using finite element method are discussed below.

5.6 Modeling Discrete Fractures Using Finite Element Method

Discrete fractures can be simulated using conventional displacement finite element method. Categorically, a distinction should be made between predefined (i.e. existing) fractures and induced fractures. In the first category the place and geometry of the fracture are known and attempts are usually made to model the mechanical behaviour of the fracture under forces normal and tangential to the fracture plane. Generally two special types of elements are used for modeling this kind of fracture: 'thin layer solid elements' and 'joint elements with zero thickness'. These elements will be discussed later in this section. The second category consists of induced fractures where the location and geometry of a crack are not known at the beginning of the analysis. In this category it is necessary to employ some techniques to modify the finite element mesh in order to accommodate the newly created fracture(s). When the fractures are established in the mesh, in accordance with the nature of the problem, a special kind of element is placed in the areas where fractures have occurred.

5.6.1 Elements for predefined fractures (interface elements)

These elements are basically used to determine the mechanical behaviour of joints and incorporate their stiffness in the global stiffness of the system.

a) Thin-layer solid element: A thin element between two other ordinary elements has been used for fracture modeling by some researchers (e.g. Desai et al., 1984). The

thickness of the thin-layer elements can be in order of $0.01a$ to $0.1a$, where 'a' is the mean dimension of the adjacent elements. These elements are solid elements with modified stiffness; other than that they usually behave like other elements.

b) Zero thickness joint elements: The first joint element with zero thickness was presented by Goodman et al. (1968). They proposed a four node element with zero thickness and used displacements instead of strains in its formulation. This element proved to be successful in modeling rock joints. Goodman's joint element can be extended to 3-dimensional elements with zero thickness where two 8-node plane elements coincide (Mahtab and Goodman, 1970). Different versions of this element have been used by other investigators (e.g. Ghaboussi et al., 1973). Other types of zero thickness elements have also been suggested (e.g. Herman, 1978). Nevertheless, there are some kinematic inconsistencies in this kind of elements common to all elements with very small thickness. These deficiencies are explained in Kalinkin and Li (1995).

5.6.2 Elements for advancing fractures

5.6.2.1 Crack at the element boundaries

In this category, cracks follow the element boundaries, therefore all of the discontinuities occur between the elements and not inside them. In this way the original mesh does not change considerably (assuming that small strain theory holds) but a fine mesh is required to capture the real geometry of the crack. Some researchers such as Ortiz et al. (1987) have proposed a 2-dimensional quadrilateral element built-up of four crossed triangles because this kind of element can capture the fractures in four different directions but the isoparametric quadrilateral elements can only model the fractures that are parallel to the sides of the elements. Obviously, the idea of considering the fractures at the element boundaries suffers from mesh dependency, therefore, a finer mesh is preferred to reduce this problem. Some techniques that have been used for modeling cracks at the element boundaries are described below.

a) Nodal grafting technique: In this technique some of the nodes in the finite element mesh are moved to other places in order to create new boundaries for fracture propagation (Ingraffea, 1977). Nodal grafting technique takes advantage of the fact that

higher order isoparametric elements can have a variable number of nodes. Therefore, some midside nodes of the elements that are located far from the fracture can be removed and put at the fracture tip. This enables the program to make a new boundary and separate two attached elements. In this way the increase in the bandwidth of the stiffness matrix will be minimum.

b) Node splitting technique: Instead of borrowing nodes from remote areas in a finite element mesh, one can introduce two nodes at places in the mesh where the possibility of fracturing is high and then split them when fracture occurs at this place. Before splitting, the nodes are connected together and have the same degree of freedom; therefore, no additional degrees of freedom will be required before fracturing. In this way the dimension of the stiffness matrix will not change and no change in the shape functions of the remote elements will be required. This technique was used by Chan (1981).

c) Distinct element method (*DEM*): In this method joints are represented by the planes of contact between intact blocks of rock or soil. In other words, the medium is considered to be made of separate blocks with joints between them. This method, which was pioneered by Cundall (1971), has proven to be useful for modeling fractured rocks. A version of this method called 'discrete element method' can be used for modeling of flow of sands or other granular materials.

5.6.2.2 Crack inside elements

In this category, same as the previous one, the configuration of the original mesh does not change considerably. However, in this case, the crack is not bounded to the element boundaries and in principle can take place anywhere. Therefore a very fine mesh to capture the geometry of the fracture is not required and mesh dependency vanishes. Elements that can accommodate internal cracks are called 'shear band elements' or 'slip elements'.

Most of the work in this area has been accomplished in the 'shear band' context and localization problem. Usually, the element interpolation function is changed by adding some suitably defined shape functions to it (Wan et al., 1992; Ortiz et al., 1987).

Sometimes these additional shape functions make the element incompatible and mesh locking occurs which has to be addressed properly.

Another approach is to modify the constitutive law of the fractured element rather than changing its shape function. Development of a shear band or fracture in the system is incorporated in the model by introducing a 'damage parameter' in the constitutive equation (Frantziskonis and Desai, 1987; Simo and Ju, 1987).

Using Cossarat granular material (Muhlhaus and Vardoulakis, 1987) is another approach. Cossarat medium is a continuum where 'grain size' of the material has an effect on the strains. Therefore, Cossarat medium can be used to determine the shear band thickness and localization of the granular materials. In fact, Cossarat medium by its built-in grain size effect improves the continuum-based analysis of crack and quantifies the shear band thickness in the medium.

5.6.2.3 Dynamic remeshing and adaptive mesh techniques

Contrary to the two previous crack modeling techniques, here, no attempt is made to keep the original finite element mesh unchanged. At each time step the whole mesh or part of it will be regenerated in order to accommodate new fracture(s). Basic advantage of this method is mesh-independency. This method was successfully developed by Ingraffea and Saouma (1984) for modeling of discrete crack propagation in reinforced and plain concrete. Later it was coupled with some fluid flow models (Shaffer et al., 1987).

Adaptive mesh technique (Zhu and Zienkiewicz,1988) follows roughly the same approach. Its basic idea is to improve the mesh configuration at each stage of the analysis based on the results of the previous stage in order to obtain more accurate results at the regions with high stress concentration and/or high gradient of displacements (or other state variables). This method, in principle, can be used in fracture problems; for instance, after finding the fracture orientation, those elements at the vicinity of the fracture zone can be deviated respectively in the next stage of the analysis to comply with the crack orientation.

Despite the advantages that dynamic remeshing and adaptive mesh techniques offer for improving the results of the finite element analysis, the amount of

computational effort in these methods are much higher than the other methods. The reason is that at each step of the analysis, the whole finite element mesh must be re-analyzed because the mesh configuration is changing continuously.

5.7 Modeling Moving Front of Fluid and Heat in the Fractures

5.7.1 Fluid flow inside the fractures

A particular fluid component can be transported by molecular diffusion and also by convection (bulk flow). Although diffusion alone can cause component movement in a no-flow system, usually both diffusion and convection occur.

Darcy's law, for a long time, has been used to describe the fluid seepage in porous media which is basically a diffusion process. The generalized form of Darcy's law holds in the presence of a temperature gradient even when the permeability, viscosity, and density are functions of temperature. Modifications of Darcy's law to account for turbulence and other inertial effects also are considered to be valid in the presence of temperature variations (Pratts, 1982).

Fluid flow inside the fractures depends upon the aperture, roughness of the walls, and geometry of the system of fractures. When fractures are well connected to each other and the aperture is large, turbulent bulk flow can dominate the situation. In this case, the original Darcy's law is no longer valid. Witherspoon et al. (1980), in a review of various laboratory results showed that the assumption of laminar flow in fractures is valid for Reynolds number less than about 2300. Reynolds number is an indicator for flow regimes (laminar, transient, or turbulent). Wilson and Witherspoon (1970), in a comprehensive review of laminar flow through fractures concluded that when fracture wall roughness increases the Reynolds number drops from 2000 to about 200. In the present study it is postulated that hydraulically induced fractures are not large and their apertures do not exceed 3 to 4 millimeters (Settari et al., 1989). Fractures are considered to be filled with solid particles (this is especially true for shear fractures), hence, despite the higher permeability that the fractures introduce to the system relative to the rest of the medium, fluid flow inside the fractures can still be analyzed using Darcy's law.

5.7.2 Heat transfer inside fractures

A condition generally assumed to prevail in all reservoir processes is that every point within the reservoir is in thermodynamic equilibrium (Spillete, 1965; Collins, 1976). Even though the pressure and temperature vary from location to location within the reservoir (so that on a global basis there is neither mechanical nor thermal equilibrium), it is assumed that local equilibrium exists.

Another condition generally assumed to prevail is that the fluids and the reservoir soil/rock minerals in any small element of volume are at the same temperature. This implies that there is essentially no time lag between the temperatures of the fluids in the pore and the average temperature of the surrounding minerals. Obviously this assumption can be a close approximation only in cases where the size of the mineral grains is relatively small (Jenkins et al., 1954). That the temperatures of a fluid and of its adjacent grains are the same is a good working assumption in most applications of practical importance (Pratts, 1982).

In general, there are three mechanisms of transferring heat: conduction, convection, and radiation. Heat conduction is the process by which heat is transferred through nonflowing materials by molecular collisions from a region of high temperature to a region of low temperature. Heat convection is the term commonly used to describe the process by which energy is transferred by a flowing fluid. Radiation is the process by which heat is transferred by means of electromagnetic waves. There is little thermal radiation through opaque materials such as rocks, therefore, it is not considered to be an important heat transfer mechanism in porous media (Pratts, 1982). In oilsand the most important heat transfer mechanism is found to be conduction (Settari, 1989).

5.7.3 Leak-off problem

An integral part of the propagation of fractures is the flow of fluid within them. The resulting aperture of the fracture and the pressure distribution due to fluid flow inside the fracture are highly interdependent. The viscosity of the fluid inside the

fracture and the leakage of fluid to the surrounding region are considered to be important in the propagation of fracture (Atukorala, 1983).

Seepage of fluid from the fracture face into the surrounding material is called fracturing fluid loss or simply 'leak-off'. Factors that affect the amount of leak-off are (Veatch et al., 1989):

1) permeability and porosity of the formation;

2) pressure differential between the fracture and the formation;

3) formation-fluid viscosity, temperature and compressibility;

4) fracturing fluid and fluid-filtrate viscosity and temperature;

5) type and quantity of fluid-loss additive;

6) type and quantity of gelling agent;

7) formation (or fluid) temperature.

5.8 Hydraulic Fracture Modeling in This Study

The smeared approach for modeling of crack is relatively simple and straight forward: stiffness of fractured elements are reduced to a reasonable value and the medium is treated as a continuum. Also permeability of the fractured elements are modified to let the fluid pass more easily. There is no limitation on the direction of the crack in the smeared approach and redefinition of the finite element mesh after cracking is not required. However, smeared approach is unable to follow the fracturing process exactly, and it does not represent the nature of the crack which is actually a discontinuity in the medium. On the other hand, almost all of the existing hydraulic fracture models (two-dimensional closed form solutions and two-or three-dimensional numerical models) assume that in hydrofracturing process one or a few dominant planar fractures take place. In the present study in order to identify whether a single dominant fracture or a fracture zone with little or no specific direction will take place, it was decided to apply discrete fracture approach, even though it is more rigorous. In this way it is possible to capture the geometry and pattern of dominant fractures.

To identify fracture initiation two criteria are considered: tensile fracture and shear fracture. Failure in rocks is usually attributed to tension and failure in soils is

usually considered to be due to shear. Studies on the geotechnical properties of oilsands in shear and tension have been performed (Dusseault, 1977; Agar, 1984; Kosar, 1989) and their results can be used in the numerical analysis. It could have been possible to apply other fracture mechanic criteria such as G_c, J-integral or mixed mode fracture criteria, however, no experiment has been performed to determine the critical values of G_c or J_c for oilsands.

Fracturing process is simulated by using the node splitting technique. This technique requires that at the zone which is prone to cracking each node in the finite element mesh be introduced with double nodes with the same coordinates. During the analysis, whenever the stresses at the double nodes exceed the tensile strength of the medium or satisfy the requirements for shear cracking, double nodes split into two separate nodes and the mesh geometry will change. Since the problem is solved by marching in time, at the next time step the problem will be solved with the new geometry having a crack (separated nodes) inside the mesh. If at this time step stresses at the nearby double nodes are high enough to satisfy either the tensile or shear fracture criteria, node splitting will take place again and in this way crack propagation can be modeled. It is worth noting that before splitting, the degree of freedom for the double nodes is the same. This means that double nodes will not increase the total number of degrees of freedom (i.e. total number of unknowns) and the dimensions of the general stiffness matrix will not change. This advantage reduces the computational time and enhances the efficiency of the program.

Based on small strain theory, change in displacements $\{\Delta U^*\}$ (and the corresponding pore pressures $\{\Delta P^*\}$ and temperatures $\{\Delta T^*\}$) are assumed to be small at any time step, hence nodal coordinates can be updated at the end of each time step. In this manner the configuration of the fracture and its aperture can be updated continuously.

For modeling the flow of fluid and/or heat inside the fracture, a new type of 'fracture element' is introduced. This fracture element is a 6-node isoparametric rectangular element which is shown in Figure (5-14). This kind of element can be used in areas of the mesh where the possibility of fracturing is high. For instance, a zone

around a notch or a zone close to the fluid injection area are prone to fracturing. If the estimation of the zone of fracturing, in advance, is difficult, these fracture elements can be used throughout the entire mesh. Initially, the fracture elements are embedded inside the mesh between other elements; their thickness is zero and they are absent from the analysis. When 4 out of 6 nodes of a fracture element split due to the tensile or shear fracture, the program automatically activates the fracture element. Therefore, the geometry of the mesh will change and the effects of the activated fracture element will be taken into account.

Due to the very low stiffness of the fracture elements relative to the other elements, their stiffnesses are set to zero. However, fracture elements are very important in transmitting fluid and/or heat through the medium due to their high conductivities. Therefore, they possess all of the terms related to the fluid flow and heat transfer exactly the same as the other elements. The injected fluid/heat, finds these elements easier and quicker paths to flow through.

As mentioned before, shear fractures are usually 'filled' and have low permeabilities but tensile fractures are normally 'unfilled' and have high permeabilities. Conceptually, tensile fractures are clean fractures but often this is not the case especially when the crack opening is small and physical bonds between aggregates might still be in place. Even in a clean fracture, because of closeness of fracture, roughness of the walls, and change in the direction of fracture plane, permeability inside the fracture has a finite value. Some investigators have used parallel plate theory to determine the absolute permeability of fractures. Witherspoon et al. (1980) and Ryan et al. (1987) among others, have shown that this theory accurately describes the flow through natural and induced fractures. In accordance with the discussion above, a finite value for permeability is considered for fracture elements.

An important feature of hydraulic fracturing is the existence of pressure and temperature gradients inside the fractures. Some researchers (Daneshy, 1973; Wiles and Roegiers, 1982) assumed a gradient based on empirical results and field data and tried to improve the results of their models based on these assumptions. This issue can be addressed by using the proposed fracture elements with finite permeability. By

assigning a realistic permeability coefficient for fracture elements, a pressure gradient would be automatically applied to the analysis. Similarly, by introducing a heat capacitance for fracture elements it is also possible to establish a thermal gradient.

Although not used in this study, a routine has been coded in the program that accounts for changes in hydraulic conductivity during the analysis. In this routine hydraulic conductivity is continuously updated with respect to the void ratio, fluid density and fluid viscosity. Fluid density and viscosity, in turn, are functions of pore pressure and temperature.

It should be noted that after node splitting, fracture elements will automatically be activated, but sometimes the aperture is so small that the area of the fracture element is negligible(less that $10^{-7}m^2$). For these elements a nominal thickness will be considered in the analysis until the aperture and the element area are large enough to effectively participate in the global stiffness matrix.

The mathematical and the finite element formulations of this study are quite general, but since it is a first attempt to model the hydraulic fracturing process using a fully coupled thermal hydro-mechanical fracture finite element model, it was decided to model the problem in two dimensions to ensure that the model can adequately handle the complicated physical process and can accurately capture all of the key issues of the problem. For the same reason a single phase compressible fluid is considered in the model as a first stage.

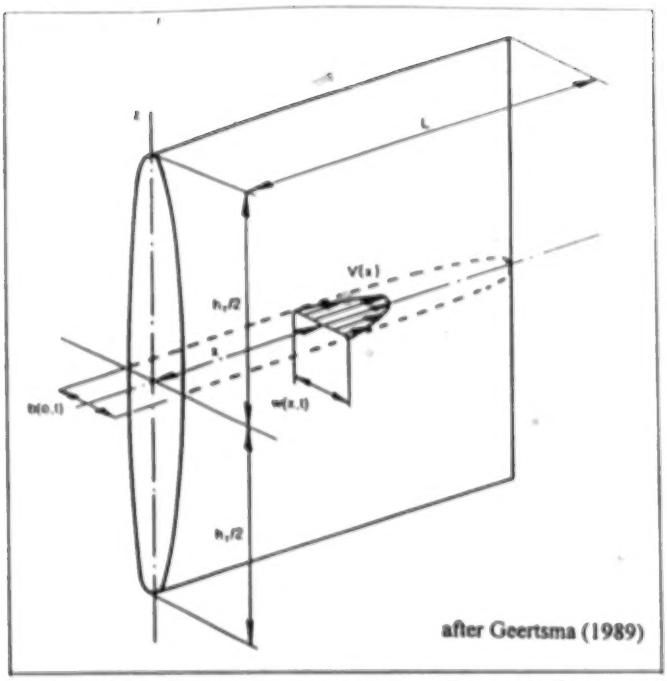

Figure (5-1) Schematic Representation of Linearly Propagating Fracture According to Perkins and Kern (1961)

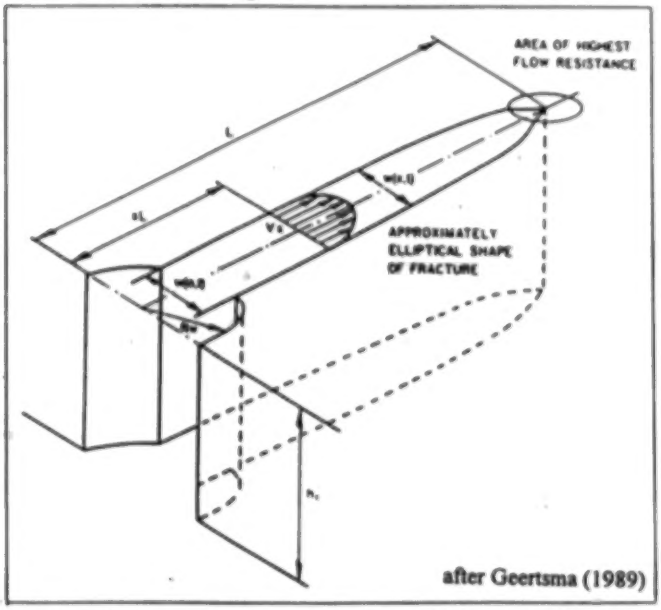

Figure (5-2) Schematic Representation of Linearly Propagating Fracture According to Geertsma and DeKlerk (1969)

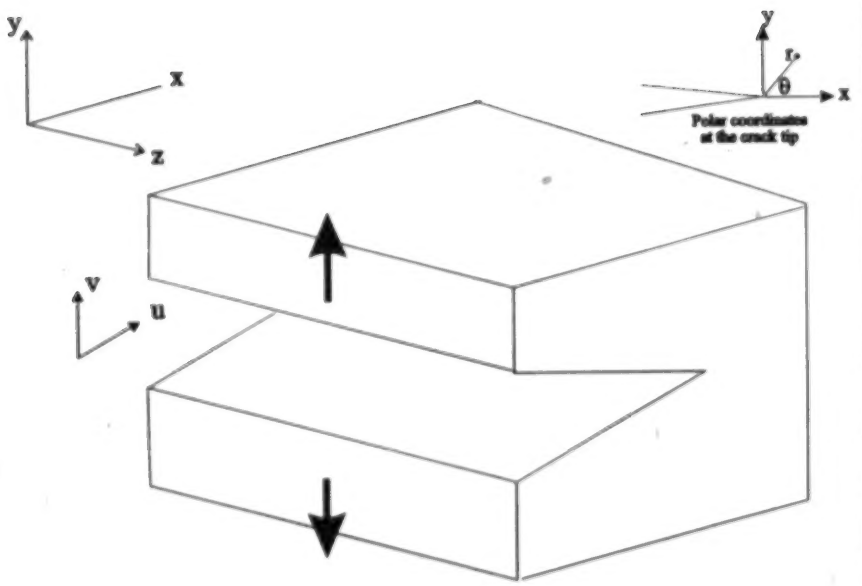

Figure (5-3) Stresses and displacements around a crack tip of mode I

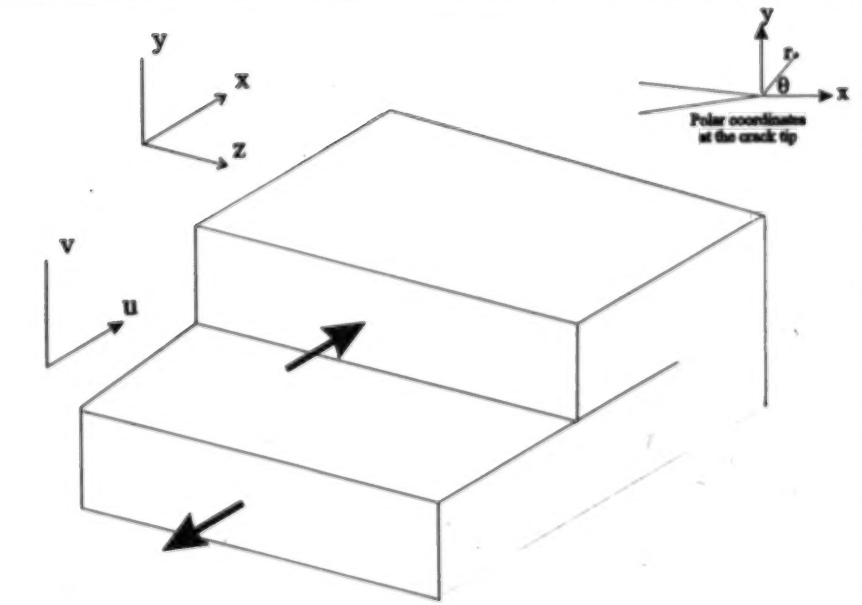

Figure (5-4) Stresses and displacements around a crack tip of mode II

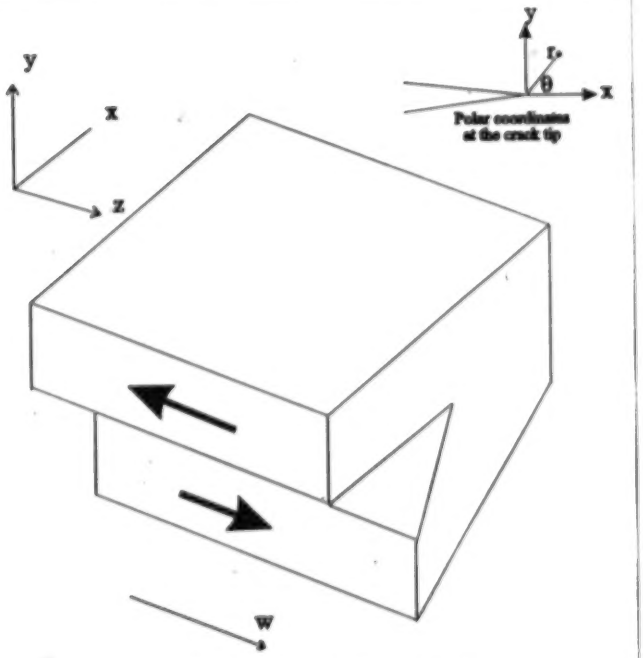

Figure (5-5) Stresses and displacements around a crack tip of mode III

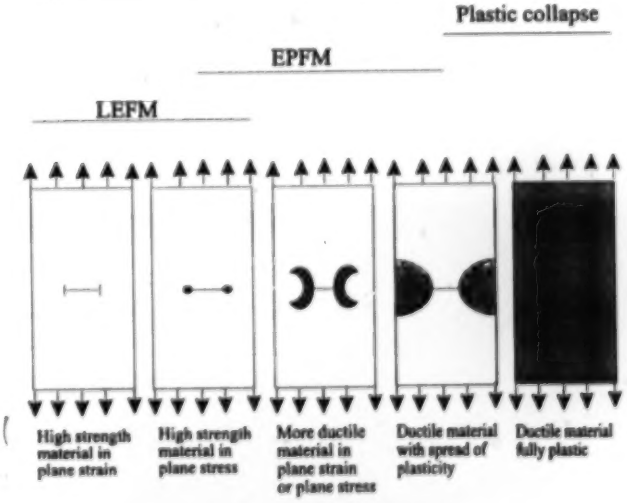
Plastic collapse
EPFM
LEFM
High strength material in plane strain
High strength material in plane stress
More ductile material in plane strain or plane stress
Ductile material with spread of plasticity
Ductile material fully plastic

Figure (5-6) Crack tip plastic zone and applicability of different analysis schemes (after Ewalds and Wanhill, 1984)

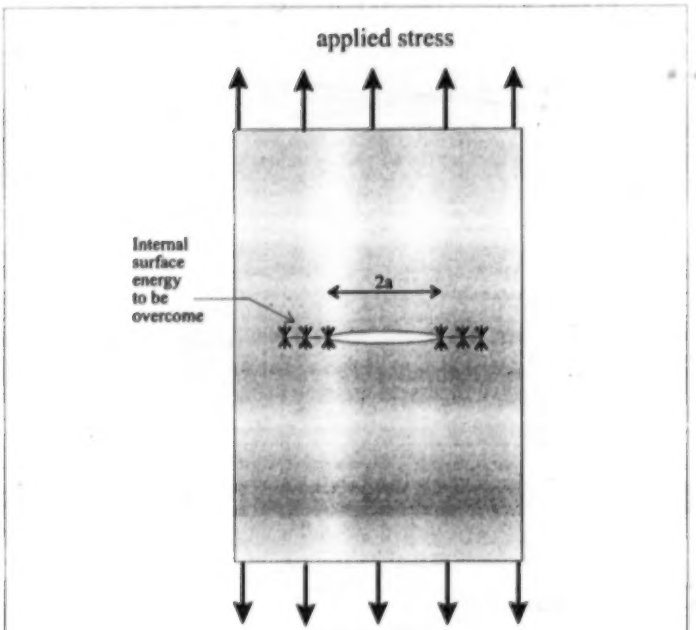

Figure (5-7) Griffith criterion of specific surface energy

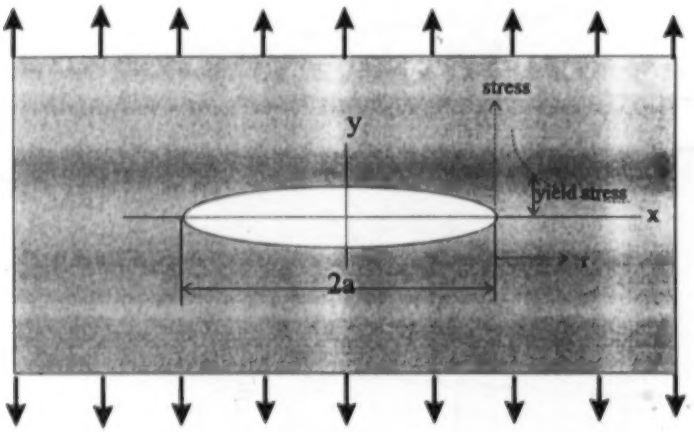

Figure (5-8) Irwin criterion, stress intensity factor

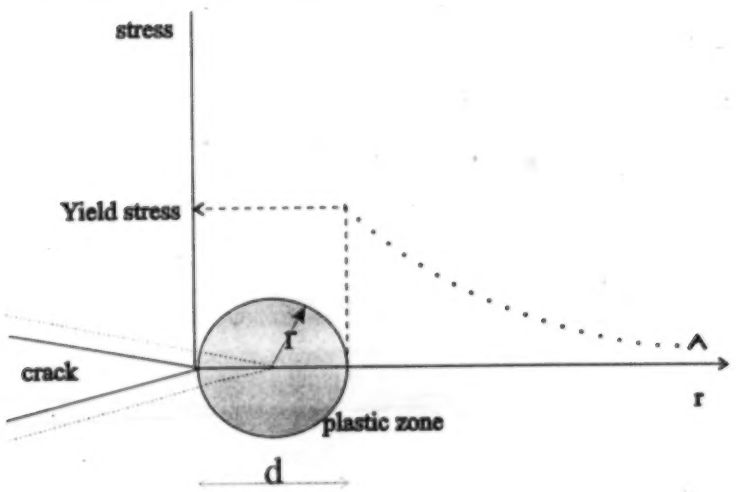

Figure (5-9) Crack tip plastic zone (Irwin method)

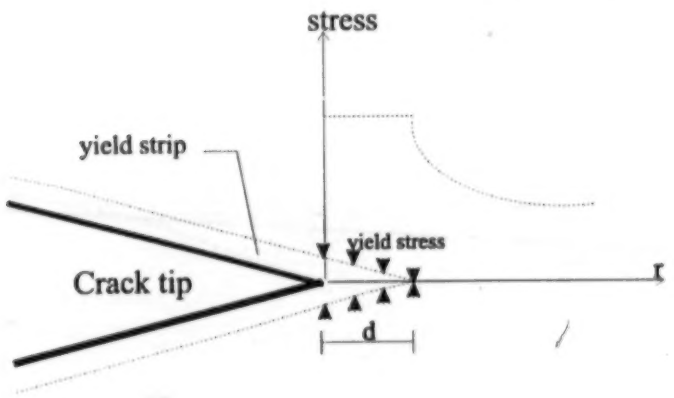

Figure (5-10) Crack tip plastic zone (Dugdale method)

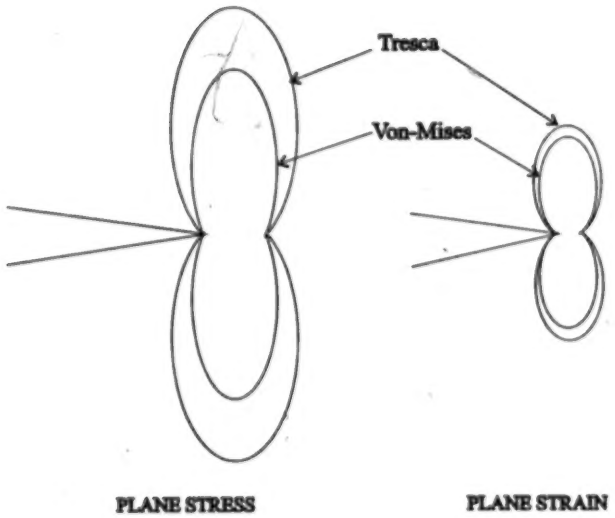

Figure (5-11) Comparing dimensions of plastic zone in plane stress and plane strain

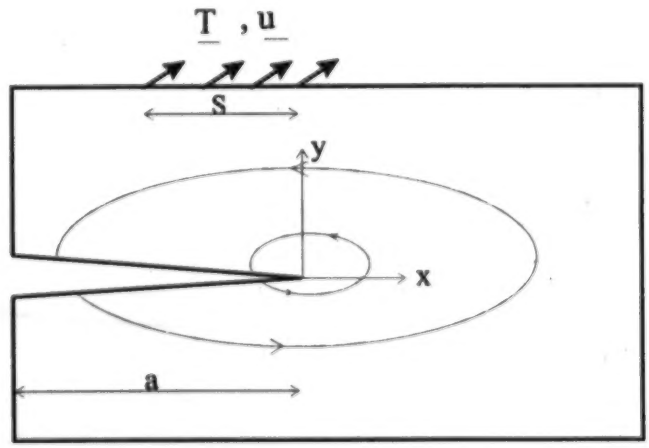

Figure (5-12) Closed contours for J-integral

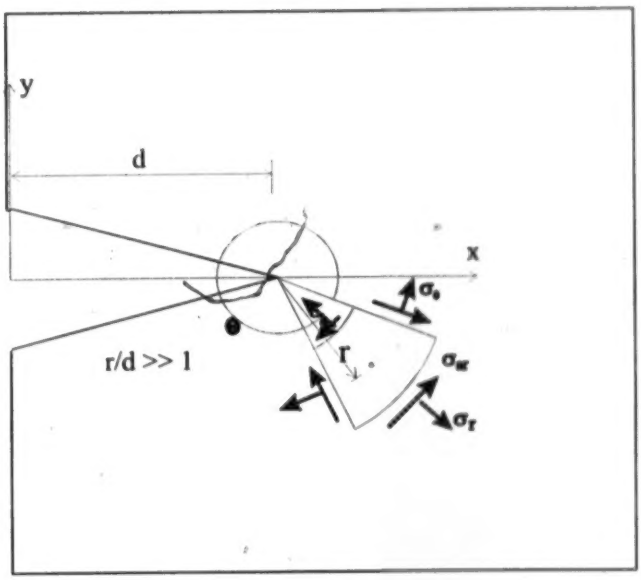

Figure (5-13) Crack tip coordinates for mixed mode stress criterion and strain energy release rate criterion

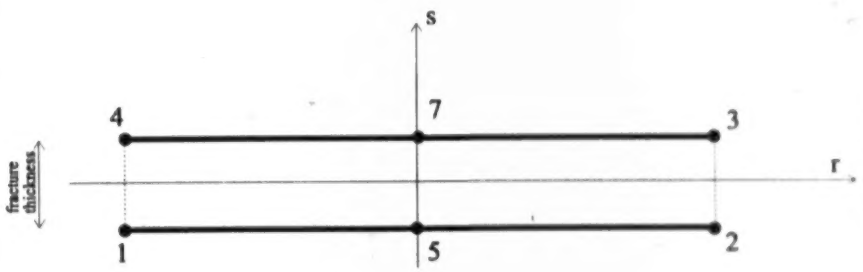

Figure (5-14) 6-node Rectangular Fracture Element

Chapter 6

Implementation and Verification of the Model

6.1 Introduction

The mathematical and finite element formulations described in chapter 4 and the method described in chapter 5 for modeling of hydraulic fracture were coded in a computer program using FORTRAN language. Although other more advanced languages could have been used, FORTRAN was chosen for two reasons. The first was that the Program for Incremental Stress Analysis (PISA®/FORTRAN) was used as the source and library code which was written in FORTRAN at the time this study was conducted. The second reason is that FORTRAN compilers are still more efficient than 'C' compilers. This is because FORTRAN compilers have been continuously modified and improved during the last twenty five years and are now more powerful and efficient than those of other languages. This advantage is especially important when a large volume of data processing is required for handling big problems.

PISA®/FORTRAN by itself is a finite element program for stress analysis in geotechnical engineering. It calculates displacements and stresses at different points inside a domain such as embankments, excavations, tunnels, etc. for two or three dimensional problems. It can handle drained, undrained, and also creep analysis. There are several constitutive models for predicting soil behaviour in PISA®/FORTRAN, consisting of elastic models (linear elastic and hyperbolic elastic) and elastoplastic models (Tresca, Von-mises, Mohr-Coulomb, Drucker-Prager and Modified Cam-Clay). Using PISA®/FORTRAN as a source and library code for the present study and

combining the two codes lead to a new numerical model which offers the following capabilities for geotechnical, reservoir, and environmental engineering purposes:

1) Time dependent analysis of stresses and deformations

2) Consolidation analysis (coupled time dependent deformation analysis with pore pressure dissipation)

3) Coupled thermal fluid flow and stress analysis in the reservoir

4) Analysis of crack initiation and propagation in the geological medium caused by heat, pore fluid pressure and/or stresses

5) Modeling of hydraulic fracturing processes in soil or rock

An important point to note is that the thermal effects on the soil behaviour are not yet fully understood. Although some studies have been conducted on temperature dependency of yield surface and hardening parameter of soil, there is no established model in this area (Leroueil and Marques, 1996). Hence, in this study, constitutive models for soils are assumed to be temperature independent.

As mentioned in chapter 4, for coupling of thermal hydro-mechanical processes three partial differential equations of equilibrium, fluid flow, and heat transfer are solved simultaneously through the following general matrix form:

$$\begin{bmatrix} K_{11} & K_{12} & K_{13} \\ K_{21} & K_{22} & K_{23} \\ K_{31} & K_{32} & K_{33} \end{bmatrix} \begin{Bmatrix} \{\Delta U^*\} \\ \Delta P^* \\ \Delta T^* \end{Bmatrix} = \begin{Bmatrix} F_1 \\ F_2 \\ F_3 \end{Bmatrix} \qquad (6\text{-}1)$$

Since the problem is time dependent, state variables (unknowns) are incremental values. After solving the system of equations, the incremental values will be added to the corresponding values at nodes at the previous time step and march through the time.

For calculating displacements, 8-node rectangular isoparametric elements are used (6-node triangular elements are also coded in the program). For calculating pore pressure and temperature, however, 8-node rectangular elements are changed to 4-node rectangular elements by appropriate shape functions. Generally, it has been observed (Christian, 1977; Johnston, 1981) that in order to obtain compatible coupled fields, the displacement interpolation should be one order higher than the pore pressure interpolation. Also Aboustit et al. (1985) have reported that the use of a 4-node

rectangular element for pore pressures along with a 8-node rectangular element for displacements resulted in less oscillation in the analysis of a consolidation problem (comparing to the case in which a 8-node element was used for both pore pressure and displacements).

Each of the components of the *[K]* and *{F}* are determined for each of the elements individually and then assembled to make the global stiffness matrix and load vector. Global stiffness matrix is stored by using the extended skyline method (Chan, 1986), then, the system of linear equations are solved by using Gaussian elimination technique. Details of the finite element programming can be found in Appendix A.

For modeling fracture, two criteria, one tensile and the other shear, are implemented in the model as described in chapter 5. At the end of each time step stresses are calculated at the 'integration points'. These stresses are used to obtain the stresses at each 'nodal point'. Stresses at the nodes are then examined individually to determine whether they satisfy the tensile fracture or shear fracture criterion. If fracture occurs, double nodes are split and two free nodes are created. Splitting of double nodes occurs at the end of each time step, therefore, in the next time step the analysis is based on a new mesh which has been generated by the fracturing process. In this way the pattern of fracture can be traced in time. In order to transfer the fluid pressure and/or heat through the fractures, special 6-node rectangular fracture elements with zero initial thickness are used.

6.2 Program Verification

In this chapter the developed model will first be applied to some small assembly of elements to ensure that each component in the stiffness matrix -either individually or coupled with other components- works properly and the results are satisfactory. Then two solved problems of thermal hydro-mechanical interaction will be examined in plane strain and axisymmetric conditions and the results will be compared with the existing analytical or numerical solutions. At the third stage fracturing process will be examined by simulation of a one dimensional fracture propagation caused by hot fluid injection.

6.3 Patch Tests

6.3.1 Coupling deformation and fluid flow

A patch of four rectangular elements is considered in Figure (6-1). A constant displacement equal to 0.001 is imposed on the top of the mesh. Pore fluid pressure is considered to be equal to 10.0 everywhere inside the domain except at the top which is set to zero and stays zero to represent a free drainage boundary. In this example components that are contributing to the global stiffness matrix are $[K_{11}]$, $[K_{12}]$, $[K_{21}]$ and $[K_{22}]$. Other parameters that are used in the analysis are summarized in Table (6-1).

The results shown on Figures (6-2) and (6-3) indicate that dissipation of pore pressure basically occurs within 5 seconds. During these steps the vertical displacements deviate from linear variation but approach the linear situation as the pore pressure decreases. Figure (6-3) shows small oscillation in the pore pressure. Oscillation in the pore pressure, in a coupled fluid flow-deformation analysis, has been reported by a number of researchers (Aboustit et al., 1985; Lewis et al., 1986) which can be attributed to the coupling process or the time increment that is used.

6.3.2 Coupling of deformation and heat transfer

The same patch of element as above is used, but in this case instead of having a constant pore pressure, a unit heat flux from the bottom of the domain is applied and the temperature at the top is kept at zero degree (Figure 6-4). Again, a constant displacement equal to 0.001 is imposed on the top of the mesh. The temperature is expected to increase gradually in the medium until it reaches the steady state condition. Components that are contributing to the global stiffness matrix are $[K_{11}]$,$[K_{13}]$ and $[K_{33}]$. The $[K_{31}]$ that represents the effect of displacements on changing the temperature is negligible and is considered to be zero in the analysis. Other parameters that are used in the analysis are summarized in Table (6-1).

If the coefficient of thermal expansion for soil is zero there would be no interaction between heat and deformations and the nodal displacements will linearly diminish to zero from top to the bottom of the specimen. With a non-zero thermal

expansion coefficient the linear variation of vertical displacements will change due to the thermal effect, as shown in Figure (6-5). Figure (6-5) indicates that other than the top nodes with prescribed displacements, the displacement values at other nodes are the sum of the downward settlement and upward thermal expansion.

Figure (6-6) shows the gradual increase of the temperature in the system until it reaches the steady state condition.

6.3.3 Coupling fluid flow and heat transfer

This test uses a different assembly of elements consisting of four elements in a row. It is assumed that heat flux is acting on both ends simultaneously such that a constant temperature equal to 10.0 degrees at both ends of the mesh is maintained (Figure 6-7). Other parameters used in the analysis are listed in Table (6-1). The objective is to observe the change in pore pressure caused by heat flux. It is expected that the temperature will increase at the inside nodes until it reaches steady state condition (i.e. 10.0 degrees everywhere). The result is shown in Figure (6-8). The pore pressure generated by an increase in temperature is depicted in Figure (6-9). This figure indicates that although the pore pressure increases as the temperature is increased, there is no significant difference in the pore pressure throughout the domain. It is interesting to see the displacements induced by these elevating temperatures and pore pressures. This is shown in Figure (6-10) which displays a gradual expansion of the domain until it reaches steady state condition. Figure (6-10) demonstrates the coupling process among all three components, namely displacements, pore fluid pressure, and thermal effects.

6.4 Plane Strain Thermo-Elastic Consolidation (1D. Consolidation)

The first verification test of the model is a thermo-elastic consolidation problem solved by Aboustit et al. (1985) and also by Lewis et al. (1986). In this case a column of linear elastic material is subjected to a unit surface pressure and a constant surface temperature of $T = 50^{o}$. The finite element mesh is shown in Figure (6-11). The same mesh was used in both of the solutions mentioned above. The pore pressure is kept equal to zero at the top surface; everywhere else the boundaries of the soil are sealed (no

fluid flow) and insulated (no heat flow). Other parameters used in the analysis are summarized in Table (6-2).

The time domain is shown in Table (6-3). Almost the same temporal discretization shown in Table (6-3) is used in both studies mentioned above. The reason is that this kind of discretization has provided good agreement with the analytical solution for 'isothermal' consolidation (Sandhu, 1976).

All stiffness matrix components shown in equation (6-1) are present in this analysis except $[K_{31}]$ and $[K_{23}]$. The matrix $[K_{31}]$ is negligible and $[K_{23}]$, the contribution of heat to fluid flow, is set to zero since this matrix is not taken into account in those papers mentioned above. At the beginning, a nine point integration scheme was used to reduce the reported oscillation in the results, but since no significant improvement were observed, a four point integration was employed later.

The results are shown in Figures (6-12) to (6-14). Figure (6-12) shows that displacements at nodes 7, 27, and 37 fit well with the results obtained by Lewis et al. (1986), except the peak values are a little higher. After the peak, the displacements become negative (i.e. heave). The same result is reported by Lewis et al. (1986) for the values after peak. Figure (6-13) illustrates the same pattern for pore pressure variation between Lewis et al. (1986) and this study. Figure (6-13) clearly indicates the dissipation of pore pressure in time at different nodes, but the results of this study show that the rate of dissipation seems to be slower than that reported by Lewis et al. (1986). It should be noted that modeling pore pressure is the most difficult part of the analysis since it is very sensitive to the time increment Δt and oscillation occurs at early times due to the coupling process between pore pressure and displacements. Figure (6-14) demonstrates an excellent match between the values of temperature in this study and those of Lewis et al. (1986).

6.5 Axisymmetric Thermo-Elastic Consolidation (2D. Consolidation)

In the second example, attempts are made here to simulate the consolidation process around a cylindrical heat source in an axisymmetric condition. The effects of a cylindrical radiating heat source, buried in a thermo-elastic soil, were investigated by

Booker and Savvidou (1985) where an analytic solution for a point-heat source was numerically integrated over the surface of a cylindrical canister. Apparently, this is the only analytical solution available for such a problem as reported by Lewis et al. (1986) and Vaziri and Britto (1992).

The finite element discretization for this example, which is adopted from Lewis et al. (1986), is depicted in Figure (6-15), and consists of 27 elements and 106 nodes. Booker and Savvidou (1985) provided an analytical solution for a particular case of a cylindrical heat source where $\frac{a'}{a_*} = \frac{1}{4}$, $\frac{c}{\kappa} = 2.0$ and ν=0.4 with a' soil thermal expansion coefficient, ν Poisson's ratio, c coefficient of consolidation, κ coefficient of thermal diffusivity and $a_* = \beta_s(1-\phi) + \beta_w(\phi)$ where β_S and β_W are coefficients of thermal expansion for solid particles and fluid respectively; and ϕ represents the porosity. A set of possible data which satisfies the above ratios is summarized in Table (6-2). The heat source was simulated by a constant heat input of 1000.0 for each of the two elements of the source. Temporal discretization was the same as Table (6-3).

Results are illustrated on Figures (6-16) to (6-18) which are the horizontal displacements, pore pressures, and temperatures at three different nodes *R/Ro=1*, *R/Ro=2* and *R/Ro=5* (*Ro* is the radius of the cylindrical heat source). Figure (6-16) indicates that displacements gradually increase up to a certain level, then level off and remain constant when the generated pore pressures are dissipated and temperatures reach to a steady state condition. Figure (6-17) shows the pore pressure generation and dissipation caused by the radiating heat source. For *R/Ro=1* the time to reach to the maximum pore pressure in the numerical solution is behind the analytical one, but for *R/Ro*=2 and *R/Ro*=5 the maximum values occur at the same time and their magnitudes are pretty close. Variation of temperature with time is shown in Figure (6-18) which indicates a good agreement between analytical and numerical solutions. It should be noted that the analytical results by Booker and Savvidou (1985) do not provide the exact solution for this problem because of the difference between a point heat source and a cylindrical heat source. Nevertheless, in their analytical solution, the determination of

the temperature was completely uncoupled from that of the displacements and pore pressures.

6.6 Thermal Hydro-Mechanical Fracture Propagation (1D. Fracture)

So far all the examples have been used to examine the accuracy of the results obtained from the model for simulation of coupled thermal hydro-mechanical problems. In this section the ability of the model to simulate a one dimensional fracture propagation will be examined and node splitting and activation of the fracture elements will be demonstrated.

Figure (6-19) shows the finite element mesh for this test. As shown, in the middle row double nodes are used in order to accommodate the embedded 6-node fracture elements. Fracture elements are absent at the beginning but will be activated when fracturing begins. Also, a notch is provided where a fluid with high pressure and temperature is injected into the medium. The initial pore pressure and temperature in the medium are set to zero. A fluid flux of 0.1×10^{-5} m/sec and a heat flux of 10.0 J/sec are applied inside the notch. Generally, the induced stresses at the nodes are examined to determine whether the tensile or shear fracture criteria are satisfied. The criterion which is first satisfied governs the situation and causes the double nodes to split. The fracturing process continues until a static condition for the fracture is obtained.

Table (6-4) shows how the fracture propagates and fracture elements are activated at different time steps.

Figure (6-20) shows the variation of pore pressure at nodes 18 and 29 at the injection boundary and at nodes 1 and 45 which are far from the injection zone. It is seen that, the pore pressures are generally higher at the injection point. When 6 seconds have elapsed, fracture elements are activated. Since the permeability of the fracture elements are set to ten times greater than the soil matrix, the pore pressure drops because the fluid suddenly finds easier paths to flow. After activation of all fracture elements the pore pressure again starts to increase. The effect of activation of fracture elements on nodes 1 and 45 (which are located far from the injection boundaries) is not large, as expected. Variation of pore pressure along the mesh and inside the induced

fracture are depicted in Figures (6-21) and (6-22) respectively. It should be noted that due to the activation of the fracture elements the pore pressure at some nodes becomes negative, however, negative values decrease as the node gets closer to the right boundary where a zero pore pressure is imposed. In other words, the imposed zero pore pressure at the right boundary causes pore pressures at nodes 7 and 9 in Figure (6-21) to become closer to zero compared to the pore pressures at nodes 5. The same thing happens for nodes 24 and 26 in Figure (6-22) compared to node 22.

Figure (6-23) compares the variation of temperature at node 18 which is located at the injection zone and node 1 which is located far from the injection area. As expected, temperature at the injection zone is higher. Variation of temperature along the mesh and also inside the induced fracture are illustrated on figure (6-24) and (6-25), respectively. As the figures show, due to the injection of the hot fluid the temperature is gradually and smoothly increasing towards steady state condition.

6.7 Discussion

The developed thermal hydro-mechanical fracture finite element model was examined in this chapter and the results were shown to be satisfactory. However, there were some differences between the analytical and numerical solutions in section (6.5) which can be attributed to two reasons. The first reason is that the analytical solution, by itself, is not exact because a cylindrical heat source is considered to be a point-heat source (the analytical solution for a point-heat source was numerically integrated over the surface of a cylinder). The second reason is embedded in the nature of the numerical solution and its spatial and temporal discretizations.

As discussed in chapter 4, discretizations in space and time are required for solving the system of partial differential equations using finite element method. Each of these discretizations introduces some degree of approximation (error) to the solution. Generally, finer meshes are preferred for spatial discretization because the results of the finite element analysis asymptotically converge to the exact solution as the finite element mesh becomes finer. On the other hand, with finer meshes number of the elements increases, therefore, the amount of the computational effort for solving the

problem grows rapidly. This point becomes more important in time-dependent analysis. Time marching requires analyzing the problem for each small time increment. Changes in the state variables during each time increment is calculated in the analysis in order to modify the values of the state variables continuously. In some cases, where the time increment chosen for the analysis is small, a huge number of steps is required to solve the problem. For example in the thermal consolidation analysis performed in sections (6-4) and (6-5), 'Δt' was originally 0.01 second and the ultimate time was around 10^4 to 10^5 seconds. This indicates that with a constant Δt=0.01 sec, 10^6 to 10^7 steps of the analysis are required. Obviously this amount of computational work for each example was not possible. Temporal discretization scheme shown in Table (6-3) was an attempt to reduce the number of steps that was required in the analysis. Although using different Δt's in the analysis causes some oscillation in the results which reduces the degree of accuracy, but it is inevitable when the number of the required time steps is large. Reducing the computational time and effort is the reason that explains why fairly coarse meshes were used in sections (6-4) and (6-5). In fracture problems where the configuration of the mesh is changing continuously due to the fracture propagation, the problem is more severe. Since at each time step a new mesh with modified geometry has to be analyzed, therefore, the amount of computational work that can be saved and reused in the next steps of the analysis is very limited. Furthermore, in large problems since the place of the fracture(s) is not known at the beginning, a large number of fracture elements are embedded between other elements inside the mesh. When these elements are activated, the number of elements involved in the analysis suddenly grows and the program continuously demands more time and memory for analyzing the problem.

There are some differences between the results of this study and those of Lewis et al. (1986) in sectiion (6.4) which lie in the differences between two formulations as described below.

- Primary unknowns in Lewis et al. (1986) are the total (updated) values of $\{U\}$, P and T. This led to a set of nonlinear partial differential equations and unsymmetric global stiffness matrix. This set of nonlinear $P.D.E$ was then linearized and symmetry

was restored by means of partitioning procedure and staggered scheme. In this study incremental values of $\{\Delta U\}$, ΔP, and ΔT are considered to be the primary unknowns. In this case, all of the incremental terms of second or higher order are ignored to obtain a set of linear algebraic equations. Furthermore, no attempt has been made to retain the symmetry of the global stiffness matrix.

- The developed model in this study has the capability to consider changes of the fluid density in space.

- Shape functions used for 'P' and 'T' are different from those in Lewis et al. (1986).

- Changes in porosity($\partial\phi/\partial t$) in the heat transfer equation is neglected in Lewis et al. (1986) but is considered in this work.

- Effects of the elevation in the heat transfer equation is neglected in the heat transfer equation by Lewis et al. (1986). Such effects can be significant when one is dealing with well-bore problems.

- Fluid velocity in the heat transfer equation in Lewis et al. (1986) is considered to be known thus causing a minor uncoupling between flow and heat equations.

- There are no inertia and damping effects in the equilibrium equation in Lewis et al. (1986).

- Heat capacity of fluid at constant pressure and at constant volume are considered to be the same in Lewis et al. (1986).

- No capability of fracture modeling exists in Lewis et al. (1986).

For fracture modeling, results presented in section (6-6) show the ability of the model to calculate the principal stresses at the nodes and split them if the stresses at those nodes satisfy the appropriate fracture criterion. Then, fracture elements are created that can transmit high 'P' and 'T' through the fracture. Detailed evaluation of the model for predicting fracture initiation and fracture pattern is explained in the next chapter where the results of the numerical model are compared to the experimental data obtained from large scale hydraulic fracture chamber tests.

	Patch test #1	Patch test #2	Patch test #3
mass coefficient ($kN/m.sec^{-2}$)	0.00	0.00	0.00
damping coefficient ($kN/m.sec^{-1}$)	0.00	0.00	0.00
soil/rock thermal expansion (1/°C)	0.00	0.3×10^{-3}	0.5×10^{-4}
fluid thermal expansion (1/°C)	0.00	0.9×10^{-2}	0.1×10^{-5}
fluid compressibility (kPa^{-1})	0.145×10^{-7}	0.145×10^{-7}	0.1×10^{-2}
soil heat capacitance (J/m^3 .°C)	0.00	0.10	$0.2\times10^{+4}$
fluid heat capacitance (J/m^3.°C)	0.00	0.00	0.00
thermal conductivity (J/sec.m.°C)	0.00	0.05	40.0
soil density (ton/m^3)	2.49	2.49	2.49
fluid density (ton/m^3)	1.00	1.00	1.00
fluid viscosity (kPa.sec)	0.1×10^{-5}	0.1×10^{-5}	0.1×10^{-5}
absolute permeability (m^2)	0.4×10^{-10}	0.4×10^{-10}	0.4×10^{-10}
modulus of elasticity (kPa)	20000.0	20000.0	$0.2\times10^{+7}$
Poisson's ratio	0.25	0.25	0.25
acceleration of gravity (m/sec^2)	9.81	9.81	9.81
initial porosity	0.6	0.3	0.15
θ	1.00	1.00	1.00

Table (6-1) Input data for patch tests

	Plane Strain test	Axisymmetric test	Fracture test
mass coefficient ($kN/m.sec^{-2}$)	0.00	0.00	0.00
damping coefficient ($kN/m.sec^{-1}$)	0.00	0.00	0.00
soil/rock thermal expansion(1/°C)	0.9×10^{-6}	0.203×10^{-6}	0.9×10^{-6}
fluid thermal expansion (1/°C)	0.00	0.630×10^{-5}	0.1×10^{-5}
fluid compressibility (kPa^{-1})	0.00	0.00	0.5×10^{-3}
soil heat capacitance (J/m^3 .°C)	40.0	40.0	5.00
fluid heat capacitance (J/m^3.°C)	40.0	40.0	0.00
thermal conductivity (J/sec.m.°C)	0.20	1.03	20.0
soil density (ton/m^3)	0.00	0.00	0.00
fluid density (ton/m^3)	1.00	1.00	1.00
fluid viscosity (kPa.sec)	0.1×10^{-5}	0.1×10^{-5}	0.1×10^{-5}
absolute permeability (m^2)	0.4×10^{-12}	0.4×10^{-11}	5.5×10^{-12}
modulus of elasticity (kPa)	6000.0	6000.0	$0.6\times10^{+8}$
Poisson's ratio	0.40	0.40	0.40
acceleration of gravity (m/sec^2)	9.81	9.81	9.81
initial porosity	0.1	0.1	0.3
θ	1.00	1.00	1.00

Table (6-2) Input data for thermoelastic consolidation and fracture problems

Time increment (seconds)	Number of time steps
0.01	10
0.1	10
1	10
10	10
100	10
1000	10

Table (6-3) Time increments for thermo-consolidation problems

Time (sec.)	Split nodes	Activated elements
1	-	-
2	-	-
3	-	-
4	-	-
5	29	-
6	30	11
7	31,32,33	12
8	34,35,36,37,38	13,14
9	-	-
10	-	-

Table (6-4) Fracturing sequence in time

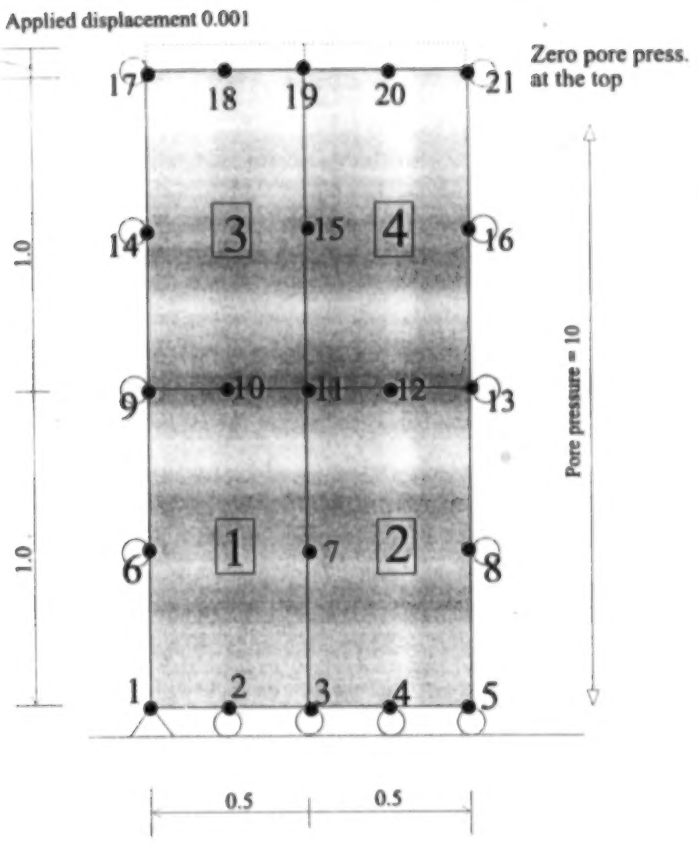

Figure (6-1) Finite element mesh and boundary conditions for coupling of deformation and fluid flow analysis

Figure (6-2) Variation of vertical displacements with time

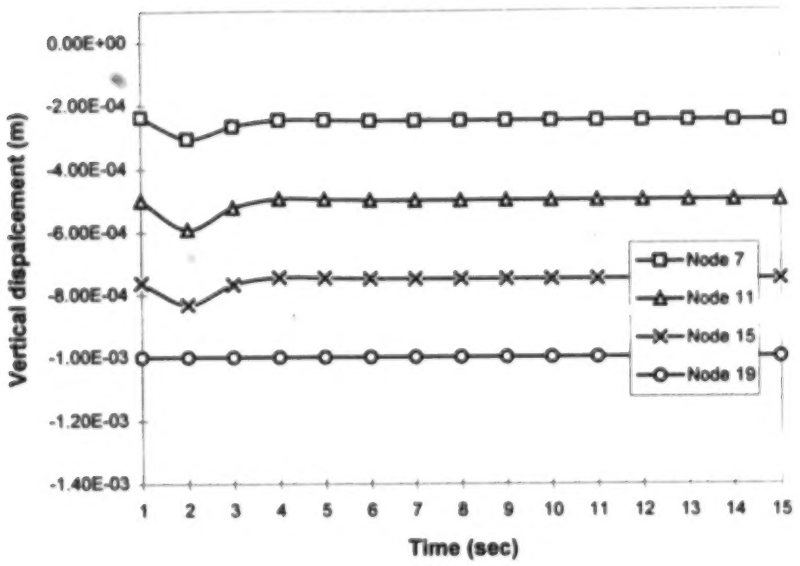

Figure (6-3) Variation of pore pressure with time

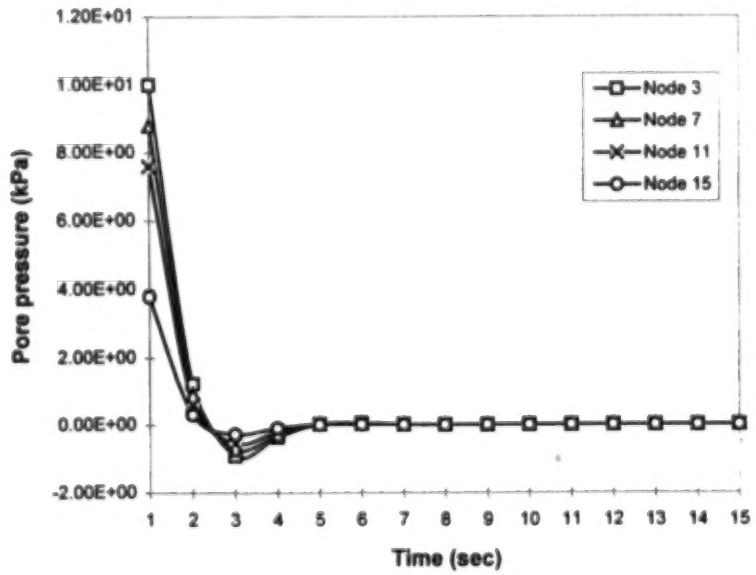

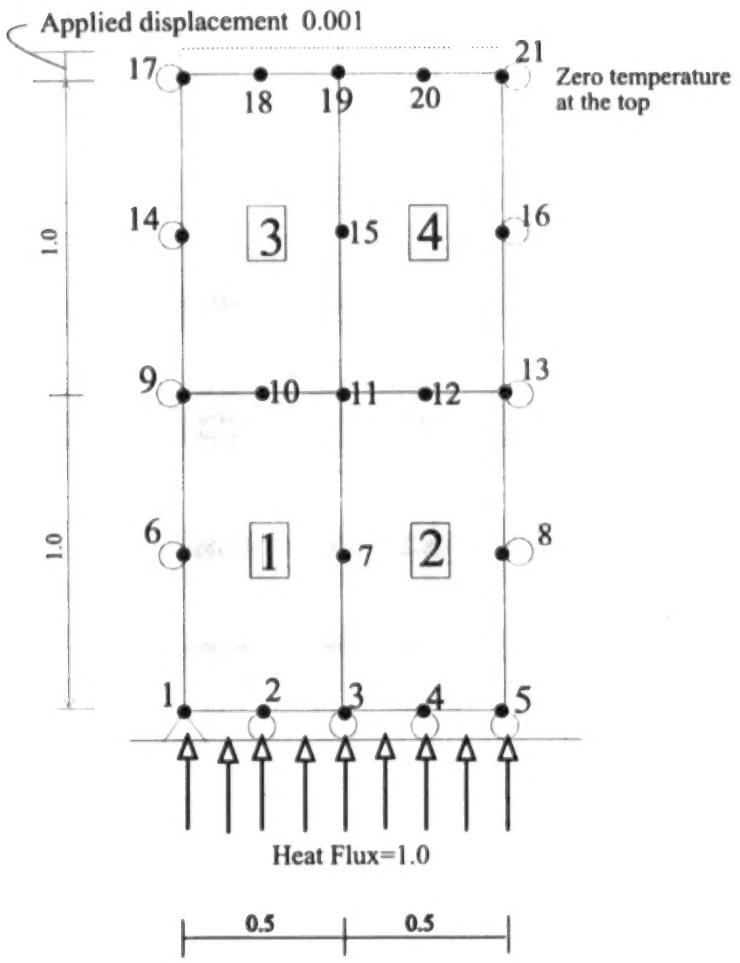

Figure (6-4) Finite element mesh and boundary conditions for coupling of deformation and heat transfer analysis

Figure (6-5) Variation of displacements with time

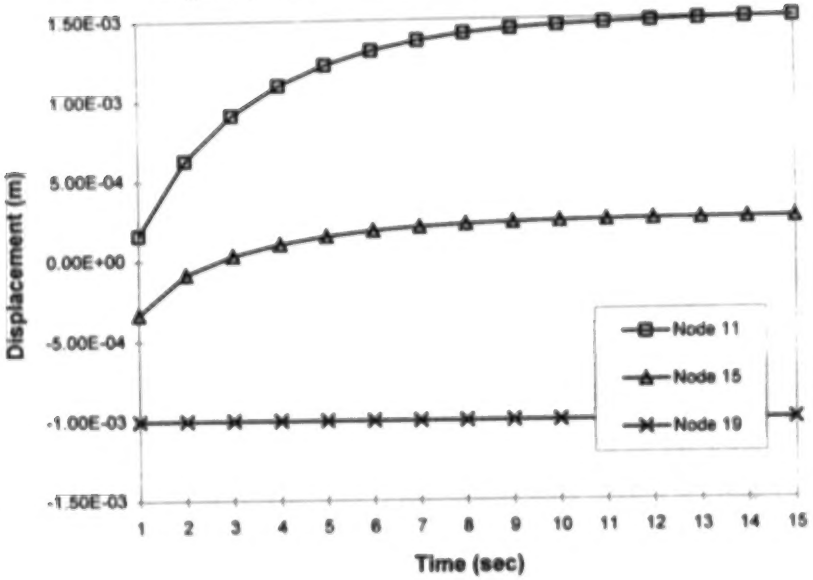

Figure (6-6) Variation of temperature with time

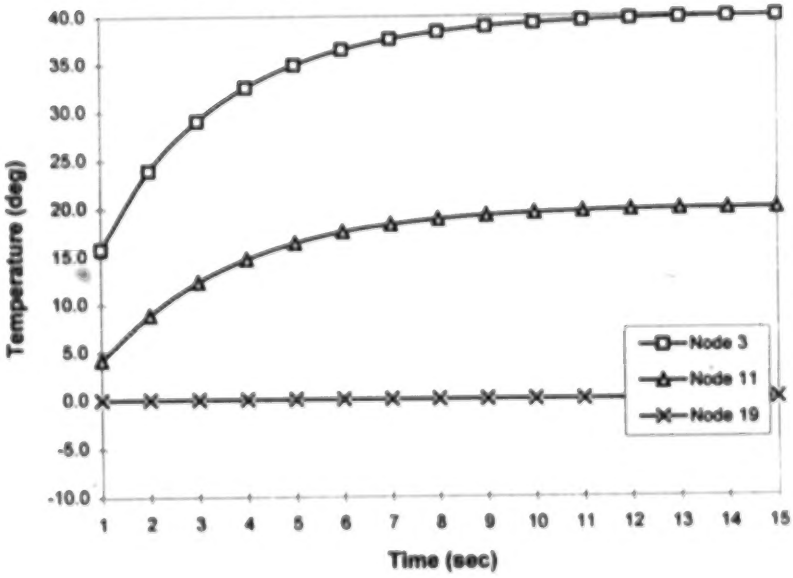

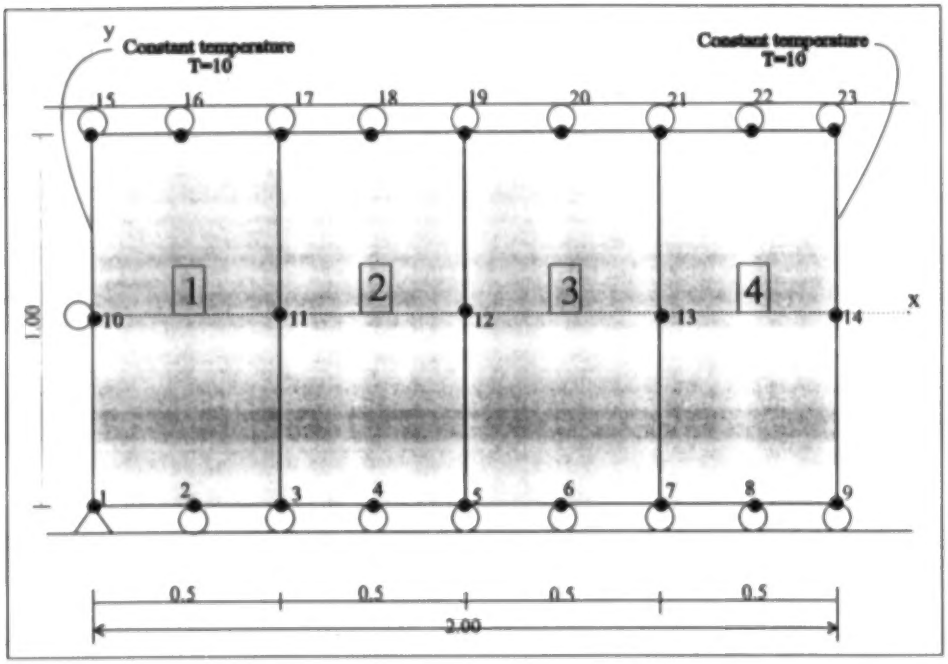

Figure (6-7) Finite element mesh and boundary conditions
for coupling of fluid flow and heat transfer

Figure (6-8) Variation of temperature with time

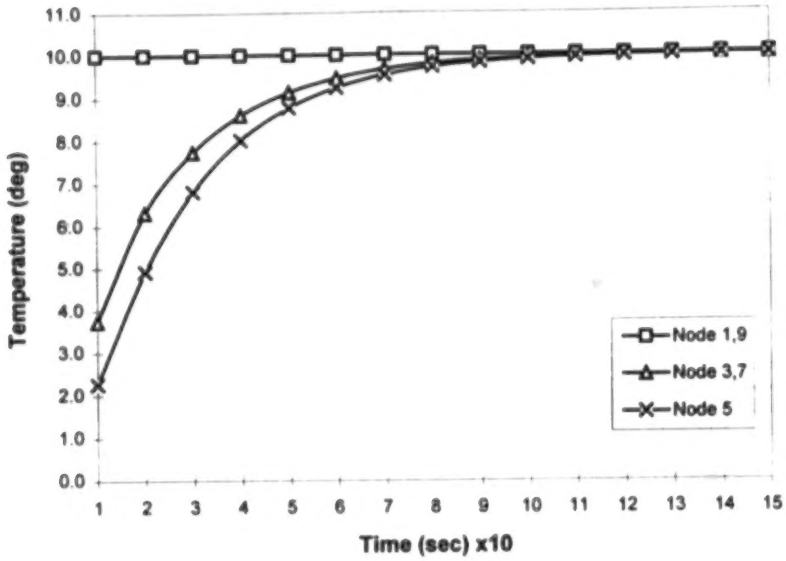

Figure (6-9) Variation of pore pressure (induced by temperature) with time

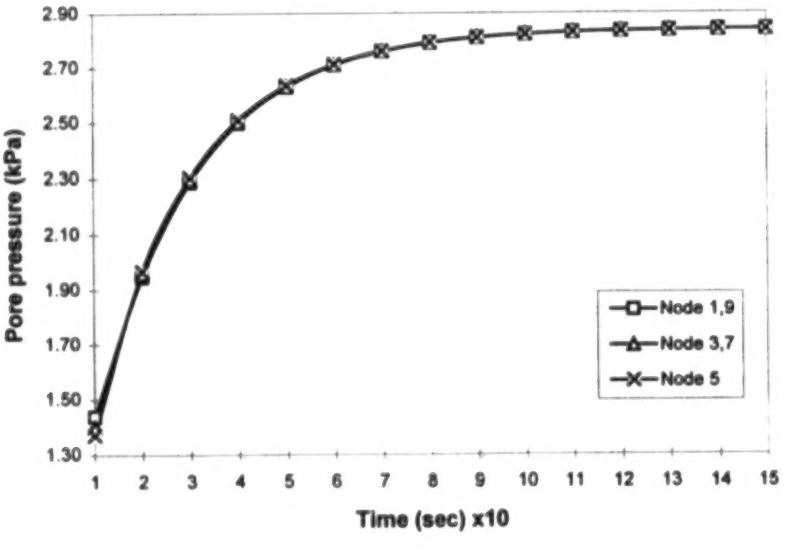

Figure (6-10) Variation of horizontal displacement with time (displacement induced by the effects of pore pressure and temperature)

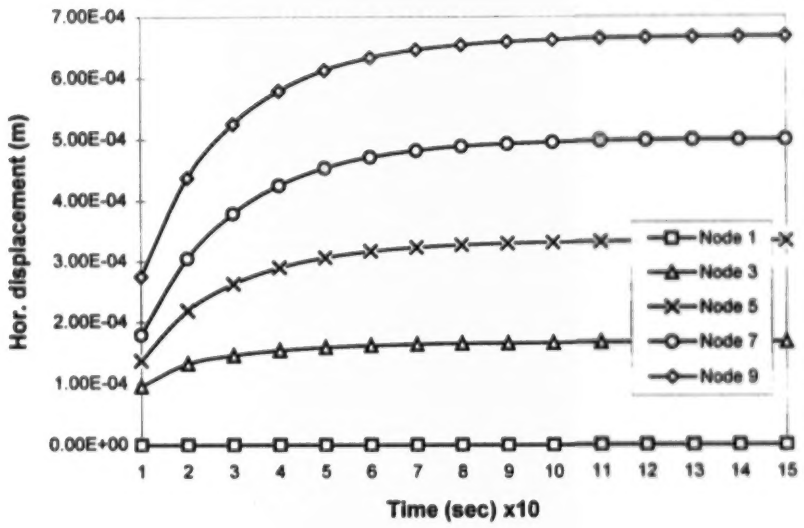

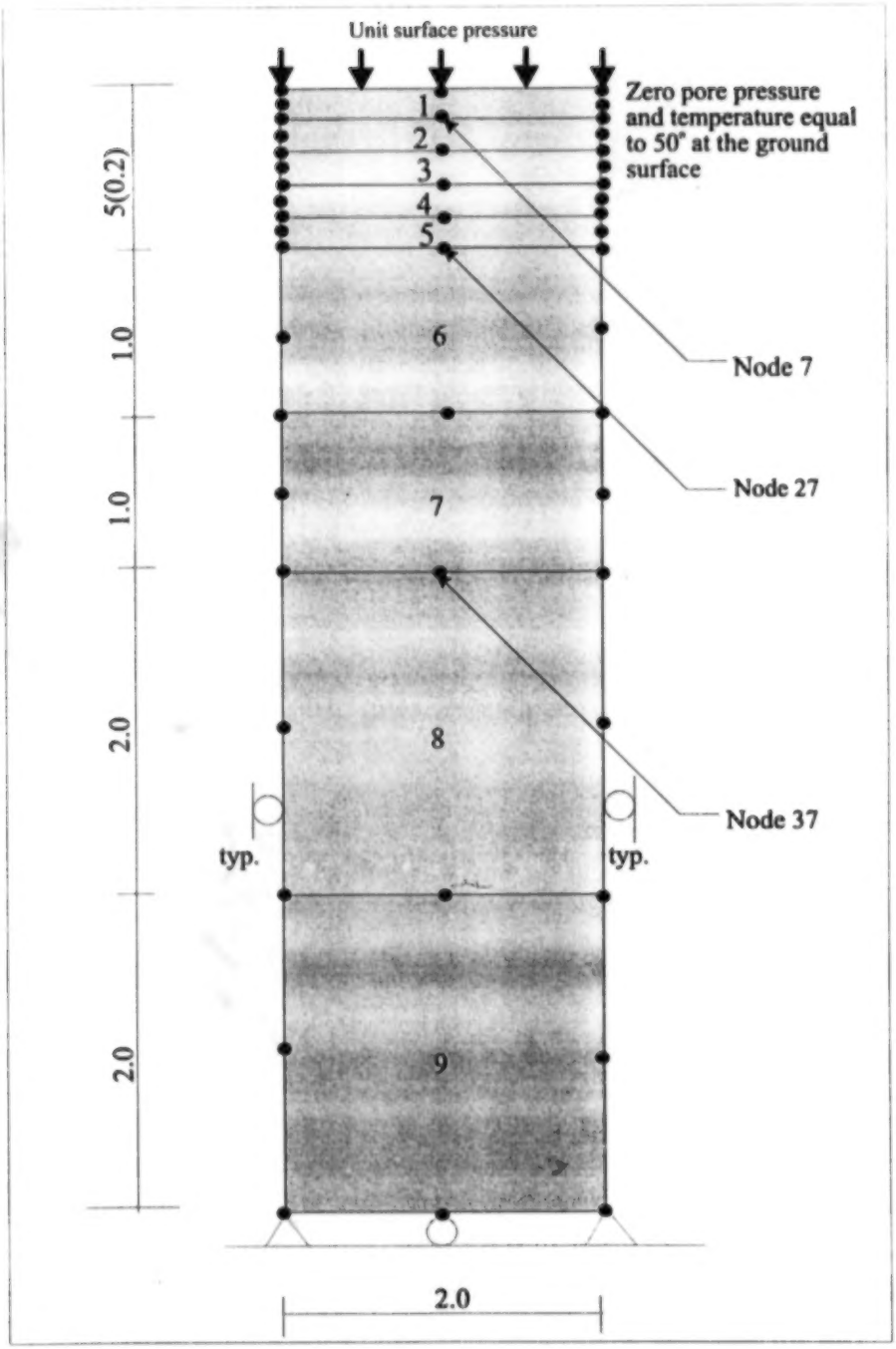

Figure (6-11) Plane strain thermo-elastic consolidation

Figure (6-12) Variation of settlement with time
(Symbols: from Lewis et al. (1986), Lines: Finite element model)

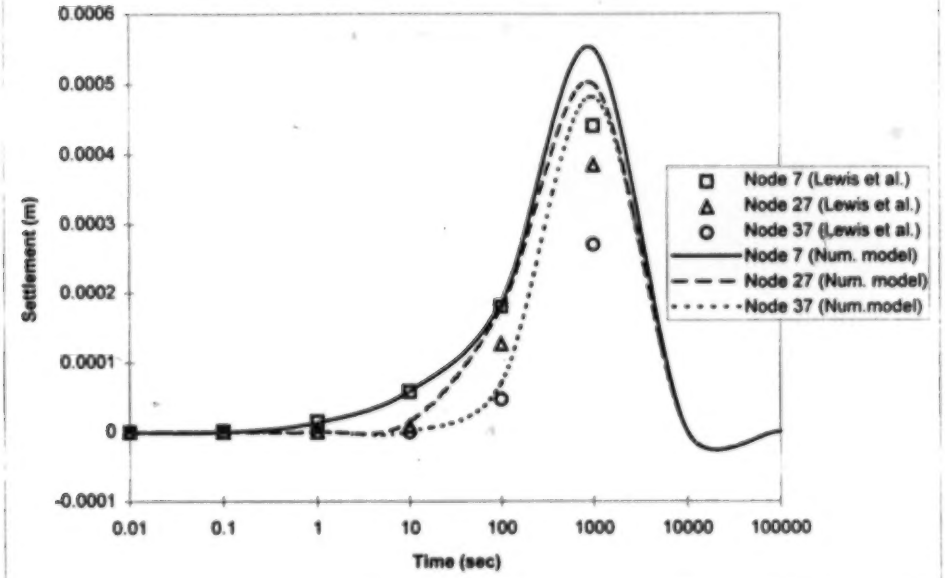

Figure (6-13) Variation of pore pressure with time
(Symbols: from Lewis et al. (1986), Lines: Finite element model)

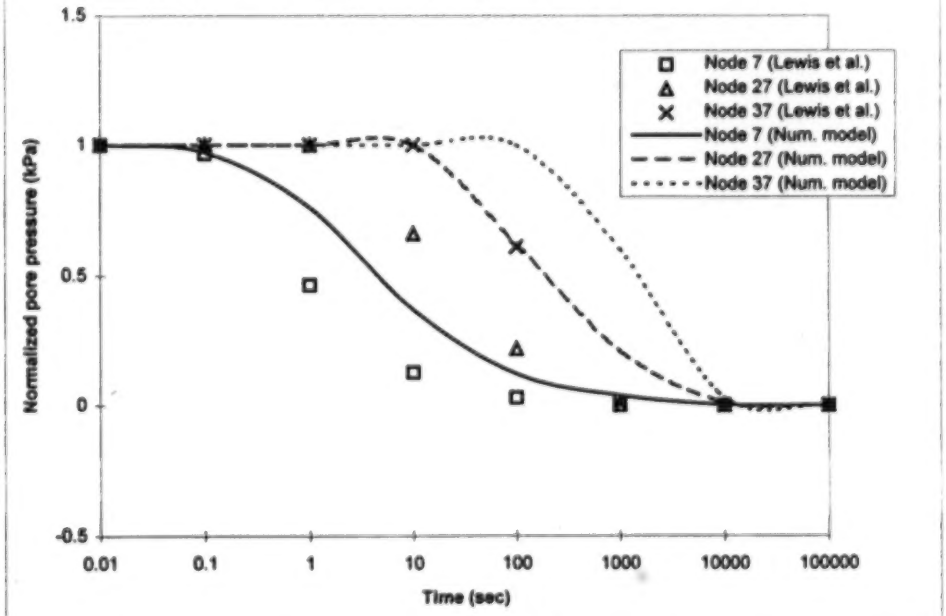

Figure (6-14) Variation of temperature with time

(Symbols: from Lewis et al. (1986), Lines: Finite element model)

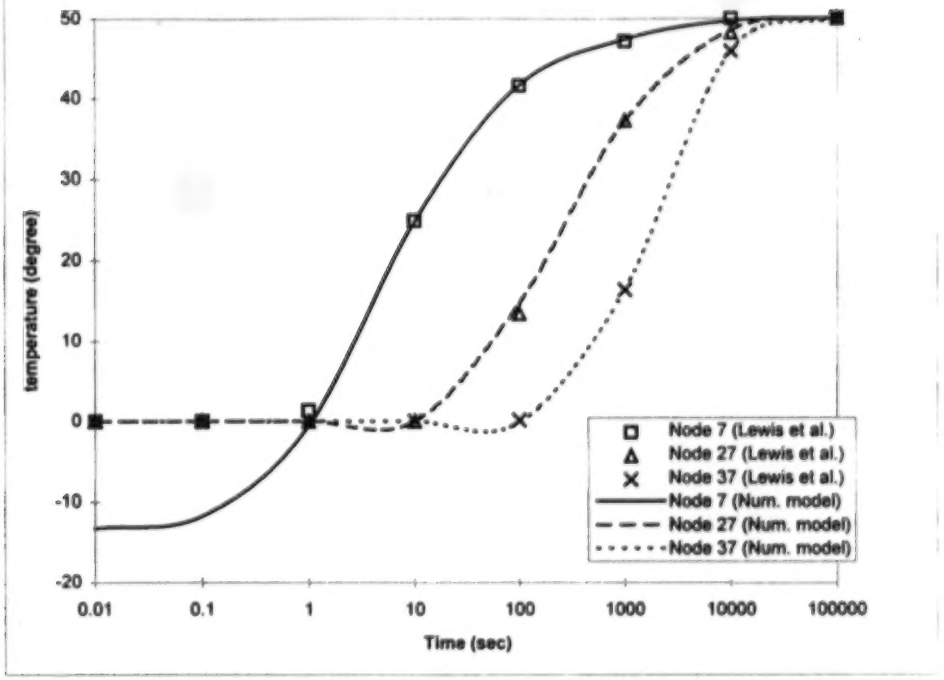

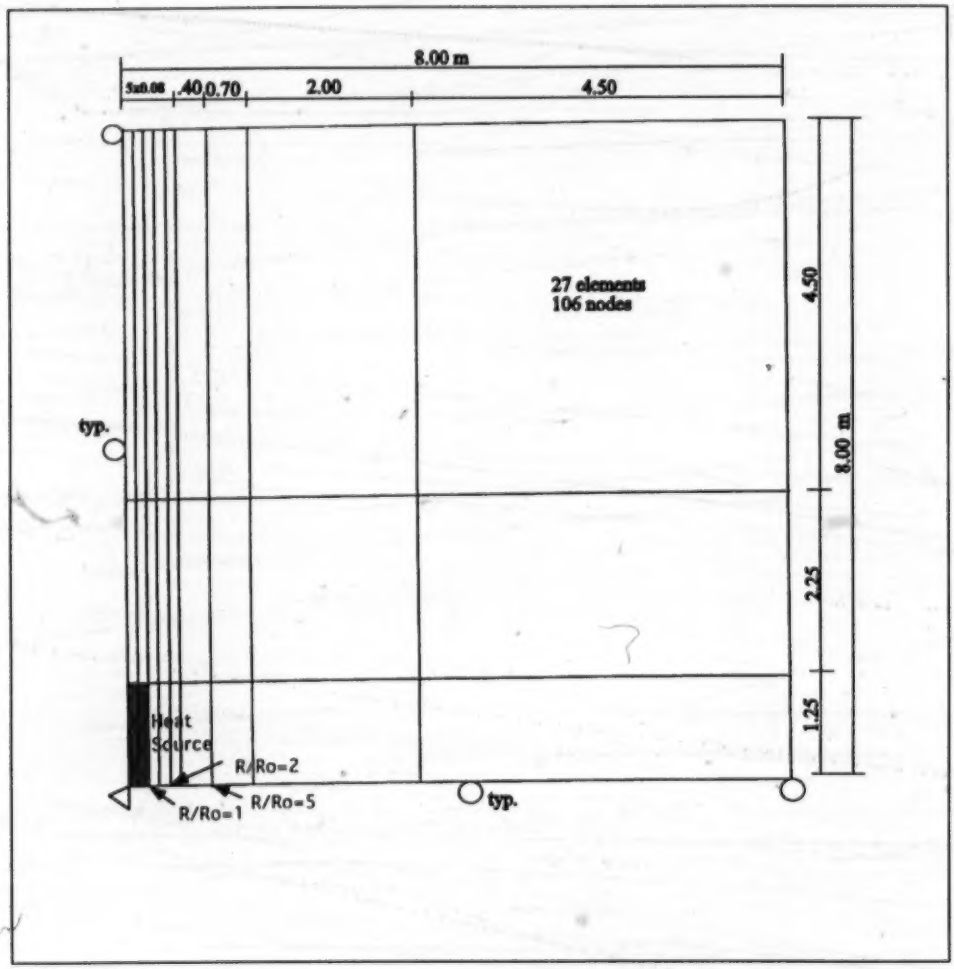

Figure (6-15) Finite element mesh for axisymmetric thermo-elastic consolidation problem (from Lewis et al., 1986)

Figure (6-16) Comparison between analytical and numerical solutions for horizontal displacements (Symbols: Lewis et al. 1986, Lines: Finite element model)

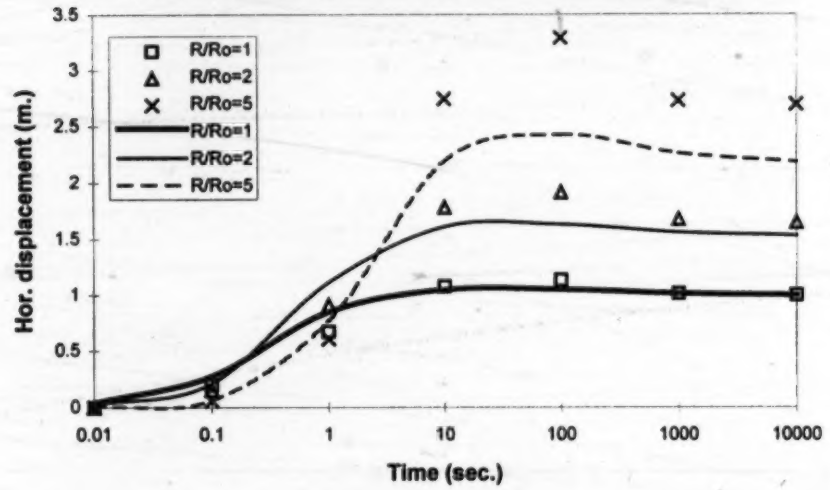

Figure (6-17) Comparison between analytical and numerical solutions for pore pressure (Symbols: analytical, Lines: finite elemnt model)

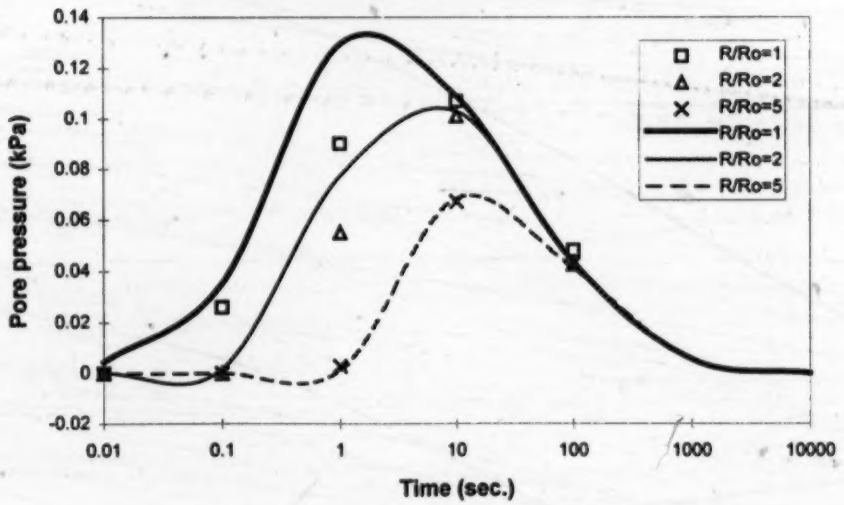

Figure (6-18) Comparison between analytical and numerical solutions for temperature
(Symbols: analytical, Lines: finite element model)

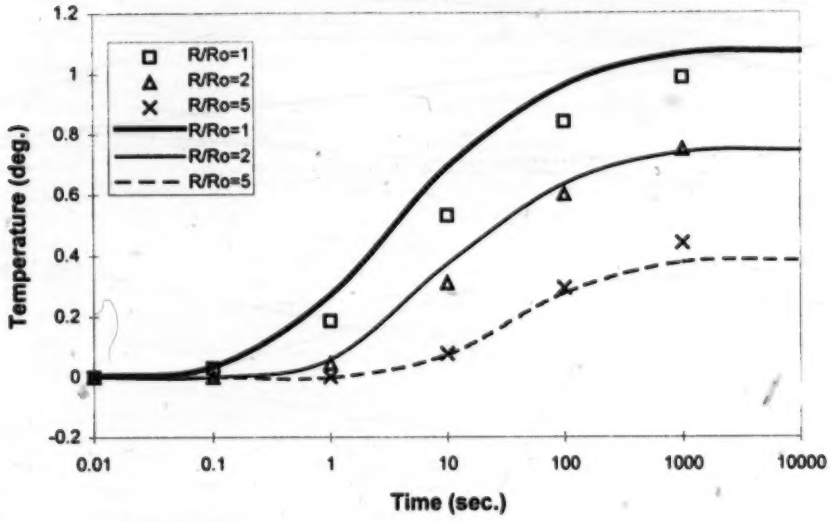

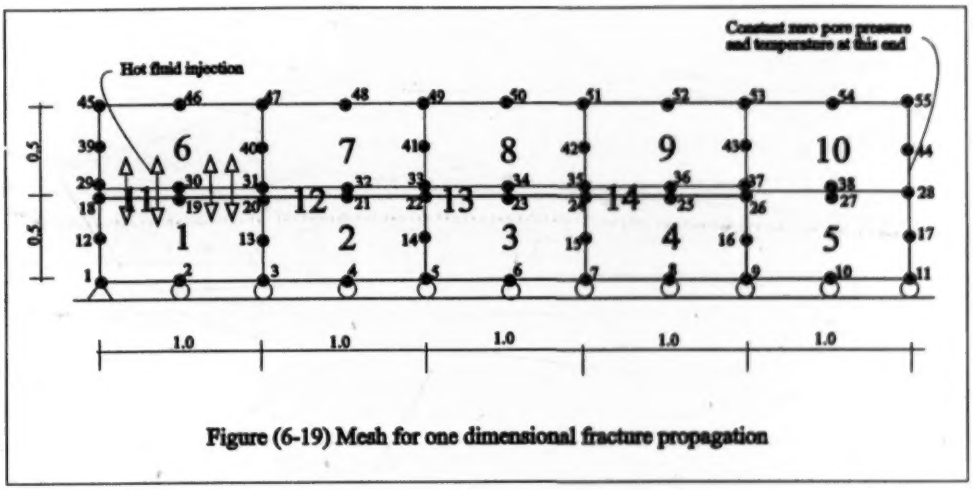

Figure (6-19) Mesh for one dimensional fracture propagation

Figure (6-20) Variation of pore pressure at some nodes in the soil and at the fracture

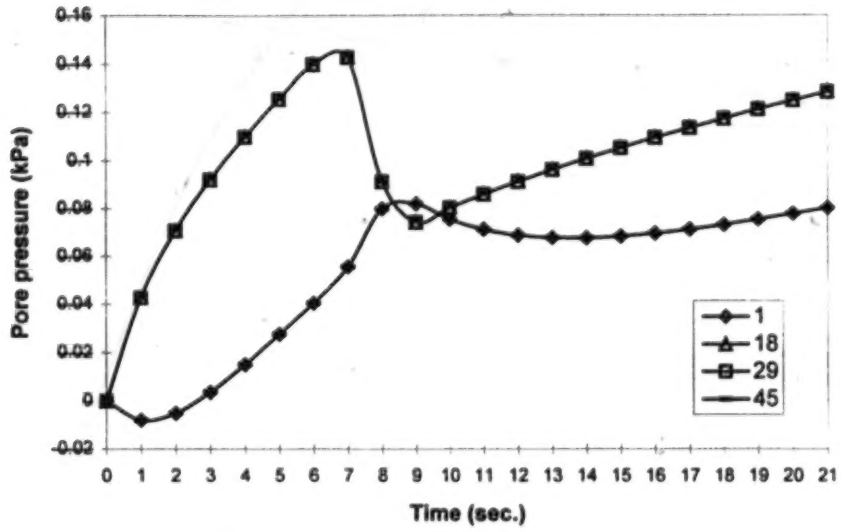

Figure (6-21) Variation of pore pressure in the soil due to the effect of fracturing

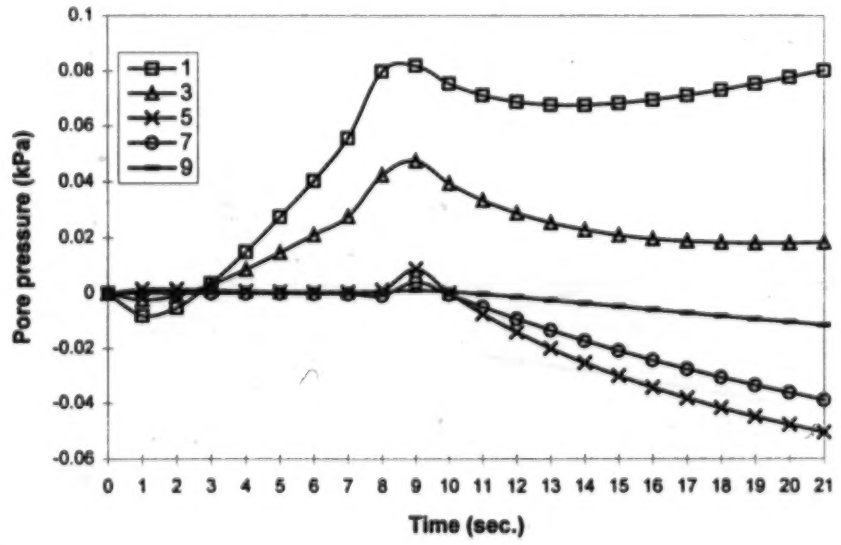

Figure (6-22) Variation of pore pressure along the fracture

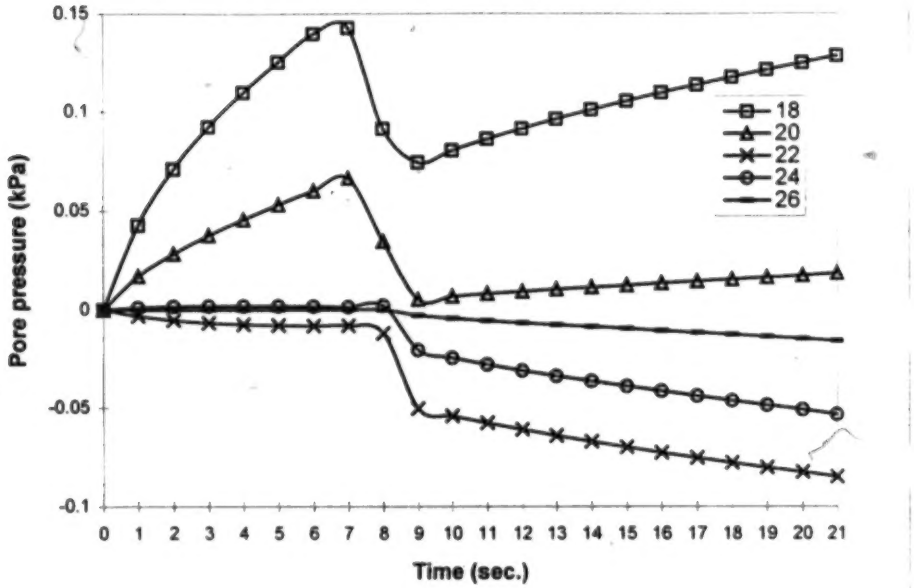

Figure (6-23) Variation of temperature in the soil and at the fracture

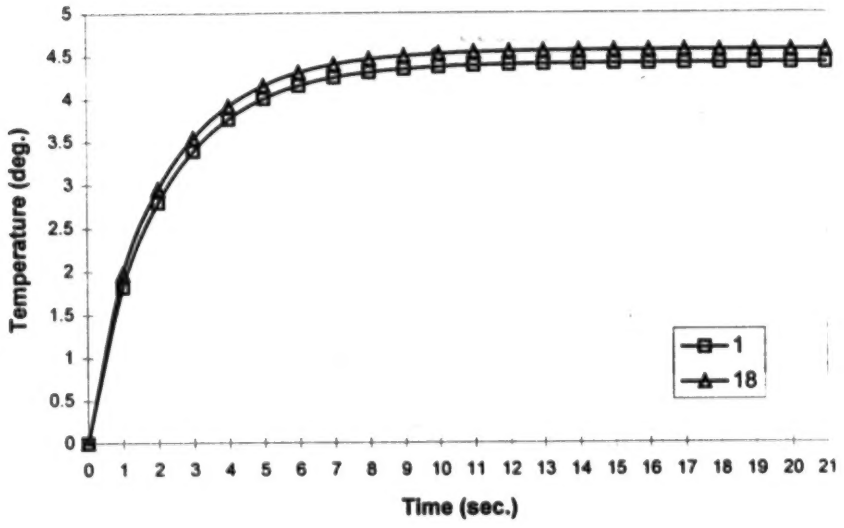

Figure (6-24) Variation of soil temperature due to hot fluid injection

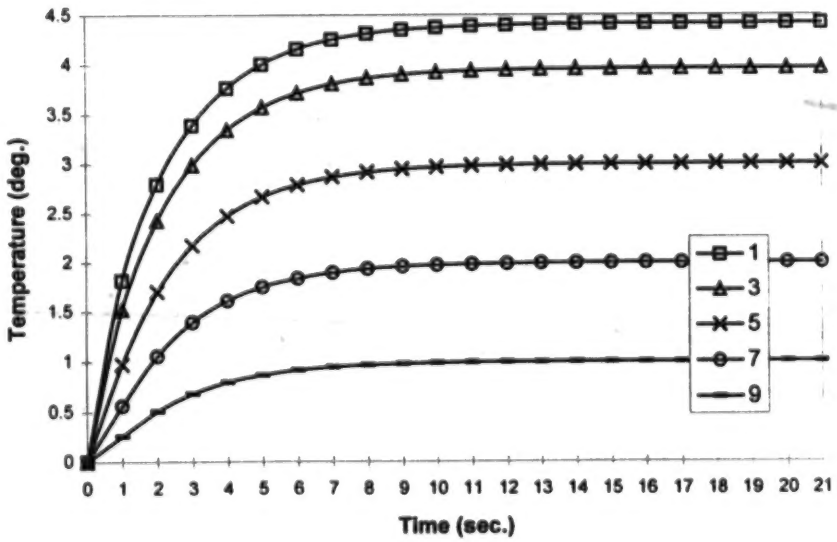

Figure (6-25) Variation of temperature along the fracture due to hot fluid injection

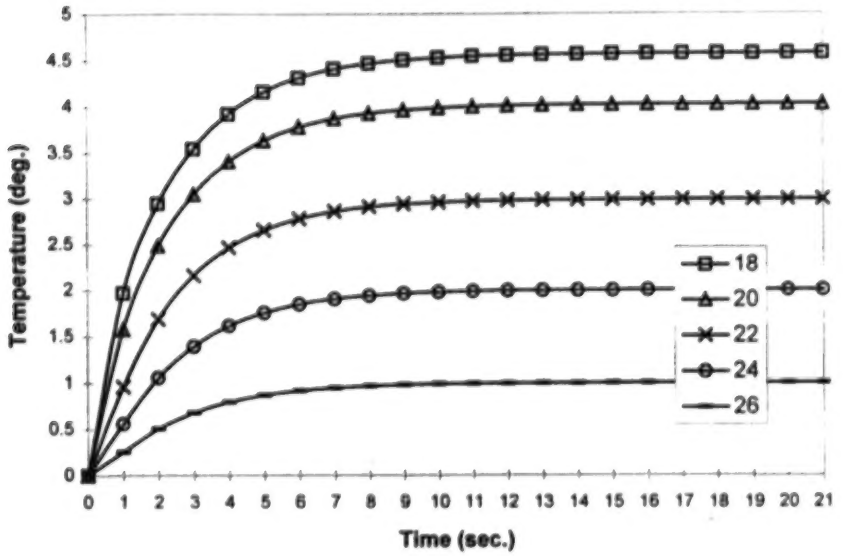

Chapter 7

Modeling Hydraulic Fracture Experiments on Large Scale Triaxial Chambers

7.1 Introduction

The amount of oilsand that can be extracted by open pit mining is approximately 5% of the Alberta's total oilsand deposits. Due to the high viscosity of bitumen, extraction of the remaining oilsands requires application of enhanced and tertiary recovery methods. Therefore, hydraulic fracturing will become even more important for the oilsand industry in Alberta and elsewhere in the future. Optimization of the hydraulic fracturing treatment is not possible without having design tools such as numerical models. Numerical modeling also plays an important role in decision making and management of the costly technical operations by providing valuable information through the simulation of different types of treatments. However, numerical models must be validated by laboratory and/or field data to become realistic and reliable design tools. In this chapter, it is intended to validate the developed numerical model against the large scale hydraulic fracturing laboratory experiments.

7.2 Earlier Experimental Studies

In the previous chapters it has been emphasized that hydraulic fracturing process in an oil reservoir is a complicated issue that combines the complexities of simulating non-isothermal multiphase flow with stress and deformation analysis in a porous

medium. That is why data which is needed to validate the numerical models are difficult to collect from the field, since the required monitoring systems and observation wells are far beyond the budget that is usually available. Furthermore, unknown boundary conditions, geological complexities, as well as human factors cause difficulties in the interpretation of the field data. Some in-situ hydraulic fracturing studies have been performed by Bjerrum et al. (1974), Bjerrum and Andersen (1972), Penman (1976), and Vaughan (1971). A review of these tests shows that generally the pressure required to cause hydraulic fracturing is highly variable and depends on in-situ stresses, rate of fluid injection, fluid pressure, strength and deformation characteristics of the soil/rock, shape of the borehole, and the drilling technique. Unfortunately, the individual effects of each of these factors cannot be evaluated from the results of in-situ tests.

On the other hand, laboratory experiments are found to be useful and can provide insight into the actual hydraulic fracturing process. This is because in the laboratory environment there are more controls on different aspects of the test and it is possible to provide well-defined boundary conditions. Moreover, more instrumentation can be installed to monitor the changes of different factors in the hydraulic fracture experiment. Laboratory investigations on hydraulic fracturing have been carried out primarily for rocks and to some extent for soils.

Haimson (1968) conducted borehole hydraulic fracturing tests on rock and found that in the case of impermeable rock where minor principal stress is normal to the axis of the borehole, the pressure required to cause hydraulic fracturing was equal to the sum of the tensile strength of the rock and twice the minor principal stress. In permeable rock, he found that the pressure required to cause fracturing cannot be measured with certainty, however, he concluded that it was always greater than the minor principal stress and less than the pressure required for fracturing in impermeable rock.

Zobak et al. (1977), Midlin and Masse (1979), and Cheung and Haimson (1989) have conducted hydraulic fracturing experiments on rocks. The main focus of these studies was breakdown and shut-in pressures, and orientation of fractures. Effects of

injection rate, fracture fluid, well orientation, etc. have been studied in some of these works.

Some investigators studied the interaction between a hydraulically driven fracture and a pre-existing fracture (Lamount and Jessen, 1963; Anderson and Larson, 1978; Hanson et al., 1981; Warpinski et al., 1981; Blanton, 1982; Teufel and Clark, 1984). These experiments were primarily focused on whether or not a fracture is contained by structural planes in rocks.

A few experimental studies have been conducted to understand the whole process of fracture propagation and to produce data for verification of numerical models (Rubin, 1983; Medlin et al.,1984; Guo, 1993).

Guo (1993) studied the breakdown and shut-in pressures and well communication by conducting a number of experiments on large block specimens of Gypstone. The main objective of this research was to evaluate the effects of the minor principal stress (σ_3) and injection rates on fracture propagation. In this work, three principal stresses, boundary displacements, and bottomhole pressure were measured. Leak-off was also studied in the experiments. Abnormally high breakdown pressures were observed which could not be fully explained by various breakdown models. However, by using the concept of stress intensity factor for mode *I* fracture (K_{IC}), it was possible to explain the high breakdown pressures. Using an extended form of the fracture initiation criterion as:

$$\begin{cases} K_I - K_{IC} = 0 \\ \partial(K_I - K_{IC}) / \partial L = 0 \end{cases} \qquad (7\text{-}1)$$

made it possible to explain several phenomena such as rate dependent, size-dependent, fracture fluid-dependent, and σ_3-dependent responses of breakdown pressure. This research has produced considerable experimental data for evaluating the numerical models for hydraulic fracturing in rocks.

Experimental studies in hydraulic fracturing in soils have been carried out by Nobari et al. (1973), Jaworski et al. (1981), Mori et al. (1987), Komak panah (1990), and Murdoch (1992).

Nobari et al. (1973) studied the fracture mode, the orientation of the fracture plane, and the manner in which failure progressed during hydraulic fracturing. They concluded that hydraulic fracturing occurs through tensile fracture on the plane of the minor principal stress. They also found that for soils under conditions of more 'uniform stress', hydraulic fracturing begins at a point of low effective stress and propagates only if the soil stresses at neighboring points are reduced or the water pressure is increased. This indicated that hydraulic fracturing in soil does not propagate rapidly as it does for some materials such as glass or rock.

Jaworski et al. (1981), by conducting hydrofracturing test on cohesive soils in cubic specimens found that the hydraulic fracturing process is a linear function of the initial horizontal total stress. This was confirmed later by Mori et al. (1987). The minimum value of the fracturing pressure was found to be equal either to the sum of the initial minor principal total stress and the tensile strength of the soil (by Jaworski et al.) or to the unconfined compression strength of the soil (by Mori et al.).

Komak panah (1990), based on the experiments on compacted cohesive and cohesionless soils in hollow cylindrical specimens, found that hydraulic fracturing may be initiated by shear failure near the borehole when total stresses reach the failure condition of the soil in an unconsolidated undrained case. He also developed a theoretical foundation for his study based on Mohr-Coulomb failure criterion.

Murdoch (1992) performed more than 100 hydraulic fracturing experiments on silty clay soil confined within a rectangular triaxial loading cell. He used dyed glycerin as injection fluid. He found that water content plays a major role in hydrofracturing, and for unsaturated soils with positive pore pressure, pore water fills the crack tip rather than the injection fluid which can control hydraulic fracturing development in soils. He concluded that increase in water content decreases the pressure required to initiate and propagate fracture and increases the duration of stable propagation.

Recently, a joint *CANMET* /industry /*AOSTRA* funded project was undertaken by Golder Associates to perform hydraulic fracturing experiments in large scale triaxial chambers. This project examined the effects of different stress states, injection rates, and leak-off on the initiation and propagation of hydraulic fracturing in oilsand. Pattern

of fracture propagation was studied by careful examination of the specimen after each test. The ultimate goal of this work was to provide a framework to evaluate, verify, and refine analytical models for fracturing in uncemented sands. The results of this experimental study are used to validate the developed numerical model.

7.3 Description of Large Scale Hydraulic Fracture Experiments

The project* consisted of three phases which were carried out between April 1990 and July 1994. The main objectives of the study were (1) to provide a better understanding of the mechanisms of hydraulic fracture formation and propagation in uncemented oilsands under condition of high leak-off, (2) to determine the effect of fluid injection rate on the fracturing process, and (3) to determine the influence of different stress fields on the fracture pattern. These experiments were carried out in a large triaxial stress chamber shown schematically in Figure (7-1). The chamber can accommodate samples of up to 1.00 meter high and 1.40 meter in diameter. The quartz sand was used which was saturated with a viscous fluid, such as invert liquid sugar. The injection fluid was dyed invert liquid sugar (phases *I* and *II*) and dyed water (phase *III*) in order to trace the fracture. As Figure (7-1) shows, a hollow steel pipe with an outside diameter of 33.5 mm perforated at mid-sample height was used to simulate the injection well. Principal stresses of up to 1000 kPa can be applied independently through a circumferential (σ_h) and upper (σ_v) cavity as illustrated in the figure.

---

* This project was jointly funded by:
-Canada Center for Mineral and Energy Technology (*CANMET*)
-Imperial oil Resources Canada Ltd.
-Shell Canada Ltd.
-Mobil Oil Canada (phase 1)
-Japan Canada Oilsand Ltd. (phase 3)
-Alberta Oilsand Technology and Research Authority (*AOSTRA*)
-Golder associates Ltd.

7.3.1 Materials used

Lane mountain 125 quartz sand was chosen for the laboratory tests. Its behavior was reported to be similar to oilsand which exhibits high dilatancy and post peak softening during triaxial compression under low effective confining stresses (such as those associated with hydraulic fracture). Results of typical drained triaxial tests on McMurray formation oilsand at in-situ stresses, and on dense Lane Mountain sand at 350 kPa stress are shown in Figures (7-2) and (7-3), respectively. The '*p-q*' diagram for Lane mountain sand based on the tests on small scale triaxial samples is shown in Figure (7-4). The specific gravity of Lane mountain sand grains was determined to be 2.65 and its permeability to water was measured to be 4.56×10^{-3} cm/sec and to invert liquid sugar 4.0×10^{-6} cm/sec.

Glycerin or invert liquid sugar was used as the resident fluid and injection fluid. Both of these liquids are clear, colourless, viscous and fully soluble in water. The viscosity of Glycerin at 20°C is 1.49 Pa-sec, and viscosity of invert liquid sugar is 1.6 Pa-sec. The viscosity of either liquids may be adjusted to any lower level by mixing with water. There is no chemical reaction between Glycerin or liquid sugar and any component of the triaxial stress chamber. Tests in phase *I* began with using Glycerin as the resident fluid but later it was replaced by invert liquid sugar up to the end of the phase *III* of the project.

7.3.2 Procedures

Samples were prepared by pluviation of dry sand from a hopper located directly above the chamber. The hopper was exactly the same diameter as the sample to obtain one dimensional pluviation conditions. Prior to pluviation, the injection well was installed and instrumentation for measuring sand deformation and pore fluid pressure changes were suspended at strategic points in the sample. The instrumentation was placed on three levels, two above the injection zone and one below (Figure 7-5). The injection well was simulated by a hollow steel pipe with an outside diameter of 33.5

mm and inside diameter of 25.4 mm. The pipe was perforated at mid-sample height over an interval of 50.0 mm with 8 rows of 3.5 mm diameter holes.

Boundary conditions were free draining at the top and bottom of the chamber which were connected to a constant pressure equal to +200 kPa. A 200 kPa back pressure was applied to all of the tests in three phases in order to maintain the sample in a fully saturated condition. No radial drainage was allowed.

Before starting the fracture tests some supplementary tests were carried out to provide additional information regarding the geomechanical and fluid flow characteristics of the samples prior to hydraulic fracturing. These supplementary tests were constant head permeability test, subfracture pressure injectivity test, drained loading test, and pore pressure parameter '*B*' test. Pore fluid pressures, vertical stress, radial stress, injection pressures, and injection flow rate were recorded electronically during the tests.

At the end of each test, the sample was excavated in horizontal lifts, normally 1.5 to 3.0 cm in thickness, under black light. When the lift was completely excavated, locations of dye were marked with black string. The black light was then turned off. Next, under normal light, a photograph of the sample surface was taken with a camera located directly above the chamber. This procedure was repeated for each lift. The photographs showing the locations of the dye were digitized and plotted in three dimensions to show the fracture pattern in the test.

A list of the tests that were performed in three phases is shown in Table (7-1). For more information about the equipment, sample preparation technique, monitoring systems, data acquisition method, and individual test procedures, the reader can refer to the reports by Golder Associates Ltd. (1991-1994).

7.3.3 Review of the results of the large scale hydraulic fracture experiments

7.3.3.1 Review of phase *I* experiments

A total of 8 hydraulic fracture tests were conducted in phase *I* (Table 7-1). In 6 tests the initial minor principal stress was vertical, expecting a horizontal fracture, and one test was carried out with horizontal minor principal stress in order to create a

vertical fracture. Test #2 was aborted due to a fitting leak. Different injection rates were employed to evaluate changes in fracture propagation. Injection fluid and resident fluid were the same in this phase of experiments.

The data from phase *I* experiments indicated that different failure mechanisms occurred depending on the injection rate used in the test. However, the exact mechanism was not identified. Two possible mechanisms of failure were described in the phase *I* report as follow:

- "Tensile failure or parting which occurs when the rate of fluid injection into an uncemented sand mass exceeds the rate of flow that can occur through the interconnected pores in the sand. If the fluid pressure at this injection rate is greater than the total minor principal stress, there can be tensile stress in the sand matrix. Since an uncemented sand will not support such stresses, the sand grains are forced apart and a parting propagates through the sand."

- "Shear failure occurs when the shear forces at a sand grain contact exceeds the shear resistance at the contact. Increase in the pore fluid pressure from fluid injection into the sand mass results in a decrease in the normal forces at contacts between sand grains and therefore a reduction in shear resistance. When the shear resistance falls below the shear force, the sand grains slide relative to one another. In dense sand, the shear sliding results in a less densely packed array of sand grains. The volume of the void spaces in the sand mass is increased and the sand is therefore more permeable along the shear surfaces."

Generally, in phase *I* experiments, the pattern of fracture was more extensive in samples where higher injection rates were used. Although a horizontal or vertical fracture surface was expected (based on the applied stresses), no planar fracture was observed in this phase of study. Typical experimental results of pore pressure measurement and fracture pattern from test #4 of phase *I* are shown in Figures (7-6) and (7-7).

7.3.3.2 Review of phase *II* experiments

A total of 5 hydraulic fracture tests were carried out in phase *II* experiments (Table 7-1). One test was performed with constant pressure injection, and 4 tests were performed with constant flow rate injection. Injection fluid and resident fluid were the same (invert liquid sugar) throughout this phase.

Initial stress state for all of the tests in phase *II* was 600 kPa horizontal, 400 kPa vertical, and 200 kPa back pressure. This stress state results in a K_O $(= \frac{\sigma'_h}{\sigma'_v})$ value of 2.0 indicating that a horizontal fracture surface was anticipated. The objective of phase *II* experiments was to determine the effect of fluid injection rate on fracture propagation. Fluid injection rates ranged from 0.4 ml/sec to 200 ml/sec.

The data obtained from phase *II* experiments indicated evidence of shear failure of the specimen at all fluid injection rates. No dominant fracture plane was observed during phase *II* experiments. In general, propagation of the dye into the samples in this phase was less than that observed in phase *I* tests even though the amount of dyed fluid injected in phase *II* was greater. The dye patterns suggested that the observed fractures in the tests were dominated by the influence of sand dilation. Expansion of the initial fracture cavity resulted in shear strains in the sand surrounding the fracture. These shear strains, in turn, caused the sand to exhibit a tendency to dilate. However, since the sand's potential for expansion was limited by the material surrounding it, there was a relatively large increase in the effective confining stress on the sand surrounding the fracture. As a result, the large injection pressures were offset by large local stresses in the sand matrix (which exceeded the minimum confining stress on the sample) and limited the propagation of the fracture.

For one of the tests of this phase a numerical simulation, using program *FLAC* (Itasca, 1995), was carried out. It showed that when the samples were subjected to effective confining stresses corresponding to a K_O value of 2.0, the stresses in the sample were very close to shear failure envelope.

Typical experimental results of pore pressure measurement and fracture pattern from test #5 of phase *II* are shown in Figures (7-8) and (7-9).

7.3.3.3 Review of phase *III* experiments

Six hydraulic fracture tests were conducted in phase *III* experiments. Hydraulic fractures were generated under various applied stresses and fluid injection rates (Table 7-1). The injection fluid in this phase was water which is less viscous than the resident pore fluid (invert liquid sugar). In two tests a notch was created in the sample at the point of fluid injection.

The fracture patterns produced during phase *III* tests were extremely complex even though the parameters in the tests were selected to create a single tensile fracture. These parameters included K_o, injection rate, magnitude of effective confining stresses, volume of injection fluid, and injection zone geometry. Reducing K_o, increasing the injection rate, and creating a notch to help nucleation of a fracture did not cause planar fracture. However, these measures did change the breakdown pressure and altered the fracture patterns.

A single or closely spaced distribution of fractures orientated primarily perpendicular to the initial minimum applied stress was not generated in any of the large scale hydraulic fracture tests carried out during the laboratory program.

Generally, peak injection pressures were found to be much higher than the stresses applied to the sample.

Typical experimental results of pore pressure measurement and fracture pattern from test #1 of phase *III* are shown in Figure (7-10) and (7-11)

7.4 Numerical Modeling of the Chamber Tests

In this study, test #4 of the experiments carried out in phase *II* was selected for numerical modeling. The reasons for this selection were:

1) In the tests conducted in phase *I*, some important factors were not known. For example, for five out of eight tests in phase *I*, permeabilities of the samples were not measured, the resident pore fluid was changed, and position of the piezometers was far from the fracture zone leading to poor results. Also, friction at the top and bottom boundaries added some ambiguity to the problem.

2) In phase *III* tests, water was used as the injection fluid, invert liquid sugar as the resident fluid. The aim of the tests was to determine the effect of high leak-off on the fracture pattern by using water which has a lower viscosity as compared with invert liquid sugar. This is, in fact, a two-phase miscible flow problem for which the results of the developed numerical model may not be exact.

3) Supplementary tests such as the injectivity test and steady state fracture test were carried out in some tests in phase *II* prior to the fracture test. These supplementary tests might have caused some disruption of the sand matrix and altered the stresses in the vicinity of the injection zone which have significant effects on the test results (phase *II* report, pp.23 and 36). These supplementary tests were not performed for tests 4 and 5.

Based on the above reasons tests 4 and 5 of phase *II* were found to be the most suitable for numerical modeling in this study. These two tests were basically performed under the same experimental conditions but at different injection rates. In test 5 a higher injection rate was used to evaluate the effect of high injection rate on the fracturing process.

7.4.1 Fracture propagation in elastic medium

The sample dimensions and position of instrumentation are shown in Figure (7-12). Two permeability tests carried out on the saturated sample gave permeability values of 4.9 and 4.6 Darcys. Horizontal and vertical boundary tractions of 600 kPa and 400 kPa, respectively, were applied on the sample with a 200 kPa back pressure required to keep the sample fully saturated. The K_o value was equal to 2 for this test which indicated that horizontal fracture planes were expected. In this test 250 ml of dyed liquid sugar was injected into the sample in 8.3 seconds (30 ml/sec.).

The finite element model consisted of 704 elements (260 eight-node rectangular elements and 444 six-node fracture elements) with 1562 nodes (including the double nodes) were used. Due to axial symmetry only half the sample was analyzed which is shown in Figure (7-13). The boundary conditions are:

Bottom boundary: Fixed in the horizontal and vertical directions, free drainage

Top boundary: Free, free drainage

Left boundary: Fixed in the horizontal direction, no drainage allowed

Right boundary: Free, no drainage allowed

Time increment for the analysis was chosen to be one second. A three dimensional axisymmetric analysis was carried out considering a linear elastic behaviour for sand with elastic modulus equal to 41050 kPa and Poisson's ratio of 0.25. Permeability of the fracture elements was considered to be 100 times greater than that of the surrounding soil matrix ($100k_{mix}$). The test was simulated by injecting fluid at the perforated area of the wellbore. The injection flux was 0.0052 m/sec (30 ml/sec). In this analysis nodal coordinates were not updated and a nominal thickness equal to 2mm was considered for the fracture elements. Other input data for the analysis are summarized in Table (7-2).

The variation of pore fluid pressure at the injection zone is shown in Figure (7-14). Although the calculated peak pressure is slightly higher than the measured pressure, the overall behaviour is very similar. The initial slopes of the two curves are different; this is because in the finite element analysis the stresses were examined at the end of each time step to identify the possibility of fracture. For instance, if the time increment is 1 second, no fracture will occur until the end of this time step. Obviously, in reality fractures can occur much sooner (e.g. a fraction of second). Therefore, the fluid finds some paths to flow easily and the pore pressure does not build up very quickly.

As seen in Figure (7-14), at the beginning of injection there is a jump in the pore pressure, then, during eight seconds of continuous injection the pore pressure remains fairly constant and at the end of injection, both calculated and measured curves show a decline in pore pressure.

Pore pressures at the piezometers installed at a distance of 75mm from the injection pipe (Figures (7-5) and (7-12)) are compared with the numerical solution in Figures (7-15) and (7-16). Piezometers were installed in three levels but pore pressure

in two of them did not change much and their results were similar. A good agreement between the numerical results and measured values in the lab can be observed.

The fracture pattern obtained from the numerical model is shown in Figure (7-17). The sequence shows the fracture pattern at the onset of injection; 4 seconds after starting injection; at the end of injection (8 seconds after starting injection); and at 30 seconds. The actual fracture pattern observed in the laboratory is shown in Figure (7-18). Despite the fact that $K_O = 2.0$, neither the numerical model nor the experimental results show the anticipated planar fracture. The numerical model shows a fracture zone which gradually expands as the injection continues.

It should be noted that only tensile fracturing criterion was used in the model, and the tensile strength of the sand was assumed to be zero.

Since the actual permeability of the fractures relative to the soil matrix is not known, the permeabilities of the fractures were varied from 100 to 1000 times of the permeability of the sand. The pore pressure variation for these cases are plotted in Figure (7-19). It can be observed that, increasing the permeability of the fracture elements from 100 $k_{mtx.}$ to 1000 $k_{mtx.}$ has a significant effect on reducing the pore pressure. It is interesting to see how the fractures propagate when the permeability of the fracture elements is increased. These are shown in Figures (7-20) and (7-21).

Variations of pore pressure at the piezometers installed at 75mm distance from the injection well (Figures (7-5) and (7-12)), when permeability of the fracture elements are modified, are demonstrated on Figures (7-22) and (7-23).

Extent of the fracture zone predicted by the numerical model is comparable to the observed fracture zone in the lab. Based on Figure (7-18) if one considers the darker middle part only, the extent of fracture relative to the outside diameter of the injection well (hollow steel pipe), *d*, is *4.1*. If the curved fracture on top of the main fracture zone in Figure (7-18) is taken into account, the extent of fracture will be increased to *9.2d*. Extent of fracture based on the results of the numerical model are *5.34d*, *6.05d*, and *6.59d* when permeability of the fractures are considered to be $100k_{mtx}$, $500k_{mtx}$, and $1000k_{mtx}$ respectively. In all cases the extent of fracturing predicted by the numerical model is close to the observed values in the laboratory experiment.

Injection generally causes a very high pressure gradient at the injection zone and the finite element method does not work well at these zones due to high pressure gradient. In order to reduce the effect of this problem on fracture propagation, a series of analyses was performed with prescribed pore pressure at the injection zone. The prescribed pore pressures were simulated based on the laboratory observed values. Results in this case are depicted in Figures (7-24) which indicate less extensive fracture patterns, but as one increases the permeability of the fracture elements the patterns become closer to the injection case.

By using the numerical model, it is possible to detect the onset of crack initiation. In other words, the model can be used as a guide to identify the minimum injection flux required to nucleate a fracture in the ground. In this case, the model shows that fracture starts with an injection flux as low as 9×10^{-5}m/sec provided that it is injected for 8 seconds. If it is desired to reduce the time of injection to 1 second the injection flux must be increased to 23×10^{-5} m/sec.

7.4.2 Effect of changes in soil permeability on the fracture behaviour

In order to investigate the effect of soil permeability on fracturing, the following two cases were considered:

a) Horizontal permeability was increased by one order of magnitude and the vertical permeability was kept constant;

b) Vertical permeability was increased by one order of magnitude and the horizontal permeability was kept constant.

Variation of pore pressure in two cases is shown in Figure (7-25). The results indicate that higher horizontal permeability leads to higher pore pressure but the pore pressure drops sharply after one second of injection. Higher vertical permeability has little effect on reducing peak pore pressure. Pore pressures for cases (a) and (b) move progressively closer to each other at later time especially after 15 seconds where both cases show almost the same pore pressure; both of which are less than the laboratory measured pore pressure. This confirms that higher permeability causes more fluid leak-off and leads to rapid decrease in pore pressure.

Fracture patterns for both cases are illustrated in Figure (7-26). It should be noted that the fracture patterns clearly follow the pore pressure distribution in the soil with drainage at the top and bottom of the sample.

The analysis results show that further increase in the soil permeability, for example by increasing the permeability by two orders of magnitude, no fracturing would occur and the injected fluid simply drains through the porous medium. This demonstrates the importance of the permeability of the material on the fracturing process in porous media.

7.4.3 Effect of different fracture initiation criteria

In order to study the effect of a change in the fracture initiation criterion on the fracture pattern and the pore pressure, it is necessary to know the critical values for fracture initiation. Unfortunately, in the case of oilsand there is no experimental data available on the critical values of strain energy density (G_C) or J-integral (J_C) etc. for tensile or shear modes of fracture. Here, a simple shear fracture criterion is used to demonstrate the capability of the program to incorporate different kinds of fracture criteria. It is assumed that fracture will initiate whenever:

$$q \geq \alpha \times p + \beta \tag{7-2}$$

where

$$q = \{\frac{1}{6}[(\sigma_1 - \sigma_2)^2 + (\sigma_2 - \sigma_3)^2 + (\sigma_3 - \sigma_1)^2]\}^{\frac{1}{2}} \tag{7-3}$$

$$p = \frac{1}{3}(\sigma_1 + \sigma_2 + \sigma_3) \tag{7-4}$$

$\sigma_1 > \sigma_2 > \sigma_3$ principal stresses

α and β are material parameters. In this example the following values are used:

$\alpha = 0.781$

$\beta = 53.0$

These parameters are chosen based on the values obtained from the triaxial compression tests that were performed in phase *I* of the laboratory experiments. A comparison between the fracture patterns in three cases is depicted in Figure (7-27). Case(a) shows the same fracture pattern from Figure(7-17) which is based on the tensile fracture

criterion. Case(b) represents the fracture pattern using the above shear criterion; and case(c) is a combination of two criteria where the fracture initiates by that criterion which is satisfied first. Pore fluid pressures are compared in Figure(7-28). In all cases the permeability of fractures are set to be 100 times greater than the permeability of the soil matrix.

7.4.4 Elastoplastic fracture propagation

In petroleum literature it is well known that oilsand compressibility is nonlinear at low stresses (e.g. Settari, 1989). In geotechnical terms this basically means that the stress-strain behaviour of oilsand is nonlinear and its bulk modulus and stiffness varies with change in stresses. Some researchers have considered a nonlinear elastic (hyperbolic) model for simulating this behaviour (Vaziri, 1986) while others have proposed an elastoplastic constitutive model (e.g. Wan et al., 1989). In this study, in order to evaluate the effects of soil failure on fracture patterns in isothermal condition, an associated Mohr-Coulomb model was employed. This model is capable of simulating high dilation which is an important characteristic of oilsand. For this model the following parameters were used:

$C_{peak}=0$, $C_{residual}=0$

$\phi_{peak}=38°$, $\phi_{residual}=38°$

E= 41050 kPa , $\nu=0.25$

Boundary tractions were, just as before, 600 kPa and 400 kPa horizontal and vertical stresses respectively, with 200 kPa back pressure. According to the Mohr-Coulomb failure criterion, the ratio of the principal stresses at yielding is given by:

$$\frac{\sigma_1-\sigma_3}{2}=\frac{\sigma_1+\sigma_3}{2}\sin\phi+C\cos\phi$$
$$\begin{cases} C=0 \\ \phi=38° \end{cases} \rightarrow \frac{\sigma_1-\sigma_3}{2}=\frac{\sigma_1+\sigma_3}{2}\sin 38 \rightarrow \frac{\sigma_1}{\sigma_3}=4.204 \qquad (7\text{-}4)$$

Pore pressure variation at the injection zone is shown in Figure (7-29). On the same figure, the results of the analysis with different permeabilities for fracture elements (500 and 1000 times greater than the permeability of soil matrix) are included.

Generally, the initial pore pressure in this case shows around 30% higher pore pressure compared to the elastic case.

Fracture patterns for elastoplastic analysis are depicted in Figure (7-30). Compared to the fracture patterns of elastic analysis they are less dispersed and the fracture zones are smaller. In order to distinguish the zone of shear failure the plots of σ_1/σ_3 at three different steps: 1, 4, and 8 seconds after starting the injection are illustrated on Figure (7-31) to (7-33). Areas with $\sigma_1/\sigma_3>4.2$ are at the state of shear failure. In Figure (7-31), a purple symmetrical shape in front of the injection area shows the failure zone. Fractures were initiated after this step at time 2 seconds. The failure zones in Figures (7-32) and (7-33) are rather scattered. This is due to the intense fracturing at the injection zone. Yield condition seems to be violated in Figures (7-32) and (7-33) since in the legend higher stress ratios can be observed, however, the areas where stress ratio has exceeded 4.2 are extremely small and invisible in these figures which can be attributed to the numerical error. Generally speaking, in the elastoplastic case, shear failure does not seem to be a dominant mode in the fracture initiation process. However, the numerical model indicates that tensile and shear fractures can simultaneously occur in the hydraulic fracturing process in a porous material. Despite the fact that the shear failure zone is small, the dilation characteristics of the material will generate compressive stresses in a confined condition, which can inhibit fracture growth. This explains why there is a less dispersed fracture zone in the elastoplastic analysis.

Extent of the fracture zone predicted by the numerical model in this case is less than that of elastic analysis. Based on the results of the numerical model, extent of fracture relative to the outside diameter of the injection well (hollow steel pipe) are *4.27d* and *5.34d* when permeability of the fractures are considered to be $100k_{mtx}$ and $500k_{mtx}$ (or $1000k_{mtx}$) respectively. Although these values are less than those in elastic analysis, they are comparable to the extent of fracture observed in the lab which were *4.0d- 9.0 d.*

7.5 Discussion

Results obtained from the numerical modeling of the hydraulic fracture experiments have revealed some interesting points. First of all, the pore fluid pressures from the numerical model show a fairly good match with the pore pressures measured by the piezometers. This indicates the ability of the model to capture the flow characteristic of the hydraulic fracturing process. The gradual decrease in pore pressure after the injection represents the consolidation process. Numerical results for the pore pressure close to the injection point are higher than those of the laboratory experiments. The reasons for the discrepancies include:

1) Existence of very high pore pressure gradient at the injection zone which cannot be adequately modeled by the finite element method.

2) At very high gradient, Darcy's law is no longer valid. In porous media the flow regime is laminar when Reynolds number is less than one and is turbulent when it is greater than ten (Collins, 1976). In most engineering applications, Reynolds number in the soil is well below unity, but with injection rate about 30 ml/sec it can become much greater and in this situation application of Darcy's law is an approximation to reality.

The numerical results can be improved in a number of ways: using a finer mesh at the injection zone, using a smaller time increment in the analysis, or modifying the compressibility of the fluid. Generally, numerical modeling of transient phenomena is sensitive to time increment used in the analysis. Therefore, modeling high injection rates is more difficult and the results may not be representative of the experimental values and in some cases numerical instability (divergence) may occur.

The numerical model indicates that permeability of the fractures has a significant effect on the pore pressures and fracture pattern in the soil. The model demonstrated that by increasing the permeability of fractures, the injected fluid can find easier paths towards the free draining boundaries thus resulting in pore pressure decline.

Permeability of the soil matrix is also important. The model shows that the pore pressure is sensitive to the permeability of the soil matrix and the fracture pattern roughly follows the pore pressure contours in the soil sample.

Application of Mohr-Coulomb constitutive model for sand showed that shear and tensile fracture occur simultaneously. Dense sand shows a highly dilatant behaviour under shear, but due to the lateral confinement, this tendency to dilate results in large increase in effective confining stresses. The large confining stresses suppress the fracture growth. Therefore, by using an elastoplastic material model, a less dispersed fracture zone is expected - this is consistent with the modeling results.

The numerical model predicts the extent of fracturing to be in the range of *5.3-6.6* times greater than the diameter of the injection well, *d*, if the behaviour of material is assumed to be linear elastic. If an elastoplastic (Mohr-Coulomb) behaviour is assumed, yielding causes the extent of fracturing to reduce to the range of *4.3d-5.3d*. These values are comparable to the experimental observations of the maximum fracture length which was between *4.0d* to *9.0d*.

One of the most important features of the numerical model is the fracture propagation pattern. The model shows that fluid injection in the triaxial chamber causes no dominant single fracture and a fracture zone consisting of a network of small horizontal and vertical cracks develops. This behaviour agrees well with the experimental observations. One of the conclusions in the final report of the experimental study conducted by Golders (1994) reads:

"There was no evidence of a single dominant tensile parting or closely spaced distribution of fractures oriented primarily perpendicular to the initial minimum applied stress in any of the fracture simulations carried out in the experimental study."

It might be interesting to note that changing the direction of the maximum and minimum applied stresses and even creating a notch in the sample at the point of fluid injection did not cause a planar fracture. The consistency between the numerical results and experimental observations suggests that despite the common belief that the hydraulic fracturing always creates a plane fracture with certain geometry, this may not be true for uncemented porous materials such as sands. In fact, the numerical model, as well as the experimental results, indicate that for uncemented reservoirs a single planar fracture is unlikely to occur and the outcome is either multiple fractures or a 'fracture zone'.

The concept of inducing a planar fracture in rocks perpendicular to the direction of minor principal stress, is theoretically sound and has been confirmed through several laboratory studies (e.g. Haimson, 1968; Rummel, 1987; Guo, 1993). In the field, however, observations in some hydraulic fracturing treatments indicate that multiple fracture branching has occurred in many cases (Medlin and Fitch, 1983; Warpinski and Teufel, 1987). Schmidt (1979) has reported very complex fracture pattern from mining back a hydraulic fracture experiment.

In soils with low permeability, such as clays, occurrence of planar fractures has been identified through laboratory experiments (Jaworski et al., 1981; Komak panah, 1990). However, hydraulic fracturing experiments on sandy soils has caused only heave and a zone of plastic deformation around the injection point and no clear fracture was observed even at high injection pressures (Komak panah, 1990).

For the oilsand reservoirs, where the permeability is significantly less than that of sand but greater than that of impermeable rocks, researchers have noted some discrepancies between the prediction of models (based on planar fracture assumptions) and field measurements (Settari, Kry and Yee, 1989). These discrepancies have been attributed to high leak-off in the reservoir.

The above mentioned field and experimental observations, the results of hydraulic fracture tests by Golder Associates (1991-1994) and the results of the numerical modeling carried out in this study, suggest that the concept of inducing a planar fracture by hydraulic fracturing may not always be true. It seems that fracture pattern primarily depends on permeability and cementation of the geologic media. Figure (7-34) shows a conceptual framework for the expected hydraulic fracture pattern in different types of soils or rocks. Considering fracture pattern, there is no fixed boundary for prediction of a dominant planar fracture or a system of numerous tiny fractures. However, a smooth transition zone between different fracture patterns exists. This transition zone depends on many factors of which cementation, permeability, and injection rate/pressure are the most important.

In this study mainly the tensile fracture criterion was used. Tensile effective stresses are the result of the development of very high pore fluid pressure within the

injection zone. It should be noted that there is no established fracture initiation criterion for tensile or shear fracture mode for oilsands. Even for mode *I*, some researchers believe that due to thermal effects in a real hydraulic fracturing treatment, high temperature causes the oilsand to behave in a plastic manner and any created fracture would be 'blunt' rather than 'sharp'. Therefore application of Griffiths' or Irwin's theories using fracture toughness (K_{IC}) as a tensile fracture initiation criterion may not be reasonable. Hence, a more accurate representation of the fracture pattern in uncemented oilsand would be possible, if a more appropriate fracture mechanics criterion is implemented in the numerical model.

Phase	Test No.	Ver. stress (kPa)	Hor. Stress (kPa)	Pore Fluid Press. (kPa)	Ko	Inj. Rate (ml/s)	Inj. Volume (ml)	Permea-bility (Darcy)	Inject -ivity	Steady state Frac. tests
1	1	400	600	-	-	96.0	927	-	-	-
1	2	Test	abort	-	-	-	-	-	-	-
1	3	460	493	432	2.2	93.5	907	-	-	-
1	4	400	600	200	2.0	20.0	80	-	-	-
1	5	400	600	200	2.0	5.0	20	-	-	-
1	6	400	600	200	2.0	5.0	18	1.5	200 200	-
1	7	400	600	200	2.0	10.0	40	4.4	200	-
1	8	600	400	200	0.5	10.0	40	2.8	200	-
2	1	400	600	200	2.0	Const. Press. 280 kPa	500	4.0 2.8 3.2	240 280 360	-
2	2	400	600	200	2.0	0.4	200	3.9 4.3 4.3	240 280 360	0.28 0.40 1.00 0.25
2	3	400	600	200	2.0	30	200	5.6 5.4	240 280 360	1.0 3.0 10.0 30.0 3.0
2	4	400	600	200	2.0	30	250	4.9 4.6	240	-
2	5	400	600	200	2.0	200	260	5.9 6.4	240	-
3	1	500	600	100	1.25	41	900	5.6 5.8 6.3	140 180 260	-
3	2	400	600	200	2.0	41	900	5.0	240	-
3	3	400	600	200	2.0	200	900	5.5 6.8	-	-
3	4	500	800	200	2.0	200	900	4.7	-	-
3	5	400	600	200	2.0	200	900	4.2	-	-
3	6	400	600	200	2.0	200	300	3.7	-	-

Table (7-1) Summary of Hydraulic Fracture Test Program

(Phase 1,2 and 3 from report of Golder Associates 1994)

	Chamber test #4 (phase 2)
mass coefficient ($kN/m.sec^{-2}$)	0.00
damping coefficient ($kN/m.sec^{-1}$)	0.00
soil/rock thermal expansion (1/°C)	-
fluid thermal expansion (1/°C)	-
fluid compressibility (kPa^{-1})	0.3×10^{-5}
soil heat capacitance (J/m^3 .°C)	-
fluid heat capacitance (J/m^3.°C)	-
thermal conductivity (J/sec.m.°C)	-
soil density (ton/m^3)	2.0
fluid density (ton/m^3)	1.33
fluid viscosity (kPa.sec)	1.49×10^{-3}
absolute permeability (m^2)	4.48×10^{-12}-4.48×10^{-10}
modulus of elasticity (kPa)	41050.0
Poisson's ratio	0.25
acceleration of gravity (m/sec^2)	9.81
initial porosity	0.48
θ	1.00

Table(7-2) Input data for modeling of fracture in chamber test

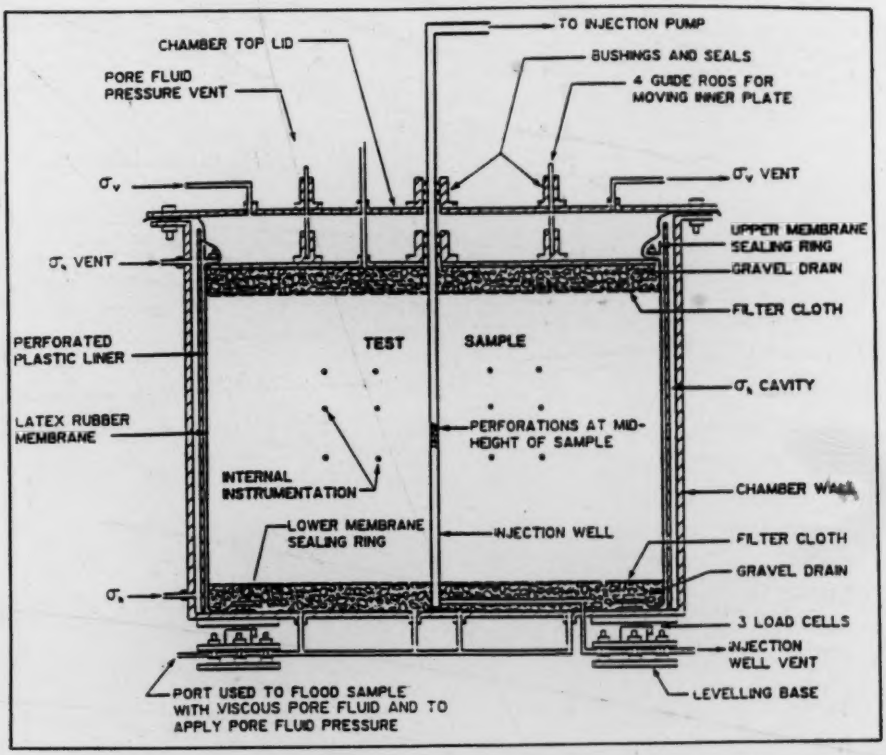

Figure (7-1) Schematic view of Large Scale Triaxial Chamber (Not to Scale) from Golders Associates Report (1991-1994)

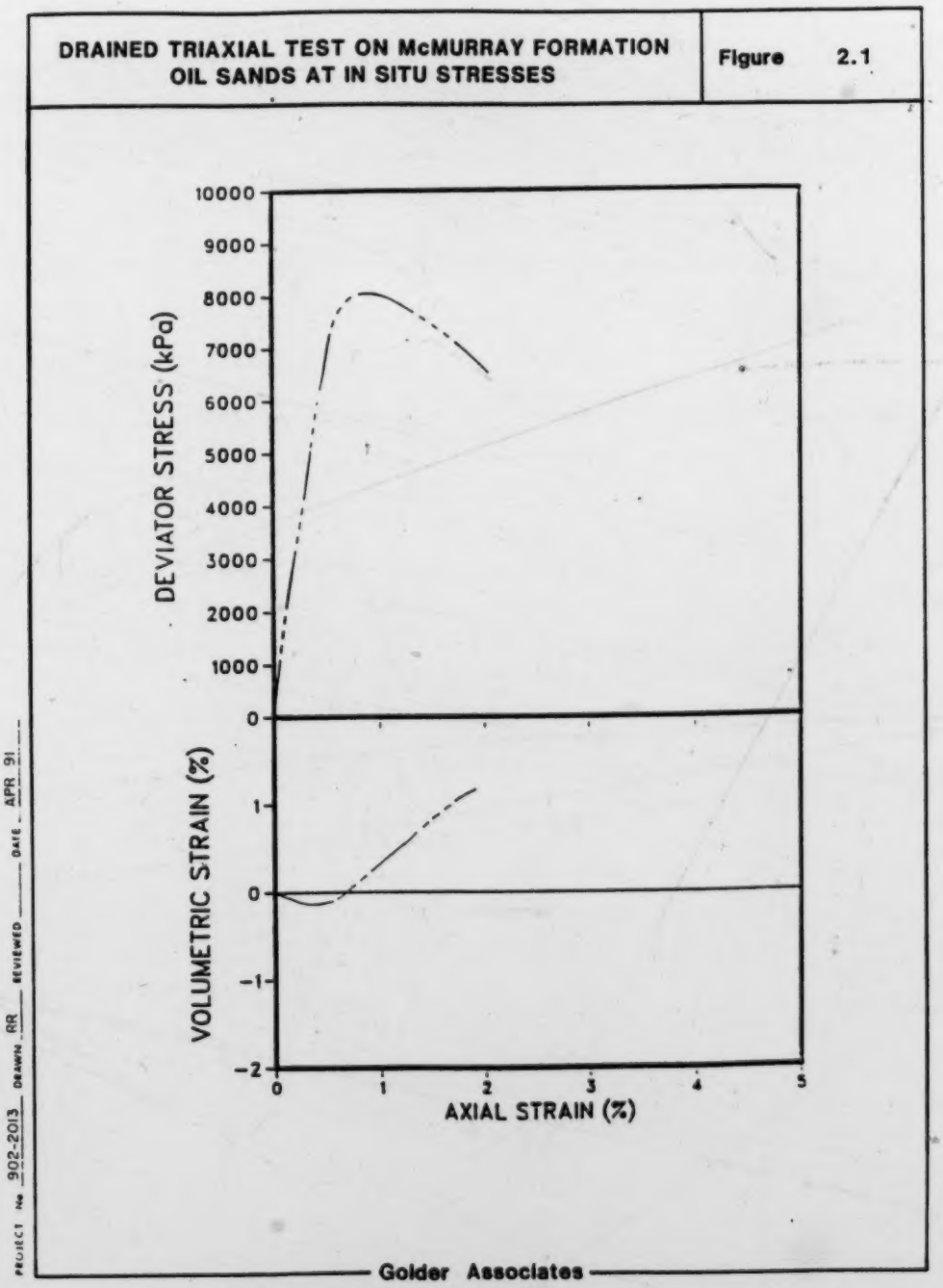

Figure (7-2) Typical drained triaxial test on McMurray oilsand
Reproduced from Golder Ass. Report (1991)

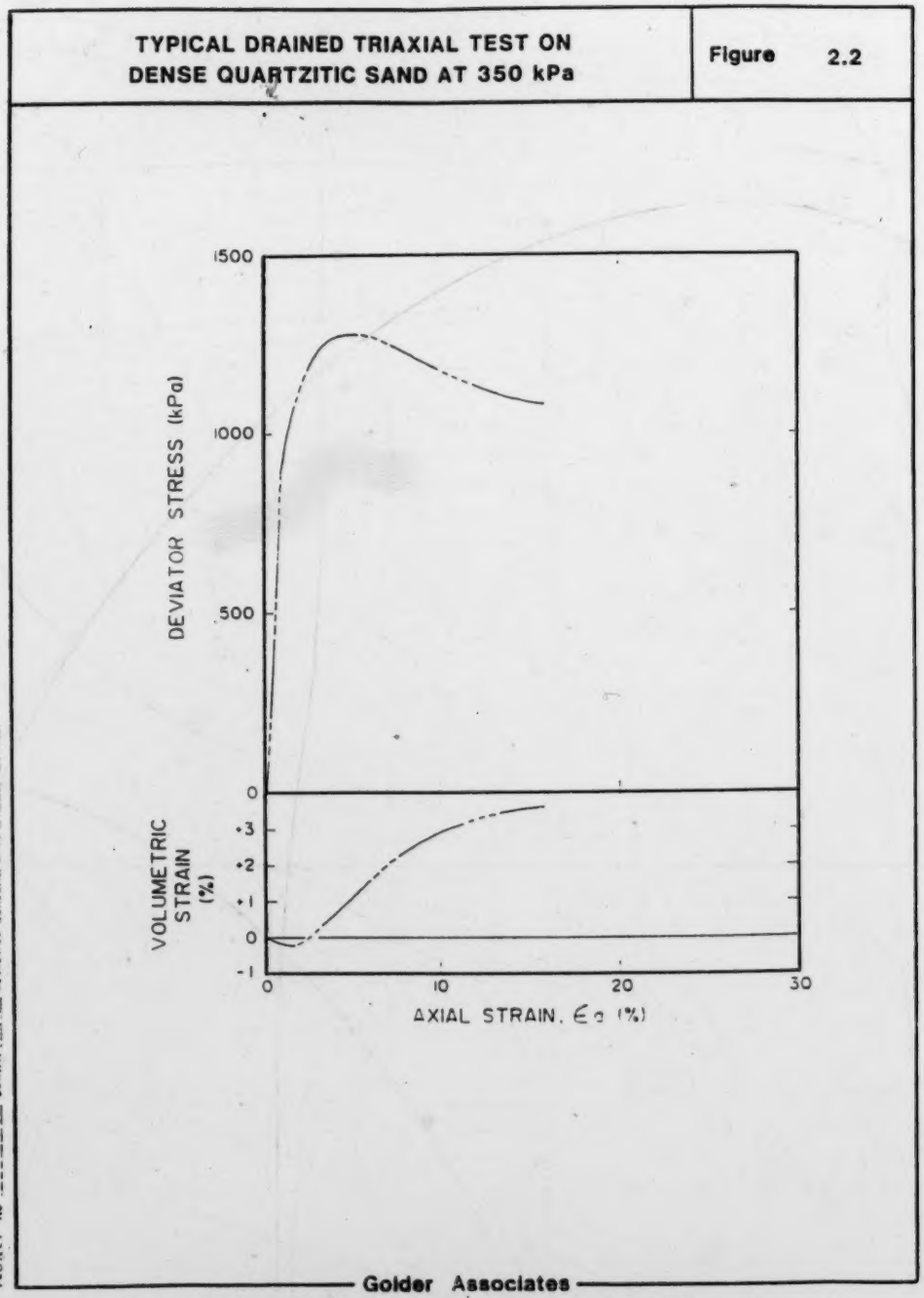

Figure (7-3) Typical drained triaxial test on Lane Mountain sand
Reproduced from Golder Ass. Report (1991)

Figure (7-4) 'p-q' diagram for Lane Mountain sand
(Results of small scale triaxial tests from Golder Ass. 1994)

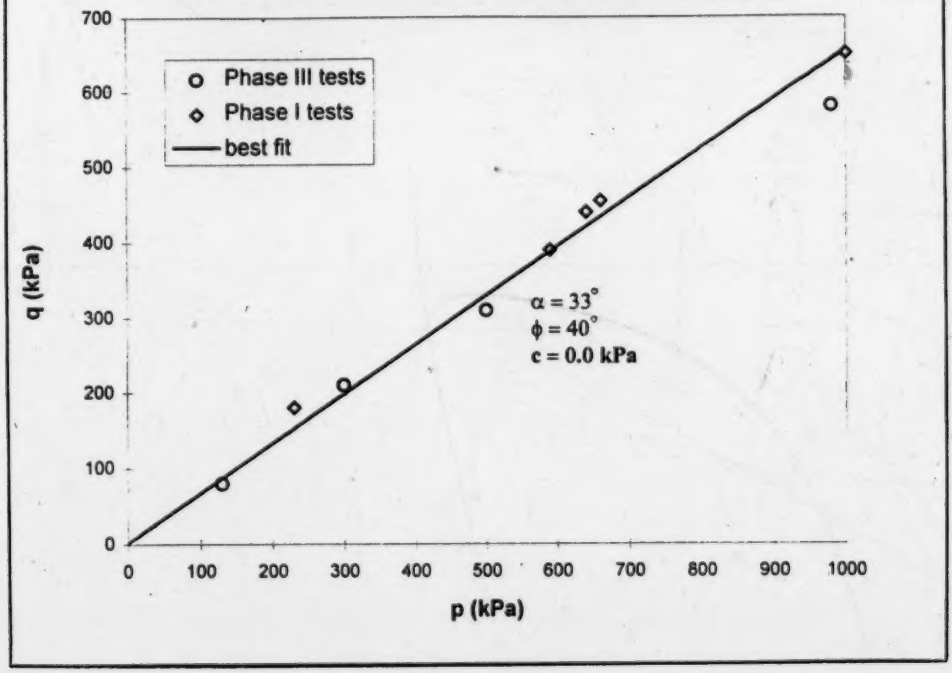

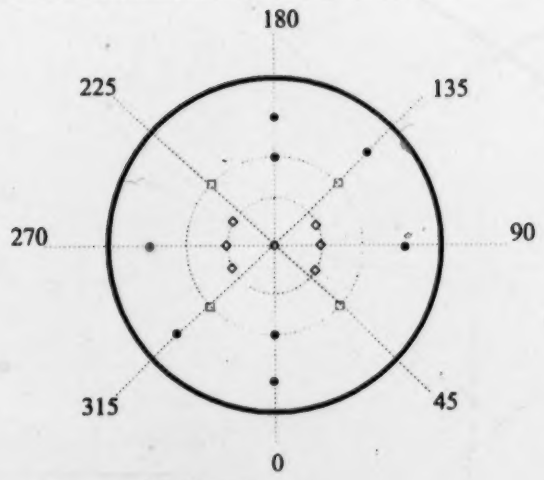

Figure (7-5) Plan view of instrumentation around the injection zone

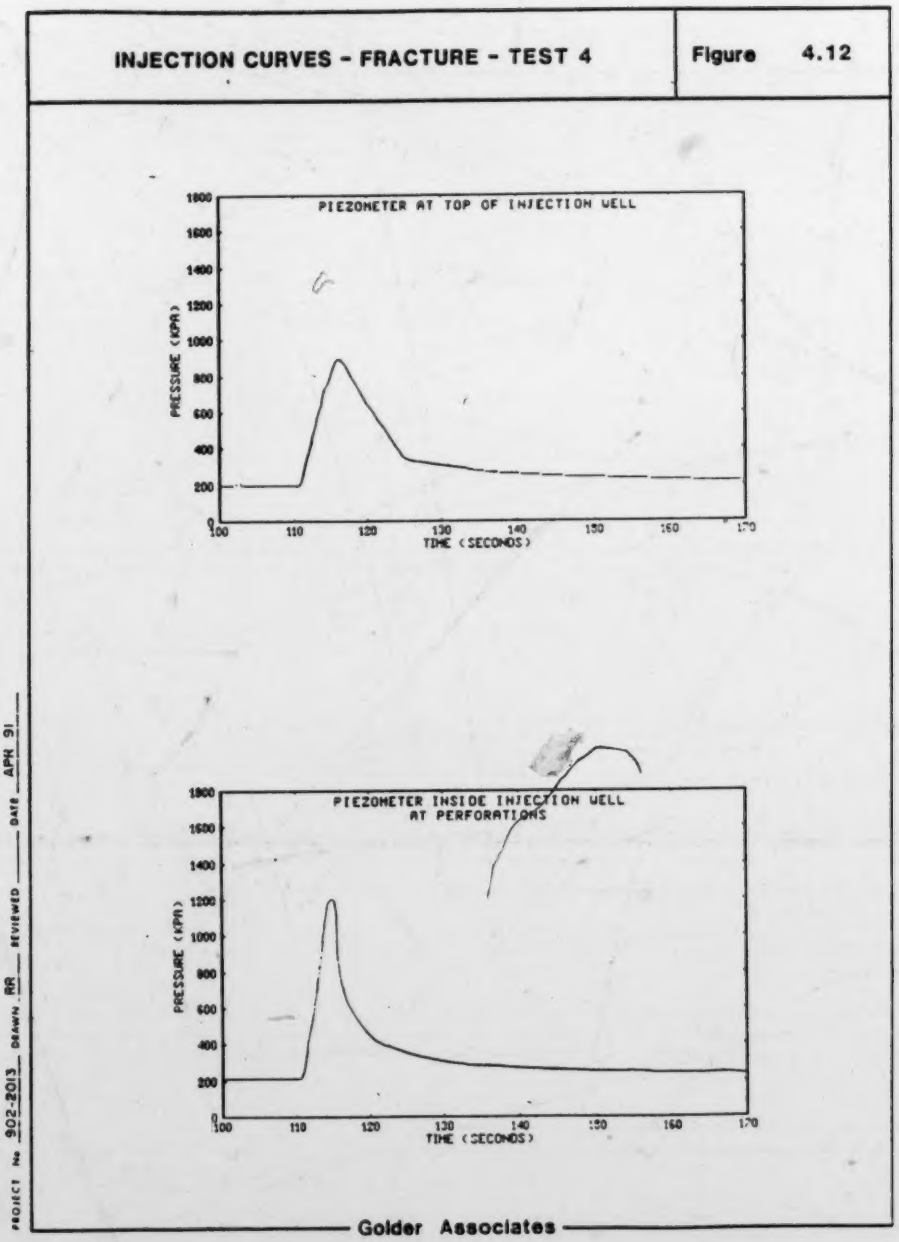
INJECTION CURVES - FRACTURE - TEST 4
Figure 4.12
PIEZOMETER AT TOP OF INJECTION WELL
PRESSURE (KPA)
TIME (SECONDS)
PIEZOMETER INSIDE INJECTION WELL AT PERFORATIONS
PRESSURE (KPA)
TIME (SECONDS)
PROJECT No 902-2013 DRAWN RR REVIEWED DATE APR 91
Golder Associates

Figure (7-6) Response of Piezometers in test #4 of Phase I

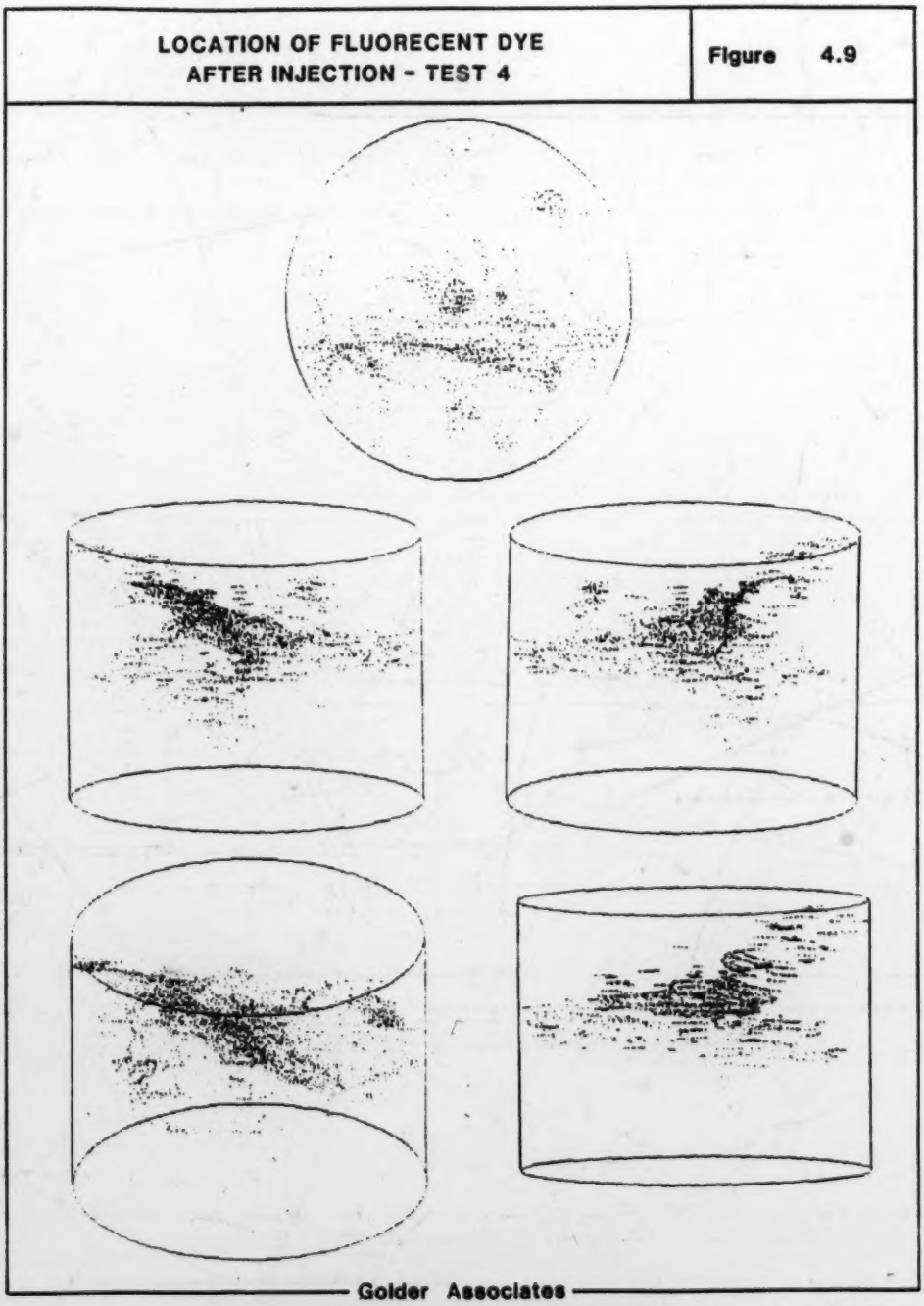
LOCATION OF FLUORECENT DYE
AFTER INJECTION - TEST 4
Figure 4.9
PROJECT No. 902-2013 DRAWN RR REVIEWED DATE APR 91
Golder Associates

Figure (7-7) Fracture Pattern, test #4 of phase I

Reproduced from Golder Ass. Report (1991)

FRACTURE TEST No. 5
RESPONSE OF FLUID PRESSURE TRANSDUCERS

Figure 3.11

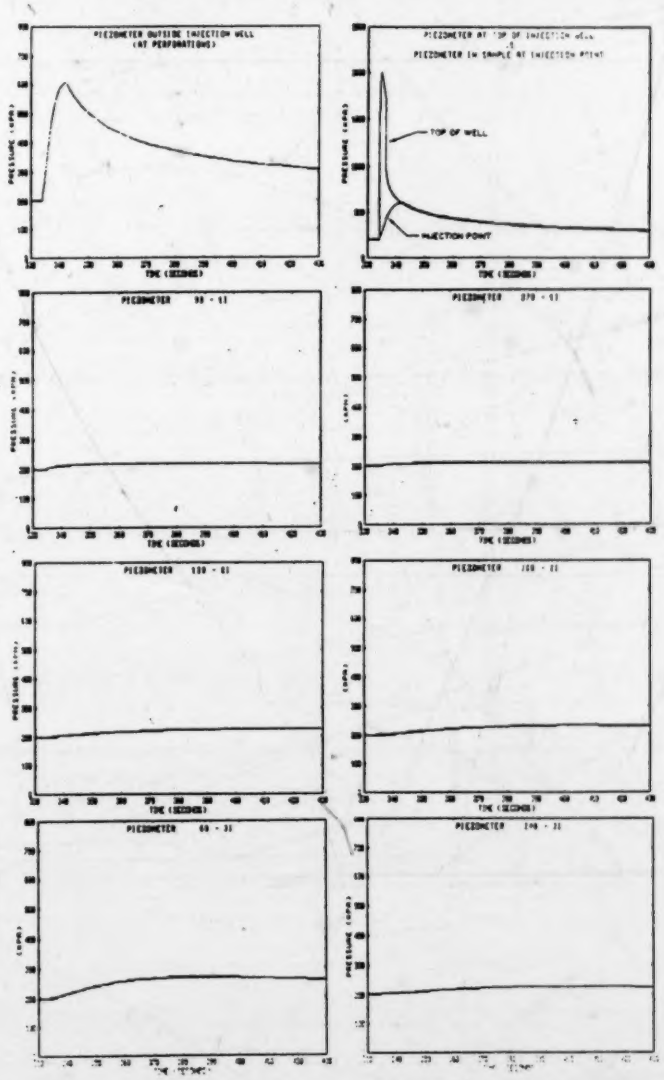

PROJECT No. 912-2055 DRAWN RR REVIEWED KHK DATE APR 92

Golder Associates

Figure (7-8) Response of piezometers, test #5 of phase II
Reproduced from Golder Ass. Report (1992)

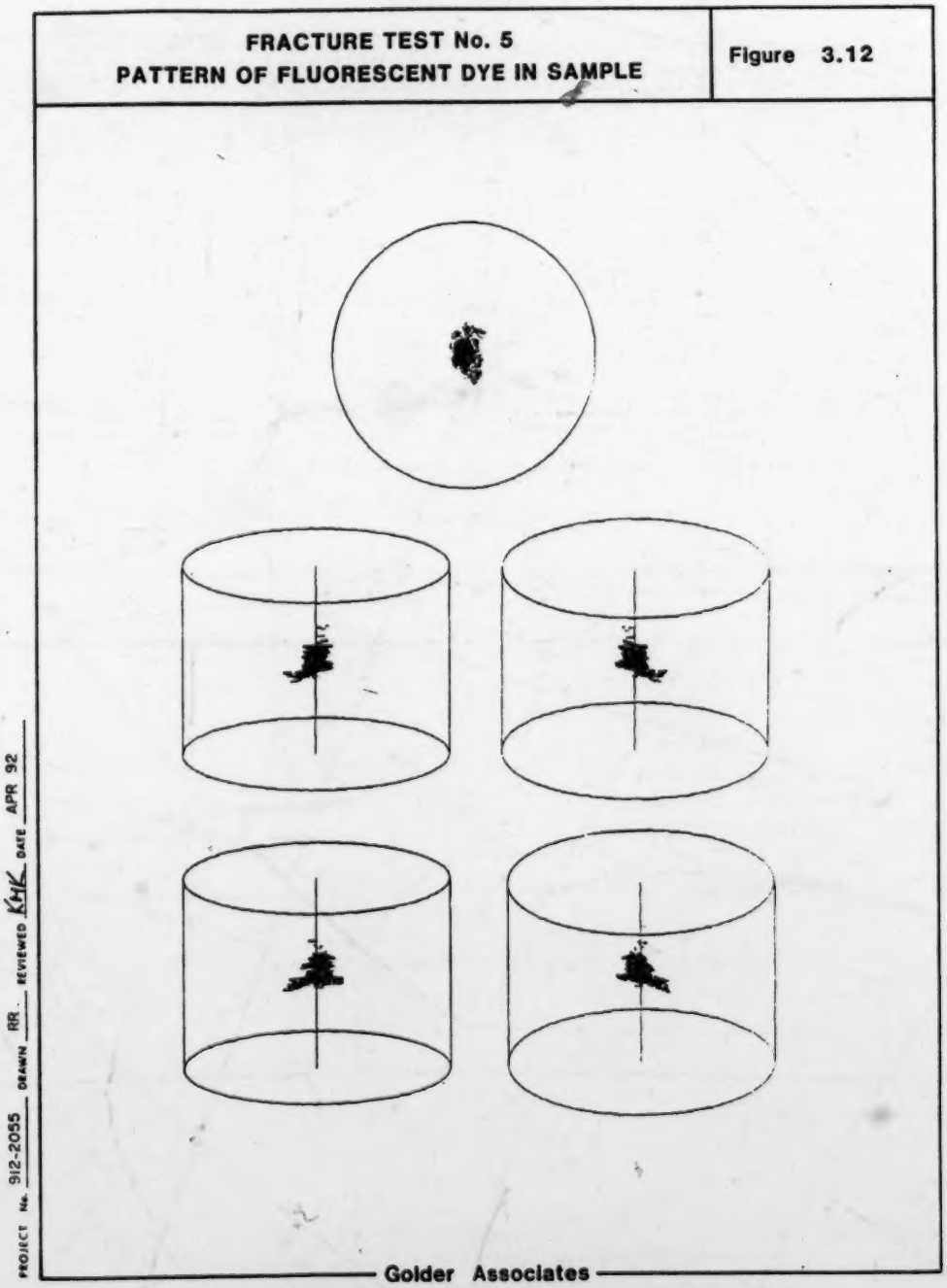
FRACTURE TEST No. 5
PATTERN OF FLUORESCENT DYE IN SAMPLE
Figure 3.12
PROJECT No. 912-2055 DRAWN RR REVIEWED KHK DATE APR 92
Golder Associates

Figure (7-9) Fracture Pattern, test #5 of phase II

Reproduced from Golder Ass. Report (1992)

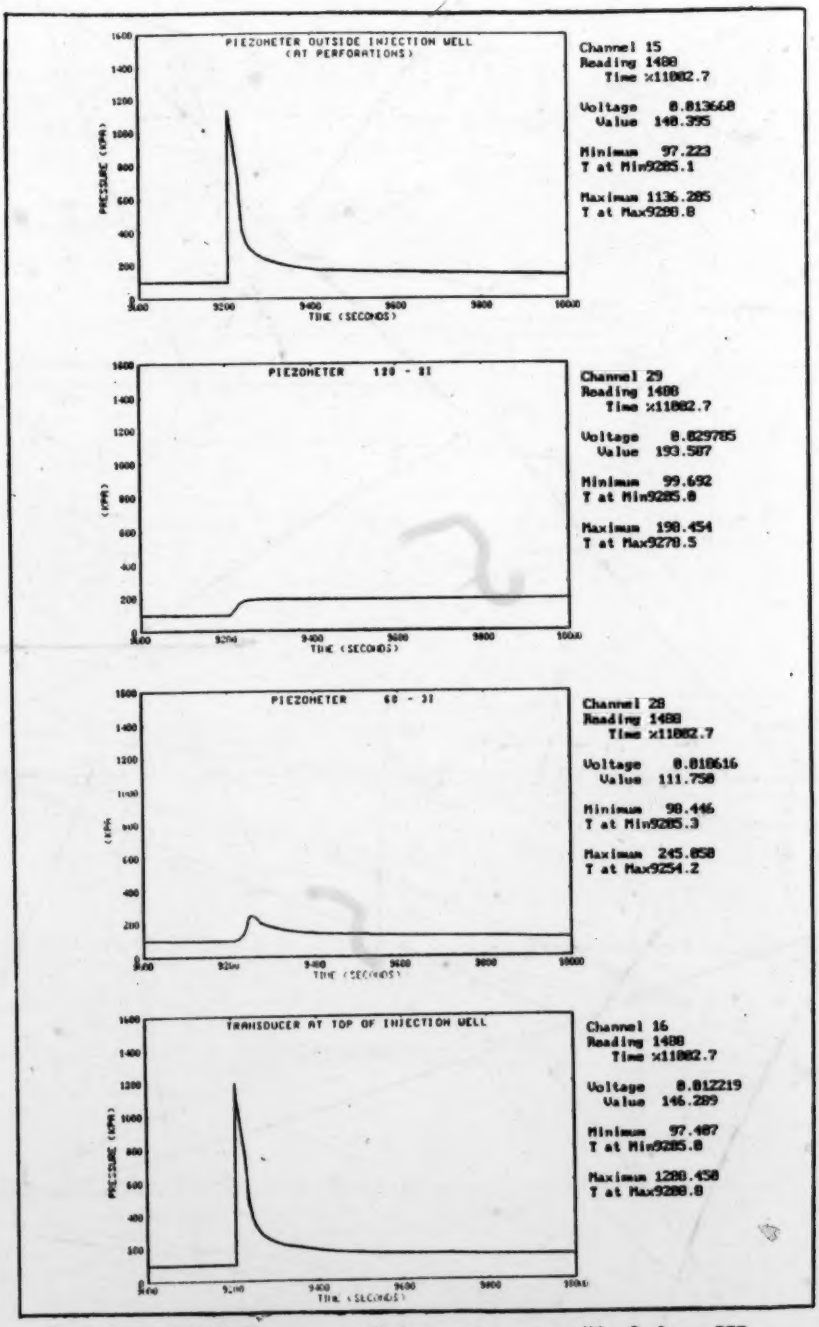

Figure (7-10) Response of piezometers, test #1 of phase III
Reproduced from Golder Ass. Report (1994)

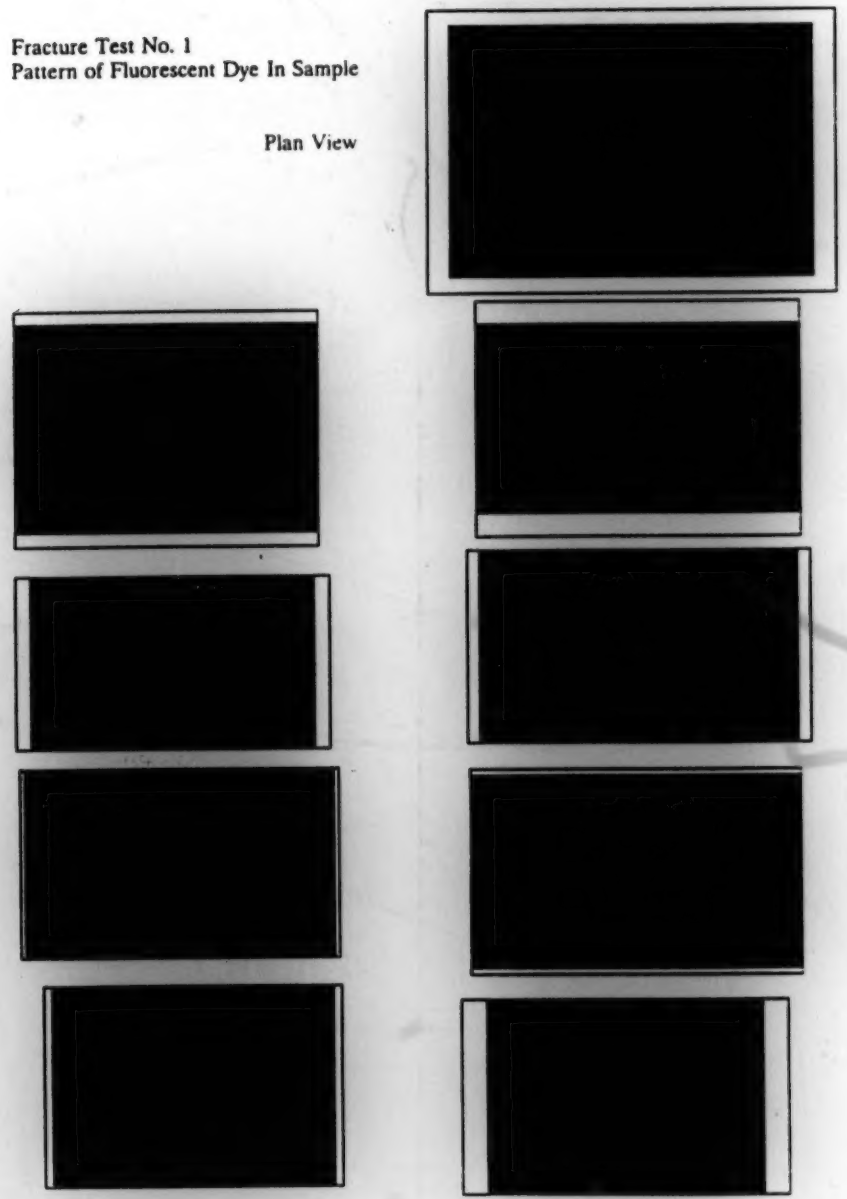

Figure (7-11a) Fracture Pattern, test #1 of phase III

Reproduced from Golder Ass. Report (1994)

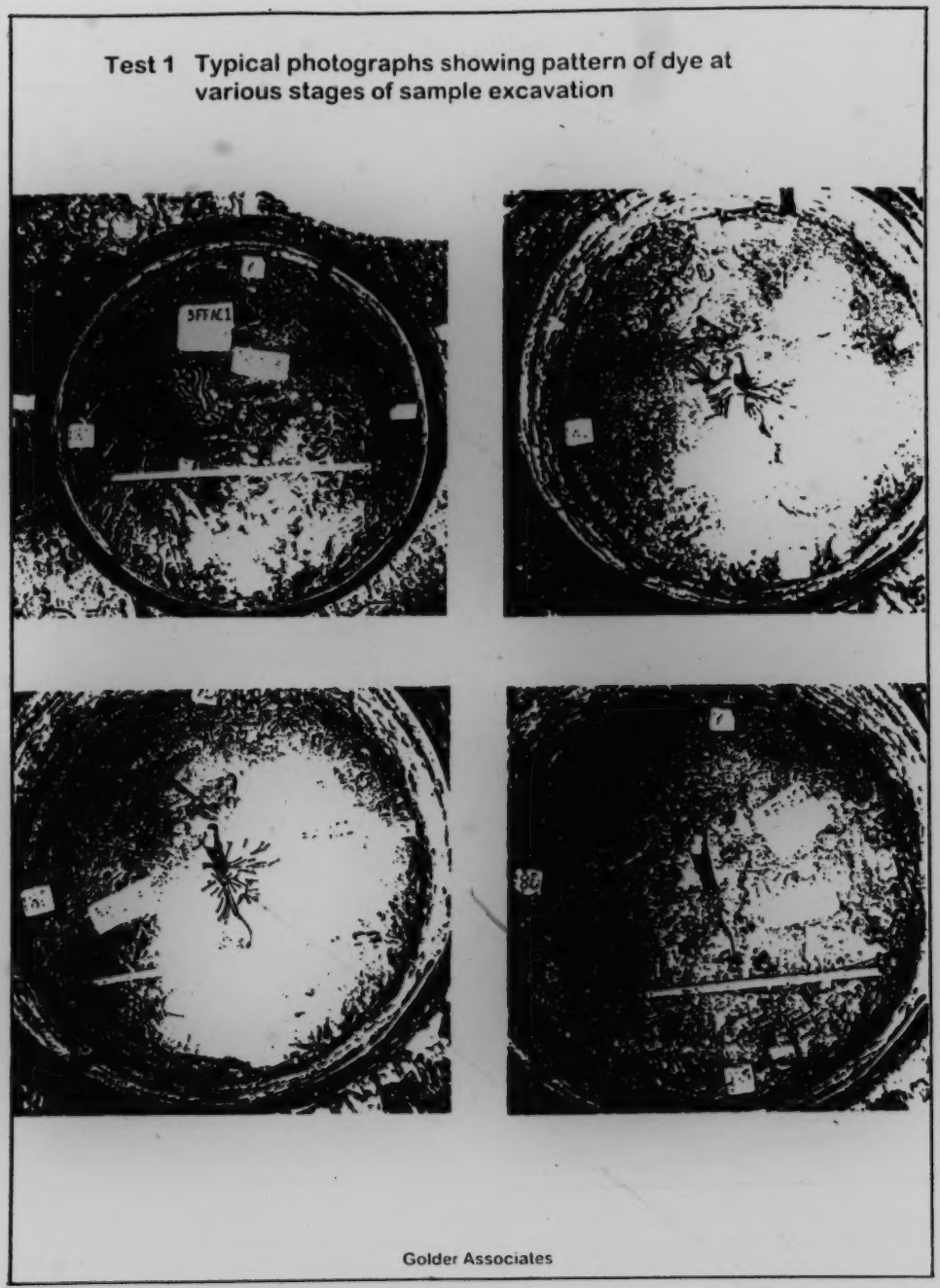

Figure (7-11b) Typical Photographs showing fracture pattern, test #1 of phase III

Reproduced from Golder Ass. Report (1994)

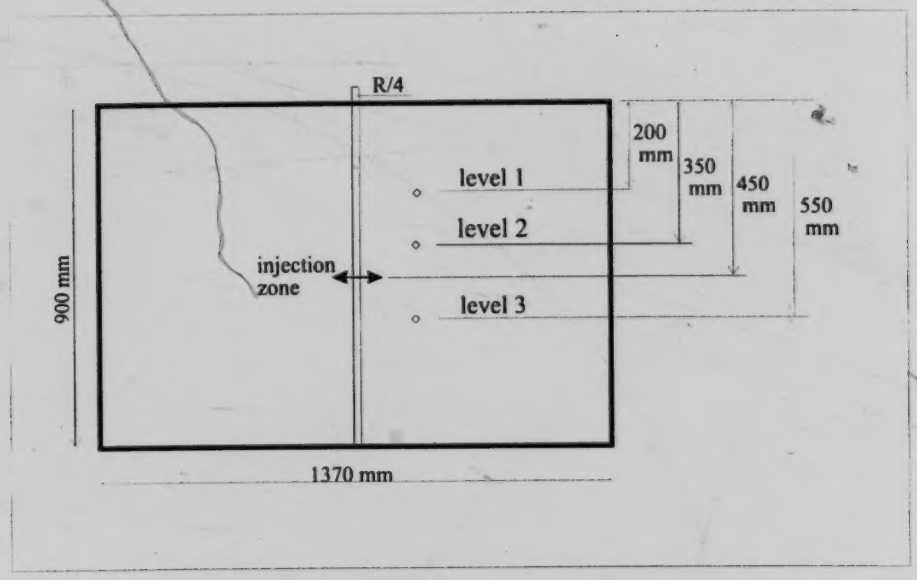

Figure (7-12) Sample dimensions and position of piezometers for test #4 of phase 2 of the experiments

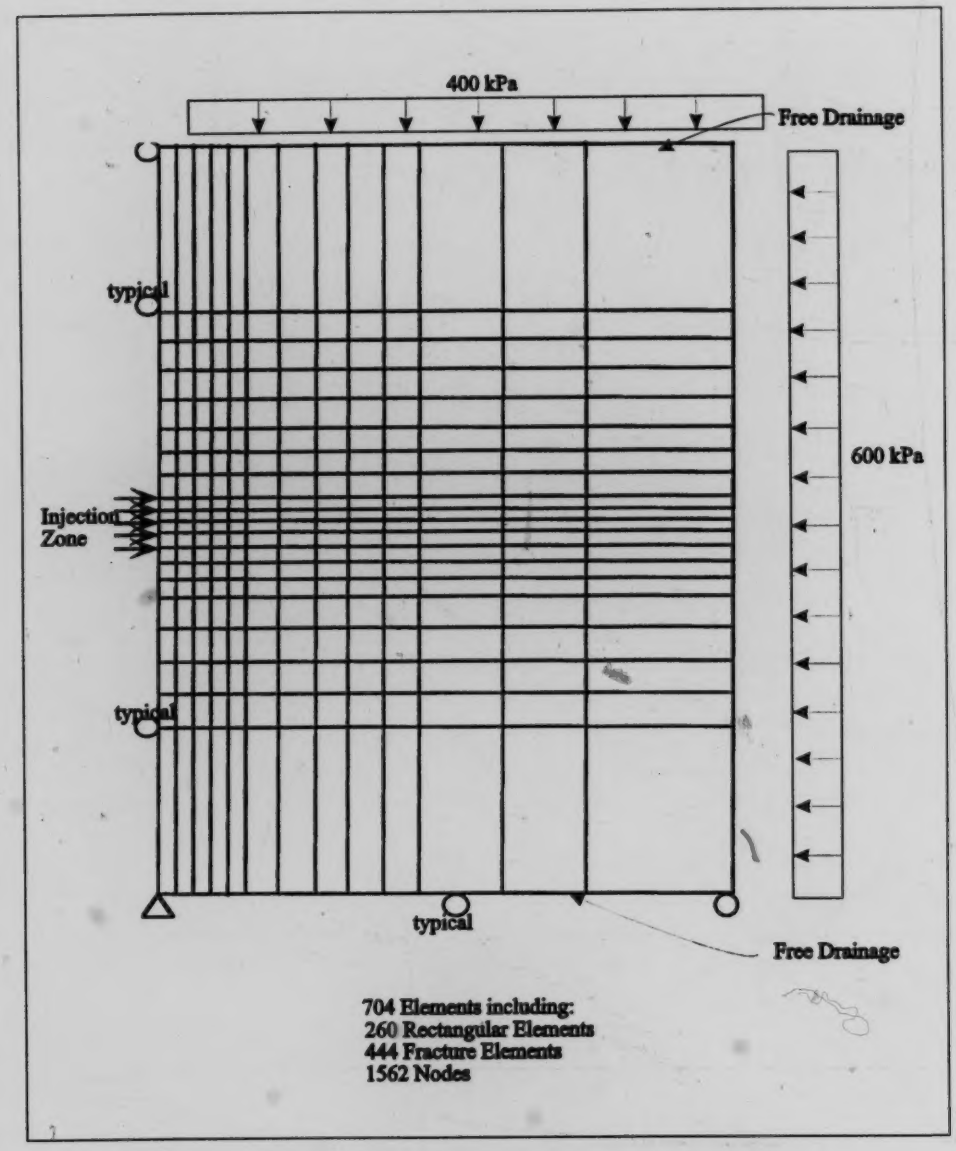

Figure (7-13) Finite Element Mesh and Boundary Conditions for Modeling Test 4 of Phase 2

Figure (7-14) Comparison between calculated and measured pore pressures (piezometer: at injection zone)

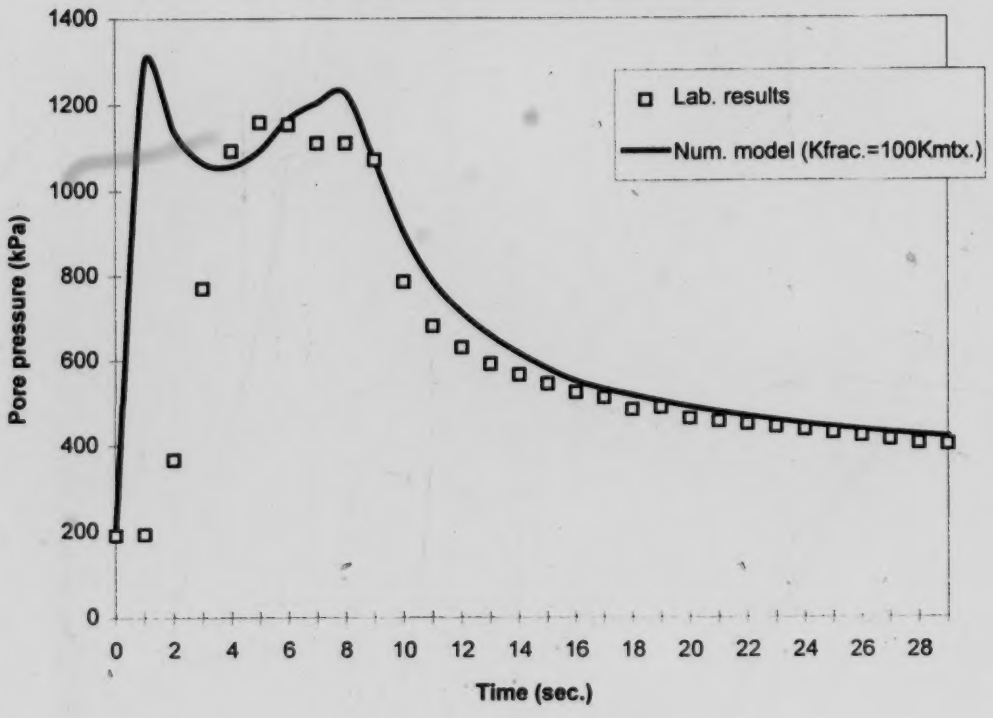

Figure (7-15) Comparison between calculated and measured pore pressures (piezometer: 100 mm above the injection zone)

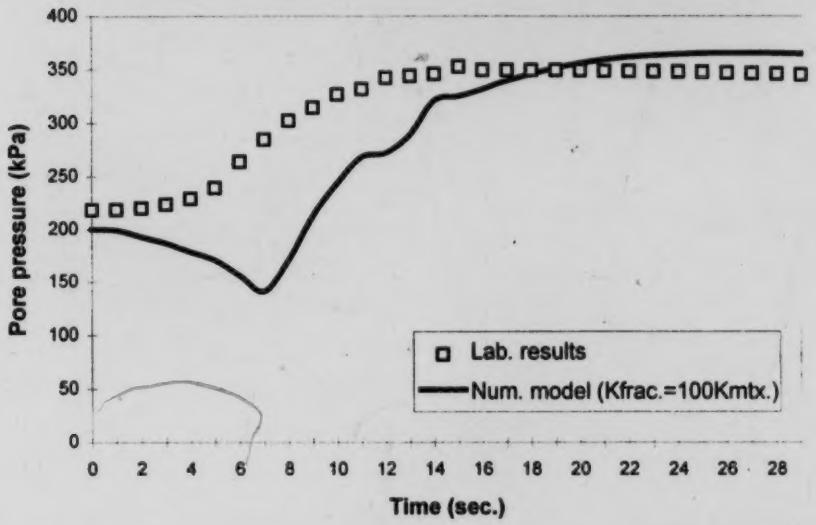

Figure(7-16) Comparison between calculated and measured pore pressures (piezometer: 100 mm below the injection zone)

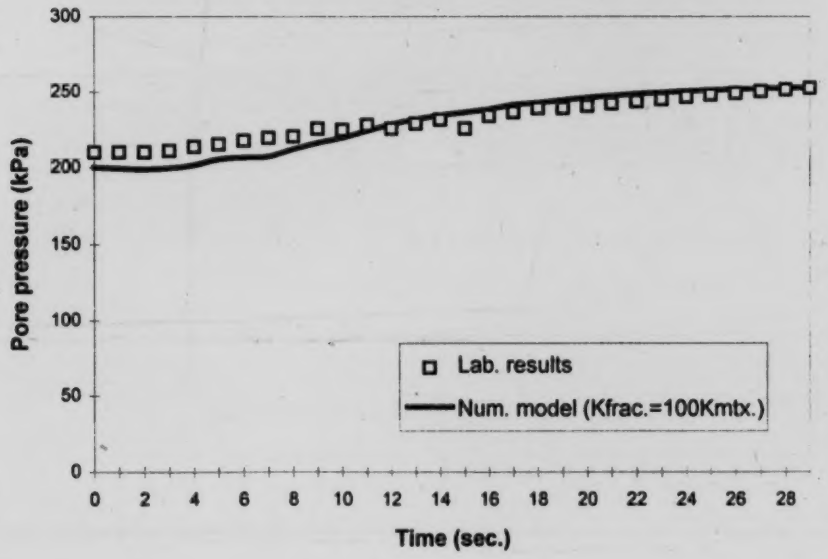

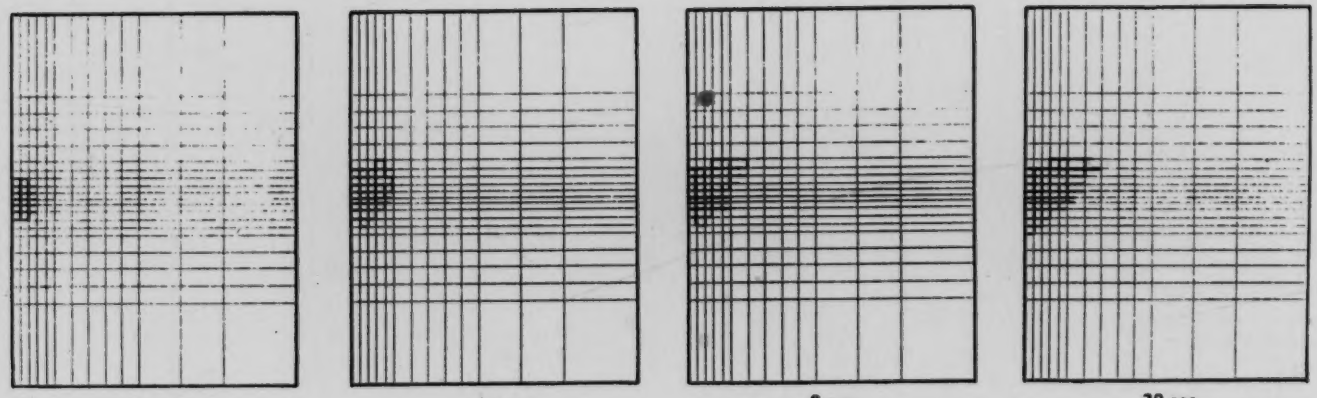

Figure (7-17) Pattern of Fracture Propagation from Numerical Model

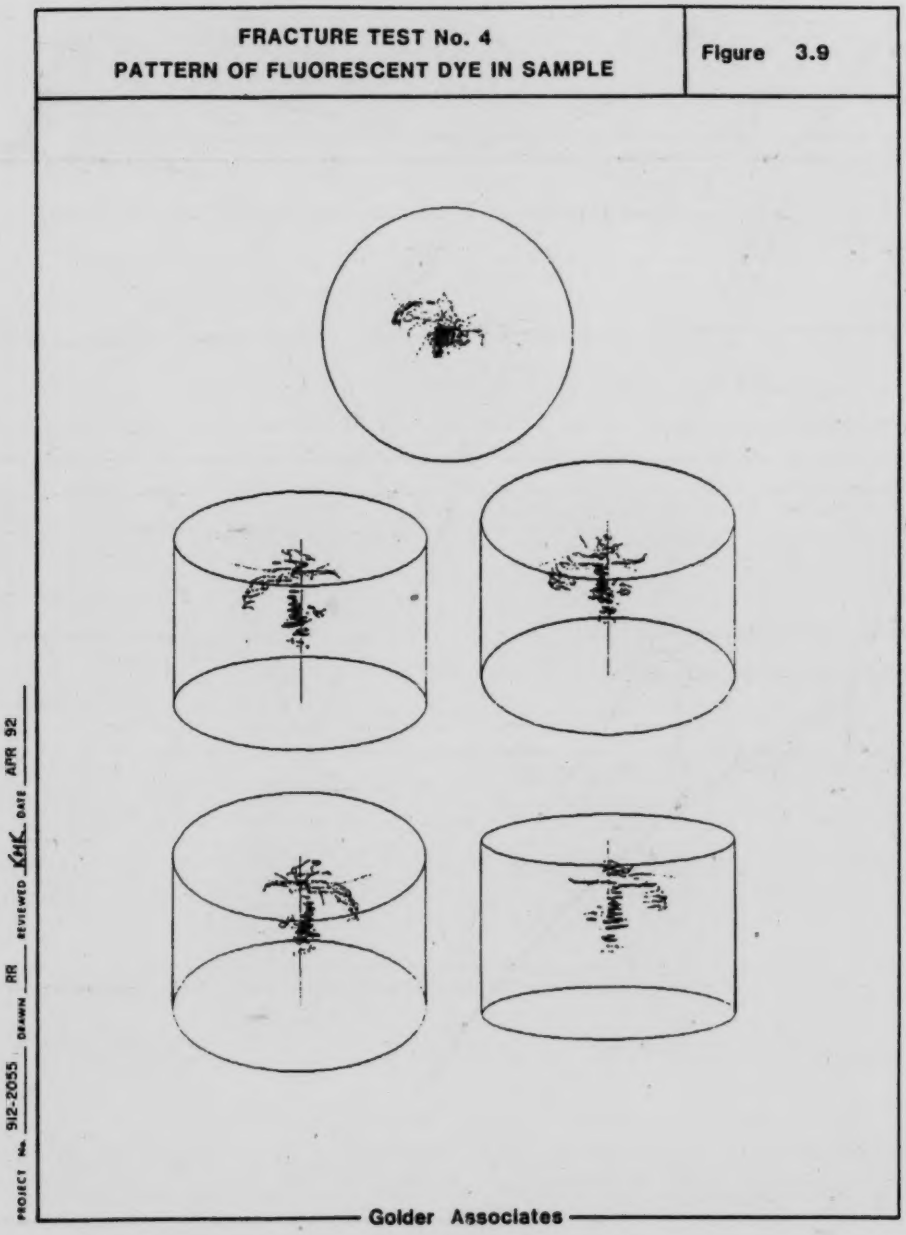
FRACTURE TEST No. 4
PATTERN OF FLUORESCENT DYE IN SAMPLE
Figure 3.9
PROJECT No. 912-2055 DRAWN RR REVIEWED KHK DATE APR 92
Golder Associates

Figure (7-18) Fracture Pattern from Laboratory Experiment
Reproduced from Golder Ass. Report (1992)

Figure (7-29) Pore pressure variation at the injection zone with associated Mohr-Coulomb model

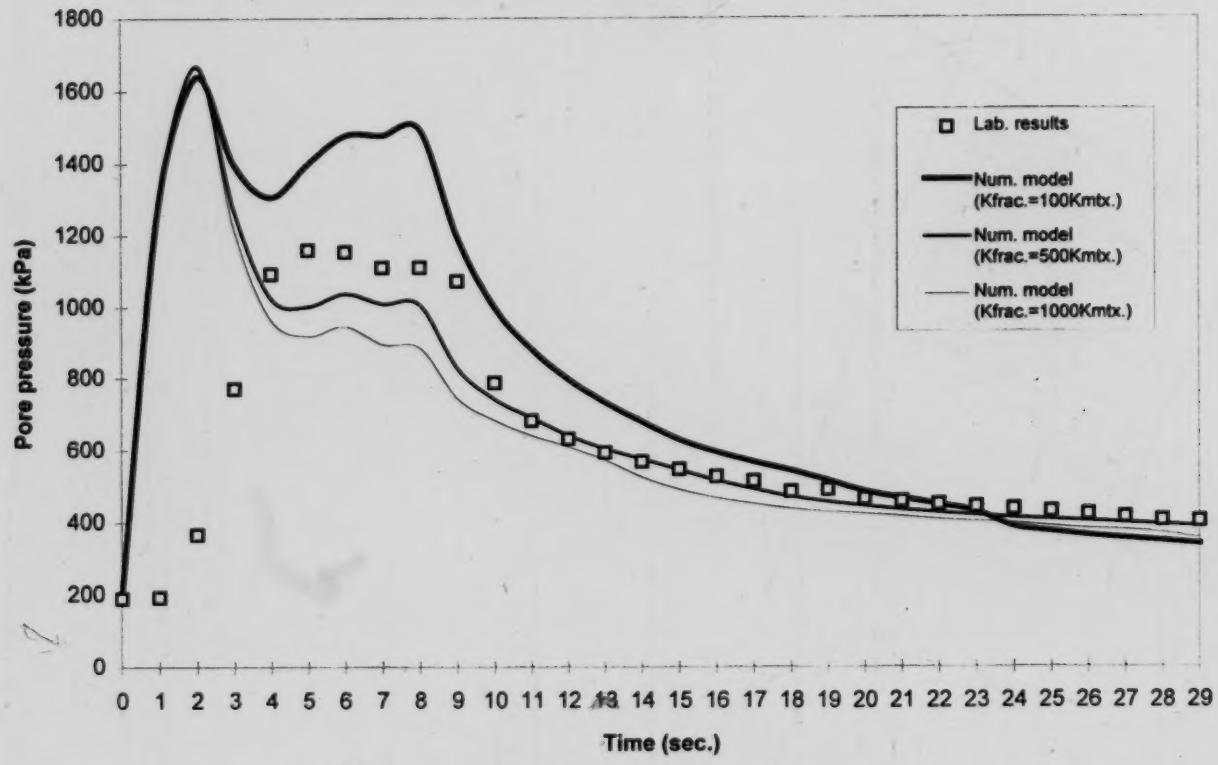

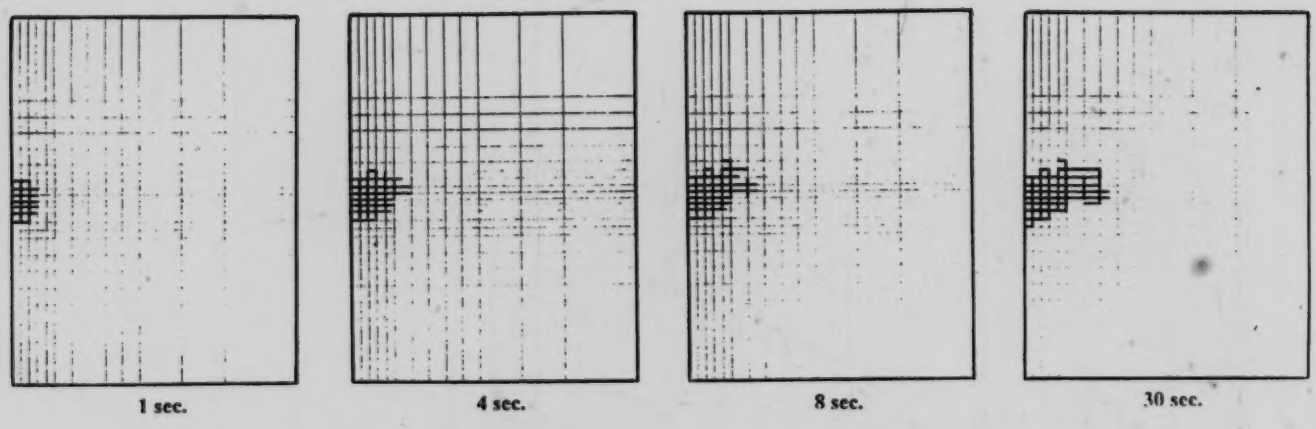

Figure (7-20) Pattern of Fracture Propagation from Numerical Modeling

(K_{frac}=500 K_{mtx})

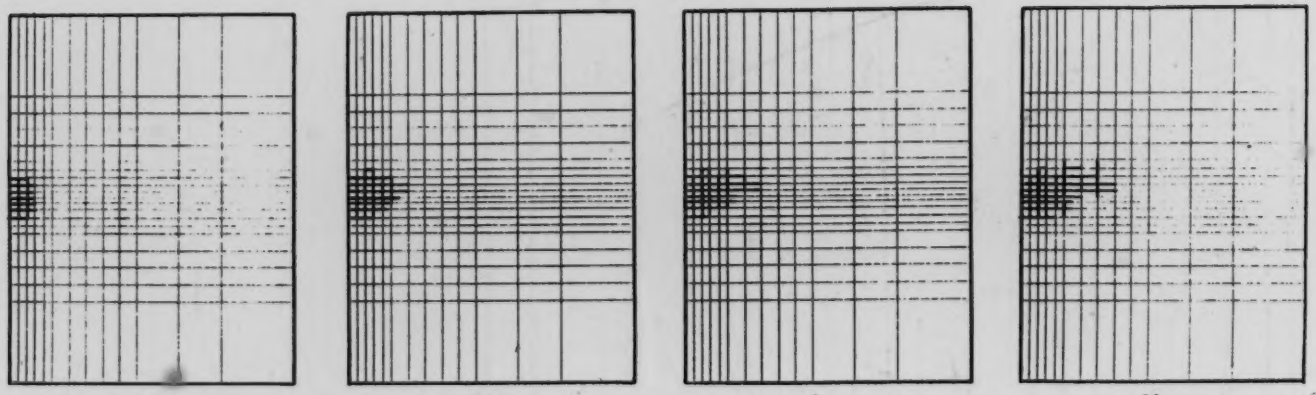

Figure (7-21) Pattern of Fracture Propagation from Numerical Modeling

(K_{frac}=1000 K_{mtx})

Figure(7-22) Pore pressure variation with different permeabilities for fracture elements
(piezometer: 100 mm above the injection zone)

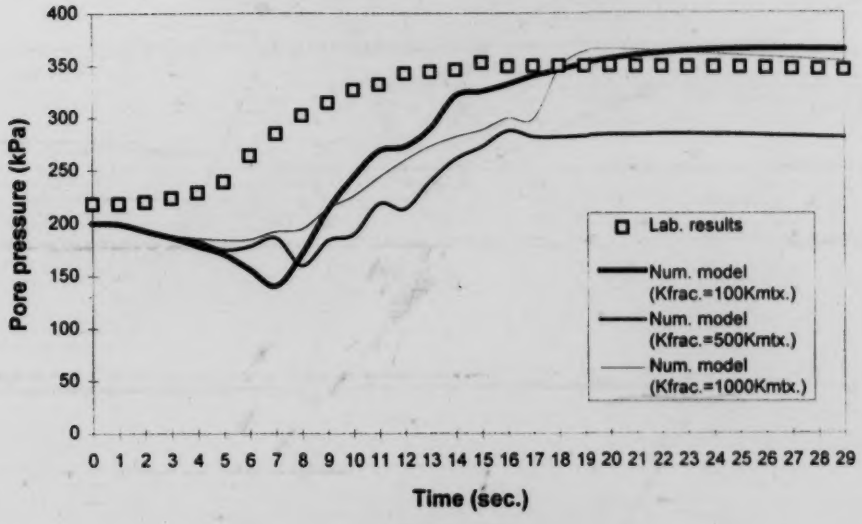

Figure(7-23) Pore pressure variation with different permeabilities for fracture elements
(piezometer: 100 mm below the injection zone)

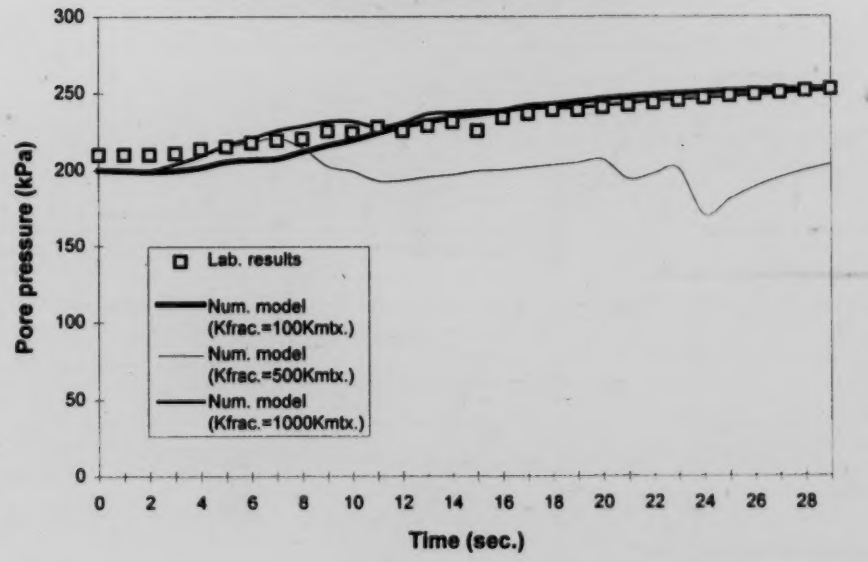

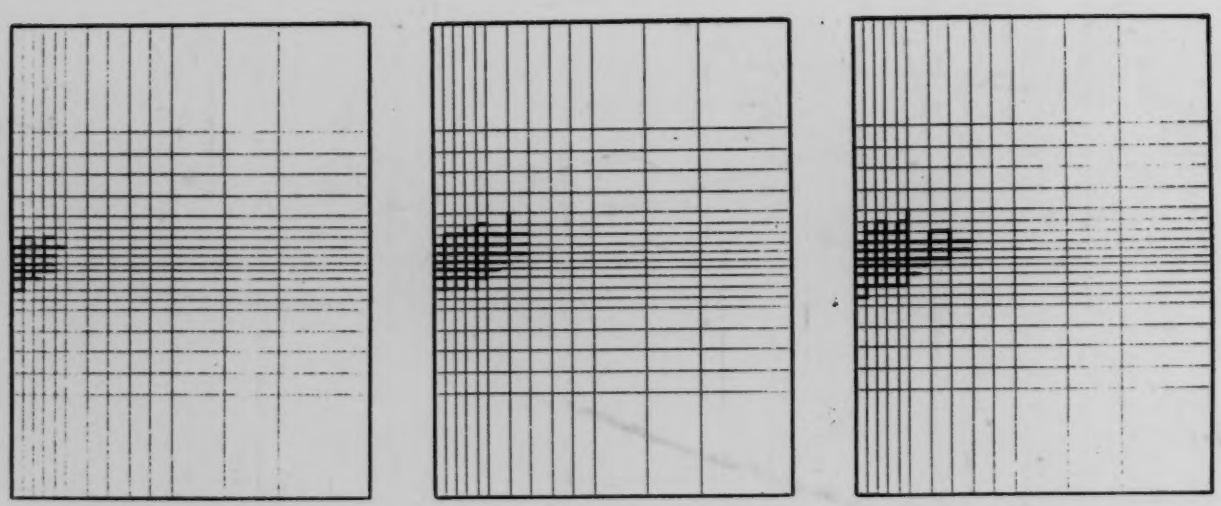

K_{frac}=100 K_{mtx} (at 30 sec.) K_{frac}=500 K_{mtx} (at 30 sec.) K_{frac}=1000 K_{mtx} (at 30 sec.)

Figure (7-24) Fracture Pattern with Prescribed Pore Pressure

(Simulating Lab. Recorded Pore Pressures)

Figure (7-25) Pore pressure variation with changing permeability of soil matrix

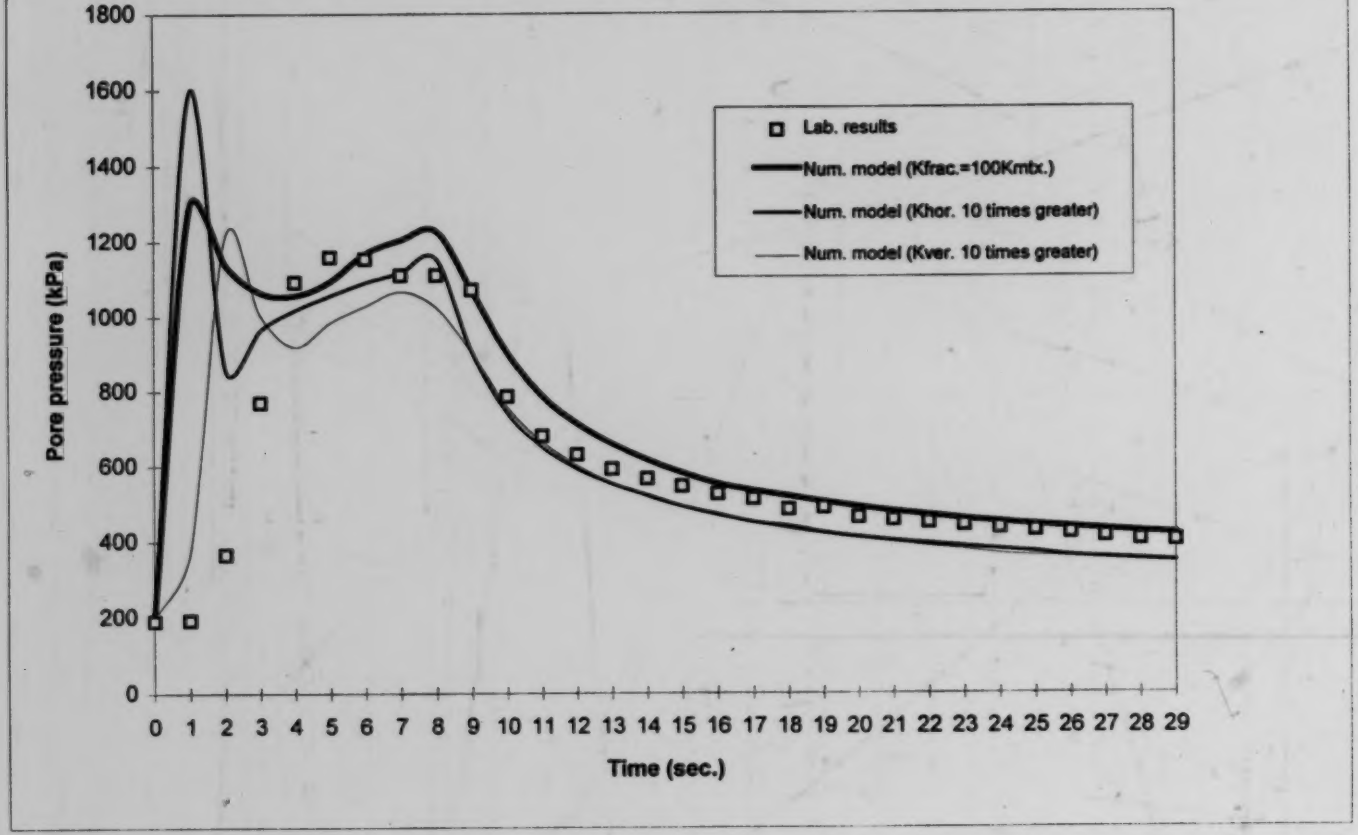

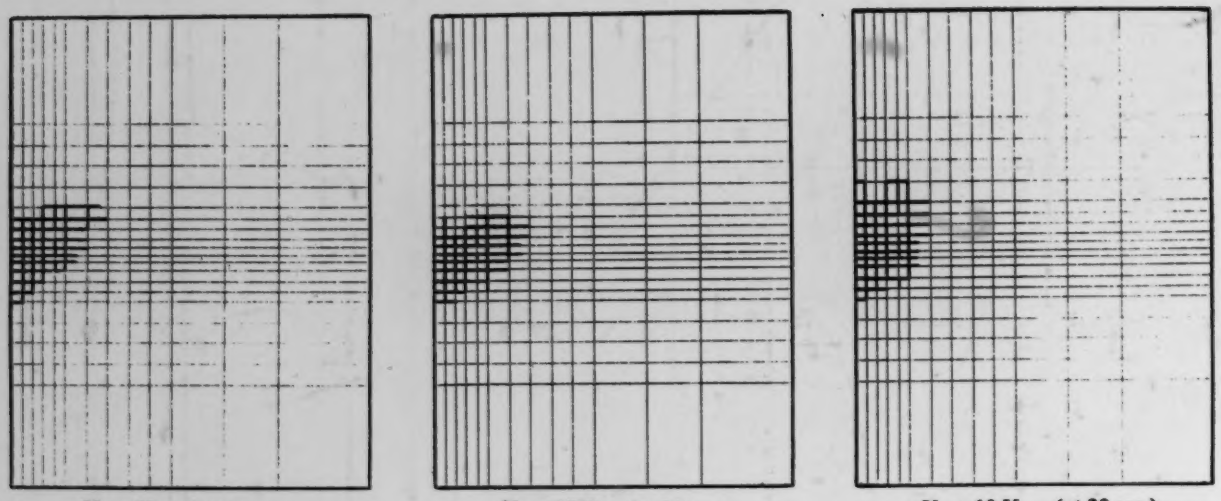

Figure (7-26) Fracture Pattern with Change in Permeability of Soil Matrix

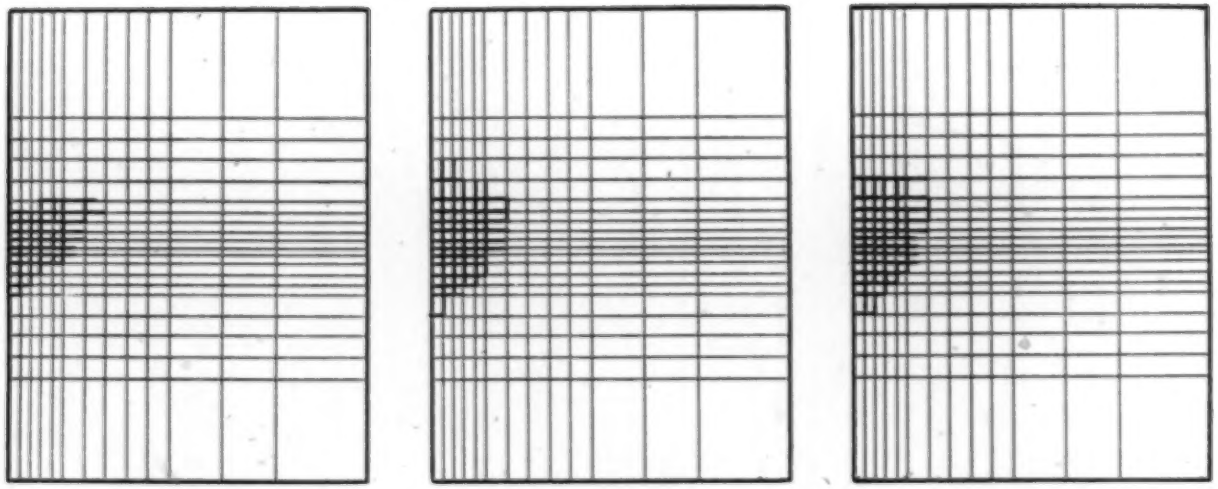

Figure (7-27) Pattern of fracture at 30 seconds with different fracture criteria

Figure (7-28) Pore pressure variation at the injection zone with different fracture criteria

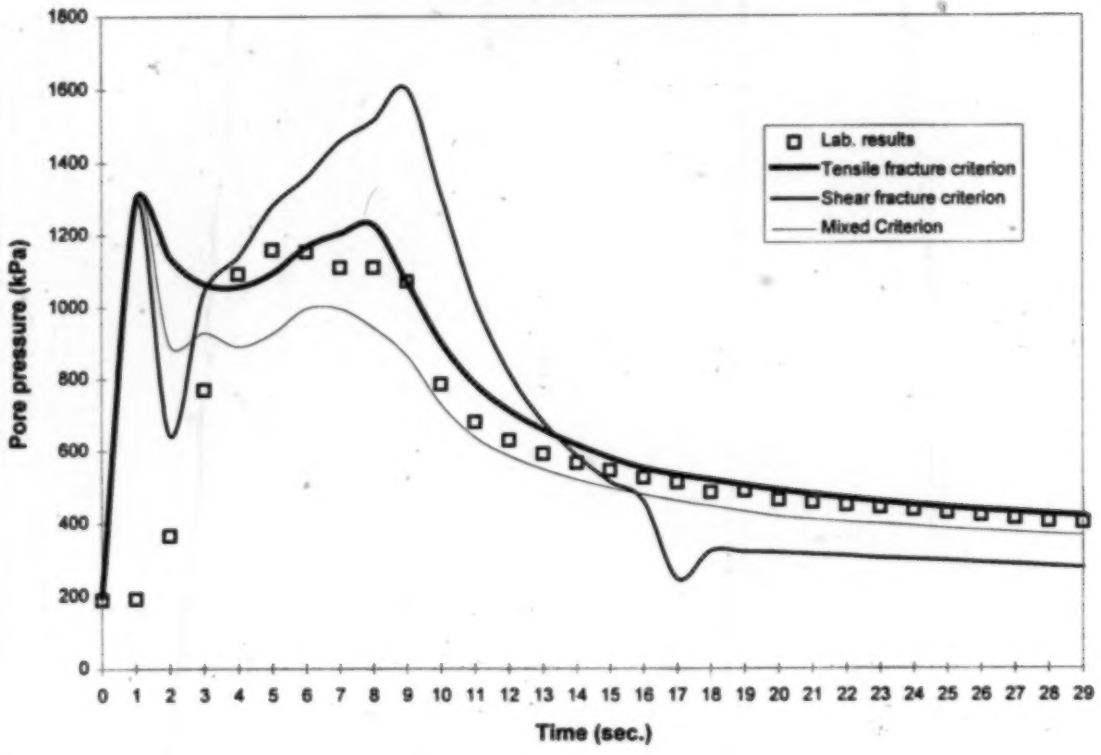

Figure (7-19) Pore pressure variation at the injection zone with different permeabilities for fracture elements

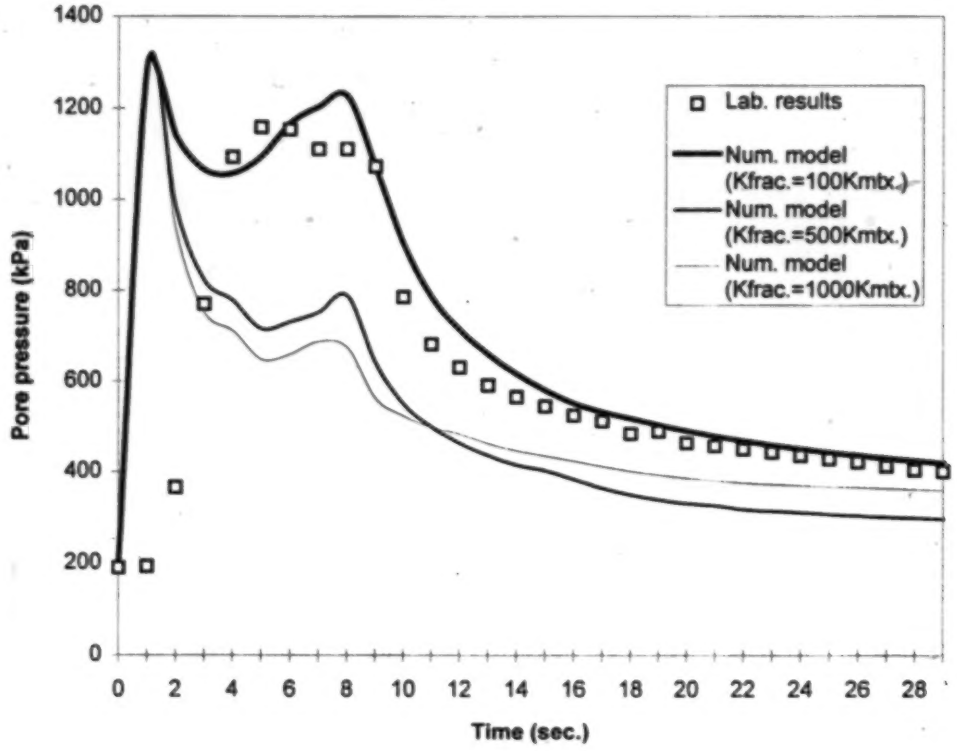

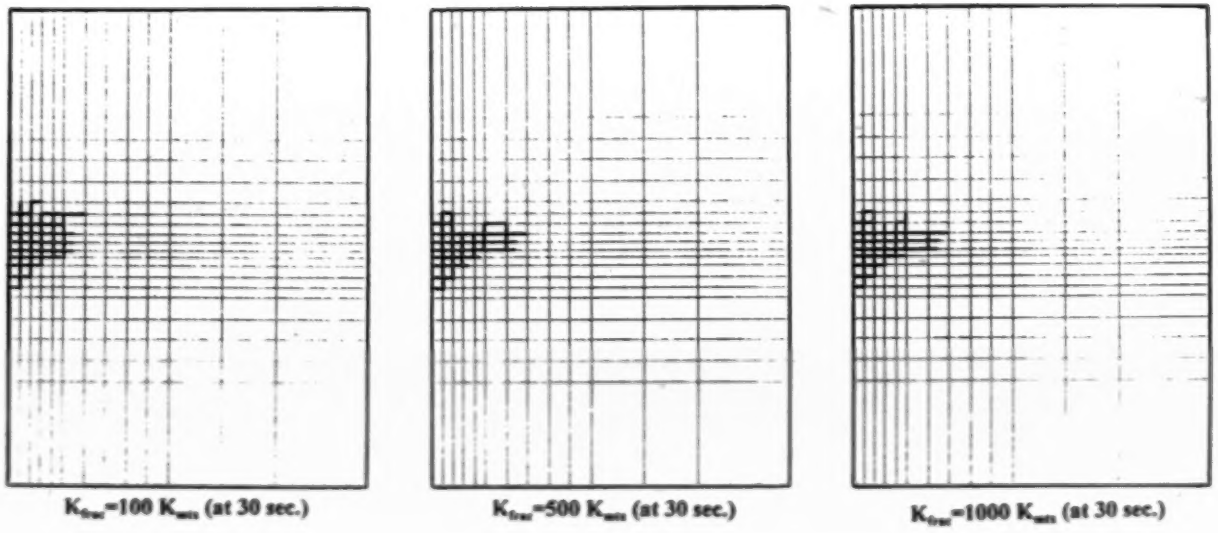

Figure (7-30) Fracture Pattern with Associated Mohr-Coulomb Model

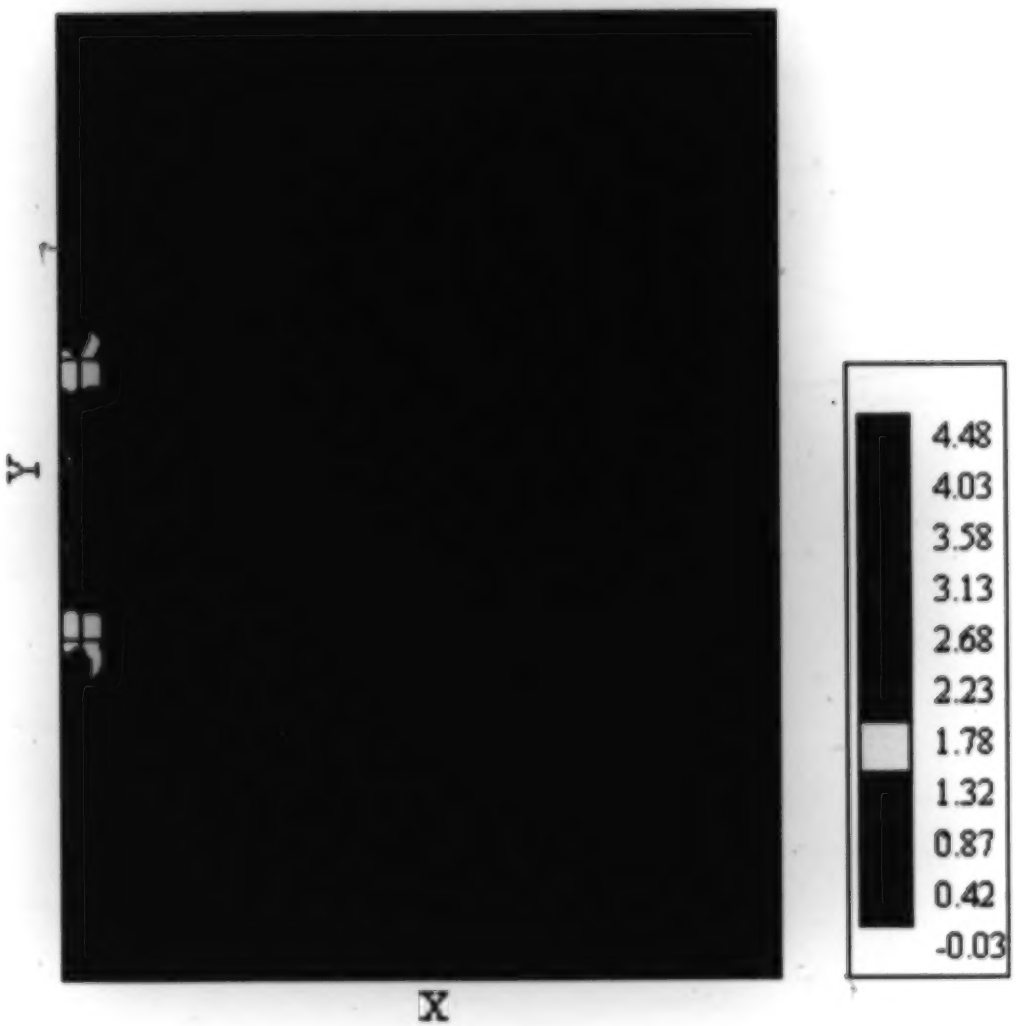

Sigma1/Sigma3 at second 1

Figure (7-31) Principal Stress Ratio indicating the Yield Zone

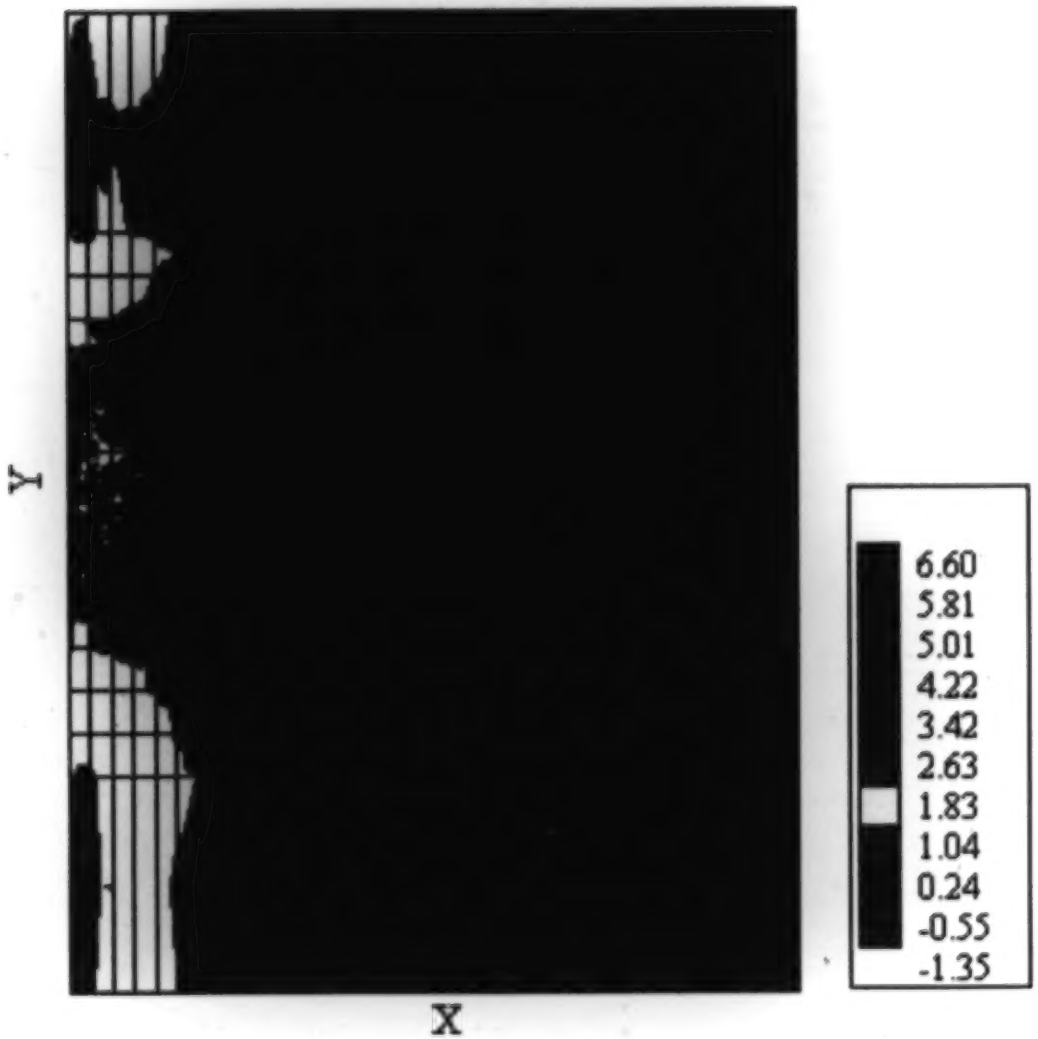

Sigma1/Sigma3 at second 4

Figure (7-32) Principal Stress Ratio indicating the Yield Zone

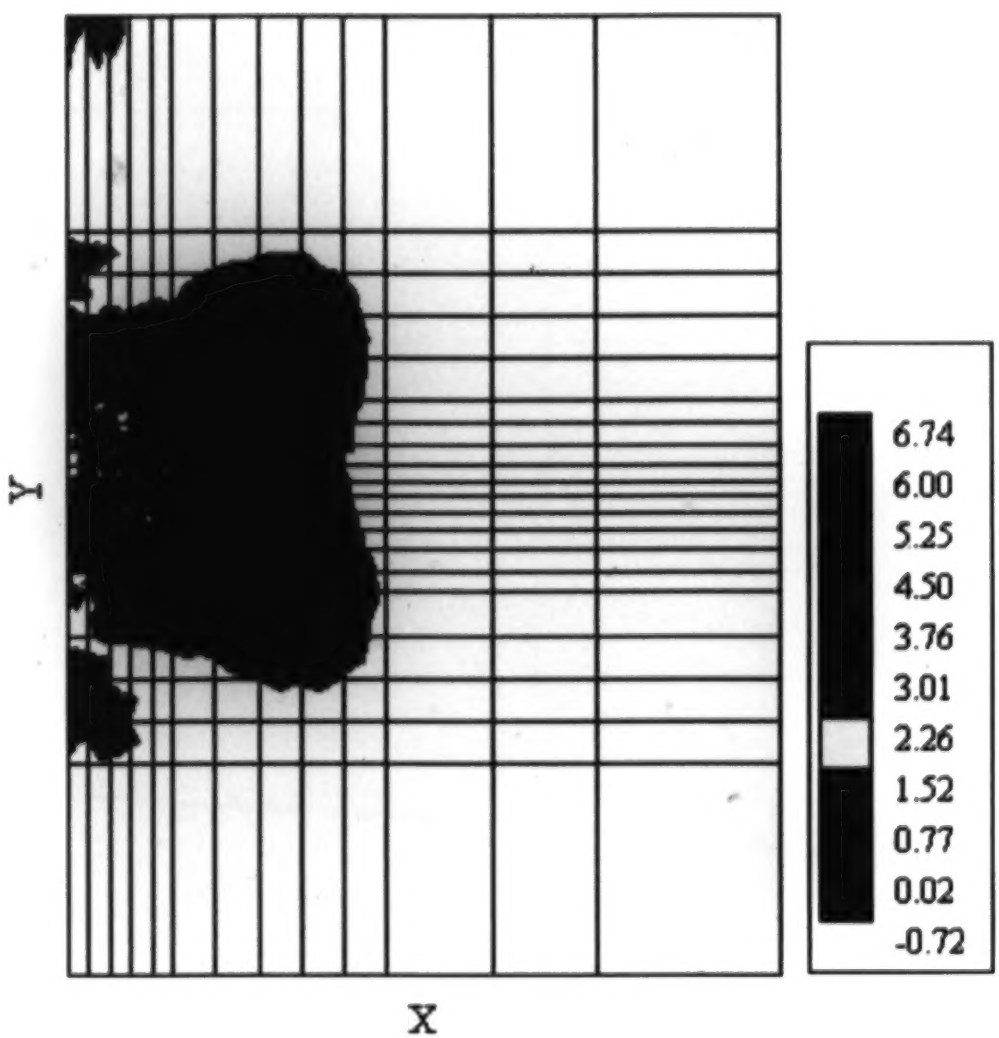

Sigma1/Sigma3 at second 8

Figure (7-33) Principal Stress Ratio indicating the Yield Zone

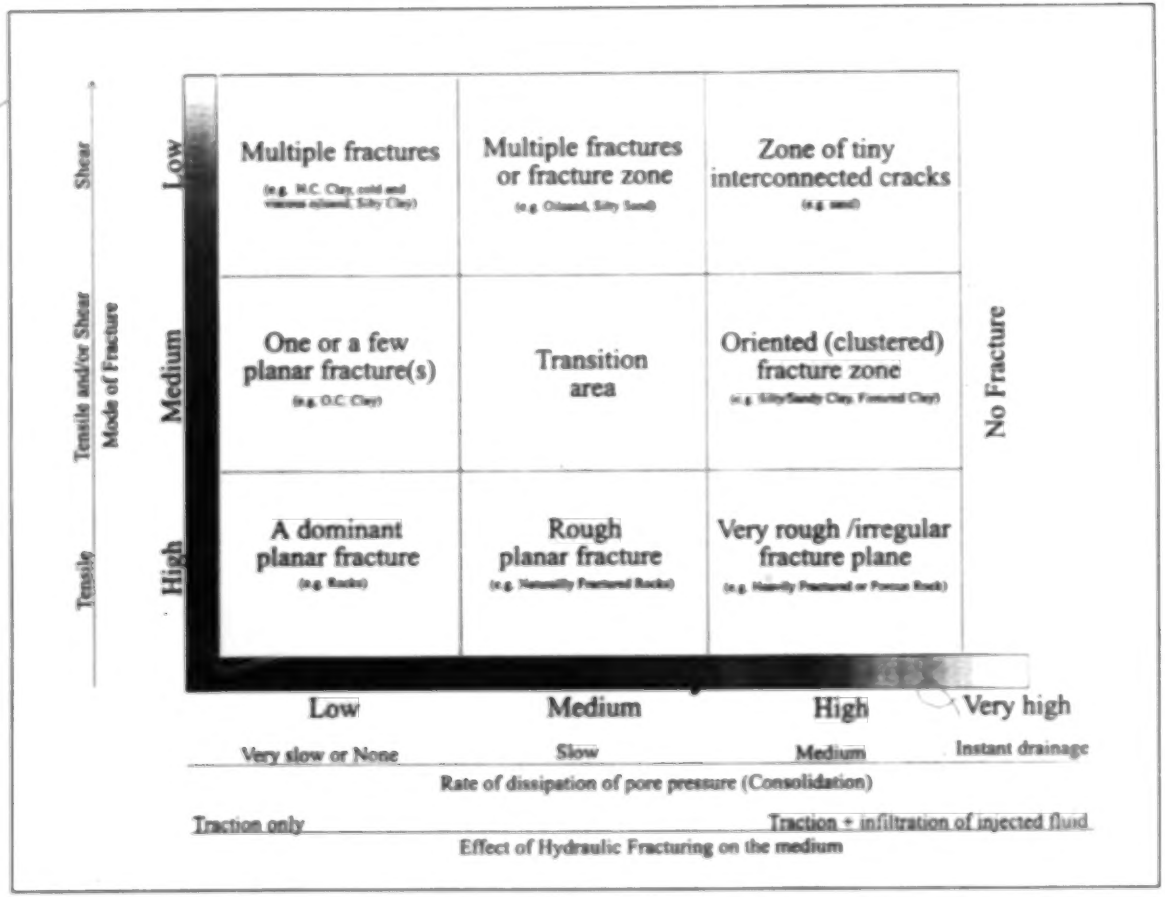

Figure (7-34) Pattern of Hydraulic Fracture in Different Geomaterials

Chapter 8
Summary and Conclusions

8.1 Summary

Since most of the Alberta oilsands are located at depths too great for economical open pit mining, application of the enhanced recovery methods for oil extraction is necessary. One of the most useful and most efficient techniques for enhanced oil recovery is hydraulic fracturing.

Hydraulic fracturing is a well-established method in the petroleum industry. Fifty years of field experience has provided valuable expertise and has invented many advanced equipment. These technological achievements warrant being combined with useful analytical and numerical tools to fulfill the demand of the industry in all theoretical and practical levels.

In the early 60's some investigators developed closed form solutions for predicting the length and opening size of a fracture and the fluid pressure required in hydraulic fracturing treatments. The basic assumption in all of these solutions was the development of a planar fracture with a predefined shape, such as an ellipse. Usually, the height of the fracture plane was considered to be equal to the injection length along the wellbore, then other dimensions and also fluid pressures were determined. These types of analytical solutions were useful at that time and some researchers tried to modify these methods for special field applications.

Over the years, the technology associated with fracturing was improved significantly and the industry moved towards highly sophisticated hydrofracturing treatments. As a result, more reliable design methods were needed for this technology. Today two dimensional and three dimensional design tools are available for modeling hydraulic fracturing, but their degree of accuracy is often uncertain. Some of these

models consider only one aspect of the problem, such as fluid flow in the reservoir or the effects of fluid flow and heat transfer in an uncoupled manner. Others are able to couple these effects and solve the problem implicitly. In most of the models, the effect of ground deformation on the behaviour of the reservoir is often overlooked. Nevertheless, all of these models have inherited the concept of planar fracture from the classical hydraulic fracturing analysis and previous closed form solutions.

Attempts to apply these models to simulate hydraulic fracturing in oilsands, have not been very successful. The problem is that field observations do not match the model predictions. For analyzing the hydraulic fracturing in uncemented soils, some of the common assumptions in the fracturing process should be re-examined carefully. For example, fracturing in rocks usually starts by tensile failure, but in an uncemented soil matrix, due to the high rate of injection, effective stresses in the soil become quite low and close to zero which may cause fracturing to occur due to shear failure. Nevertheless, contrary to rocks, planar fractures may not occur in uncemented soils. Taking these problems into consideration, and noting that initiation and propagation of a fracture depend on the stress state in the ground, it becomes clear that analysis of hydraulic fracturing, especially in soils, requires stress/deformation analysis.

In hydraulic fracturing, generally four physical processes act together, therefore, their interaction should be included in the solution. Ground deformation, fluid flow, heat transfer, and fracturing of the medium are the basic issues that are involved in the problem. Coupling of all of these processes has not been performed before in the literature. In this study, finite element method has been used as a platform for solving the problem. Three partial differential equations of equilibrium, fluid flow, and heat transfer in porous media are written in an incremental form and by applying weighted residual method, three integral equations have been obtained. These integral equations have been transformed into the finite element equations by defining appropriate integrals and considering incremental displacements ΔU, incremental pore fluid pressures ΔP, and incremental temperatures ΔT as state variables. These are the primary unknowns at each point inside the reservoir. Finally three finite element equations have

been solved simultaneously considering all of the coupling terms that are involved in the real physical problem.

The fourth aspect of the hydraulic fracture modeling is to incorporate fracturing mechanism into the model. Fracture mechanics criteria for geomaterials have been used for this purpose. There are several criteria available assuming linear elastic or elastoplastic behaviour for geomaterials. In this study, two simple fracture criteria, one for tensile fracture and the other for shear fracture, have been adopted. These criteria are based on stress state at a point inside the finite element domain. For simulation of fracture, the node splitting technique is used. In this technique, in areas which are prone to cracking, two nodes are introduced at the same point in the finite element mesh (double nodes). During the analysis, if the stresses at the double nodes exceed the tensile strength of the medium or satisfy the requirements for shear fracture, the double nodes are split into two separate nodes and a crack is created at the element boundaries. Since the problem is analyzed by marching in time, at the next time step it will be solved with the new geometry having a crack inside the mesh. If at the new time step stresses at the nearby double nodes are enough to satisfy either tensile or shear fracture criterion, node splitting will take place again to model crack propagation. A 6-node isoparametric rectangular fracture element has been developed for transmitting the fluid flow and/or heat inside the fractures. This fracture element is automatically activated when a fracture is created inside the mesh.

The mathematical and the finite element formulations of this study are quite general, but since this is the first attempt to model the hydraulic fracturing process using a fully coupled thermal hydro-mechanical fracture finite element model, it was decided to model the problem in two dimensions to ensure that the model can adequately handle the complicated physical process and can accurately capture all of the key issues of the problem. For the same reason a single phase compressible fluid is considered in the model as a first stage.

8.2 The Developed Computer Program and its Applications

A fully coupled thermal hydro-mechanical fracture finite element model has been developed in this study. The model is capable of analyzing plane strain or axisymmetric hydraulic fracture problems with different boundary conditions such as specified rate of fluid and/or heat injection, specified pressure and/or temperature, as well as specified load and/or traction.

The model has been verified in a number of ways by comparing its results to the other numerical and analytical solutions for thermal consolidation problems. For validation of the model, on the fracture part, the numerical solution was compared to the experimental results from large scale hydraulic fracturing laboratory tests.

The applications of the developed computer program for analyzing and simulating different engineering problems are described below.

1) Design of optimum (economical) hydrofracturing treatments for heavy oil reservoirs;

2) Modeling of well-communication tests with thermal effects;

3) Study of the hydraulic fracturing treatments for enhancing the permeability of the contaminated sites;

4) Determination of land subsidence due to geothermal energy production (thermo-elastic and thermo-elastoplastic consolidation);

5) Study of the effects of radioactive waste disposal in clay layers or rock formations;

6) Study of the geotechnical aspects of temperature variation in soils (e.g. effects of the heat generated by underground power cables or pipelines);

7) Study of the possibility of cracking in earth dams induced by hydraulic fracturing;

8) Design of grouting process in underlying strata of dams in order to avoid undesirable fracturing of the ground.

8.3 Conclusions

8.3.1 Numerical modeling of large scale hydraulic fracture experiments

Numerical modeling of a large scale hydraulic fracture laboratory experiment has provided some insight into the problem as noted below.

The model indicates that with application of hydraulic fracturing technique to uncemented porous materials, a dominant planar fracture is unlikely to occur and the outcome is a fracture zone consisted of interconnected tiny cracks. This finding, which is supported by experimental observations, is attributed to the high permeability and low cementation of the sand used in the laboratory experiments.

The model emphasizes the importance of pore fluid pressure and its distribution in the reservoir for initiation and propagation of fractures.

The numerical model indicates that permeability of the fractures and/or soil matrix has a drastic effect on the generated pore fluid pressures and fracture pattern.

By assuming an elastoplastic behaviour for soil, the model shows development of a yield zone at the injection area. In this case, the extent of fracturing, compared to that of an ideal elastic material, is less dispersed. In other words, the model establishes that when fluid is injected into the sample, a zone of shear failure develops which causes a tendency for dilation. Since dilation cannot take place in confined conditions, very high compressive stresses are generated which suppress fracture growth.

The maximum length of the fractures predicted by the numerical model is comparable with the observed length/extent of the fractures induced in the sand in the laboratory experiments (which are typically around 5 times greater than the diameter of the injection well).

The model establishes that in uncemented porous materials tensile and shear fractures can occur simultaneously when fluid is injected into the sample. For sand, however, at the beginning of injection the yield zone is relatively small and tension may be introduced as the dominant mode for the initiation of fracture.

8.3.2 Pattern of hydraulic fracture in different geomaterials

A new concept regarding the 'pattern' of hydraulically induced fractures in the ground has been presented in this study. This idea, which is illustrated in Figure (7-34), is described below.

In rocks and other cemented geomaterials, a distinct fracture plane approximately perpendicular to the direction of the minor principal stress has been observed during experimental hydraulic fracturing studies. Theoretical and experimental studies on rocks indicate that tension is the dominant mode of fracturing. Typically rocks have low permeability, therefore, fluid injection has little or no effect on the pore pressure in rocks and the effect of a change in pore pressure in the fracturing process is negligible. In this case, the stress/deformation field combined with fluid characteristics such as injection rate/pressure, and injectant properties dominate the initiation and propagation of fractures. The effect of fluid injection, in this case, is mainly traction.

As the porosity of rock increases and/or natural fractures in the rock become more extensive, the rock permeability increases. This causes injectivity and the amount of leak-off to increase. In this case, pore pressure in the rock changes due to the effect of leak-off. Usually, there is a hydrodynamic lag between the flow of injectant and the flow of drained pore fluid due to the consolidation process which governs the pore pressure distribution in the soil/rock. For rocks with high cementation, a rough and nearly planar fracture can be expected due to hydraulic fracturing.

On the other hand, with a gradual reduction in cementation, the possibility of inducing one dominant fracture plane gradually diminishes. At the same time decreasing the cementation implies that the possibility of shear failure is becoming more significant if the effective stresses in the soil are also reduced. Reduction in effective stresses depends on the amount of change in pore pressure, which, in turn, is a function of permeability.

For uncemented or slightly cemented materials with low permeability (such as normally consolidated clay or silty clay) experiments indicate that chance of getting multiple fractures as opposed to one single dominant fracture is high. For this class of materials, if the permeability increases, the amount of leak-off and change in pore pressure inside the medium becomes more significant. Injection of fluid with high rate/pressure in this class of materials can cause shear failure since cementation is low and high leak-off reduces the effective stresses to very small values. Therefore,

multiple tensile and/or shear fractures or a 'fracture zone' is more likely to occur for uncemented materials.

Experimental as well as numerical results suggest that, for uncemented granular materials, if the injection rate/pressure is high (relative to the permeability of the medium), fracture occurs whenever the tensile or shear fracture criterion is satisfied. Due to the granular nature of these materials, fracture should not necessarily occur at the crack tip (as is the case for fracturing in cemented materials). Therefore, in uncemented materials with high permeability (e.g. sands) a fracture zone consisting of interconnected tiny cracks may be expected in areas of high pore pressure. In fact, tensile or shear failure mechanisms in this case, may not occur independent of one another, due to very high induced pore pressures.

It should be noted that as the fracture pattern moves from a dominant fracture towards a zone of tiny cracks it becomes more dispersed, however, the length/extent of fractures becomes shorter.

If the permeability of soil/rock is very large, a very high injection rate/pressure is required to induce a hydraulic fracture which may not be possible or economical in practice. This is because of rapid drainage of water which reduces the excess pore pressure to zero.

Oilsands can be categorized as a material with very low (or no) cementation and low to medium hydraulic conductivity. Due to the existence of bitumen, oilsand's hydraulic conductivity depends on the temperature. In cold hydraulic fracturing treatments, bitumen is very viscous, hence the hydraulic conductivity is low. Therefore, a system of multiple fractures can be expected. In hot hydraulic fracturing treatments, the viscosity of bitumen reduces significantly, thus, the hydraulic conductivity is increased. With higher hydraulic conductivity, the fracture pattern shifts towards creating a zone of small cracks. This explains field observations during hydraulic fracturing treatments in oilsand, which is characterized by high leak-off and short fracture lengths.

The above conceptual framework for the expected hydraulic fracture pattern in different types of soils or rocks has been summarized in Figure (7-34). From the point

of view of fracture pattern, there is no well defined boundary for prediction of a dominant planar fracture or a system of numerous tiny cracks. However, a smooth transition zone among different fracture patterns exists. Fracture pattern in the transition zone depends on many factors; the most important of these are injection rate/pressure and the injectant properties.

8.4 Further Research

The model developed in this study is a first attempt to couple four different physical phenomena for simulating a unique problem. As a result, much more research should be conducted in the future to improve the current model. Extension of this research can be implemented in different ways. First of all, the program can be modified to solve three dimensional problems. This helps to have a better representation of the real fracture propagation in the ground. Since the formulations presented here are quite general, all that is required for 3D analysis is the development of block elements with appropriate shape functions, and to increase the size of the matrices in the finite element equations accordingly.

Evaluation of the effects of the changes in soil/rock permeability and fluid viscosity on the fracturing behaviour of the reservoir can be useful for practical purposes. Routines for updating the permeability of the soil with respect to changes in porosity and for updating fluid viscosity with respect to changes in temperature and pore pressure, are already coded in the program, but have not been used.

It is of special interest to petroleum engineers to include multiphase flow in the model; e.g. 2-phase immisible flow (water and oil) and 3-phase flow (water, oil and gas). For multiphase flow the degree of saturation of different phases should be considered as primary unknowns. This requires modifications in the formulation especially in the flow equation.

Another research area in the continuation of this study would be using other fracture criteria and evaluating their effectiveness for modeling tensile, shear, and mixed mode fractures in soils/rocks.

There is a need for laboratory investigations on fracture characteristics of oilsand and determination of fracture mechanics criteria for initiation and propagation of fractures in isothermal and non-isothermal conditions. The results of these experiments can be implemented in the numerical models for a more accurate representation of fractures in oilsand reservoirs.

Experimental investigations are also required to quantify the ranges of the values of permeability and cementation for which different patterns of fractures may be induced in the ground.

In closure, development of a program capable of handling dynamic effects in time dependent problems can improve the numerical results. On the other hand, results of the current research on modeling of crack and/or shear band, may open new horizons to the hydraulic fracture modeling.

REFERENCES

Aboustit, B. L., Advani, S.H. and Lee, J.K. (1985): "Variational Principles and Finite Element Simulations For Thermo-Elastic Consolidation", Int. J. Num. Anal. Meth. Geomech., Vol.9, pp.49-69.

Advani, S.H. and Lee, J.K. (1982): "Finite Element Model Simulations Associated With Hydraulic Fracturing", SPE Journal, Trans., AIME, Vol.22, pp.209-218

Advani, S.H., Lee, T.S. and Lee, J.K. (1990): "Three-Dimensional Modeling of Hydraulic Fractures In Layered Media, Part I and Part II", Journal of Energy Resources Technology, Vol.112, pp.1-19

Agar, J.R. (1984): "Geotechnical Behaviour of Oil Sands at Elevated Temperatures and Pressures", Ph.D. Thesis, Department of Civil Engineering, University of Alberta, Edmonton, 1984.

Agar, J.R., Morgenstern, N.R. and Scott, J.D. (1987): "Shear Strength and Stress-Strain Behaviour of Athabasca Oil Sands at Elevated Temperatures and Pressures", Can. Geotech. J., Vol.24, pp.1-10

Agar.J.G., Morgenstern, N.R. and Scott, J.D. (1983): "Geotechnical Testing of Alberta Oil Sand at Elevated Temperatures and Pressures", Proc. 24th U.S. Sym. On Rock Mech., pp. 795-805

Alberta Energy and Natural Resources (1979): "Alberta Oil Sands Facts and Figures", ENR Report No.110, 67p.

Anderson, G.D. and Larson, D.B. (1978): "Laboratory Experiments on Hydraulic Fracture Growth Near an Interface", Proc., 19th U.S. Symposium on Rock Mechanics, Mackay School of Mines, University of Nevada, pp. 333-339, 1978

Atkinson, B.K. (1987): "Introduction To Fracture Mechanics and Its Geophysical Application"; in Fracture Mechanics of Rock,(B.K. Atkinson Ed.), pp.1-26, 1987.

Atukorala, U.D. (1983): "Finite Element Analysis of Fluid Induced Fracture Behaviour in Oilsands"; M.Sc. Thesis, Department of Civil Engineering, University of British Columbia, July 1983.

Barenblatt, G.I., Zheltov, I.P. and Kochina, I.N. (1960): "Basic Concepts in The Theory of Seepage of Homogeneous Liquids in Fissured Rocks"; PMM, Vol.24, No.5 ,1960.

Bathe, K.J. (1982): "Finite Element Procedures in Engineering Analysis"; Prentice-Hall, Inc., Englewood Cliffs, N.J, Chapter 4, pp.114-194, 1982

Bazant, Z.P. (1984): "Size Effect in Blunt Fracture: Concrete, Rock, Metal"; Journal of Engineering Mechanics, ASCE, 110(4), pp.518-535, 1984.

Bazant, Z.P. (1986): "Mechanics of Distributed Cracking"; Applied Mechanics Review, ASME, 39(5), 675-705, 1986.

Bazant, Z.P., and Lin, F.B. (1988): "Nonlocal Smeared Cracking Model For Concrete Fracture"; Journal of Structural Engineering, ASCE, 114(11), pp. 2493-2510, Nov.1988.

Bazant, Z.P., and Oh, B.H. (1983): "Crack Band Theory For Fracture of Concrete", Materials and Structures; RILEM, Paris, France, 16, pp.155-177, 1983.

Bazant, Z.P., and Oh, B.H. (1984): "Rock Fracture Via Strain-Softening Finite Element"; Journal of Engineering Mechanics, ASCE, 110(7), pp.1015-1035, 1984.

Biot, M.A. (1941): "General Theory of Three Dimensional Consolidation", J. Appl. Physics, Vol.12, pp.155-164

Biot, M.A. (1955): "Theory of Elasticity and Consolidation For A Porous Anisotropic Solid", J. Applied Physics, Vol.26, pp. 459-467

Biot, M.A. (1956a): "General Solutions of The Equations of Elasticity and Consolidation For A Porous Material", J. Applied Mech., Trans. ASME, Vol.78, pp.91-96

Biot, M.A. (1956b): "Theory of Deformation of A Porous Viscoelastic Anisotropic Solid", J. Applied Physics, Vol.27, pp.459-467

Bjerrum, L. and Andersen, K.H. (1972): "In-Situ Measurements of Lateral Pressure in Clay", Proc. 5th. European Conf. Soil Mech. Found. Engr., Madrid, Spain, Vol.1, pp.11-20

Bjerrum, L., Nash, J.K.T.L., Kenard, R.M. and Gibson, R.E. (1974): "Hydraulic Fracturing in Field Permeability Testing", Geotechnique, Vol.22, No.2, pp.319-332

Blanton, T.L. (1982): "An Experimental Study of Interaction Between Hydraulically Induced and Pre -Existing Fractures", paper SPE 10847 presented at the SPE/DOE Unconventional Gas Recovery Symposium, Pittsburgh, PA, U.S.A., 1982

Booker, J.R. and Savvidou, C. (1985): "Consolidation Around A Point Heat Source", Int. J. Num. Anal. Meth. Geomech., Vol.9, pp.173-184.

Borsetto, M., Cricchi, D., Hueckel, T. and Peano, A. (1984): "On Numerical Models For The Analysis of Nuclear Waste Disposal in Geological Clay Formations", in Numerical Methods For Transient and Coupled Problems (R.W. Lewis, E. Hinton, P. Bettes and B.A. Schrefler Eds.), Pineridge Press, Swansea, pp.603-618

Borsetto, M., Garradori, G. and Peano, A. (1983): "Environmental Effects of Fluid Injection into Geothermal Reservoirs, in Numerical Methods in Heat Transfer" (R.W.Lewis, K. Morgan and B.A. Schrefler Eds.), Vol.II, J.Wiley, Chichester

Brownell, D.H., Garg, S.K. and Pritchett, J.W. (1977): "Governing Equations For Geothermal Reservoirs", Water Resources Research, Vol.13, pp.929-934

Burdekin, F.M. and Stone, D.E.W. (1966): "The Crack Opening Displacement Approach To Fracture Mechanics in Yielding", Journal of Strain Analysis, Vol.1, pp.145-153

Campanella, R.G. and Mitchell, K.J. (1968): "Influence of Temperature Variations On Soil Behaviour", J. Soil Mech. Found. Engr. Div., ASCE, SM3, 94, pp.709-734

Carter, J.P., Booker, J.R. and Small, J.C . (1979): "The Analysis of Finite Elastoplastic Consolidation", Int. J. of Num. Anal. Methods in Geomech., Vol.3, pp.107-129

Carter, J.P., Small, J.C. and Booker, J.R. (1977): "A Theory of Finite Elastic Consolidation", Int. J. of Solids Structures, Vol.13, pp.467-478

Chan, D.H. (1986): "Finite Element Analysis of the Strain Softening Materials", Ph.D Thesis, Department of Civil Engineering, University of Alberta, Edmonton, 1986.

Chan, D.H.K. (1981): "Creep and Fracture Simulation of Ice Using The Finite Element Method", M.Sc. Thesis, Department of Civil Engineering, MacMaster University, June 1981.

Chang, C.S. and Duncan, J.M. (1983): "Consolidation Analysis For Partly Saturated Clay By Using An Elasto-Plastic Effective $\sigma-\varepsilon$ Model", Int. J. Num. Anal. Meth. Geomech., Vol.17, pp.39-55

Chavent, G. and Jaffre', J. (1986): "Mathematical Models and Finite Elements For Reservoir Simulation", Elsevier Science Publishers B.V., The Netherlands

Cheung, L.S. and Haimson, B.C. (1989): "Laboratory Study of Hydraulic Fracturing Pressure Data- How Valid Is Their Conventional Interpretation?, Int. J. Rock Mech. Min. Sci. & Geomech. Abstr., vol. 26, pp. 595-604

Christian, J.T. (1968): "Undrained Stress Distribution By Numerical Methods", J. of Soil Mech. Found. Engr. Div., ASCE, Vol.94, SM6, pp.1333-1345

Christian, J.T. (1977): "Two- and Three Dimensional Consolidation", in Numerical Methods in Geomechanical Engineering (eds. C.S. Desai and J.T. Christian), pp.399-426, London McGraw-Hill

Christian, J.T. and Boehmer, J.W. (1970): "Plane Strain Consolidation By Finite Elements", J. of Soil Mech. Found. Engr. Div., ASCE, Vol.96, SM4, pp.1435-1457

Collins, R.E. (1976): " Flow of Fluids Through Porous Materials", Reinhold Publishing Corp., New York City 1961, Reprinted By Petroleum Publishing Co., Tulsa, UK, 1976

Corapcioglu, M.Y. and Karahanoglu, N. (1980): "Simulation of Geothermal Production", in Alternative Energy Sources II (T. Nejat Verizoglu Ed.), Vol. 5, Hemisphere Publ. Co., N.Y., pp.1895-1918

Cundall, P.A. (1971): "A Computer Model For Simulating Progressive Large Scale Movement in Blocky Rock Systems"; Proc. Sym., International Society of Rock Mechanics, Nancy, pp. II.8, 1971.

Daneshy, A.A. (1973): "On The Design of Vertical Hydraulic Fractures", Petroleum Engineering Journal, pp. 61-68, April 1973

Darwin, D. (1985): "Concrete Crack Propagation- Study of Model Parameters"; Proc. Finite Element Analysis of Reinforced Concrete Structures, (C. Meyer and H. Okamura, Eds.), ASCE, New York, 184-203, 1985.

Dasai, C.S., Zaman, M.M., Lightner, J.G. and Siriwardane, H.J. (1984): "Thin-Layer Element For Interfaces and Joints"; International Journal For Numerical and Analytical Methods in Geomechanics, 8, pp.19-43, 1984.

deBorst, R. (1984): "Application of Advanced Solution Techniques To Concrete Cracking and Non-Associated Plasticity"; Numerical Methods For Non-Linear Problems, (C. Taylor Et Al. Eds.), Vol. 2, Pineridge Press, Swansea, United Kingdom, pp. 314-325, 1984.

Demaison, G.J. (1977): "Tar Sands and Super Giant Oil Fields", in Oilsands of Canada-Venezuela, Redford, D.A. and Winestock, A.G., Can. Ins. of Min., Metalur. Petr. Engr., Special Vol.17, pp.9-16

Dugdale, D.S. (1960): "Yielding of Steel Sheets Containing Slits"; Journal of The Mechanics and Physics of Solids, 8, pp.100-104, 1960.

Dusseault, M.B. (1977): "Stress State and Hydraulic Fracturing in the Athabasca Oil Sands", JCPT, pp.19, July-Sept., 1977

Dusseault, M.B. (1977): "The Geotechnical Characteristics of The Athabasca Oil Sands", Ph.D. Thesis, Department of Civil Engineering, University of Alberta, Edmonton. 1977

Dusseault, M.B. and Morgenstern, N.R. (1978): "Shear Strength of Athabasca Oil Sands", Can. Geotech. J., Vol.15, pp.216-238

Erdogan, F. and Sih, G.C. (1963): "On The Crack Extension in Plates Under Plain Loading and Transverse Shear"; ASME Journal, Basic Engineering, 85, pp. 519-527, 1963.

Ertekin,T. (1978), "Numerical Simulation of The Compaction-Subsidence Phenomenon in A Reservoir For Two-Phase Non-Isothermal Flow", Ph.D. Thesis, The Pennsylvania State University, Penn.

Ewalds, H.L. and Wanhill, R.J.H. (1984): "Fracture Mechanics"; Edward Arnold, London, 1984.

Finol, A. and Farouq Ali, S.M. (1975): "Numerical Simulation of Oil Production With Simultaneous Ground Subsidence", SPEJ, 411, Oct. 1975

Frank, U. and Barkley, N. (1995):"Remediation of low permeability subsurface formations by fracturing enhancement of soil vapor extraction", J. of Hazard. Mater., vol 40, pp.191-201

Frantziskonis, G. and Desai, C.S. (1987): "Constitutive Model With Strain Softening"; Int. J. Solids Structures, Vol. 23, No. 6, pp.733-750, 1987

Fung, L.S.-K. (1992): "A Coupled Geomechanic-Multiphase Flow Model For Analysis of In-Situ Recovery in Cohesionless Oilsands", JCPT, Vol.31, No.6, Jun. 1992

Fung, L.S.K. (1990): "Simulation of Block-To-Block Processes in Naturally Fractured Reservoirs"; Proc., California Regional Meeting, SPE, pp. 51-60, Apr. 4-6, 1990.

Fung, Y.C. (1965): "Foundations of Solid Mechanics"; Prentice-Hall, Inc., Englewood Cliffs, N.J., 1965

Gdoutos, E.E. (1990): "Fracture Mechanics Criteria and Application"; Kluwer Academic Publishers, 1990.

Geertsma, J. (1957): "The Effect of Fluid Pressure Decline On Volumetric Changes of Porous Rocks", Pet. Trans. AIME, No.210, pp.310-340

Geertsma, J. (1989): "Two-Dimensional Fracture-Propagation Models", in Recent Advances in Hydraulic Fracturing (J.L. Gidley, S.A. Holditch, D.E. Nierode and R.W. Veatch Eds.), SPE Monograph Vol. 12, Capter 4, 1989

Geertsma, J. and deKlerk, F.A. (1969): "Rapid Method of Predicting Width and Extent of Hydraulically Induced Fractures", JPT (Dec. 1969), 1571-81; Trans., AIME, 246

Ghaboussi, J. and Karshenas, M. (1978): "On The Finite Element Analysis of Certain Material Nonlinearities in Geomechanics", Proc. Int. Conf. On Finite Element in Nonlinear Solids and Structures, Geilo, Norway

Ghaboussi, J. and Kim, K.J. (1982): "Analysis of Saturated and Partly Saturated Soils", Proc. Int. Symp. Num. Meth. Geomech., Zurich,1982, pp.377-390

Ghaboussi, J. and Wilson, E.L. (1973): "Flow of Compressible Fluid in Porous Elastic Media", Int. J. Num. Meth. Engr., Vol.5, pp.419-442

Ghaboussi, J., Wilson, E.L. and Isenberg, J. (1973): "Finite Element For Rock Joints and Interfaces", J. Soil Mech. Fnds. Div., ASCE, Vol.99, pp.833-848

Gidley, J.L., Holditch, S.A., Nierode, D.E. and Veatch Jr., R.W. (1989): "Recent Advances in Hydraulic Fracturing", SPE Monograph, Vol.12, 1989

Golders ass. Ltd.: "Laboratory Simulation and Constitutive Behaviour For Hydraulic Fracture Propagation in Oil Sands ,Phase II", Project No. 912-2055, Golders associates Ltd., June 1992

Golders ass. Ltd.: "Laboratory Simulation and Constitutive Behaviour For Hydraulic Fracture Propagation in Oil Sands ,Phase I", Project No. 902-2013, Golders associates Ltd., July 1991

Golders ass. Ltd.: "Laboratory Study of Hydraulic Fracture Propagation in Oil Sands, Phase III", Project No. 932-2005, Golders associates Ltd., July 1994

Goodman, R.E., Taylor, R. and Brekk, T.L. (1968): "A Model For The Mechanics of Jointed Rock"; Journal of Soil Mechanics and Foundation Division, ASCE, 94(SM3), pp.637-659, 1968.

Griffith, A.A. (1921): "The Phenomena of Rupture and Flow in Solids"; Philosophical Transactions of Royal Society of London, A221, pp.163-198. 1921.

Griffith, A.A. (1924): "The Theory of Rupture"; Proc. of First International Congress of Applied Mechanics, Delft, pp.55-63, 1924.

Guo, F. (1993): "An Experimental Study of Fracture Propagation and Well Communication by Hydraulic Fracturing", Ph.D. Thesis, Department of Civil Engineering, University of Alberta, Edmonton, 1993

Hagoort, J., Weatherill, and Settari, A. (1980): "Modeling The Propagation of Water Flood-Induced Hydraulic Fractures"; Journal of The Society of Petroleum Engineers, pp. 293-303, Aug. 1980.

Haimson, B. (1968): "Hydraulic Fracturing in Porous and Non-Porous Rock and Its Potential For Determining In-Situ Stresses at Great Depth", Technical Report No.4-68, United States Army Corps of Engineers, Missouri Division, Omaha, Feb. 1968

Haimson, B.C. (1968): "Hydraulic Fracturing in Porous and Nonporous Rock and its Potential for Determining In-Situ Stresses at Great Depth", Ph.D. Thesis, University of Minnesota, U.S.A. (1968)

Hanson, M.E., Shaffer, R.J. and Anderson, G.D. (1981): "Effects of Various Parameters on Hydraulic Fracturing Geometry", Society of Petroleum Engineers Journal, vol. 21, pp. 435-443

Harris, M.C. and Sobkowicz, J.C. (1978): "Engineering Behaviour of Oil Sans", The oil Sands of Canada and Venezuela 1977, CIM special volume 17, pp.270, 1978

Herrmann, L.R. (1978): "Finite Element Analysis of Contact Problems", J. Eng. Mech., ASCE, Vol.104, pp.1043-1059

Ingraffea, A.R. (1977): "Short Communications, Nodal Grafting For Crack Propagation Studies"; International Journal For Numerical Methods in Engineering, Vol.11, pp. 1185-1187, 1977.

Ingraffea, A.R. (1987): "Theory of Crack Initiation and Propagation in Rock", in Fracture Mechanics of Rock,(B.K. Atkinson Ed.), pp.71-110, 1987.

Ingraffea, A.R., and Saouma, V. (1984): "Numerical Modeling of Discrete Crack Propagation in Reinforced and Plain Concrete"; Application of Fracture Mechanics To Concrete Structures, (G.C. Sih and A. Ditommaso, Eds.), Martinus Nijhoff Publishers. 1984.

Irwin, G.R. (1957): "Analysis of Stresses and Strains Near The End of A Crack Traversing A Plate"; Journal of Applied Mechanics, Trans., ASME, Vol.24, pp.361-364, 1957.

Irwin, G.R. (1958): "Fracture; in Encyclopedia of Physics", Vol. VI, Elasticity and Plasticity (S.Flugge Editor), Springer-Verlag, pp.551-590, 1958.

Irwin, G.R. (1960): "Plastic Zone Near A Crack Tip and Fracture Toughness"; Proc. of The Seventh Sagamore Ordnance Material Conference, pp. IV63-IV78, 1960.

Itasca (1995): "FLAC: Fast Lagrangian Analysis of Continua", Volume 1 User's Manual.

Jaworski, G.W., Duncan, J.M. and Seed, H.B. (1981): "Laboratory Study of Hydraulic Fracturing", J. Geotech. Engr. Div., ASCE, pp.713-732, June 1981

Jenkins, R. and Aronofsky, J.S. (1954): "Analysis of Heat Transfer Processes in Porous Media- New Concepts in Reservoir Heat Engineering", Proc. 18th Technical Conference On Petroleum Production, Pennsylvania State U., University Park, PA (1954)

Johnston, P.R. (1981): "Finite Element Consolidation Analysis of Tunnel Behaviour On Clay", Ph.D. Thesis, Stanford University

Kaliakin, V.N. and Li, J. (1995): "Insight into Deficiencies Associated With Commonly Used Zero-Thickness Interface Elements", Computers and Geotechnics, Vol.17, pp.225-252

Kazemi, H., Merril, L., Porterfield, K. and Zeman, P. (1976): "Numerical Simulation of Water-Oil Flow in Naturally Fractured Reservoirs"; SPEJ, Trans., AIME, Vol.26, pp.317-326, Dec.1976.

Komak Panah, A. (1990): "Laboratory Study of Hydraulic Fracturing in Soils and Its Application To Geotechnical Engineering Practice", Ph.D. Dissertation, Graduate School of Engineering, Tohoku University, Japan,1990

Komak Panah, A. and Yanagisawa, E. (1989): "Laboratory Studies On Hydraulic Fracturing Criteria in Soil"; Journal of The Soils and Foundations, Japanese Society of Soil Mechanics and Foundation Engineering, Vol.29, No.4, pp.14-22, Dec.1989.

Kosar, K.M. (1989): "Geotechnical Properties of Oil Sands and Related Strata", Ph.D. Thesis, Department of Civil Engineering, University of Alberta, Edmonton, 1989

Kosar, K.M., Scott, J.D. and Morgenstern, N.R. (1987): "Testing To Determine The Geotechnical Properties of Oil Sands", CIM Paper 87-38-59, 38th ATM of The Pet. Soc. CIM, Calgary, Jun. 1987

Lamout, N. and Jessen, F.W. (1963): "The Effects of Existing Fractures in Rocks on the Extension of Hydraulic Fractures", Trans., AIME, vol. 228, 1963

Lee, K. and Sills, C. (1981): "The Consolidation of A Soil Stratum Including Self-Weight Effects and Large Strains", Int. J. For Num. Anal. Methods in Geomech., Vol. 5, pp.405-428

Leroueil, S. and Marques, M. (1996): "Importance of Strain Rate and Temperature Effects in Geotechnical Engineering, State of the Art", ASCE convention, Washington D.C., 60p, Nov. 1996

Lewis, R.W. , Roberts, P.J. and Schrefler, B.A. (1989): "Finite Element Modeling of Two-Phase Heat and Fluid Flow in Deforming Porous Media", Transport in Porous Media, Vol.4, pp.319-334

Lewis, R.W. and Karahanoglu, N. (1988): "Simulation of Subsidence in Geothermal Reservoirs", in Numerical Methods in Thermal Problems (R.W.Lewis, K. Morgan and B.A. Schrefler Eds.), Vol.II, Pineridge Press, Swansea, pp.326-335

Lewis, R.W. and Sukirman, Y. (1993): "Finite Element Modeling of Three-Phase Flow in Deforming Saturated Oil Reservoirs", Int. J. Num. Anal. Meth. Geomech., Vol.17, pp.577-598

Lewis, R.W., Majorana, C.E. and Schrefler, B.A. (1986): "A Coupled Finite Element Model For The Consolidation of Nonisothermal Elastoplastic Porous Media", Transport in Porous Media, Vol.1, pp.155-178.

Lewis,R.W., Roberts,G.K. and Zienkiewicz, O.C. (1976), "A Nonlinear Flow and Deformation Analysis of Consolidation Problems", 2nd. Int. Conf. On Num. Methods in Geomech., Blacksburg, Virginia, Vol.2, pp.1106-1118

Lippmann, M.J., Narasimhau, T.N. and Witherspoon, P.A. (1976): "Numerical Simulation of Reservoir Compaction in Liquid Dominated Geothermal Systems", Proc.

2nd. Int. Symp. Land Subsidence, Int. Ass. of Hydrological Sciences, Anaheim, Calif., Pub. No.121, pp.179-184

Mahtab, M.A. and Goodman, R.E. (1970): "Three Dimensional Finite Element Analysis of Jointed Rock Slopes"; Proc. of Second Congress of The International Society For Rock Mechanics, Belgrade, Vol.3, pp.353-360, 1970.

Malvern, L.E. (1969): "Introduction to the Mechanics of a Continuous Medium", Prentice-Hall, New-Jersey, 1969

Mattews, C.S., Van Meurs, P. and Volek, C.W. (1969), U.S. patent No. 3,455,391, July 15, 1969

Medlin, W.L. and Fitch, J.L. (1983): "Abnormal Treating Pressures in MHF treatments", paper 12108, Annual Technical Conference and Exhibition, San Francisco, Sept. 5-8, 1983

Medlin, W.L. and Masse, L. (1979): "Laboratory Investigation of Fracture Initiation Pressure and Orientation", Society of Petroleum Engineers Journal, vol. 19, pp. 129-144

Morgenstern, N.R. (1981): "Geotechnical Engineering and Frontier Resource Development", Geotechnique, Vol. 31, pp.303-365

Mossop, G.D. (1978): "Geological Controls On Reservoir Heterogeneity", Athabasca Oil Sands, Proc. of Aostra Seminar of Subsurface Excavation in Oil Sands, Edmonton, University of Alberta, Paper No.1, pp.26

Muhlhaus, H.B. and Vardoulakis, T. (1987): "The Thickness of Shear Bands in Granular Materials", Geotechnique, 37(3), pp.271-283, 1987.

Murdoch, L.C. (1992): "Hydraulic Fracturing of Soil During Laboratory Experiments (in Three Parts)", Geotechnique, Vol.43, No.2, pp.255-287

Muri, A. and Tamura, M. (1987): "Hydrofracturing Pressure of Cohesive Soils", Soil and Foundation, Japanese Soc. Soil Mech. Found. Engr., Vol.27, No.1, pp.14-22, Mar. 1987

Nobari, E.S., Lee, K.L. and Duncan, J.M. (1973): "Hydraulic Fracturing in Zoned Earth and Rockfill Dams", Report No. TE 73-1, Vol.9, No.8, pp.17-23, office of Research Services, University of California, Berkeley

Nordgren, R.P. (1972): "Propagation of A Vertical Hydraulic Fracture"; SPEJ, Trans., AIME, 253, pp 306-14, Aug.1972.

Ohta, H. (1992): "Embankment and Excavation under Construction"

Ortiz, M., Leroy, Y. and Needleman, A. (1987): "A Finite Element Method For Localized Failure Analysis", Computer Methods in Applied Mechanics and Engineering, Vol.63, pp.189-214

Penman, A.D.M. (1976): "Earth Pressure Measured With Hydraulic Piezometers", Grouting Engineering, London, England, Nov. 1976

Perkins, T.K. and Kern, L.R. (1961): "Width of Hydraulic Fractures"; JPT, Trans., AIME, 222, pp 937-49, Sept.1961.

Pollard, D.D. and Aydin, A. (1988): "Progress in Understanding Jointing Over The Past Century"; Geological Society of America Bulletin, 100, pp.1181-1204,1988.

Pratts, M. (1982): "Thermal Recovery"; SPE Monograph No.7, 1982.

Rashid, Y.R. (1968): "Analysis of Prestressed Concrete Pressure Vessels"; Nuclear Engineering and Design, 7(4), pp.334-335, 1968.

Rice, J.R. (1968): "A Path Independent Integral and The Approximate Analysis of Strain Concentration By Notches and Cracks", Journal of Applied Mechanics, Trans. of ASME, Vol.35, pp.379-386, 1968

Rubin, M.B. (1983): "Experimental Study of Hydraulic Fracturing in an Impermeable Material", Journal of Energy Resources Technology, vol. 105, pp. 116-124

Rummel, F. (1987): "Fracture Mechanics Approach to Hydraulic Fracturing Stress Measurements", in Fracture Mechanics of Rock (B.K. Atkinson, Ed.), Academic Press Inc. Ltd., London, 1987

Ryan, T.M., Farmer, I.W. and Kimbrell, A.F. (1987): "Laboratory Determination of Fracture Permeability", Proc. of 28th U.S. Symposium of Rock Mechanics, Tucson, pp. 593-600, 1987

Saidi, A.M. (1975): "Mathematical Simulation Model Describing Iranian Fractured Reservoirs and Its Application To Haft Kel Field"; Proc. Ninth World Petroleum Congress, 4, pp. 209-219, Japan, 1975.

Sandhu, R.S. (1968): "Fluid Flow in Saturated Porous Elastic Media", Ph.D. Thesis, Department of Civil Engineering, University of California, Berkeley

Sandhu, R.S. (1976): "Finite Element Analysis of Soil Consolidation", National Science Foundation Grant No.72-04110-A, Geotechnical Engineering Report No.6, Dept. of Civil Engineering, The Ohio State University, Columbus, Ohio

Schmidt, R. (1979): "Mine-back of a hydraulic fracture experiment", Proc. 20th U.S. Symposium on Rock Mechanics, Austin, TX, June 4-6, 1979

Scott, J.D. and Kosar, K.M. (1982): "Thermal Expansion of Oil Sands", Proc. of Forum On Subsidence Due To Fluid Withdrawal, U.S. Dept. of Energy and The Rep. of Venezuela Ministry of Mines, Oklahoma

Scott, J.D. and Kosar, K.M. (1985): "Foundation Movements Beneath Hot Structures", Proc. of 11th. Int. Conf. Soil Mech. Found. Engr., San Francisco, CA.

Settari, A. (1980): "Simulation of Hydraulic Fracturing Process", SPE Journal, Dec 1980, pp.487-500

Settari, A. (1988): "Modeling of Fracture and Deformation Processes in Oil Sands", Proc. 4th UNITAR/UNDP Conf. On Heavy Crude and Tar Sands, Edmonton, Alberta, Vol.3, pp.41-53

Settari, A. (1989): "Physics and Modeling of Thermal Flow and Soil Mechanics in Unconsolidated Porous Media"; SPE Symposium On Reservoir Simulation in Houston, Texas, SPE 18420, pp.155-166

Settari, A. and Raisbeck, J.M. (1979): "Fracture Mechanics Analysis in In-Situ Oilsand Recovery"; JCPT, pp.85-94, April-June, 1979.

Settari, A. and Raisbeck, J.M. (1981):"Analysis and numerical modeling of hydraulic fracturing during cyclic steam stimulation in oilsands", JPT, Nov. 1981, pp.2201-2212

Settari, A., Ito, Y. and Jha, K.N. (1992): "Coupling of A Fracture Mechanics Model and A Thermal Reservoir Simulator For Tar Sands", JCPT, Vol.31, No.2, pp.20-27

Settari, A., Kry, P.R. and Yee, C-T(1989): "Coupling of Fluid Flow and Soil Behaviour To Model Injection into Uncemented Oilsands"; JCPT, 28(1), pp. 81-92, Jan.-Feb. 1989.

Shaffer, R.J., Heuze, F.E., Thorpe, R.K., Ingraffea, A.R., Nilson, R.H. (1987): "Models of Quasi-Static and Dynamic Fluid-Driven Fracturing in Jointed Rocks"; SEM/RILEM International Conference On Fracture of Concrete and Rock., (S.P.Shah and S.E. Swaetz Eds.), pp. 241-250, June 1987.

Sih, G.C. (1973): "Energy-Density Concept in Fracture Mechanics"; Engineering Fracture Mechanics, 5, 1037-1040, 1973.

Sih, G.C. (1973): "Some Basic Problems in Fracture Mechanics and New Concepts"; Engineering Fracture Mechanics, Vol.5, pp. 365-377, 1973.

Sih, G.C. (1974): "Strain-Energy-Density Factor Applied To Mixed Mode Crack Problems"; International Journal of Fracture, Vol.10, pp. 305-321, 1974.

Sih, G.C. (1975): "A Three Dimensional Strain Energy Density Factor Theory of Crack Propagation"; in Mechanics of Fracture, Vol.2, (M.K.Kassir and G.C.Sih Eds.), Noordhoff Int. Publ., The Netherlands, P.P.XV-LIII, 1975.

Sih, G.C. (1977): "Strain Energy Density Theory Applied To Plate Bending Problems"; in Mechanics of Fracture, Vol.3, (G.C.Sih Ed.), Noordhoff Int. Publ., The Netherlands, P.P.XVII-XLVIII, 1977.

Simo, J.C. and Ju, J.W. (1987): "Strain- and Stress-based Continuum Damage Models-Part I and II"; Int. J. Solids Structures, Vol. 23, No. 7, pp.821-869, 1987

Small, J.C., Booker, J.R. and Davis, E.H. (1976): "Elasto-Plastic Consolidation of Soil", Int. J. Solid. Struc., Vol.12, No.6, pp.431-448

Smith, R.N.L. (1991): "Basic Fracture Mechanics"; Butterworth Heinemann Press, 1991.

Sobkowicz, J. (1982): "Mechanics of Gassy Sediments", Ph.D. Thesis, Department of Civil Engineering, University of Alberta, Edmonton, 1982

Sobkowicz, J. and Morgenstern, N.R. (1984): "The Undrained Equilibrium Behaviour of Gassy Sediments", Can Geotech. J., Vol.21, No.3, pp.439-448

Sparks, A.D.W. (1963): "Theoretical Considerations of Stress Equations for Partly Saturated Soils", Third Conference for Africa on Soil Mech. and Found. Engg, Salisbury, 1963.

Spillete, A.G. (1965): "Heat Transfer During Hot Fluid Injection into An Oil Reservoir", JCPT, pp.213-217, Oct.-Dec.1965

Tannant, D.D. (1990): "Hydraulic Response of A Fracture Zone To Excavation-Induced Shear"; Ph.D. Thesis, Department of Civil Engineering, University of Alberta, Edmonton, 1990.

Terzaghi, K. (1925): "Erbaumechanik Auf Bodenphysikalischer Grundlage (Leipzig F. Deuticke 1925)", Principles of Soil Mechanics, Eng. News Record, A Series of Articles

Teufel, L.W. and Clark, J.A. (1984): "Hydraulic Fracture Propagation in Layered Rock: Experimental Studies of Fracture Containment", Society of Petroleum Engineers Journal, vol. 24, pp. 19-23, 1984

Thomas, G.W. (1977): "Principles of Hydrocarbon Reservoir Simulation", Tabir Publishers

Tortike,W.S. (1991): "Numerical Simulation of Thermal Multiphase Flow in An Elastoplastic Deforming Oil Reservoir", Ph.D. Thesis, Department of Mining, Metallurgical and Petroleum Engineering, University of Alberta

Vaughan, P.R. (1971): "The Use of Hydraulic Fracturing Tests To Detect Crack Formation in Embankment Dam Cores", Interim Report, Department of Civil Engineering, Imperial College, London, England, 1971

Vaziri, H.H. (1986):"Nonlinear temperature and consolidation analysis", Ph.D. Thesis, Department of Civil Engineering, University of British Columbia

Vaziri, H.H. (1988): "Coupled Fluid Flow and Stress Analysis of Oil Sands Subject To Heating", JCPT, Vol.27, No.5, pp.84-91

Vaziri, H.H. and Britto, A.M. (1992): "Theory and Application of A Fully Coupled Thermo-Hydro-Mechanical Finite Element Model", SPE, Paper 25306, July 1992

Veatch, R.W., Moschovidis, Z.A., Fast, C.R. (1989): "An Overview Over Hydraulic Fracturing", in Recent Advances in Hydraulic Fracturing; (J.L. Gidley, S.A. Holditch, D.E. Nierode and R.W. Veatch Eds.), SPE Monograph, 12, pp.1-38, 1989.

Wan, R., Chan, D.H. and Kosar, K.M. (1989): "A Constitutive Model For The Effective Stress-Strain Behaviour of Oil Sands", Pet. Soc. CIM, Paper No. 89-40-66, 40th ATM of CIM, Banff, May 1989

Wan, R., Chan, D.H. and Morgenstern, N.R. (1992): "Modeling Discontinuous Behaviour and Fault Formation in Geomaterials", Conference On Fractured and Jointed Rock Masses, Lake Tahoe, June 3-5, 1992, pp.328-324

Wan, R.G. (1990): "The Numerical Modeling of Shear Bands in Geological Materials", Ph.D. Thesis, Dept. of Civil Engineering, University of Alberta, Edmonton,1990.

Wan, R.G., Chan, D.H. and Morgenstern, N. (1989): "On The Numerical Modeling of The Development of Shear Band in Geomechanics"; Third International Symposium On Numerical Models in Geomechanics, Niagara Falls, Canada, pp.319-329, May 1989.

Warpinski, N.R. and Teufel, L.W. (1987): "Influence of Geologic Discontinuities on Hydraulic Fracture Propagation", Journal of Petroleum Technology, pp. 209-220, Feb. 1987

Warpinski, N.R., Clark, J.A., Schmidt, R.A. and Huddle, L.W. (1981): "Laboratory Investigation on the Effect of In-Situ Stresses on Hydraulic Fracture Containment", paper SPE 9834 presented at the 1981 SPE/DOE Low Permeability Symposium, Colorado, U.S.A., 1981

Warren, J.E. and Root, P.J. (1963): "The Behaviour of Naturally Fractured Reservoirs"; SPEJ, Trans., AIME, 228, pp. 245-255, Sept. 1963.

Wells, A.A. (1962): "Unstable Crack Propagation in Metals: Damage and Fast Fracture", Proc. of Crack Propagation Sym., The College of Aeronautics, Vol.1, pp.210-230, Cranfield, England

Wiles, T.D. and Roegiers, J.C. (1982): "Modeling of Hydraulic Fractures Under In-Situ Conditions Using A Displacement Discontinuity Approach", Proc. 33rd ATM, Pet. Soc. CIM, Paper No. 82-33-70, June 6-9, 1982

Wilson, C.R. and Witherspoon, P.A. (1970): "An Investigation of Laminar Flow in Fractured Rocks"; Geotechnical Report No. 70-6, Berkeley, 1970.

Witherspoon, P.A., Wang, J.S.Y., Iwai, K. and Gale, J.E. (1980): "Validity of Cubic Law For Fluid Flow in A Deformable Rock Fracture"; Water Resources Research, 16(6), pp. 1016-1024, 1980.

Zheltov, Y.P. and Khristianovitch, S.A. (1955): "On The Mechanism of Hydraulic Fracturing of An Oil-Bearing Stratum", Izvest. Akad. Nauk SSR, OTN, Vol. 5, pp. 3-41 (in Russian)

Zobak, M.D., Rummel, F., Jung, R. and Raliegh, C.B. (1977): "Laboratory Hydraulic Fracturing Experiments in Intact and Pre-Fractured Rock", Int. J. Rock Mech. Min. Sci. & Geomech. Abstr., vol. 14, pp. 49-58

Zu, J.Z. and Zienkiewicz, O.C. (1988): "Adaptive Techniques in the Finite Element Method", Commun. Appl. Num. Meth., vol. 4, pp. 197-204

Appendix A

Details of the finite element formulation

A.1 Rectangular Isoparametric Elements

For displacements 8-node elements are used. In this case the displacements U and V (in x and y directions respectively) at any point inside the element can be determined based on the nodal displacements as follows:

$$U=[N]\{U^*\}$$

$$\begin{Bmatrix} u \\ v \end{Bmatrix} = \begin{bmatrix} <\phi> & 0 \\ 0 & <\phi> \end{bmatrix} \begin{Bmatrix} u^* \\ v^* \end{Bmatrix} \tag{A-1}$$

or in expanded form:

$$\begin{Bmatrix} u \\ v \end{Bmatrix} = \begin{bmatrix} \phi 1 & 0 & \phi 2 & 0 & \phi 3 & 0 & \phi 4 & 0 & \phi 5 & 0 & \phi 6 & 0 & \phi 7 & 0 & \phi 8 & 0 \\ 0 & \phi 1 & 0 & \phi 2 & 0 & \phi 3 & 0 & \phi 4 & 0 & \phi 5 & 0 & \phi 6 & 0 & \phi 7 & 0 & \phi 8 \end{bmatrix} \times$$

$$< u1^* \quad v1^* \quad u2^* \quad v2^* \quad u3^* \quad v3^* \quad u4^* \quad v4^* \quad u5^* \quad v5^* \quad u6^* \quad v6^* \quad u7^* \quad v7^* \quad u8^* \quad v8^* >^T$$

(A-2)

Shape functions ϕ for 8-node rectangular elements (Figure A-1) are quadratic functions.

$$
\begin{aligned}
\phi 1 &= 0.25(1-\xi)(1-\eta)(-\xi-\eta-1)\\
\phi 2 &= 0.25(1+\xi)(1-\eta)(\xi-\eta-1)\\
\phi 3 &= 0.25(1+\xi)(1+\eta)(\xi+\eta+1)\\
\phi 4 &= 0.25(1-\xi)(1+\eta)(-\xi+\eta-1)\\
\phi 5 &= 0.5(1-\xi^2)(1-\eta)\\
\phi 6 &= 0.5(1-\eta^2)(1+\xi)\\
\phi 7 &= 0.5(1-\xi^2)(1+\eta)\\
\phi 8 &= 0.5(1-\eta^2)(1-\xi)
\end{aligned}
\qquad \text{(A-3)}
$$

Strains $\varepsilon_x, \varepsilon_y$, and γ_{xy} are derivatives of U and V as follows:

$$
\begin{Bmatrix} \varepsilon_x \\ \varepsilon_y \\ \gamma_{xy} \\ \varepsilon_z \end{Bmatrix} =
\begin{bmatrix}
\frac{\partial\psi 1}{\partial x} & 0 & \frac{\partial\psi 2}{\partial x} & 0 & \frac{\partial\psi 3}{\partial x} & 0 & \frac{\partial\psi 4}{\partial x} & 0 & \frac{\partial\psi 5}{\partial x} & 0 & \frac{\partial\psi 6}{\partial x} & 0 & \frac{\partial\psi 7}{\partial x} & 0 & \frac{\partial\psi 8}{\partial x} & 0 \\
0 & \frac{\partial\psi 1}{\partial y} & 0 & \frac{\partial\psi 2}{\partial y} & 0 & \frac{\partial\psi 3}{\partial y} & 0 & \frac{\partial\psi 4}{\partial y} & 0 & \frac{\partial\psi 5}{\partial y} & 0 & \frac{\partial\psi 6}{\partial y} & 0 & \frac{\partial\psi 7}{\partial y} & 0 & \frac{\partial\psi 8}{\partial y} \\
\frac{\partial\psi 1}{\partial y} & \frac{\partial\psi 1}{\partial x} & \frac{\partial\psi 2}{\partial y} & \frac{\partial\psi 2}{\partial x} & \frac{\partial\psi 3}{\partial y} & \frac{\partial\psi 3}{\partial x} & \frac{\partial\psi 4}{\partial y} & \frac{\partial\psi 4}{\partial x} & \frac{\partial\psi 5}{\partial y} & \frac{\partial\psi 5}{\partial x} & \frac{\partial\psi 6}{\partial y} & \frac{\partial\psi 6}{\partial x} & \frac{\partial\psi 7}{\partial y} & \frac{\partial\psi 7}{\partial x} & \frac{\partial\psi 8}{\partial y} & \frac{\partial\psi 8}{\partial x} \\
\frac{\phi_1}{X} & 0 & \frac{\phi_2}{X} & 0 & \frac{\phi_3}{X} & 0 & \frac{\phi_4}{X} & 0 & \frac{\phi_{5}}{X} & 0 & \frac{\phi_6}{X} & 0 & \frac{\phi_7}{X} & 0 & \frac{\phi_8}{X} & 0
\end{bmatrix}
$$

$$
\times \left\langle u_1^* \quad v_1^* \quad u_2^* \quad v_2^* \quad u_3^* \quad v_3^* \quad u_4^* \quad v_4^* \quad u_5^* \quad v_5^* \quad u_6^* \quad v_6^* \quad u_7^* \quad v_7^* \quad u_8^* \quad v_8^* \right\rangle^T
$$

(A-4)

where $X = \sum_{k=1}^{8} \phi_k x_k$. The above equation can be written in a compact form as

$\{\varepsilon\} = [B]\{U^*\}$.

Volumetric strain can be defined as $\varepsilon_V = \varepsilon_X + \varepsilon_Y + \varepsilon_Z$. Now having found the strain components ε_v can be evaluated as follows:

$$
\begin{aligned}
\varepsilon_x &= B_{11}u_1^* + B_{12}v_1^* + B_{13}u_2^* + B_{14}v_2^* + B_{15}u_3^* + \ldots\\
\varepsilon_y &= B_{21}u_1^* + B_{22}v_1^* + B_{23}u_2^* + B_{24}v_2^* + B_{25}u_3^* + \ldots\\
\varepsilon_z &= 0
\end{aligned}
\qquad \text{(A-5)}
$$

Therefore:

$$
\begin{aligned}
\varepsilon_v &= (B_{11}u_1^* + B_{12}v_1^* + B_{13}u_2^* + B_{14}v_2^* + \ldots) + (B_{21}u_1^* + B_{22}v_1^* + B_{23}u_2^* + B_{24}v_2^* + \ldots)\\
\varepsilon_v &= \left[(B_{11}+B_{21}) \quad (B_{12}+B_{22}) \quad (B_{13}+B_{23}) \quad (B_{14}+B_{24})\ldots\right] \times \left\langle u_1^* \quad v_1^* \quad u_2^* \quad v_2^* \ldots \right\rangle^T
\end{aligned}
$$

(A-6)

For calculating the derivative of shape functions with respect to x and y axis, coordinates should be transformed using the Jacobian matrix. By using isoparametric formulation the coordinates of any node inside the element can be evaluated based on the nodal coordinates:

$$< x \quad y> = <\phi > [\{x^*\} \quad \{y^*\}] \tag{A-7}$$

Now from simple rule of differentiation one can write:

$$\langle dx \quad dy \rangle = \langle d\xi \quad d\eta \rangle \begin{bmatrix} \frac{\partial x}{\partial \xi} & \frac{\partial y}{\partial \xi} \\ \frac{\partial x}{\partial \eta} & \frac{\partial y}{\partial \eta} \end{bmatrix} = \langle d\xi \quad d\eta \rangle [J] \tag{A-8}$$

For any arbitrary function 'f' one can write:

$$\begin{Bmatrix} \frac{\partial f}{\partial \xi} \\ \frac{\partial f}{\partial \eta} \end{Bmatrix} = \begin{bmatrix} \frac{\partial x}{\partial \xi} & \frac{\partial y}{\partial \xi} \\ \frac{\partial x}{\partial \eta} & \frac{\partial y}{\partial \eta} \end{bmatrix} \begin{Bmatrix} \frac{\partial f}{\partial x} \\ \frac{\partial f}{\partial y} \end{Bmatrix} = [J] \begin{Bmatrix} \frac{\partial f}{\partial x} \\ \frac{\partial f}{\partial y} \end{Bmatrix} \tag{A-9}$$

where "f" represents any arbitrary function. By substituting $<\phi>$ or ϕ_1, ϕ_2, ϕ_3,... for 'f' one can obtain

$$\begin{bmatrix} \frac{\partial <\phi>}{\partial x} \\ \frac{\partial <\phi>}{\partial y} \end{bmatrix} = [J]^{-1} \begin{bmatrix} \frac{\partial <\phi>}{\partial \xi} \\ \frac{\partial <\phi>}{\partial \eta} \end{bmatrix} \tag{A-10}$$

where:

$$[J] = \begin{bmatrix} \frac{\partial x}{\partial \xi} & \frac{\partial y}{\partial \xi} \\ \frac{\partial x}{\partial \eta} & \frac{\partial y}{\partial \eta} \end{bmatrix} = \begin{Bmatrix} \frac{\partial}{\partial \xi} \\ \frac{\partial}{\partial \eta} \end{Bmatrix} \langle x \quad y \rangle \tag{A-11}$$

and by using (A-7) the Jacobian can be determined as :

$$[J] = \begin{Bmatrix} \frac{\partial <\phi>}{\partial \xi} \\ \frac{\partial <\phi>}{\partial \eta} \end{Bmatrix} \langle \{x^*\} \quad \{y^*\} \rangle \tag{A-12}$$

For eight node rectangular element:

$$[J]=\begin{bmatrix}\sum_{i=1}^{8}\frac{\partial\phi_i}{\partial\xi}x_i & \sum_{i=1}^{8}\frac{\partial\phi_i}{\partial\xi}y_i\\ \sum_{i=1}^{8}\frac{\partial\phi_i}{\partial\eta}x_i & \sum_{i=1}^{8}\frac{\partial\phi_i}{\partial\eta}y_i\end{bmatrix} \tag{A-13}$$

$$[J]^{-1}=\frac{[J^c]^T}{|J|}=\frac{\begin{bmatrix}\sum_{i=1}^{8}\frac{\partial\phi_i}{\partial\eta}y_i & \sum_{i=1}^{8}\frac{\partial\phi_i}{\partial\xi}y_i\\ \sum_{i=1}^{8}\frac{\partial\phi_i}{\partial\eta}x_i & \sum_{i=1}^{8}\frac{\partial\phi_i}{\partial\xi}x_i\end{bmatrix}}{\left((\sum_{i=1}^{8}\frac{\partial\phi_i}{\partial\xi}x_i)(\sum_{i=1}^{8}\frac{\partial\phi_i}{\partial\eta}y_i)-(\sum_{i=1}^{8}\frac{\partial\phi_i}{\partial\xi}y_i)(\sum_{i=1}^{8}\frac{\partial\phi_i}{\partial\eta}x_i)\right)} \tag{A-14}$$

For pore fluid pressure and temperature, 4-node elements (Figure A-2) are used. Pore fluid pressure 'P' and temperature 'T' at any point inside the element can be determined based on the nodal values as follows:

$$P=<\phi>\{P^*\}$$
$$P=\langle\phi_1\quad\phi_2\quad\phi_3\quad\phi_4\quad 0\quad 0\quad 0\quad 0\rangle\langle P_1^*\quad P_2^*\quad P_3^*\quad P_4^*\quad P_5^*\quad P_6^*\quad P_7^*\quad P_8^*\rangle^T \tag{A-15}$$

and similarly:

$$T=<\phi>\{T^*\}$$
$$T=\langle\phi_1\quad\phi_2\quad\phi_3\quad\phi_4\quad 0\quad 0\quad 0\quad 0\rangle\langle T_1^*\quad T_2^*\quad T_3^*\quad T_4^*\quad T_5^*\quad T_6^*\quad T_7^*\quad T_8^*\rangle^T \tag{A-16}$$

Also their derivatives can be expressed as follows:

$$\begin{Bmatrix}\frac{\partial P}{\partial x}\\ \frac{\partial P}{\partial y}\end{Bmatrix}=\begin{bmatrix}\frac{\partial\phi_1}{\partial x} & \frac{\partial\phi_2}{\partial x} & \frac{\partial\phi_3}{\partial x} & \frac{\partial\phi_4}{\partial x} & 0 & 0 & 0 & 0\\ \frac{\partial\phi_1}{\partial y} & \frac{\partial\phi_2}{\partial y} & \frac{\partial\phi_3}{\partial y} & \frac{\partial\phi_4}{\partial y} & 0 & 0 & 0 & 0\end{bmatrix}\begin{Bmatrix}P_1^*\\ P_2^*\\ P_3^*\\ P_4^*\\ P_5^*\\ P_6^*\\ P_7^*\\ P_8^*\end{Bmatrix} \tag{A-17}$$

$$\begin{Bmatrix} \frac{\partial T}{\partial x} \\ \frac{\partial T}{\partial y} \end{Bmatrix} = \begin{bmatrix} \frac{\partial \phi_1}{\partial x} & \frac{\partial \phi_2}{\partial x} & \frac{\partial \phi_3}{\partial x} & \frac{\partial \phi_4}{\partial x} & 0 & 0 & 0 & 0 \\ \frac{\partial \phi_1}{\partial y} & \frac{\partial \phi_2}{\partial y} & \frac{\partial \phi_3}{\partial y} & \frac{\partial \phi_4}{\partial y} & 0 & 0 & 0 & 0 \end{bmatrix} \begin{Bmatrix} T_1^* \\ T_2^* \\ T_3^* \\ T_4^* \\ T_5^* \\ T_6^* \\ T_7^* \\ T_8^* \end{Bmatrix} \tag{A-18}$$

Shape functions $<\phi>$ for 4-node rectangular elements are linear functions as follows:

$$\begin{aligned} \phi_1 &= \frac{1}{4}(1-\xi)(1-\eta) \\ \phi_2 &= \frac{1}{4}(1+\xi)(1-\eta) \\ \phi_3 &= \frac{1}{4}(1+\xi)(1+\eta) \\ \phi_4 &= \frac{1}{4}(1-\xi)(1+\eta) \end{aligned} \tag{A-19}$$

In order to obtain the derivatives of shape functions with respect to x and y, Jacobian matrix can be determined in the same way as described earlier.

$$[J] = \begin{bmatrix} \sum_{i=1}^{4} \frac{\partial \phi_i}{\partial \xi} x_i & \sum_{i=1}^{4} \frac{\partial \phi_i}{\partial \xi} y_i \\ \sum_{i=1}^{4} \frac{\partial \phi_i}{\partial \eta} x_i & \sum_{i=1}^{4} \frac{\partial \phi_i}{\partial \eta} y_i \end{bmatrix} \tag{A-20}$$

Numerical integration is employed to determine the integrals for each element by using Gauss sample points in two directions.

A.2 Triangular Elements

For displacements 6-node elements are used (Figure A-3). Displacements u and v at any points inside the element are:

$$\begin{aligned} U &= NU^* \\ \begin{Bmatrix} u \\ v \end{Bmatrix} &= \begin{bmatrix} <\phi> & 0 \\ 0 & <\phi> \end{bmatrix} \begin{Bmatrix} u^* \\ v^* \end{Bmatrix} \end{aligned} \tag{A-21}$$

or

$$\begin{Bmatrix} u \\ v \end{Bmatrix} = \begin{bmatrix} \phi_1 & 0 & \phi_2 & 0 & \phi_3 & 0 & \phi_4 & 0 & \phi_5 & 0 & \phi_6 & 0 \\ 0 & \phi_1 & 0 & \phi_2 & 0 & \phi_3 & 0 & \phi_4 & 0 & \phi_5 & 0 & \phi_6 \end{bmatrix} \times \langle u_1^* \quad v_1^* \quad u_2^* \quad v_2^* \quad u_3^* \quad v_3^* \quad u_4^* \quad v_4^* \quad u_5^* \quad v_5^* \quad u_6^* \quad v_6^* \rangle^T \tag{A-22}$$

Shape functions $<\phi>$ for 6-node triangular elements are as follows (area coordinates are being used):

$$\begin{aligned} \phi_1 &= \zeta_1(2\zeta_1 - 1) \\ \phi_2 &= \zeta_2(2\zeta_2 - 1) \\ \phi_3 &= \zeta_3(2\zeta_3 - 1) \\ \phi_4 &= 4\zeta_1\zeta_2 \\ \phi_5 &= 4\zeta_2\zeta_3 \\ \phi_6 &= 4\zeta_3\zeta_1 \end{aligned} \tag{A-23}$$

strains are $\varepsilon = B\,U^*$ i.e.,

$$\begin{Bmatrix} \varepsilon_x \\ \varepsilon_y \\ \gamma_{xy} \end{Bmatrix} = \begin{bmatrix} \frac{\partial\phi_1}{\partial x} & 0 & \frac{\partial\phi_2}{\partial x} & 0 & \frac{\partial\phi_3}{\partial x} & 0 & \frac{\partial\phi_4}{\partial x} & 0 & \frac{\partial\phi_5}{\partial x} & 0 & \frac{\partial\phi_6}{\partial x} & 0 \\ 0 & \frac{\partial\phi_1}{\partial y} & 0 & \frac{\partial\phi_2}{\partial y} & 0 & \frac{\partial\phi_3}{\partial y} & 0 & \frac{\partial\phi_4}{\partial y} & 0 & \frac{\partial\phi_5}{\partial y} & 0 & \frac{\partial\phi_6}{\partial y} \\ \frac{\partial\phi_1}{\partial y} & \frac{\partial\phi_1}{\partial x} & \frac{\partial\phi_2}{\partial y} & \frac{\partial\phi_2}{\partial x} & \frac{\partial\phi_3}{\partial y} & \frac{\partial\phi_3}{\partial x} & \frac{\partial\phi_4}{\partial y} & \frac{\partial\phi_4}{\partial x} & \frac{\partial\phi_5}{\partial y} & \frac{\partial\phi_5}{\partial x} & \frac{\partial\phi_6}{\partial y} & \frac{\partial\phi_6}{\partial x} \end{bmatrix} \times \langle u_1^* \quad v_1^* \quad u_2^* \quad v_2^* \quad u_3^* \quad v_3^* \quad u_4^* \quad v_4^* \quad u_5^* \quad v_5^* \quad u_6^* \quad v_6^* \rangle^T \tag{A-24}$$

For calculating the derivative of shape functions with respect to x and y, the Jacobian matrix for triangular elements is to be determined in terms of area coordinates.

$$\begin{Bmatrix} \frac{\partial<\phi>}{\partial x} \\ \frac{\partial<\phi>}{\partial y} \end{Bmatrix} = [J]^{-1} \begin{bmatrix} 1 & 0 & -1 \\ 0 & 1 & -1 \end{bmatrix} \begin{Bmatrix} \frac{\partial<\phi>}{\partial\zeta_1} \\ \frac{\partial<\phi>}{\partial\zeta_2} \\ \frac{\partial<\phi>}{\partial\zeta_3} \end{Bmatrix} \tag{A-25}$$

$$\text{where } [J]=\begin{bmatrix}1 & 0 & -1\\ 0 & 1 & -1\end{bmatrix}[J]^{*}=\begin{bmatrix}1 & 0 & -1\\ 0 & 1 & -1\end{bmatrix}\begin{Bmatrix}\dfrac{\partial<\phi>}{\partial\zeta_1}\\ \dfrac{\partial<\phi>}{\partial\zeta_2}\\ \dfrac{\partial<\phi>}{\partial\zeta_3}\end{Bmatrix}\left\langle\{x^{*}\}\quad\{y^{*}\}\right\rangle \tag{A-26}$$

In more details:

$$[J]=\begin{bmatrix}1 & 0 & -1\\ 0 & 1 & -1\end{bmatrix}\begin{bmatrix}\dfrac{\partial\phi_1}{\partial\zeta_1} & \dfrac{\partial\phi_2}{\partial\zeta_1} & \dfrac{\partial\phi_3}{\partial\zeta_1} & \dfrac{\partial\phi_4}{\partial\zeta_1} & \dfrac{\partial\phi_5}{\partial\zeta_1} & \dfrac{\partial\phi_6}{\partial\zeta_1}\\ \dfrac{\partial\phi_1}{\partial\zeta_2} & \dfrac{\partial\phi_2}{\partial\zeta_2} & \dfrac{\partial\phi_3}{\partial\zeta_2} & \dfrac{\partial\phi_4}{\partial\zeta_2} & \dfrac{\partial\phi_5}{\partial\zeta_2} & \dfrac{\partial\phi_6}{\partial\zeta_2}\\ \dfrac{\partial\phi_1}{\partial\zeta_3} & \dfrac{\partial\phi_2}{\partial\zeta_3} & \dfrac{\partial\phi_3}{\partial\zeta_3} & \dfrac{\partial\phi_4}{\partial\zeta_3} & \dfrac{\partial\phi_5}{\partial\zeta_3} & \dfrac{\partial\phi_6}{\partial\zeta_3}\end{bmatrix}\begin{bmatrix}x_1 & y_1\\ x_2 & y_2\\ x_3 & y_3\\ x_4 & y_4\\ x_5 & y_5\\ x_6 & y_6\end{bmatrix} \tag{A-27}$$

For pore fluid pressures and temperatures, 3-node element (*CST*) is used.

$P=<\phi>\{P^{*}\}$

$$P=\left\langle\phi_1\quad\phi_2\quad\phi_3\quad 0\quad 0\quad 0\right\rangle\left\langle P_1^{*}\quad P_2^{*}\quad P_3^{*}\quad P_4^{*}\quad P_5^{*}\quad P_6^{*}\right\rangle^{T} \tag{A-28}$$

$T=<\phi>\{T^{*}\}$

$$T=\left\langle\phi_1\quad\phi_2\quad\phi_3\quad 0\quad 0\quad 0\right\rangle\left\langle T_1^{*}\quad T_2^{*}\quad T_3^{*}\quad T_4^{*}\quad T_5^{*}\quad T_6^{*}\right\rangle^{T} \tag{A-29}$$

Also:

$$\begin{Bmatrix}\dfrac{\partial P}{\partial x}\\ \dfrac{\partial P}{\partial y}\end{Bmatrix}=\begin{bmatrix}\dfrac{\partial\phi_1}{\partial x} & \dfrac{\partial\phi_2}{\partial x} & \dfrac{\partial\phi_3}{\partial x} & 0 & 0 & 0\\ \dfrac{\partial\phi_1}{\partial y} & \dfrac{\partial\phi_2}{\partial y} & \dfrac{\partial\phi_3}{\partial y} & 0 & 0 & 0\end{bmatrix}\begin{Bmatrix}P_1^{*}\\ P_2^{*}\\ P_3^{*}\\ P_4^{*}\\ P_5^{*}\\ P_6^{*}\end{Bmatrix} \tag{A-30}$$

$$\begin{Bmatrix}\dfrac{\partial T}{\partial x}\\ \dfrac{\partial T}{\partial y}\end{Bmatrix}=\begin{bmatrix}\dfrac{\partial\phi_1}{\partial x} & \dfrac{\partial\phi_2}{\partial x} & \dfrac{\partial\phi_3}{\partial x} & 0 & 0 & 0\\ \dfrac{\partial\phi_1}{\partial y} & \dfrac{\partial\phi_2}{\partial y} & \dfrac{\partial\phi_3}{\partial y} & 0 & 0 & 0\end{bmatrix}\begin{Bmatrix}T_1^{*}\\ T_2^{*}\\ T_3^{*}\\ T_4^{*}\\ T_5^{*}\\ T_6^{*}\end{Bmatrix} \tag{A-31}$$

Shape functions for *CST* are as follows:

$$\begin{aligned}\phi_1 &= \zeta_1 \\ \phi_2 &= \zeta_2 \\ \phi_3 &= \zeta_3\end{aligned} \tag{A-32}$$

Jacobian matrix for *CST* in terms of area coordinates will be:

$$[J] = \begin{bmatrix}1 & 0 & -1 \\ 0 & 1 & -1\end{bmatrix}[J^*] = \begin{bmatrix}1 & 0 & -1 \\ 0 & 1 & -1\end{bmatrix}\begin{Bmatrix}\dfrac{\partial <\phi>}{\partial \zeta_1} \\ \dfrac{\partial <\phi>}{\partial \zeta_2} \\ \dfrac{\partial <\phi>}{\partial \zeta_3}\end{Bmatrix}\begin{Bmatrix}\{x^*\} & \{y^*\}\end{Bmatrix} \tag{A-33}$$

In more details:

$$[J] = \begin{bmatrix}1 & 0 & -1 \\ 0 & 1 & -1\end{bmatrix}\begin{bmatrix}\dfrac{\partial \phi_1}{\partial \zeta_1} & \dfrac{\partial \phi_2}{\partial \zeta_1} & \dfrac{\partial \phi_3}{\partial \zeta_1} \\ \dfrac{\partial \phi_1}{\partial \zeta_2} & \dfrac{\partial \phi_2}{\partial \zeta_2} & \dfrac{\partial \phi_3}{\partial \zeta_2} \\ \dfrac{\partial \phi_1}{\partial \zeta_3} & \dfrac{\partial \phi_2}{\partial \zeta_3} & \dfrac{\partial \phi_3}{\partial \zeta_3}\end{bmatrix}\begin{bmatrix}x_1 & y_1 \\ x_2 & y_2 \\ x_3 & y_3\end{bmatrix} \tag{A-34}$$

This Jacobian matrix will be inserted in (A-25). Determination of integrals for triangular elements is confined to the pattern shown for 4 integration points. This leads to a cubic numerical integration.

A.3 Boundary Conditions

Boundary conditions may be applied on one or more sides of the element (Figure A-4). There are three types of boundary conditions namely surface traction, fluid flux, and heat flux. For each of these there exists an integral which has to be numerically evaluated:

$$\int_{S_e} [N]^T \{\bar{t}_S\} dS = \{T_S\} \tag{A-35}$$

$$\int_{S_e} \{N_F^T\} \rho_f < \bar{v} > \{n\} dS_e = \{N_e\} \tag{A-36}$$

$$\int_{S_L} \{N_T^T\} < \bar{L}_e > \{n\} dS_L = \{N_L\} \tag{A-37}$$

Apart from ρ_t and ϕ_t, which are some values measured at time 't' at the Gauss points, the rest are the shape functions N and N_P (or N_T) and a vector of known values of traction (t_S), fluid velocity (v) and volumetric heat flux (L_e) at the boundaries.

A.3.1 Traction boundary condition

According to the Figure(A-5) one can write:

$$dS=(\text{thickness}).(dx^2+dy^2)^{1/2}$$

$$dS=\text{thick}\{(dx/d\xi)^2+(dy/d\xi)^2\}^{1/2}.d\xi \tag{A-38}$$

$$dS=\text{thick.det}\, J.d\xi$$

For side 1-2 (η=-1 , ξ varies):

$$\phi_1 = -\frac{\xi}{2}(1-\xi), \phi_2 = \frac{\xi}{2}(1+\xi), \phi_3 = 0, \phi_4 = 0, \phi_5 = (1-\xi)(1+\xi), \phi_6 = 0, \phi_7 = 0, \phi_8 = 0 \tag{A-39}$$

For side 2-3 (ξ=+1 ,η varies):

$$\phi_1 = 0, \phi_2 = -\frac{\eta}{2}(1-\eta), \phi_3 = \frac{\eta}{2}(1+\eta), \phi_4 = 0, \phi_5 = 0, \phi_6 = (1+\eta)(1-\eta), \phi_7 = 0, \phi_8 = 0 \tag{A-40}$$

For side 3-4 (η=+1 , ξ varies):

$$\phi_1 = 0, \phi_2 = 0, \phi_3 = \frac{\xi}{2}(1+\xi), \phi_4 = -\frac{\xi}{2}(1-\xi), \phi_5 = 0, \phi_6 = 0, \phi_7 = (1-\xi)(1+\xi), \phi_8 = 0 \tag{A-41}$$

For side 4-1 (ξ=-1 , η varies):

$$\phi_1 = -\frac{\eta}{2}(1-\eta), \phi_2 = 0, \phi_3 = 0, \phi_4 = \frac{\eta}{2}(1+\eta), \phi_5 = 0, \phi_6 = 0, \phi_7 = 0, \phi_8 = (1+\eta)(1-\eta) \tag{A-42}$$

For instance for side 1-2 the shape function *[N]* would be:

$$[N]=\begin{bmatrix} -\frac{\xi}{2}(1-\xi) & 0 & \frac{\xi}{2}(1+\xi) & 0 & 0\ 0\ 0\ 0 & (1-\xi)(1+\xi) & 0 & 0\ 0\ 0\ 0\ 0\ 0 \\ 0 & -\frac{\xi}{2}(1-\xi) & 0 & \frac{\xi}{2}(1-\xi) & 0\ 0\ 0\ 0 & 0 & (1-\xi)(1+\xi) & 0\ 0\ 0\ 0\ 0\ 0 \end{bmatrix}$$

(A-43)

Assuming a 'parabolic' stress distribution on the element side on which traction 't_S' is applied.

$$\{\bar{t}_S\}=\begin{Bmatrix}\bar{t}_X\\ \bar{t}_S\end{Bmatrix} \tag{A-44}$$

$$t_X = a\xi^2 + b\xi + c \tag{A-45}$$

ξ=-1 ; t_X=XF1 $\qquad$ a=0.5(XF1-2XF2+XF3)

ξ=0 ; t_X=XF2 $\qquad$ ===> $\qquad$ b=0.5(XF3-XF1)

ξ=+1 ; t_X=XF3 $\qquad$ c=XF2

Therefore: $$t_x = \frac{(XF1-2XF2+XF3)}{2}\xi^2 + \frac{(XF3-XF1)}{2}\xi + XF2 \tag{A-46}$$

Similarly $$t_Y = \frac{(YF1-2YF2+YF3)}{2}\xi^2 + \frac{(YF3-YF1)}{2}\xi + YF2 \tag{A-47}$$

Therefore $\{\bar{t}_S\}$ can be introduced as follows:

$$\{\bar{t}_S\}=\begin{Bmatrix}\frac{[XF1-2(XF2)+XF3]}{2}\xi^2 + \frac{(XF3-XF1)}{2}\xi + XF2\\ \frac{[YF1-2(YF2)+YF3]}{2}\xi^2 + \frac{(YF3-YF1)}{2}\xi + YF2\end{Bmatrix} \tag{A-48}$$

Derivatives $dx/d\xi$ and $dy/d\xi$ are:

For side 1-2

$$\frac{dx}{d\xi}=[-\frac{(1-\xi)}{2}+\frac{\xi}{2}]x_1+[\frac{1+\xi}{2}+\frac{\xi}{2}]x_2+[-(1+\xi)+(1-\xi)]x_3=(\xi-\frac{1}{2})x_1+(\xi+\frac{1}{2})x_2-2\xi x_3 \tag{A-49}$$

$$\frac{dy}{d\xi}=[-\frac{(1-\xi)}{2}+\frac{\xi}{2}]y_1+[\frac{1+\xi}{2}+\frac{\xi}{2}]y_2+[-(1+\xi)+(1-\xi)]y_3=(\xi-\frac{1}{2})y_1+(\xi+\frac{1}{2})y_2-2\xi y_3 \tag{A-50}$$

For side 2-3

$$\frac{dx}{d\eta} = (\eta - \frac{1}{2})x_2 + (\eta + \frac{1}{2})x_3 - 2\eta x_6 \qquad \text{(A-51)}$$

$$\frac{dy}{d\eta} = (\eta - \frac{1}{2})y_2 + (\eta + \frac{1}{2})y_3 - 2\eta y_6 \qquad \text{(A-52)}$$

For side 3-4

$$\frac{dx}{d\xi} = (\xi + \frac{1}{2})x_3 + (\xi - \frac{1}{2})x_4 - 2\xi x_7 \qquad \text{(A-53)}$$

$$\frac{dy}{d\xi} = (\xi + \frac{1}{2})y_3 + (\xi - \frac{1}{2})y_4 - 2\xi y_7 \qquad \text{(A-54)}$$

For side 4-1

$$\frac{dx}{d\eta} = (\eta - \frac{1}{2})x_1 + (\eta + \frac{1}{2})x_4 - 2\eta x_8 \qquad \text{(A-55)}$$

$$\frac{dy}{d\eta} = (\eta - \frac{1}{2})y_1 + (\eta + \frac{1}{2})y_4 - 2\eta y_8 \qquad \text{(A-56)}$$

Therefore, if the boundary traction is specified on side 1-2 of the element, the general form of equation (A-35) to be integrated numerically would be:

$$\{T\} = Thick.\sum_{-1}^{1}\int \begin{bmatrix} -\frac{\xi}{2}(1-\xi) & 0 & \frac{\xi}{2}(1+\xi) & 0 & \dots & 0 \\ 0 & -\frac{\xi}{2}(1-\xi) & 0 & \frac{\xi}{2}(1+\xi) & \dots & 0 \end{bmatrix}^T$$
$$\begin{Bmatrix} \frac{XF1 - 2(XF2) + XF3}{2}\xi^2 + \frac{XF3 - XF1}{2}\xi + XF2 \\ \frac{YF1 - 2(YF2) + YF3}{2}\xi^2 + \frac{YF3 - YF1}{2}\xi + YF2 \end{Bmatrix} \sqrt{((\xi - \frac{1}{2})x_1 + (\xi + \frac{1}{2})x_2 - 2\xi x_5)^2 + ((\xi - \frac{1}{2})y_1 + (\xi + \frac{1}{2})y_2 - 2\xi y_5)^2}\, d\xi$$

(A-57)

If the element is triangular (Figure A-6), the procedure is the same, but the shape function should be modified as follows:

For side 1-2

$$\phi_1 = -\frac{\xi}{2}(1-\xi), \phi_2 = \frac{\xi}{2}(1+\xi), \phi_3 = 0, \phi_4 = (1-\xi)(1+\xi), \phi_5 = 0, \phi_6 = 0 \qquad \text{(A-58)}$$

For side 2-3

$$\phi_1 = 0, \phi_2 = -\frac{\eta}{2}(1-\eta), \phi_3 = \frac{\eta}{2}(1+\eta), \phi_4 = 0, \phi_5 = (1-\eta)(1+\eta), \phi_6 = 0 \qquad \text{(A-59)}$$

For side 3-1

$$\phi_1 = -\frac{\eta}{2}(1-\eta), \phi_2 = 0, \phi_3 = \frac{\eta}{2}(1+\eta), \phi_4 = 0, \phi_5 = 0, \phi_6 = (1+\eta)(1-\eta) \qquad \text{(A-60)}$$

For example, for side 1-2 matrix *[N]* representing shape functions would be:

$$[N] = \begin{bmatrix} -\frac{\xi}{2}(1-\xi) & 0 & \frac{\xi}{2}(1+\xi) & 0 & 0 & 0 & (1-\xi)(1+\xi) & 0 & 0 & 0 & 0 & 0 \\ 0 & -\frac{\xi}{2}(1-\xi) & 0 & \frac{\xi}{2}(1+\xi) & 0 & 0 & 0 & (1-\xi)(1+\xi) & 0 & 0 & 0 & 0 \end{bmatrix} \qquad \text{(A-61)}$$

A.3.2 Flow and heat boundary conditions

Since only the normal component of fluid flow and/or heat flow can enter the medium (elements), it is assumed that flow and heat boundary conditions are given in the direction normal to the boundary. For example (A-37) can be written as follows:

$$\{N_L\} = \sum_e \int_{S_{L_e}} \{N_T^T\} < \bar{L}_e > \{n\} dS = \sum_e \int_{S_{L_e}} \{N_T^T\} < \bar{L}_{e_X}, \bar{L}_{e_Y} > \begin{Bmatrix} n_X \\ n_Y \end{Bmatrix} dS =$$

$$\sum_e \int_{S_{L_e}} \{N_T^T\} \bar{L}_e dS = \sum_e \int_{S_{L_e}} \{N_T^T\} \bar{L}_e \sqrt{dx^2 + dy^2} = \sum_e \int_{-1}^{+1} \{N_T^T\} \bar{L}_e \sqrt{(\frac{dx}{d\xi})^2 + (\frac{dy}{d\xi})^2}\, d\xi \qquad \text{(A-62)}$$

For this class of boundary conditions 4-node rectangular elements are being used, so the shape functions are :

For side 1-2 (η=-1 ,ξ variable)

$$\phi_1 = \frac{1-\xi}{2}, \phi_2 = \frac{1+\xi}{2}, \phi_3 = 0, \phi_4 = 0, \phi_5 = 0, \phi_6 = 0, \phi_7 = 0, \phi_8 = 0 \qquad \text{(A-63)}$$

For side 2-3 (ξ=+1 , η variable)

$$\phi_1 = 0, \phi_2 = \frac{1-\eta}{2}, \phi_3 = \frac{1+\eta}{2}, \phi_4 = 0, \phi_5 = 0, \phi_6 = 0, \phi_7 = 0, \phi_8 = 0 \qquad \text{(A-64)}$$

For side 3-4 (η=+1 , ξ variable)

$$\phi_1 = 0, \phi_2 = 0, \phi_3 = \frac{1+\xi}{2}, \phi_4 = \frac{1-\xi}{2}, \phi_5 = 0, \phi_6 = 0, \phi_7 = 0, \phi_8 = 0 \qquad \text{(A-65)}$$

For side 4-1 (ξ=-1 , η variable)

$$\phi_1 = \frac{1-\eta}{2}, \phi_2 = 0, \phi_3 = 0, \phi_4 = \frac{1+\eta}{2}, \phi_5 = 0, \phi_6 = 0, \phi_7 = 0, \phi_8 = 0 \qquad \text{(A-66)}$$

Shape function *[N]* for sides of the element are:

Side 1-2 $$[N_T]=\left\langle \frac{1-\xi}{2} \quad \frac{1+\xi}{2} \quad 0 \quad 0 \quad 0 \quad 0 \quad 0 \quad 0 \right\rangle \tag{A-67}$$

Side 2-3 $$[N_T]=\left\langle 0 \quad \frac{1-\eta}{2} \quad \frac{1+\eta}{2} \quad 0 \quad 0 \quad 0 \quad 0 \quad 0 \right\rangle \tag{A-68}$$

Side 3-4 $$[N_T]=\left\langle 0 \quad 0 \quad \frac{1+\xi}{2} \quad \frac{1-\xi}{2} \quad 0 \quad 0 \quad 0 \quad 0 \right\rangle \tag{A-69}$$

Side 4-1 $$[N_T]=\left\langle \frac{1-\eta}{2} \quad 0 \quad 0 \quad \frac{1+\eta}{2} \quad 0 \quad 0 \quad 0 \quad 0 \right\rangle \tag{A-70}$$

$\bar{L}_e$ volumetric thermal energy flux normal to the surface S_{le} on the element sides are:

Side 1-2 $$\bar{L}_e = \frac{1-\xi}{2}\bar{L}_{em_1} + \frac{1+\xi}{2}\bar{L}_{em_2} \tag{A-71}$$

Side 2-3 $$\bar{L}_e = \frac{1-\eta}{2}\bar{L}_{em_2} + \frac{1+\eta}{2}\bar{L}_{em_3} \tag{A-72}$$

Side 3-4 $$\bar{L}_e = \frac{1+\xi}{2}\bar{L}_{em_3} + \frac{1-\xi}{2}\bar{L}_{em_4} \tag{A-73}$$

Side 4-1 $$\bar{L}_e = \frac{1-\eta}{2}\bar{L}_{em_4} + \frac{1+\eta}{2}\bar{L}_{em_1} \tag{A-74}$$

Where $dS=\sqrt{dx^2+dy^2} = \sqrt{(\frac{dx}{d\xi})^2+(\frac{dy}{d\xi})^2}.d\xi$ (A-75)

Side 1-2 $$\frac{dx}{d\xi} = \frac{dNx^*}{d\xi} = \frac{dN}{d\xi}x^* = -\frac{1}{2}x_1 + \frac{1}{2}x_2 \tag{A-76}$$

$$\frac{dy}{d\xi} = \frac{dNy^*}{d\xi} = \frac{dN}{d\xi}y^* = -\frac{1}{2}y_1 + \frac{1}{2}y_2 \tag{A-77}$$

Side 2-3 $$\frac{dx}{d\eta} = -\frac{1}{2}x_2 + \frac{1}{2}x_3 \tag{A-78}$$

$$\frac{dy}{d\eta} = -\frac{1}{2}y_2 + \frac{1}{2}y_3 \tag{A-79}$$

Side 3-4 $$\frac{dx}{d\xi} = \frac{1}{2}x_3 - \frac{1}{2}x_4 \tag{A-80}$$

$$\frac{dy}{d\xi} = \frac{1}{2}y_3 - \frac{1}{2}y_4 \tag{A-81}$$

Side 4-1 $$\frac{dx}{d\eta} = -\frac{1}{2}x_1 + \frac{1}{2}x_4 \tag{A-82}$$

$$\frac{dy}{d\eta} = -\frac{1}{2}y_1 + \frac{1}{2}y_4 \tag{A-83}$$

Therefore the integral for side 1-2, for instance, would be:

$$\begin{Bmatrix} N_{L_1} \\ N_{L_2} \\ N_{L_3} \\ N_{L_4} \\ N_{L_5} \\ N_{L_6} \\ N_{L_7} \\ N_{L_8} \end{Bmatrix} = Thick \int_{-1}^{+1} \left\langle \frac{1-\xi}{2} \quad \frac{1+\xi}{2} \quad 0 \quad 0 \quad 0 \quad 0 \quad 0 \quad 0 \right\rangle^T \left(\frac{1-\xi}{2}\bar{L}_{en_1} + \frac{1+\xi}{2}\bar{L}_{en_2} \right) \sqrt{\left(\frac{X_2 - X_1}{2}\right)^2 + \left(\frac{Y_2 - Y_1}{2}\right)^2}\, d\xi$$

(A-84)

This is the vector that represents heat boundary condition normal to the boundary surface. It is noteworthy that although shape function and derivatives for side 3-4 are different from the other sides, integration for all sides leads to a unique result. Therefore a unique formulation can be used for all sides of the element.

If triangular element is used, shape functions would be as follows:

Side 1-2

$$\phi_1 = \frac{1-\xi}{2}, \phi_2 = \frac{1+\xi}{2}, \phi_3 = 0, \phi_4 = 0, \phi_5 = 0, \phi_6 = 0 \tag{A-85}$$

Side 2-3

$$\phi_1 = 0, \phi_2 = \frac{1-\eta}{2}, \phi_3 = \frac{1+\eta}{2}, \phi_4 = 0, \phi_5 = 0, \phi_6 = 0 \tag{A-86}$$

Side 3-1

$$\phi_1 = \frac{1-\eta}{2}, \phi_2 = 0, \phi_3 = \frac{1+\eta}{2}, \phi_4 = 0, \phi_5 = 0, \phi_6 = 0 \tag{A-87}$$

Shape function in this case will be

Side 1-2 $$N_T = \left\langle \frac{1-\xi}{2} \quad \frac{1+\xi}{2} \quad 0 \quad 0 \quad 0 \quad 0 \right\rangle \tag{A-88}$$

Side 2-3 $$N_T = \left\langle 0 \quad \frac{1-\eta}{2} \quad \frac{1+\eta}{2} \quad 0 \quad 0 \quad 0 \right\rangle \tag{A-89}$$

Side 3-1 $$N_T = \left\langle \frac{1-\eta}{2} \quad 0 \quad \frac{1+\eta}{2} \quad 0 \quad 0 \quad 0 \right\rangle \tag{A-90}$$

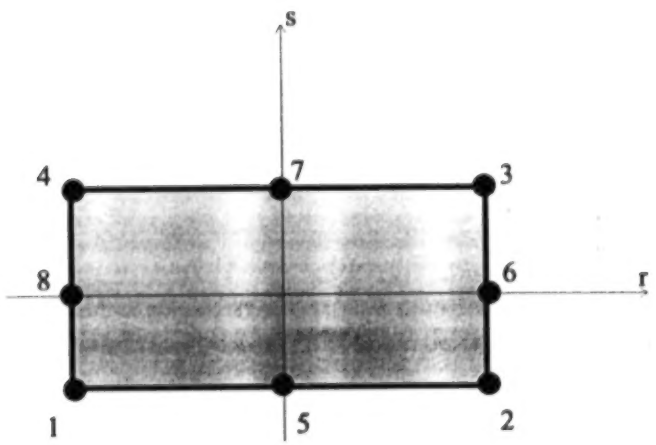

Figure (A-1) 8-node rectangular element for displacements

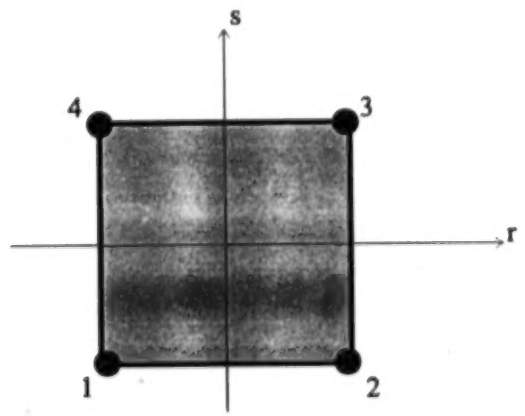

Figure (A-2) 4-node rectangular element for pore pressures and temperature

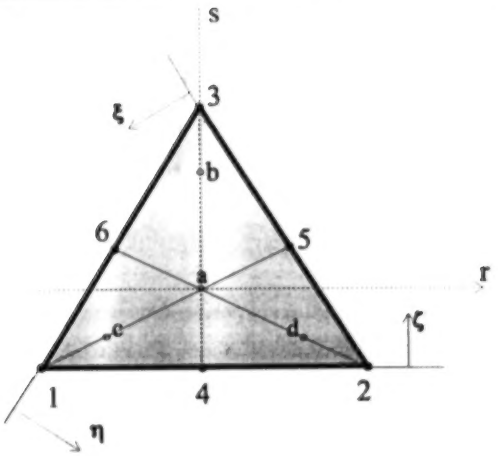

a: 1/3,1/3,1/3 (weight=-27/48)
b: 0.6,0.2,0.2 (weight=25/48)
c: 0.2,0.6,0.2 (weight=25/48)
d: 0.2,0.2,0.6 (weight=25/48)

Figure (A-3) 6-node triangular element

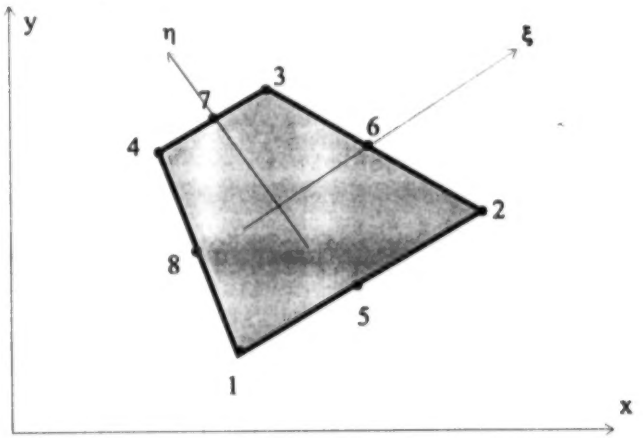

Figure (A-4) Local and global coordinates for 8-node rectangular element

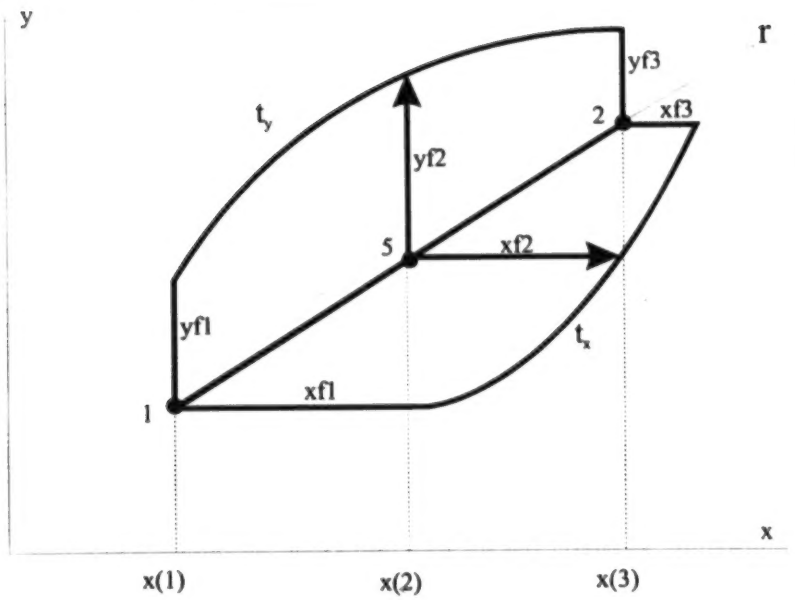

Figure (A-5) Traction on the element boundary in two directions

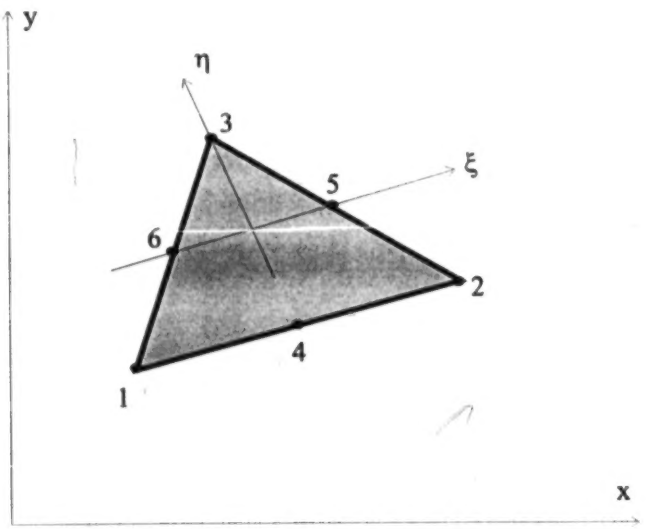

Figure (A-6) Local and global coordinates for 6-node triangular element

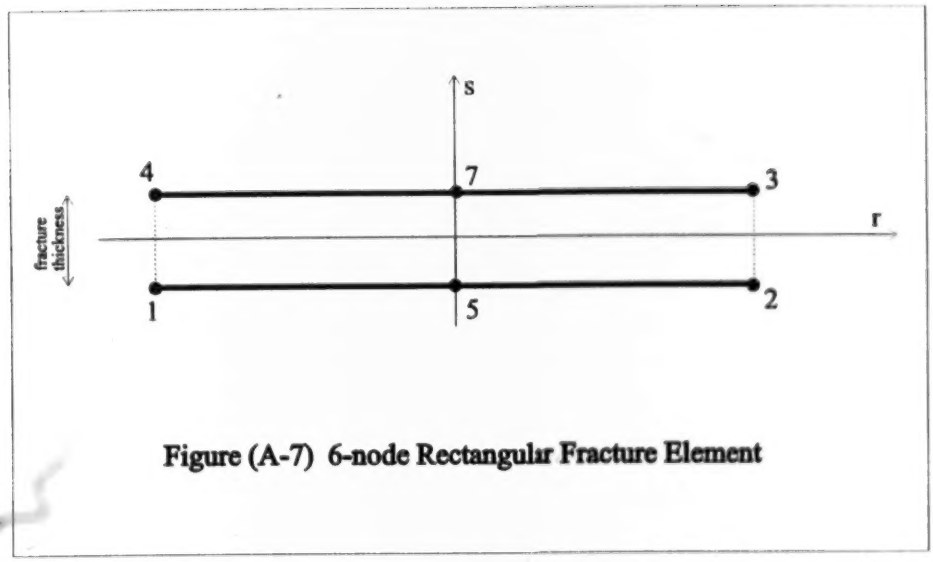

Figure (A-7) 6-node Rectangular Fracture Element